Two-Part Reactive Formulations for Intranasal Delivery of Benzodiazepines

A DISSERTATION
SUBMITTED TO THE FACULTY OF THE
UNIVERSITY OF MINNESOTA
BY

Davin Rautiola

IN PARTIAL FULFILLMENT OF THE REQUIREMENTS
FOR THE DEGREE OF
DOCTOR OF PHILOSOPHY

Advisor
Ronald A. Siegel, ScD

August 2019

Acknowledgements

A great number of highly skilled, passionate individuals worked together to make this body of work possible. Their labors and gracious guidance were indispensable to the project, my education, and my personal growth.

Foremost among them is my advisor, Dr. Ronald A. Siegel. He is a brilliant mentor whom I will forever admire for his astounding breadth of knowledge and ability to reconcile multiple disciplines to form an objective view of the world. Many members of the Siegel Research Group also made significant contributions to this work: Dr. Mamta Kapoor laid the foundation for intranasal delivery of prodrug/enzyme systems; Rafael Castro and Carolyn Rath helped orientate me to the project when I joined the group; Joel Updyke assisted with enzyme stability studies; Hari Gopalakrishnan assisted with characterization of the midazolam system; Roshini 'Hailie' Jadoo assisted with imaging drug precipitates; and longstanding group members Dr. Anasuya Sahoo, Krutika Jain, and Allison Siehr routinely provided helpful feedback and valuable insights.

In league with Dr. Siegel, my unofficial secondary advisor, Dr. James C. Cloyd, was equally impactful to my success and growth. As Director of the Center for Orphan Drug Research (CODR), Dr. Cloyd provided many of the resources and connections necessary to progress the project from *in vitro* formulation development to pre-clinical *in vivo* studies. His expertise in rescue therapies for seizure emergencies is unparalleled. It was a privilege to learn from him and the rest of the CODR team. Without diminishing the contributions of those unnamed, I would like to express my gratitude to some of the team

members specifically: Patricia D. Maglalang spent many long hours with me to prepare, perform, present, and publish the *in vivo* study; Dr. Lisa D. Coles' astute observations and command of pharmacokinetics were essential at nearly every step, from study design to results interpretation; and Usha Mishra, who is not only an excellent analytical chemist, but a pleasure to work with as well.

Our other University of Minnesota based collaborators included those that hail from the Institute for Therapeutics Discovery and Development (ITDD): Dr. Gunda I. Georg and Dr. Michael A. Walters helped guide the strategy for selection and production of test articles; Dr. Narsihmulu Cheryala synthesized the prodrugs; and Dr. Kathryn M. Nelson provided enzyme. From the College of Veterinary Medicine: Dr. Edward 'Ned' E. Patterson and Dr. Jessica A. Lawrence provided CT scans of canine nasal cavities. From the Earl E. Bakken Medical Devices Center: Davis Fay provided CT segmentation training, and Geoffrey Dybicz worked on the case and trigger mechanism for the functional nasal spray device prototype.

External collaborators included those from HealthPartners Institute: Dr. Leah R. Hanson, Dr. Jared M. Fine, Aleta L. Svitak, and Katherine A. Faltesek were instrumental in the conduct of the *in vivo* study. Histopathology was conducted at Colorado Histo-Prep by Dr. Rajan Bawa, Dr. Paul K. Hildebrandt, and Matthew Stone. And Dr. Robert K. Schultz of Sollievo Pharmaceuticals, Inc. helped guide translational aspects of the project.

Members of the faculty and student body in the Department of Pharmaceutics also shared their resources, time, and knowledge. Cell culture was performed in Dr. William

F. Elmquist's lab with assistance from Dr. Gautham Gampa and Dr. Minjee Kim. Polarized microscopy was performed in Changquan Calvin Sun's lab with assistance from Kunlin Wang. Solid state characterization was performed in Dr. Raj Suryanarayanan's lab with assistance from Dr. Seema Thakral and Dr. Sampada Koranne.

At various stages throughout this project, generous financial support was received from the University of Minnesota's NIH Research Evaluation and Commercialization Hub (MN-REACH), Epilepsy Foundation, American Epilepsy Society, Academic Health Center University of Minnesota, and Sollievo Pharmaceuticals, Inc. Parts of this work were carried out in the Characterization Facility, University of Minnesota, which receives partial support from NSF through the Materials Research Science and Engineering Centers (MRSEC) program. Financial support in the form of fellowships was received through a 3M Science and Technology Fellowship in Drug Delivery, Theodore H. Rowell Graduate Fellowship, Pre-Doctoral Fellowship in Pharmaceutical Sciences from the American Foundation for Pharmaceutical Education (AFPE), Pre-Doctoral Fellowship in Pharmaceutics from the Pharmaceutical Research and Manufacturers of America (PhRMA) Foundation, and Graduate School Excellence Research Grant from the University of Minnesota.

Finally, a special thanks to my committee members, Dr. Ronald A. Siegel (advisor), Dr. James C. Cloyd (chair), Dr. Timothy S. Wiedmann, and Dr. Raj Suryanarayanan, for setting aside time in their busy schedules to review this dissertation and participate in my oral defense.

Dedication

This work is dedicated to the lovely Madeleine Filloux. Thank you for being unwavering in your support and being a beacon of sanity through the tribulations that abound in graduate studies. I am fortunate to have such a strong, independent partner to show me how to be a better person. And I am excited for the next adventure in life with you by my side.

Abstract

A seizure emergency occurs when an individual experiences a seizure that lasts for more than five minutes (status epilepticus) or multiple distinct seizures with incomplete recovery between them (acute repetitive seizures). A patient experiencing a seizure emergency must be treated as quickly as possible to avoid lasting neurological damage and other life-threatening complications. Benzodiazepines are the primary rescue medications used to treat seizure emergencies, the most commonly used being intravenous lorazepam or rectal diazepam. Despite the effectiveness of these drugs, the delivery routes are not ideal for first-line, outpatient treatments. A skilled caregiver must be present to administer drugs intravenously, and the social stigma associated with rectal administration results in low compliance. Intranasal delivery is an attractive alternative because it requires little training, is easily performed by non-medical personnel, carries a low risk of injury to the patient, and can provide a rapid therapeutic effect. However, formulating a benzodiazepine nasal spray is challenging because these drugs have very low aqueous solubilities.

One strategy to circumvent solubility issues relies on *in situ* production of drug from co-administration of soluble reactants. Herein, we describe how a prodrug/enzyme reaction or an acid/base reaction can be used to deliver a benzodiazepine in an aqueous vehicle with a volume and pH appropriate for intranasal administration. When the soluble components of these two-part reactive formulations are mixed at the time of administration, a metastable supersaturated solution of the benzodiazepine is produced. The supersaturated state of the benzodiazepine provides a large chemical activity gradient for rapid absorption across the nasal mucosa and into systemic circulation. *In vitro*

characterization of the reaction kinetics and supersaturation behaviors for diazepam prodrug/enzyme reactions, midazolam prodrug/enzyme reactions, and midazolam acid/base reactions demonstrated that these two-part formulations generate predictable levels of supersaturated drug. An *in vivo* pharmacokinetic study in rats showed that rapid absorption and high bioavailability of diazepam results from intranasal administration of a diazepam prodrug/enzyme formulation. Furthermore, a dual chamber nasal spray device capable of mixing and atomizing the components of a two-part formulation was designed, prototyped, and tested. These two-part reactive formulations, coupled with the specialized nasal spray device, exemplify a new intranasal drug delivery strategy that may be applicable to a variety of other drugs with poor stability or low solubility.

Table of Contents

List of Tables

List of Figures

Abbreviations

Abbreviation	Name
A	Arrhenius frequency factor
AA	amino acid
Abs	absorbance
ANOVA	analysis of variance
AOP	*Aspergillus oryzae* protease
APB	aminopeptidase B
APN	aminopeptidase N
AUC	area under the curve
AVF	avizafone
A_X	mole amount of species X
BZD	benzodiazepine
C	concentration
CBS	citrate buffered saline
$C_{DZP,lim}$	solution concentration limit for diazepam
C_{ind}	induction concentration
CL_{int}	intrinsic clearance
cLogD	calculated log of octanol/water partition coefficient at specified pH
C_{max}	maximum concentration
$C_{nasal,DZP,sol}$	nasal cavity concentration of diazepam in solution
CT	computed tomography
d	distance
DMEM	Dulbecco's modified Eagle’s medium

DTE	drug targeting efficiency
DZP	diazepam
DZP_{open}	open ring diazepam
E_a	activation energy
ee	enantiomeric excess
ε	molar absorptivity
F	bioavailability
FBS	fetal bovine serum
f_u	faction unbound
HEPES	4-(2-hydroxyethyl)-1-piperazineethanesulfonic acid
ΔH_f	molar heat of fusion
ΔH_s	molar heat of solidification
ID	internal diameter
IM	intramuscular
IN	intranasal
IPA	isopropanol
IPTG	isopropyl β-D-1-thiogalactopyranoside
IS	internal standard
IV	intravenous
JM109	*E. coli* bacteria strain
k_2	cyclization rate constant
$k_{a,DZP}$	diazepam absorption rate constant
$k_{a,ORI}$	open ring intermediate absorption rate constant
k_{cat}	catalytic rate constant

k_{deg}	degradation rate constant
k_{in}	rate constant into membrane compartment
K_M	Michaelis constant
k_{out}	Rate constant out of membrane compartment
K_P	partition coefficient
ℓ	path length
λ	wavelength
λ_z	terminal rate constant
LLPS	liquid-liquid phase separation
L*p*NA	lysine-*para*-nitroanilide
Lys-MDZ_{pro}	lysyl-midazolam prodrug
MAD	nasal mucosal atomization device
Man	mannitol
MDCKII-wt	wild type Madin-Darby canine kidney epithelial cells
MDZ	midazolam
MDZ_{open}	open ring form of midazolam
MDZ_{open}•2HCl	dihydrochloride salt of the open ring form of midazolam
MDZ_{pro}	prodrug of midazolam
MES	2-(N-morpholino)ethanesulfonic acid
MeOH	methanol
NBF	Neutral buffered formalin
NCA	noncompartmental analysis
ND	not determined
ORI	open ring intermediate

P	stagnation pressure
P_{app}	apparent permeability coefficient
PBPK	physiologically based pharmacokinetic model
PBS	phosphate buffered saline
Phe-MDZ_{pro}	phenylalanyl-midazolam prodrug
*p*NA	*para*-nitroaniline
ppt	precipitate
pQE-30 Xa	DNA vector construct
PVA	polyvinyl alcohol
Q	blood flow rate
R	blood to plasma ratio (or ideal gas constant)
R^2_{adj}	adjusted square correlation coefficient
RMSE	root mean square error
RNPEP	aminopeptidase B gene
rt	room temperature
Rxn	reaction
S	degree of supersaturation (or surface area)
SD	standard deviation
SE	standard error
S_{lim}	degree of supersaturation at $[X]_{lim}$
t	time
T	temperature
$t_{1/2}$	half-life
$t_{1/2,z}$	terminal half-life

T_{cc}	cold crystallization temperature
TEER	transepithelial electrical resistance
T_g	glass transition temperature
θ	cone angle
t_{ind}	induction time
T_m	melting temperature
t_{max}	time to peak concentration
Tre	trehalose
Tris	tris(hydroxymethyl)aminomethane
V	volume
V_{max}	maximum reaction velocity
$[X]_t$	concentration of species X at time t
$[X]_{lim}$	upper limit of metastable zone for species X
$[X]_{eq}$	thermodynamic equilibrium concentration of species X

Chapter 1: Introduction

1.1 Background

1.1.1 Seizure emergencies

Seizure activity is defined as abnormally excessive or synchronous neuronal activity in the brain.[1] The symptoms of a seizure can vary from subtle loss of awareness as occurs with absence seizures to complete loss of consciousness coupled with convulsions as occurs with tonic-clonic seizures. The duration of seizure activity can also vary. Some are brief, isolated events while others can be prolonged episodes lasting several minutes or more. Seizures that last longer than 5 minutes (status epilepticus) or present in clusters with only temporary or partial recovery between events (acute repetitive seizures) are serious medical emergencies that require immediate treatment.[2] As little as 15 minutes of continuous seizure activity can damage neurons and cause focal neurological deficits, cognitive impairment, or epileptogenesis.[2,3] There are also life threatening complications associated with prolonged seizure activity such as hypoxia, metabolic acidosis, hyperthermia, aspiration, or pulmonary edema. Mortality increases with seizure duration.

It is estimated that 126,000 - 195,000 cases of status epilepticus occur per year in the United States, with costs associated from hospital visits on the order of $4 billion/year.[4-6] Of those cases, 22,200 - 42,000 cases result in death.[6] The risk of injury or death is mitigated by prompt medical treatment.[7] However, treatment of seizure emergencies can be significantly delayed if the patient must wait for medical personnel or transportation to the emergency room. A study performed at one emergency room found the average delay to treatment was 85 minutes.[2,8] Epileptic patients who experience an aura before the onset

of a seizure, receive a warning from a seizure prediction device, or are conscious between clustered events may be able to self-administer a rescue therapy to prevent an oncoming episode.[9] Furthermore, a rescue therapy could be carried by the patient or included in first aid kits in places like airplanes to be administered by bystanders during a seizure emergency. Therefore, there is a need for outpatient treatments that can be administered immediately at the onset of a seizure by non-medical personnel.

1.1.2 Benzodiazepines as rescue therapy

Benzodiazepines are the primary rescue medications used to treat seizure emergencies such as status epilepticus. This class of drugs includes lorazepam, diazepam (DZP), and midazolam (MDZ). An intravenous (IV) injection of lorazepam or diazepam, or an intramuscular injection of MDZ are the recommended first-line treatment options.[10] However, a medical professional must be present to perform IV administration because there is risk of infiltration, hematoma, air embolism, phlebitis, infection, extravascular drug delivery, or intraarterial injection if done incorrectly. Intramuscular drug delivery can also be problematic, especially for non-medical personnel. The technique requires training and comes with similar risks of improper injection or injury. It can be particularly difficult to carry out on obese or emaciated individuals, in the presence of multiple layers of clothing, or in public places. Other benzodiazepine-based treatment modalities have been developed for outpatient use, each exhibiting advantages and disadvantages. The only outpatient first-line treatment approved in the US is Diastat®, rectally administered DZP. This product demonstrated that outpatient management of seizure emergencies by nonmedical personnel is possible, safe, and highly effective.[11] However, there is social stigma associated with

rectal administration and patients often object to this route despite its proven benefits.[12] A product for buccal administration of MDZ is available in Europe under the trade name Buccolam®. Buccal administration carries the risk of aspiration and inconsistent absorption due to ictal salivation.[13] Intranasal (IN) delivery of benzodiazepines is an attractive alternative because it leads to rapid onset of therapeutic effect, requires little training, is easily performed, and carries a low risk of injury.[14]

1.1.3 Intranasal delivery

Benzodiazepines are small, lipophilic drugs. Systemic delivery of these types of drugs by IN administration offers several important advantages that make the IN route attractive over other routes of administration, especially for outpatient treatments requiring a rapid onset of therapeutic effect. Four of these advantages are well known and commonly cited.[14,15] 1) Peak plasma concentrations can be quickly attained due to the large surface area, high vascularization, and thin epithelium of the nasal mucosa; 2) First pass metabolism can be avoided, thus improving the bioavailability of some drugs; 3) The nasal cavity is easily accessed during a medical emergency, posing a lower risk of injury to the patient compared to parenteral routes of administration; 4) Operation of nasal spray devices does not require special skills, dosing is generally intuitive and easily performed. An additional key advantage is less obvious and is the subject of this dissertation: the nasal cavity, as such, offers a convenient location where drug can be produced *in situ* from the administration of two-part reactive formulations.

The nasal cavity is a dynamic environment that enables rapid drug absorption, but also limits the amount of time available for drug absorption. The bulk of the liquid

introduced into the nasal cavity by a nasal spray pump initially deposits in the less permeable atrium region of the nasal cavity, just past the nasal valve.[16,17] The surface area of epithelium exposed to drug expands from the area of initial deposition as the formulation mixes with nasal secretions and gets carried across the highly permeable respiratory mucosa at a rate of 5–6 mm/min by mucociliary clearance.[18,19] The total surface area of the nasal cavity has been reported to be 150–250 cm^2 with mucosal thicknesses varying from 0.3–5 mm.[20-24] The respiratory mucosa, containing the turbinates, provides most of the surface area. In this region the 40–100 μm thick epithelium is the rate limiting barrier to absorption, with porous subepithelial tissue and a dense network of fenestrated capillaries acting as an effective sink for rapid drug absorption.[25]

The capillary beds allow drug to enter directly into the systemic circulation, thereby bypassing gastric and hepatic first pass metabolism. For some drugs, such as butorphanol, avoiding first pass metabolism by IN delivery can result in a substantial increase in bioavailabilty.[26] However, the transit time for lateral transport of drugs across the surface of the mucosa by mucociliary clearance is generally 15–20 minutes.[19] Slower absorption and lower bioavailability may result for any portion of the dose that gets cleared to the digestive tract.

In emergency situations, IN administration can be faster than IV administration. A retrospective study performed by Inokuchi et al. compared the efficacy of IV versus IN delivery of a DZP parenteral formulation for the treatment of status epilepticus.[27] These authors found that IN DZP was administered nine times faster than IV DZP (1 min IN vs 9.5 min IV), and the difference in time to seizure termination after dosing was not

statistically significant between the two routes (3 min IN vs 0.5 min IV, p=0.43). Although nasal pain and hemorrhaging from IN administration of commercial parenteral formulations containing organic solvents were mentioned in the medical records, they concluded that IN administration of DZP is safe, effective, and can be implemented outside of hospital settings. Off-label IN administration of parenteral benzodiazepine formulations (usually MDZ) to treat seizure emergencies is fairly common; however, there is currently no nasal spray benzodiazepine product on the market (reasons discussed below). A benzodiazepine rescue medication specifically formulated and approved for IN administration would permit outpatient treatment, with potential to reduce emergency department visits and improve the quality of life for patients who experience seizure emergencies.

1.1.4 Solubility of benzodiazepines

The poor aqueous solubility of benzodiazepines presents a challenge in formulating them as nasal sprays. The thermodynamic aqueous solubilities of MDZ and DZP are 55 ± 4 μM (0.018 ± 0.001 mg/mL) and 130 ± 11 μM (0.037 ± 0.003 mg/mL) respectively, at pH 7.4 and 32 °C.[28] In comparison, the therapeutic dose of IN DZP or IN MDZ is 0.1-0.3 mg/kg.[29-31] The volume of liquid that can be reliably deposited in the human nasal cavity without causing loss by runoff of excess solution through the nasal vestibule or drainage into the nasopharynx is less than 200 μL.[22,24] Most commercial nasal spray products deliver 50-140 μL dose volumes, but the optimum volume for an adult is 100 μL per half-cavity.[32,33] Therefore, drugs must be sufficiently potent and concentrated to be candidates for the IN route.

There are several low volume IN formulations of DZP and MDZ currently being developed which utilize co-solvents or other additives to improve solubility.[29,34] One such IN formulation of MDZ contains propylene glycol and uses a low pH of 4 to achieve adequate solubility.[35] The use of organic solvents or a formulation pH below normal nasal pH can be highly irritating to nasal mucosa. Transient epistaxis, nasal discomfort, nasal congestion, and rhinitis have been reported as common adverse events with these formulations.[30,36,37] Furthermore, the time to maximum plasma concentration (t_{max}) for these formulations can be delayed. For IN DZP formulations containing solubilizers have been reported with t_{max} in the range of 0.75-1 hr.[12,37] MDZ is more rapidly absorbed (t_{max} = 10-30 min) following IN administration and has a relatively rapid onset of effect, but its bioavailability is intermediate and variable, with fraction absorbed F = 60-70% ± 20-25%.[12] Limited and variable absorption exposes patients to the risk of inconsistent response.

1.1.5 Two-part, reactive formulation strategy

Water is the preferred solvent for nasal spray formulations. Organic co-solvents or other solubilizing additives reduce the driving force for permeation of drug across membranes[38,39] and can irritate or injure sensitive nasal tissues.[34,40] One strategy to formulate lipophilic drugs in aqueous solutions employs a water-soluble prodrug and typically relies on endogenous enzymes for *in vivo* biotransformation to active drug.[41] Our group has been developing an extension to this strategy that involves either the co-administration of a prodrug with its converting enzyme or co-administration of other reactive precursors to produce a supersaturated solution of active drug at the site of

administration (Figure 1 and Figure 3). The precursors are designed to be highly water soluble, so they can be formulated to therapeutically relevant concentrations for IN delivery at physiological pH without the use of organic co-solvents. In addition to overcoming solubility issues, the supersaturated state of benzodiazepine produced by these two-part reactive formulations provides an increased driving force for enhanced permeation of the drug across nasal mucosa. A series of *in vitro* experiments demonstrated enhanced permeation of drug across cell membranes using aqueous prodrug/enzyme formulations.[28,42,43] Therefore, an earlier t_{max} and more complete absorption is expected, resulting in a rapid onset of therapeutic effect and the ability to abort a seizure emergency quickly.

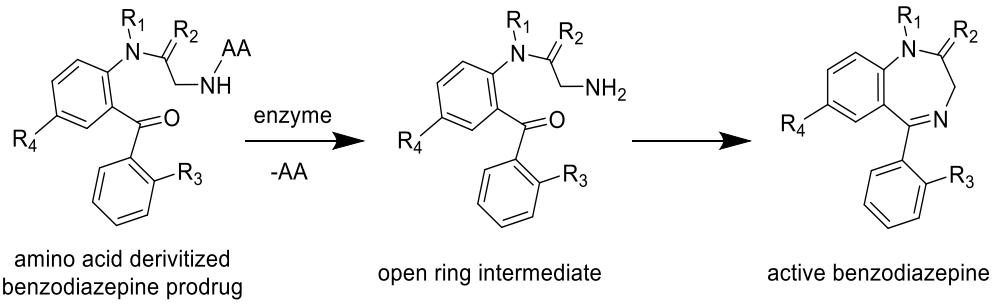

Figure 1. Hydrolysis of amino acid derivatized benzodiazepine prodrugs. Enzymatic hydrolysis of the amino acid moiety (AA) from the soluble prodrug produces an open ring intermediate that spontaneously cyclized to form the insoluble active drug. Core structure of benzodiazepines shown with R denoting substitution locations that give rise to specific benzodiazepines, such as DZP or MDZ.

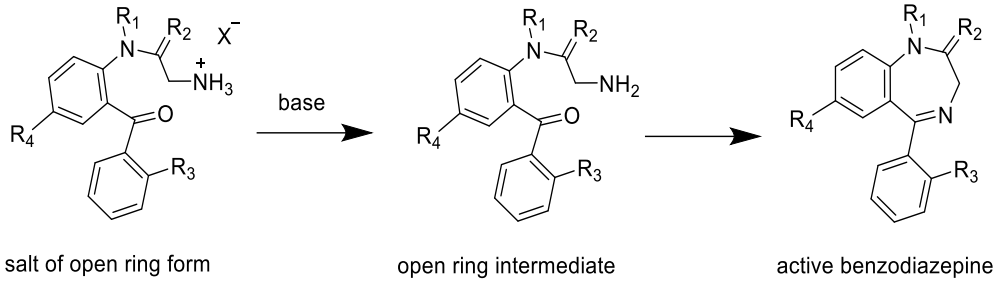

Figure 2. Soluble salt precursor combined with a base to form active benzodiazepine. Salts of open ring forms of benzodiazepines are soluble but produce low pH solutions. Combining the acidic salt with a base liberates the open ring intermediate, which spontaneously cyclizes to form the active benzodiazepine and a solution pH appropriate for IN delivery. The symbol X^- is a counter anion such as a chloride.

Although this work is focused on the IN delivery of benzodiazepines to treat seizure emergencies, the two-part reactive formulation approach to enhance drug permeation and overcome drug solubility issues may be applicable to a variety of therapeutics. Drugs that were previously considered unsuitable for IN delivery due to poor solubility may be reevaluated for IN delivery as co-administered soluble precursors. Examples of conditions that may benefit from this two-part reactive formulation approach for rapid IN drug delivery are numerous and include panic disorders, pain, migraines, erectile dysfunction, allergic reactions, nausea, cardiac events, or motion sickness.

1.2 Chapter descriptions

1.2.1 Chapter 2. Conversion of a soluble diazepam prodrug to supersaturated diazepam for rapid intranasal delivery: kinetics and stability

System examined: This chapter discusses the supersaturation behavior of DZP generated from a prodrug/enzyme reaction. Avizafone (AVF), a water-soluble lysyl-prodrug of DZP, was converted to DZP using a fungal enzyme, *Aspergillus oryzae* protease (AOP). Enzymatic hydrolysis of the lysine moiety from avizafone releases an open ring intermediate species (ORI) that spontaneously cyclizes to form DZP.

Initial hypothesis: We hypothesized that the rate, extent, and time course of DZP supersaturation from AVF hydrolysis would be dependent on reaction conditions (pH, buffer agent, tonicity, enzyme concentration, etc.), and optimizing these parameters would allow the identification of a formulation that balances the DZP production rate with the absorption rate across membranes without leading to precipitation of DZP.

Methods: The reaction conditions were varied, and solution concentrations for the AVF, ORI, and DZP were monitored using a second derivative spectroscopic method. The time points and concentrations at which DZP began to phase separate under each condition were determined by light scattering. And the precipitates were analyzed for crystallinity.

Conclusions: Phase separation of DZP in prodrug/enzyme formulations that produce DZP concentrations in excess of the upper limit of supersaturation would not be detrimental to IN delivery of DZP by virtue of the precipitate being amorphous rather than

crystalline. The presence of the amorphous precipitate leads to a constant, predictable, and maximal level of supersaturation. Pharmaceutical formulations of DZP prodrug/enzyme combinations should utilize buffering agents, pH, and enzyme concentrations that achieve the highest rate of DZP production and absorption without causing nasal tissue irritation. In the case of AVF/AOP, a formulation pH at the upper bound of the physiological pH range of the nasal cavity provided the fastest reaction rate. The rate of DZP production increased with AOP concentration until a maximum was reached, then counterintuitively slowed with increasingly higher enzyme concentrations.

1.2.2 Chapter 3. Intranasal co-administration of a diazepam prodrug with a converting enzyme results in rapid absorption of diazepam in rats

System examined: This chapter discusses an *in vivo* pharmacokinetic study performed in rats to test IN delivery of DZP using a prodrug/enzyme formulation. The prodrug, AVF, was co-administered with the converting enzyme, human aminopeptidase B (APB).

Initial hypothesis: We hypothesized that intranasal administration of a prodrug/enzyme formulation would result in rapid and complete absorption of DZP into systemic circulation, with correspondingly rapid distribution into the brain.

Methods: A rat model was used to test the hypothesis. The plasma and brain pharmacokinetics of IN AVF/APB were compared with IN AVF and IV DZP. In addition to standard noncompartmental pharmacokinetic analyses, we augmented an established

physiologically based pharmacokinetic (PKPB) model to incorporate mechanistic components, including enzyme reaction kinetics, absorption of both ORI and DZP across the nasal mucosa, supersaturation of DZP, and liquid-liquid phase separation of DZP.

Conclusions: The results indicated that IN co-administration of AVF with APB is a viable method to rapidly deliver DZP into systemic circulation and subsequently to the brain.

1.2.3 Chapter 4. Substrate stabilizes human aminopeptidase B during lyophilization

System examined: For the DZP prodrug/enzyme formulation, both AVF and APB would need to have adequate stability to be used in a pharmaceutical product. Their solution and solid state stabilities were investigated.

Initial hypothesis: We hypothesized that the prodrug substrate, AVF, would stabilize the enzyme, APB, in the solid state by docking in the active site (i.e. substrate binding pocket) and preventing the collapse of the active site during lyophilization.

Methods: Solutions of AVF, APB, and other excipients were combined at low temperatures to prevent substrate turnover. The solutions were then snap frozen, lyophilized, and stored. When the lyophilizates were reconstituted in warm buffer, DZP production initiated. The DZP concentration-time profiles were used to infer the concentration of active APB remaining in each sample after lyophilization and storage.

Conclusions: Co-lyophilization of the enzyme, APB, with a low concentration of its substrate, AVF, imparted initial stability on par with a high concentration of the commonly used lyoprotectant, trehalose. The combination of substrate and trehalose provided a greater stabilizing effect than either additive alone. The use of a substrate as stabilizer for lyophilizing enzymes may be applicable to a variety of substrate/enzyme pairs.

1.2.4 Chapter 5. Reactive formulations for intranasal delivery of midazolam

System examined: In this chapter, MDZ prodrug/enzyme reactions and MDZ acid/base reactions were investigated. Both two-part reactive formulation approaches produce an open ring intermediate species (ORI) that spontaneously cyclizes to form MDZ.

Initial hypothesis: We hypothesized that production of ORI using an acid/base reaction would result in faster reaction rates and thus more rapid delivery of MDZ than could be achieved by cleavage of an amino acid moiety from a prodrug using an enzyme.

Methods: UV spectroscopy was used to determine the upper limit of supersaturation for MDZ and measure the time course of MDZ prodrug/enzyme reactions and MDZ acid/base reactions. Drug transport studies were performed with selected formulations using canine kidney epithelial cell monolayers as a model for nasal epithelium.

Conclusions: The ORI cyclization step was found to be slow and rate limiting. Thus, rapid liberation of ORI from both prodrug/enzyme reactions and acid/base reactions

resulted in accumulation of ORI in solution. The permeability of ORI and MDZ were pH dependent, with the fastest rates of permeation for both observed at the highest pH tested, pH 7.4. The MDZ prodrug/enzyme reaction was not amenable to formulation at therapeutic concentrations near this pH because the pH dependent solubility of the prodrug was not favorable. Conversely, the MDZ acid/base reaction could be formulated to very high concentrations and the amount of base component adjusted such that a specific pH could be easily obtained.

1.2.5 Chapter 6. Nasal spray device for administration of two-part drug formulations

System examined: The reactive components of a two-part reactive formulation must be either inactivated or kept separate from each other during storage. At the time of administration, mixing the components or otherwise activating them creates a metastable solution that can be sprayed into the nasal cavity to deliver drug. In this chapter, a specialized nasal spray device capable of mixing components of a drug formulation and atomizing the mixture as part of the actuation process is presented.

Initial hypothesis: Rapid reconstitution of a lyophilizate and subsequent atomization of the mixture can be automated in a dual chamber nasal spray device, thereby enabling convenient storage and administration of two-part reactive formulations for intranasal delivery of benzodiazepines.

Methods: A pneumatically driven, dual chamber nasal spray device that utilizes single dose drug cartridges was designed, prototyped, and tested. Testing included measurements of spray cone angle as a function of stagnation pressure, dye formulation deposition experiments using silicone nasal cavity molds, measurements of enzyme degradation upon spraying using a DZP prodrug/enzyme formulation, and visualization of the pH profiles of spray patterns produced by an MDZ acid/base formulation.

Conclusions: The performance of the nasal spray device was dependent on the formulation properties. In most cases, lyophilizates could be rapidly reconstituted and atomized without an issue, thus demonstrating the potential to use a device such as the one described here to administer two-part drug formulations. However, the slow dissolution of formulations with collapsed lyophilizates or lyophilizates that contained a lot of mass (e.g. >25 mg AVF) tended to clog the atomizer tip. The device parameters (pressure, atomizer tip orifice size, etc.) would need to be optimized for specific formulations. Furthermore, instantaneous dissolution of lyophilizates and content uniformity between individual spray droplets does not appear to be critical since mixing and continued dissolution can occur on the surface of the nasal mucosa.

Chapter 2: Conversion of a soluble diazepam prodrug to supersaturated diazepam for rapid intranasal delivery: kinetics and stability

The contents of this chapter were published in:

Rautiola D, Cloyd JC, Siegel RA. Conversion of a soluble diazepam prodrug to supersaturated diazepam for rapid intranasal delivery: Kinetics and stability. *Journal of Controlled Release*. **2018** Nov 10; 289:1-9.

2.1 Summary

The low aqueous solubility of diazepam (DZP) presents a challenge in formulating nasal sprays without the use of organic solvents. One approach to overcome this challenge involves co-administration of a soluble prodrug, avizafone (AVF), with a converting enzyme to produce supersaturated DZP at the site of administration. In addition to overcoming solubility issues, the supersaturated state of DZP provides an increased driving force for enhanced permeation across nasal mucosa. However, supersaturated solutions are metastable, and there is a limit to the degree of supersaturation (S) that can be reached without causing spontaneous phase separation of the solute. The aim of this article was to determine how formulation parameters affect the rate of DZP supersaturation, maximum degree of supersaturation, and phase separation kinetics. A model enzyme, *Aspergillus oryzae* protease (AOP) was used to convert AVF to DZP, via an open ring intermediate (ORI). A second derivative UV spectroscopic method was developed to simultaneously monitor DZP solution concentration and the time course of DZP phase separation. Fitting a kinetic model, with prior knowledge of the enzyme kinetic parameters, the rate constant for conversion of ORI to DZP was found to be 0.470 ± 0.012 min^{-1}. Kinetics and supersaturated solution stability were studied as a function of formulation parameters, including temperature, pH, buffering agent, AVF concentration, and enzyme concentration. The maximum aqueous solution concentration for DZP at 32 ^{o}C was determined to be 1.22 ± 0.03 mM DZP (S = 9.38) and was insensitive to changes in formulation parameters, excepting temperature. Supersaturated solutions of DZP could be maintained at the maximum concentration for more than 24 hr, even in the presence of phase separated DZP. Polarized light microscopy, PXRD, and DSC analysis indicated that

the phase separated DZP was amorphous upon formation and remained so for more than 24 hr. Our findings suggest that co-administration of AVF with a suitable human converting enzyme will provide a viable mechanism for IN delivery of DZP and result in very rapid and complete absorption to quickly terminate seizure emergencies.

2.2 Introduction

Patients with epilepsy who experience acute repetitive seizures or sustained seizure activity (status epilepticus) require immediate medical attention. Left untreated, these seizure emergencies can result in death or debilitating neurological deficits, and it is estimated that costs associated with hospital visits due to status epilepticus are on the order of $4 billion/year.[4,5] Thus, there is substantial interest in developing formulations of diazepam (DZP) for rapid outpatient treatment of seizure emergencies. Currently the only approved outpatient treatment is a rectal diazepam gel (Diastat®), which relies on a drug delivery route that is inconvenient and acceptable to very few. Among possible alternative routes of administration, intranasal (IN) drug delivery is noninvasive and offers the potential for rapid drug absorption.[29,34,44] However, the low aqueous solubility of DZP presents a challenge in formulating nasal sprays. The nasal cavity accommodates up to 200 µL of liquid, so IN formulation concentrations must be high.[24,33,45] The aqueous thermodynamic equilibrium solubility of DZP ($[DZP]_{aq,sat}$) is 130 ± 11 µM (0.037 ± 0.003 mg/mL) at pH 7.4 and 32 °C.[28] In comparison, the therapeutic dose of IN DZP is 0.1-0.3 mg/kg with a maximum of 20 mg/dose.[29,30,36] Extensive literature, reviewed in ref [34], exists in which the solubility of DZP is improved by adding organic cosolvents and surfactants.

While these formulations enable liquid sprays, the additives are irritating and potentially toxic.

A prodrug approach can be utilized to overcome the poor aqueous solubility of DZP. Avizafone (AVF) is a soluble prodrug of DZP reported by Hassall *et al.* in 1977 and subsequently developed by the French military to terminate seizures caused by battlefield nerve agents.[46,47] The dihydrochloride salt of AVF is so hydrophilic that the solid material will deliquesce when exposed to the atmosphere. Structurally, AVF is a Lys-Gly dipeptide derivative of a 2-methylamino-5-chlorobenzophenone, which is susceptible to enzymatic hydrolysis of lysine (Lys) at the peptide bond (Figure 3). Cleavage of the N-terminal Lys by an endopeptidase produces an open ring intermediate (ORI) form of DZP, which undergoes intramolecular condensation to close the diazepine ring [48].

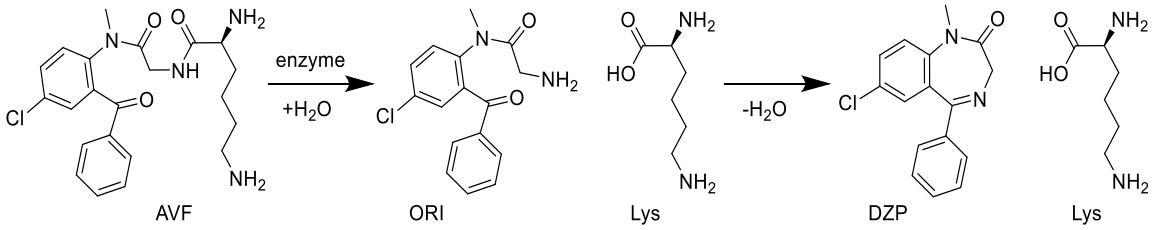

Figure 3. Hydrolysis of AVF to form DZP. Transformation of the hydrophilic prodrug AVF to hydrophobic active drug DZP progresses through an open ring intermediate, ORI.

AVF has a large polar surface area, so it is expected to have low membrane permeability and IN bioavailability.[19] Indeed, we showed previously that the apparent permeability coefficient (P_{app}) of AVF across wild type Madin-Darby canine kidney epithelial cell (MDCKII-wt) monolayers is negligible compared to $P_{app} = 2.2 \times 10^{-5}$ cm/s for DZP.[28] Therefore, we have been investigating the feasibility of co-administering AVF

with a converting enzyme to produce DZP *in situ*.[28,42,49] Following rapid mixing at the point of administration, the prodrug/enzyme systems can quickly generate supersaturated solutions of DZP when the initial molar concentration of AVF ($[AVF]_0$) exceeds the equilibrium solubility of DZP, with degree of supersaturation $S = [DZP]_{aq}/[DZP]_{aq,sat}$. Since the flux of a drug that passively diffuses across mucosal membranes is proportional to its thermodynamic activity gradient, the supersaturated solution of DZP on the apical side of the nasal mucosa is expected to be more rapidly absorbed compared to DZP whose solubility is increased by incorporating a cosolvent, surfactant, or other solubilizing additive.[38,39]

Supersaturated solutions are metastable and will ultimately form crystalline precipitates.[50,51] When supersaturated concentrations are sufficiently high, the solute can phase separate to form a concentrated amorphous phase that precedes crystallization, as illustrated in Figure 4. This process is known as 'oiling out' or liquid-liquid phase separation (LLPS).[52,53] The amorphous precipitate is in quasi-equilibrium with the relatively dilute, but still supersaturated solution. If absorption of drug, either directly from the solution or from the coexisting amorphous precipitate, is faster than crystallization, then crystallization will be averted.

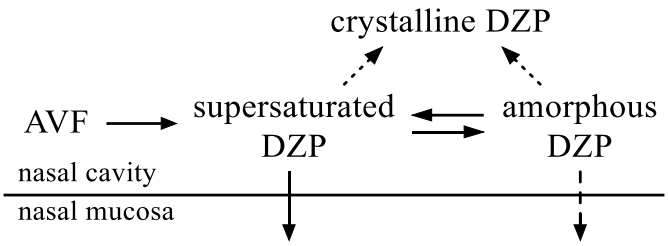

Figure 4. Supersaturation of DZP produced enzymatically from AVF drives absorption and precipitation. Dotted arrows indicate the slow crystallization process. Dashed arrow indicates potential absorption directly from the amorphous precipitate.

The aim of the work presented in this article was to determine how formulation parameters affect the rate of DZP supersaturation, maximum degree of supersaturation, and precipitation kinetics. Kinetic studies of conversion of aqueous AVF to supersaturated DZP and subsequent phase separation of DZP were performed *in vitro*. Effects of temperature, pH, buffering agent, AVF concentration, and enzyme concentration on these processes were determined using second derivative UV spectroscopy to measure DZP solution concentrations and zero order UV spectroscopy to monitor for phase separation. When the DZP concentration exceeded a critical concentration (C_{ind}), phase separation commenced and caused light scatting. This scattering was detected in the zero order spectra as a sharp increase in the extinction (Ext) of incident light at the induction time (t_{ind}). Analysis of the precipitated phase by polarized light microscopy, differential scanning calorimetry (DSC), and powder x-ray diffraction (PXRD) indicated that the phase separated DZP was initially amorphous and kinetically stable against crystallization for several days. The amorphous precipitate was also shown to undergo rapid dissolution. Therefore, the precipitate can serve as a high activity reservoir, available to supply the concentration gradient driving DZP absorption through the nasal mucosa. Direct transfer

of DZP from the amorphous precipitate into the mucosal membrane is also a possibility (Figure 4).

2.3 Methods

2.3.1 Materials

Diazepam USP (DZP, cat# 803899) was purchased from Fagron, Inc. *Aspergillus oryzae* protease (AOP, 1470 U/mL, cat# P6110), 4-(2-hydroxyethyl)-1-piperazineethanesulfonic acid (HEPES, cat# H4034), and 2-(N-morpholino)ethanesulfonic acid (MES, cat# M3671) were purchased from Sigma-Aldrich Corporation. (AOP was selected to probe the potential utility of an enzyme/prodrug combination *in vitro*; it is not a suitable enzyme for a commercial drug product owing to its fungal origin and ill-defined composition.) Phosphate buffered saline (PBS, 20 mM phosphate and 100 mM NaCl) was prepared from sodium phosphate dibasic and sodium phosphate monobasic purchased from Fisher Scientific. S-avizafone dihydrochloride (AVF, 99% ee) was synthesized from 5-chloro-2-methylaminobenzophenone according to the procedure described previously.[42]

2.3.2 UV spectroscopy

UV measurements to simultaneously determine [AVF], [ORI], $[DZP]_{aq}$, and t_{ind} (see below) were performed in a quartz cuvette (path length 1 cm) in an Agilent Technologies, Inc. Cary 100 Bio UV/Vis Double Beam Spectrophotometer equipped with a temperature controller. Prior to data collection, working solutions of the AVF and AOP reactants were prepared in buffer and equilibrated to the desired experimental temperature. Reaction progress was monitored by collecting scans over time in the vicinity of 338 nm

at a scan rate of 600 nm/min using the Cary WinUV version 3.10(246) Scan Application. At low concentrations where all species were in solution, the scans revealed isosbestic points at 301 and 338 nm, with maximum absorption sensitivity at 315 nm. Phase separation of DZP at high concentrations was detected by the appearance of a broadband scattering contribution to the spectrum which eliminated the isosbestic points. As shown in the Appendices A1 Section 2, the concentration of DZP in solution at time t ($[DZP]_{aq,t}$) could be monitored by taking the second derivative of extinction, Ext_t, at λ = 338 nm, and using the formula

$$[DZP]_{aq,t} = \frac{d^2Ext_t / d\lambda^2 - \ell\left(d^2\varepsilon / d\lambda^2\right)_{AVF}[AVF]_0}{\ell\left[\left(d^2\varepsilon / d\lambda^2\right)_{DZP} - \left(d^2\varepsilon / d\lambda^2\right)_{AVF}\right]} \quad (1)$$

where ε is molar absorptivity and ℓ is the optical path length. At 32 °C, where most of our measurements were made, this expression reduced to

$$[DZP]_{aq,t} = (0.183\ M\ nm^2)\frac{d^2Ext_t}{d\lambda^2} - 0.0495[AVF]_0 \quad (2)$$

where $[AVF]_0$ was the initial molar concentration of AVF.

2.3.3 Polarized light microscopy

AVF (2.00 mM) was hydrolyzed by 8.0 U/mL AOP in pH 7.4 PBS at 32 ^oC to form DZP precipitates. Aliquots of the reaction mixture were removed at regular time points to view under a Nikon P-1 microscope equipped with a Nikon 40x/0.65 NA - WD 0.65 Pol objective, Nikon Digital Sight DS-Fi1 camera, and temperature-controlled stage. Images were captured using NIS-Elements F 3.0 software.

2.3.4 Powder x-ray diffraction (PXRD)

AVF (7.9 mg) was dissolved in 100 μL of 20 mM phosphate buffer pH 7.4 containing 4.0 U/mL AOP, and the solution was immediately transferred to a PXRD sample holder. The reaction was allowed to proceed for 1 hr at room temperature, during which DZP precipitate settled to the bottom of the holder. A Kimwipe was used to wick away the supernatant containing the soluble species. The solid residue remaining on the bottom of the sample holder was dried at room temperature for 1 hr before analysis. The PXRD patterns of the residue and a crystalline DZP standard were obtained using a Bruker D8 ADVANCE X-ray Powder Diffractometer with Diffrac-Plus data acquisition and analysis software package. Scan parameters: 2θ range 8-35, number of steps 1373, time/step 0.5 sec.

2.3.5 Differential scanning calorimetry (DSC)

Precipitate from the reaction of 20 mg AVF with 8.0 U/mL AOP in 500μL of 20 mM phosphate buffer pH 7.4 at 32 ºC was collected by filtration and dried under high vacuum at room temperature for 5 hr. Approximately 3.5 mg of the collected solid was placed in an aluminum Tzero pan. Measurements were performed in triplicate from 0-190 ºC at a rate of 10 °C/min under nitrogen purge (50 mL/min) using a TA Instruments Q2000 V24.11 Build 124 DSC with a standard cell and Universal V4.5A software. Glass transition temperatures (T_g) were determined at the inflection point. Melting temperature ranges (T_m) were determined by the onset and peak of the melting endotherm. Similar measurements were made with crystalline DZP.

2.4 Results

2.4.1 Governing equations for the reaction and parameter identification

The following equations were assumed to describe enzymatic conversion of AVF to ORI followed by cyclization of ORI to aqueous DZP, as depicted in Figure 3:

$$\frac{d[AVF]}{dt} = -\frac{V_{max}[AVF]}{K_M + [AVF]} \tag{3}$$

$$\frac{d[ORI]}{dt} = \frac{V_{max}[AVF]}{K_M + [AVF]} - k_2[ORI] \tag{4}$$

$$\frac{d[DZP]_{aq}}{dt} = \begin{cases} k_2[ORI] & [DZP]_{aq} \le [DZP]_{aq,lim} \\ 0 & [DZP]_{aq} > [DZP]_{aq,lim} \end{cases} \tag{5}$$

where K_M and V_{max} are the usual Michaelis-Menten parameters and k_2 is a first order rate constant. The initial conditions at t = 0 were [AVF] = $[AVF]_0$ and [ORI] = [DZP] = 0. Equation 5 assumes an upper limit to the DZP concentration ($[DZP]_{aq,lim}$) and that any DZP produced in excess of this limit will phase separate as an amorphous precipitate with negligible crystallization. In this article, C_{ind} is distinct from $[DZP]_{aq,lim}$ since the concentration at which DZP begins to phase separate does not necessarily coincide with the concentration in quasi-equilibrium with the amorphous precipitate.

In previous work, where the disappearance of AVF in the presence of AOP was tracked using HPLC, we found K_M = 3.38 ± 0.34 mM and V_{max} = 0.518 ± 0.030 mM/min (± SEM) with 0.25 U/mL AOP in pH 7.4 buffer at 32 °C.[42] Using these values, the only parameter requiring adjustment to fit the data was k_2. Equations 3-5 were integrated, and

the method of least squares fitting to DZP concentration-time profile data was used to provide the best estimate for k_2.

Figure 5 shows the best fit of Equations 3-5 obtained with $[AVF]_0$ = 65 µM converted by 0.25 U/mL AOP in pH 7.4 PBS at 32 ºC. The cyclization rate constant, $k_2 \pm$ SD, was determined to be 0.470 ± 0.012 min^{-1} (half-life $t_{1/2}$ = 1.47 min). The fit is quite good, excepting minor systematic deviations at early times, which suggest slight overestimation of k_2. Better fits might have been obtained by re-estimating K_M and V_{max}, but we did not pursue this route. In addition to the $[DZP]_t$ curve, we plot the inferred values of $[ORI]_t$ and $[AVF]_t$. As expected, the substrate AVF is depleted by the enzyme, while the intermediate ORI's concentration rises and falls with increasing time.

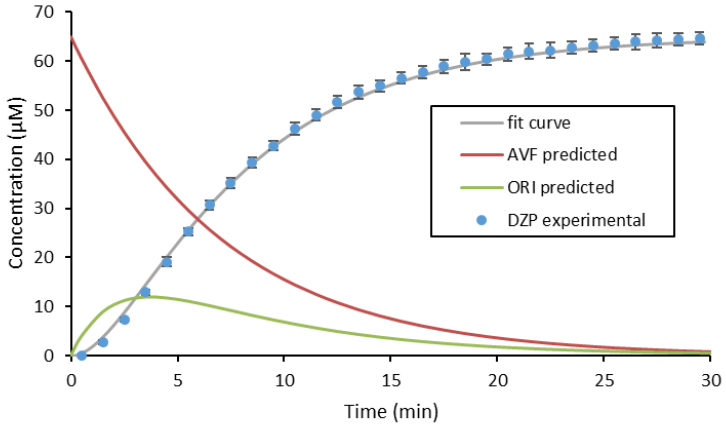

Figure 5. Kinetics of conversion of AVF to DZP, with ORI intermediate. Blue points: $[DZP]_{aq}$ measured at 315 nm during conversion of 65 µM AVF by 0.25 U/mL AOP in pH 7.4 PBS at 32 ºC. Grey curve: fit of Equations 3-5 used to determine k_2. Red curve: [AVF] predicted using Equation 3. Green curve: [ORI] predicted using Equations 4 and 5 with determined k_2.

2.4.2 Varying prodrug (AVF) concentration

Figure 6A displays the concentration-time profiles of DZP at different initial AVF concentrations. Increasing $[AVF]_0$ increased the rate of the reaction as expected but did not significantly affect C_{ind}. Solid curves are predictions based on Equations 3-5, with K_M, V_{max}, and k_2 all fixed. Given the uncertainties in these parameter values, the predictions can be regarded as satisfactory, despite minor nonrandom residuals. For $[AVF]_0$ = 3.90, 3.00, 2.00, and 1.25 mM, C_{ind} was found to be constant at 1.22 ± 0.01 mM DZP (± SD). Samples with $[AVF]_0$ at or exceeding 2.00 mM became visibly turbid and there was a substantial increase in measured Ext at 338 nm at t_{ind} (Figure 6B). Turbidity from the precipitation of DZP is demonstrated in Figure 7 (note that these images were captured at room temperature).

For $[AVF]_0$ = 1.25 mM, which is a molar concentration near $[DZP]_{aq,lim}$, the $[DZP]_{aq}$ plateau occurred at 1.22 mM. After reacting for 1 hr, the 1.25 mM $[AVF]_0$ samples appeared completely translucent to the naked eye; however, light scattering was detectable at t_{ind} = 30 min (corresponding to C_{ind} = 1.21 mM) when the axis of the Ext measurements at 338 nm or 400 nm was sufficiently scaled (Figure 6C inset). For samples with $[AVF]_0 < C_{ind}$, completion of the reaction was evident by the $[DZP]_{aq}$ plateaus near $[AVF]_0$. In these sub-C_{ind} samples, supersaturation persisted with no precipitate detectable for more than 24 hr.

With high $[AVF]_0$ (3.90 and 3.00 mM) there were oscillations accompanied by a dip in $[DZP]_{aq}$ observed immediately after t_{ind}. When the AVF substrate was exhausted, $[DZP]_{aq}$ recovered from these dips and rose to a plateau near C_{ind} (Figure 6D). It is unclear

if this behavior was due to depletion of aqueous DZP by precipitate particle growth outpacing dissolution and enzymatic DZP production, or an artifact in the measurement due to excessive precipitate in these samples. Precipitate suspended in the reaction mixture eventually settled to the bottom of the sample cuvette after about 2 hr, leading to reduced turbidity and a decrease in the Ext measurements.

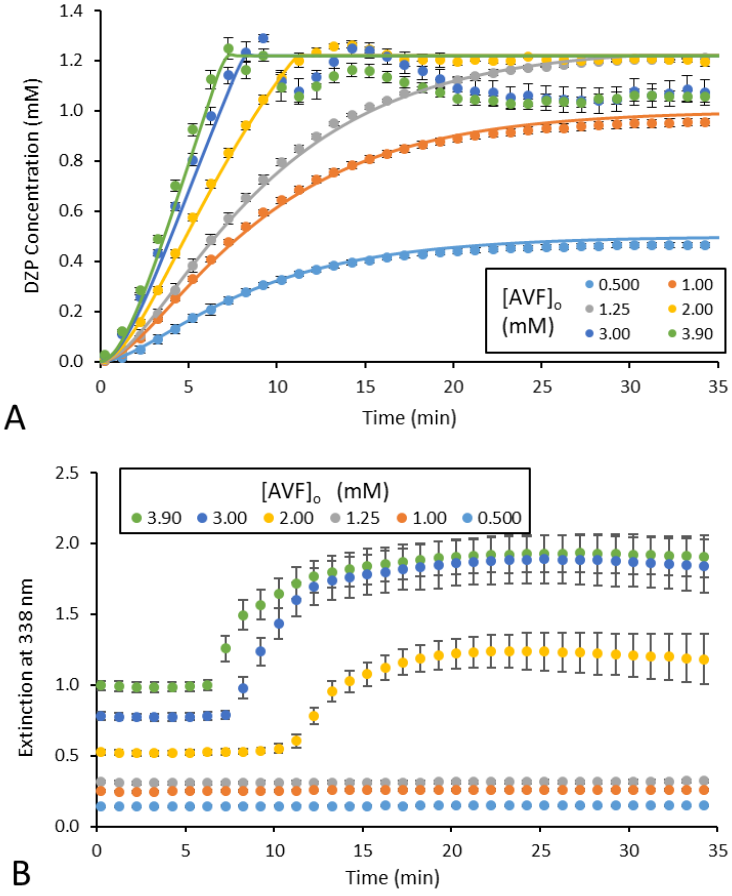

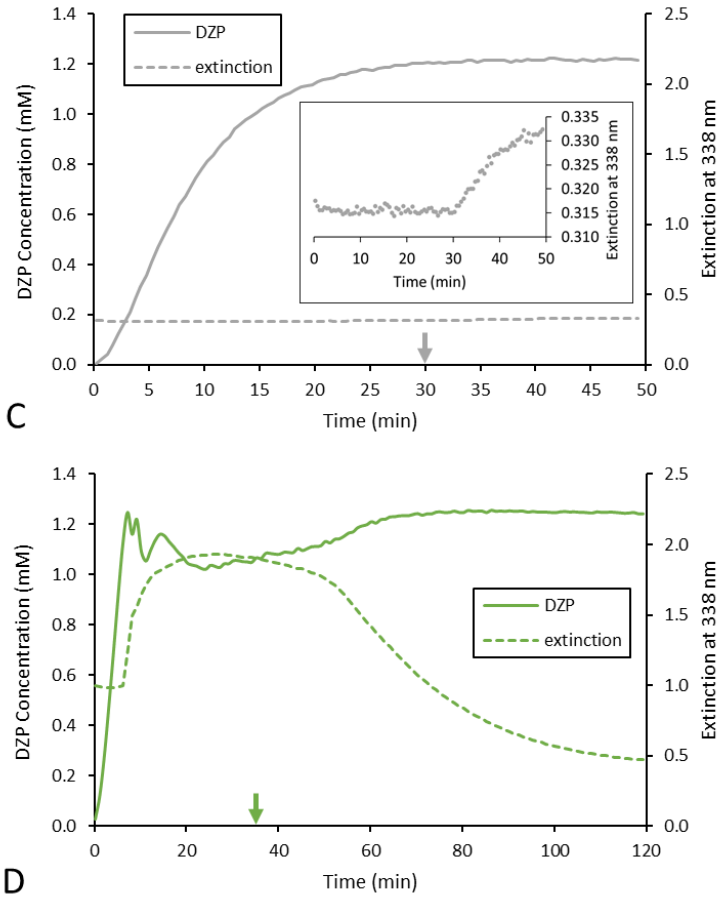

Figure 6. Effect of varying AVF concentration. (**A**) Concentration-time profiles of aqueous DZP following enzymatic conversion from 0.500, 1.00, 1.25, 2.00, 3.00, and 3.90 mM initial AVF converted by 0.25 U/mL AOP in pH 7.4 PBS at 32 °C, n = 3. Averages of experimental data shown as points with model predictions overlaid as lines. (**B**) Ext measurements corresponding to data in A. (**C**) 1.25 mM AVF experimental data from A, n = 1. Grey arrow: 98% conversion of $[AVF]_0$ to DZP at t = 30.3 min. Inset shows light scatting from DZP phase separation was detected at t = 30.0 min. (**D**) 3.90 mM AVF experimental data from A, n = 1. Green arrow: 98% conversion of $[AVF]_0$ to DZP at t = 35.3 min.

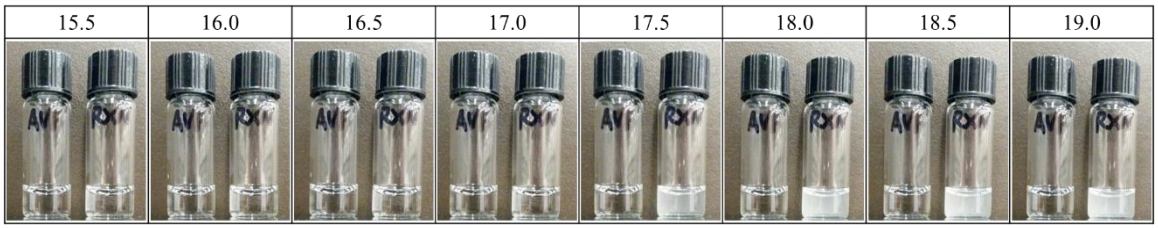

Figure 7. Time-lapse images of DZP precipitation. Turbidity due to precipitation of DZP appears suddenly, with $17.0 < t_{ind} < 17.5$ min at room temperature (~24 ^{o}C). Left vial: 2.00 mM AVF control. Right vial: 2.00 mM AVF with 0.25 U/mL AOP in pH 7.4 PBS. Times indicated above the images are in minutes.

Concentrations above C_{ind} were not sustainable for more than a few minutes as $[DZP]_{aq}$ quickly dropped to or below the upper limit of the metastable zone. After the enzymatic conversion of AVF was complete, $[DZP]_{aq}$ persisted at high concentrations in the metastable zone (Figure 8). The concentrations began to decrease after 24 hr standing at room temperature, but stayed well above $[DZP]_{aq,sat}$. This decrease was attributed to the slow crystallization of DZP, a separate process from the rapid precipitation, i.e. phase separation, of amorphous DZP. For $[AVF]_0$ = 1.00, 1.25, and 1.50 mM; $[DZP]_{aq,26days}$ = 0.79, 0.95, and 1.16 mM with S = 6.10, 7.34, and 8.89 respectively. It should be noted that the relevant time frame for IN delivery is on the order of tens of minutes. Thus, crystallization would not be relevant in the therapeutic context. More evidence that the immediate precipitate is amorphous will be presented below.

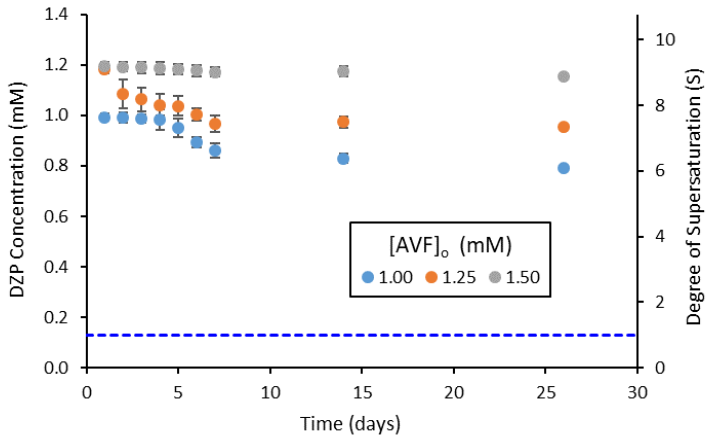

Figure 8. Kinetic stability of supersaturated DZP left standing. Extended time points for concentration-time profiles of 1.00, 1.25, and 1.50 mM AVF converted to DZP by 0.25 U/mL AOP in pH 7.4 PBS, n = 3. The enzymatic reactions were conducted at 32 °C for 1 hr, after which the samples were allowed to stand at room temperature. Blue dashed line: spectrum of DZP in buffer at $[DZP]_{aq,sat}$ = 0.130 mM (S = 1.00).

2.4.3 Varying enzyme (AOP) concentration

Increasing the concentration of the AOP also increased the rate of the reaction (Figure 9A) and the onset of turbidity (Figure 9B) as expected, but only for [AOP] ≤ 4.0 U/mL. The rate of DZP production saturated at ~3.6 mM/min with 4.0 U/mL AOP due, in part, to the finite value of k_2. With [AOP] > 4.0 U/mL, increasing the enzyme concentration resulted in progressively slower rates of DZP production as shown in Figure 9C. This 'hook effect' was attributed to unspecified interactions between the reaction species and components of the AOP preparation (refer to the Discussion section for more details). These interactions sequester AVF, effectively reducing the concentration of AVF available to enter the active site of the enzyme. In a similar fashion, binding of ORI hinders its cyclization. If we introduce scaling factors α and β, then an empirical correction for the effective concentrations for AVF and ORI can be obtained by

$$[\mathrm{AVF}]_{\mathrm{eff}} = \frac{[\mathrm{AVF}]}{1+\alpha[\mathrm{AOP}]} \quad (6)$$

$$[\mathrm{ORI}]_{\mathrm{eff}} = \frac{[\mathrm{ORI}]}{1+\beta[\mathrm{AOP}]} \quad (7)$$

Modifying the right-hand side of Equations 3-5 with the effective concentrations of AVF and ORI provided a more accurate prediction of the change in solution concentrations of DZP when the amount of AOP was varied. The values of the scaling factors, α and β, were determined concurrently by performing a least-squares fit of the modified differential equations to a matrix of DZP concentration-time profiles for t = 0.00 – 4.75 min generated by reacting AOP = 0.075 – 8.0 U/mL with 2.00 mM AVF in PBS pH 7.4 at 32 ^{o}C to give α = 0.629 and β = 0.00813.

The isosbestic point at 338 nm remained consistent prior to precipitation when [AOP] was varied (Figure 9B), confirming that ε for each of the reaction species was not affected by AOP in this region. With faster rates of DZP production there were decaying oscillations in $[DZP]_{aq}$ near C_{ind} observed immediately after t_{ind}. At very low AOP concentrations, thus slow reaction rates, these oscillations were imperceptible and C_{ind} more closely reflected $[DZP]_{aq,lim}$.

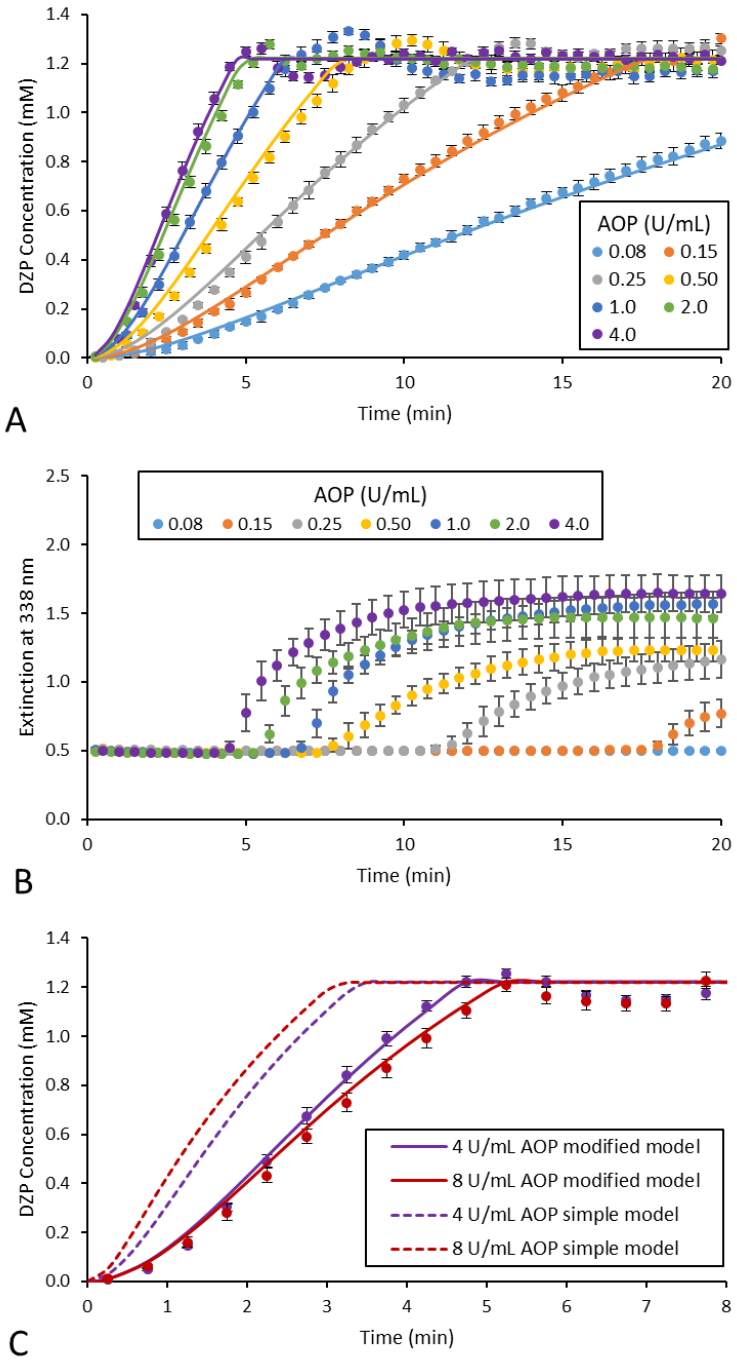

Figure 9. Effect of varying AOP concentration. 2.00 mM AVF converted by AOP in pH 7.4 PBS at 32 °C, n = 3. Averages of experimental data shown as points with model predictions overlaid as lines. (**A**) Concentration-time profiles with AOP = 0.075, 0.15, 0.25, 0.50, 1.0, 2.0, or 4.0 U/mL. (**B**) Ext measurements corresponding to data in A. (**C**)

The rate of DZP production decreased when the concentration of AOP was increased from 4.0 to 8.0 U/mL.

2.4.4 Varying temperature

Ideally, a nasal spray device containing AVF and a converting enzyme would be operated near room temperature. The components would be combined in a mixing chamber and then sprayed into the nasal cavity where nasal mucosal temperatures range from 30.2 ± 1.7 ^{o}C to 34.4 ± 1.1 ^{o}C and fluctuate with the respiratory cycle.[54] Because portable devices might be used at different temperatures, we looked at the effect of temperature over the range 20 – 40 ^{o}C on the AVF/AOP system. Within this temperature range, $d^2\varepsilon/d\lambda^2$ at 338 nm for AVF and ORI had negligible temperature dependence while $d^2\varepsilon/d\lambda^2$ for DZP decreased with increasing temperature (Appendices A1, Figure A1.54). Slopes for the linear portion of the DZP concentration-time profiles increased with increasing temperature (Figure 10A). At each temperature, there was an abrupt increase in Ext measurements at 338 nm, corresponding to phase separation of DZP when $[DZP]_{aq}$ reached C_{ind}. With lower temperatures, both C_{ind} and $[DZP]_{aq,lim}$ decreased, although the effect of temperature was less prominent for C_{ind} (Figure 10B).

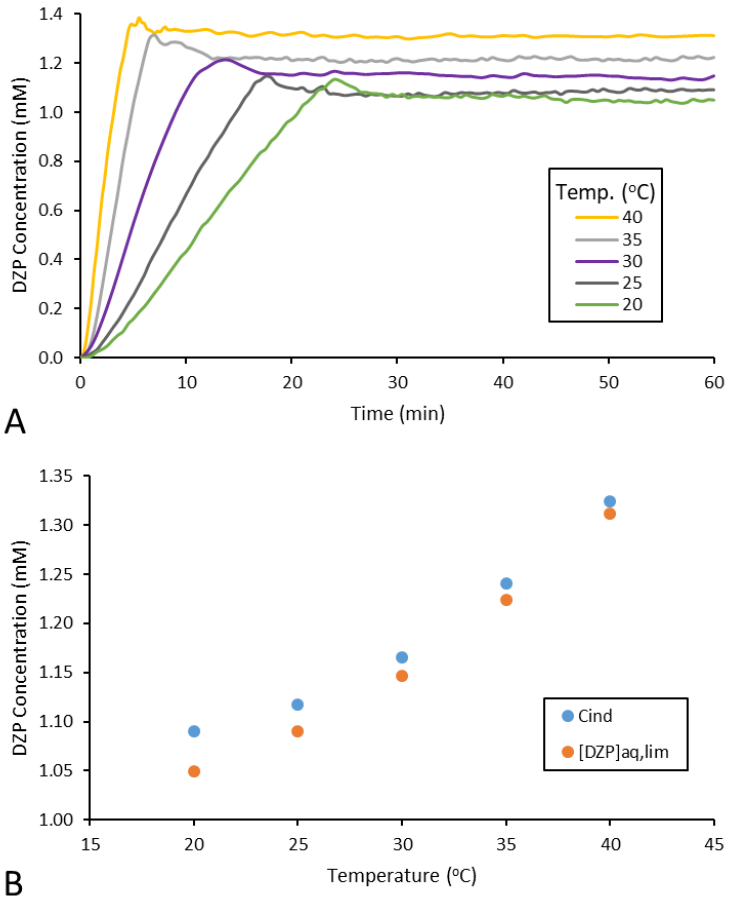

Figure 10. Effect of varying temperature. (**A**) Concentration-time profiles of 2.00 mM AVF converted by 0.25 U/mL AOP in pH 7.4 PBS at 20 - 40 °C. Precipitation occurred at $t_{ind,40C}$ = 4.75 min, $t_{ind,35C}$ = 6.5 min, $t_{ind,30C}$ = 13.3 min, $t_{ind,25C}$ = 18.0 min, and $t_{ind,20C}$ = 24.5 min. (**B**) C_{ind} and $[DZP]_{aq,lim}$ decreased with temperature.

2.4.5 Varying pH

The average anterior pH of the nasal cavity is 6.40 (range: 5.17 – 8.13) and average posterior pH is 6.27 (range: 5.20 – 8.00).[55] Nasal sprays should be formulated within the normal pH range in order to avoid irritating the mucosa and reduce the amount of buffer needed to overcome the natural buffering capacity of nasal mucus. The identity of the buffering agent used to control pH for the AVF/AOP system did not markedly affect the

enzyme activity, C_{ind}, or $[DZP]_{aq,lim}$ (Figure 11A). However, there was a reduction in the rate of DZP production (188 to 23.6 µM/min) when pH was lowered from 7.4 to 6.0 (Figure 11B). Lowering pH to 6.0 did not affect C_{ind} or $[DZP]_{aq,lim}$ since these concentrations are related to the intrinsic solubility of the amorphous form and the pK_a of DZP is ~3.

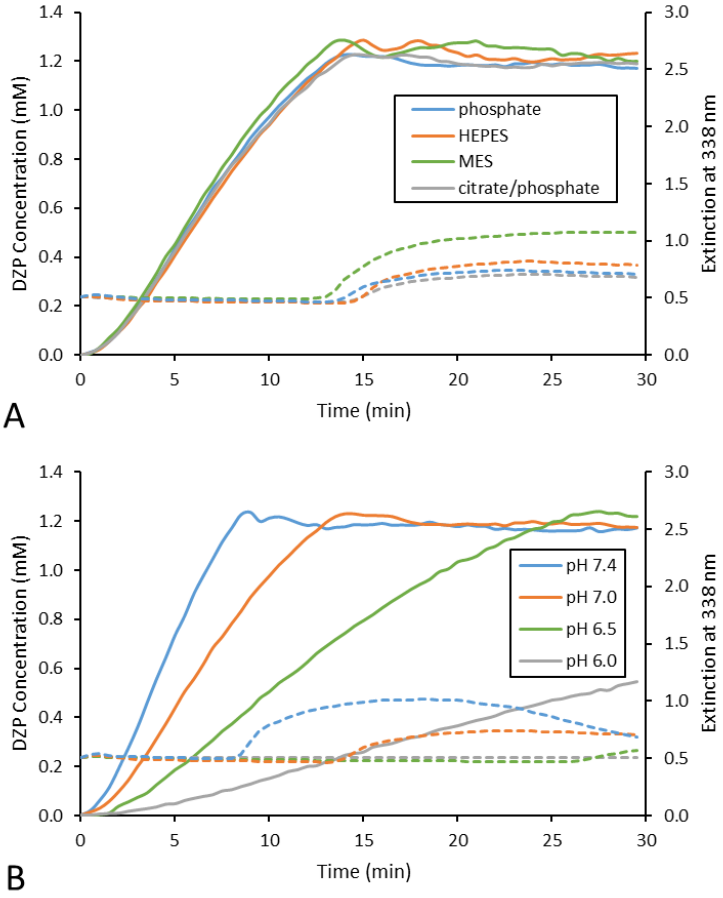

Figure 11. Effect of buffing agent and pH. Concentration-time profiles (solid lines) of 2.00 mM AVF converted by 0.50 U/mL AOP at 32 ºC overlaid with zero order Ext measured at 338 nm (dashed lines). (**A**) Reactions performed at pH 7.0 with 20 mM of the indicated buffer agent. Solutions were made isotonic by adding NaCl. (**B**) Reactions performed in PBS pH 6.0 – 7.4.

2.4.5 Nature of the precipitate

DSC (Figure 12A) and PXRD (Figure 12B) comparisons between crystalline DZP standards and DZP precipitate formed from the enzymatic conversion of AVF indicated that the initial precipitate was amorphous. The melting temperature (T_m) range observed for the crystalline DZP standard was 130.8 – 132.4 ^oC (onset to peak) with molar heat of fusion ΔH_f = 26.0 kJ/mol. These measurements agree with the literature, which reports T_m = 131.5 – 134.5 ^oC and ΔH_f = 25.8 – 27.1 kJ/mol.[56-58] Melting endotherms were not observed in the DSC curves of the precipitate samples. Instead, a glass transition (T_g) was found with an inflection point at 45.3 ± 0.8 ^oC (± SD), close to previously reported values of T_g for amorphous DZP, 46.8 ± 0.2 ^oC [57] and 42.1 ± 0.4 ^oC.[58] The characteristic diffraction peaks that would be expected for a crystalline sample of DZP were observed in the PXRD pattern of the DZP standard, while only an amorphous halo was observed for the reaction precipitate. Polarized light microscope images of crystalline DZP standard in buffer showed irregular, angular particles with birefringence (Figure 12C). However, images of the precipitate formed by enzymatic conversion of AVF display spherical particles and a lack of birefringence, confirming the amorphous nature of the precipitate (Figure 12D).

Further evidence that the DZP precipitate was non-crystalline was obtained by demonstrating its rapid dissolution and high solubility (Figure 13). Samples with $[AVF]_0$ = 2.00 mM and 0.25 U/mL AOP were allowed to generate DZP beyond t_{ind} (11 min) to accumulate precipitate. At t = 20 min, conversion of AVF to DZP was expected to be 89% complete by enzyme kinetics and $[DZP]_{aq,20min}$ was measured to be 1.21 ± 0.02 mM, S =

9.34 (i.e. 68% of the generated DZP was in solution and 32% was phase separated). At this time point, the volume of the reaction mixture was doubled by adding buffer. DZP precipitate immediately returned to solution upon dilution of the reaction mixture, as was evident by the elimination of light scattering and determination of a new solution concentration, ($[DZP]_{aq,20.5min}$ = 0.852 ± 0.009 mM, S = 6.56, experimentally compared to 0.890 mM, S = 6.85, theoretical). These observations also confirm that the Lys endopeptidase activity of AOP was unaffected by the presence of the DZP precipitate.

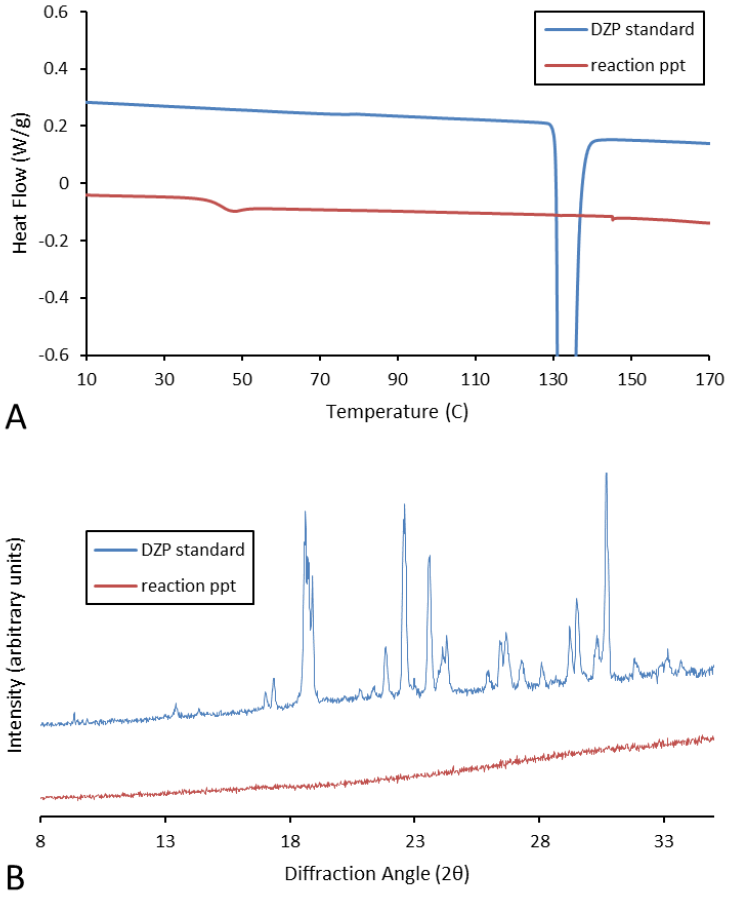

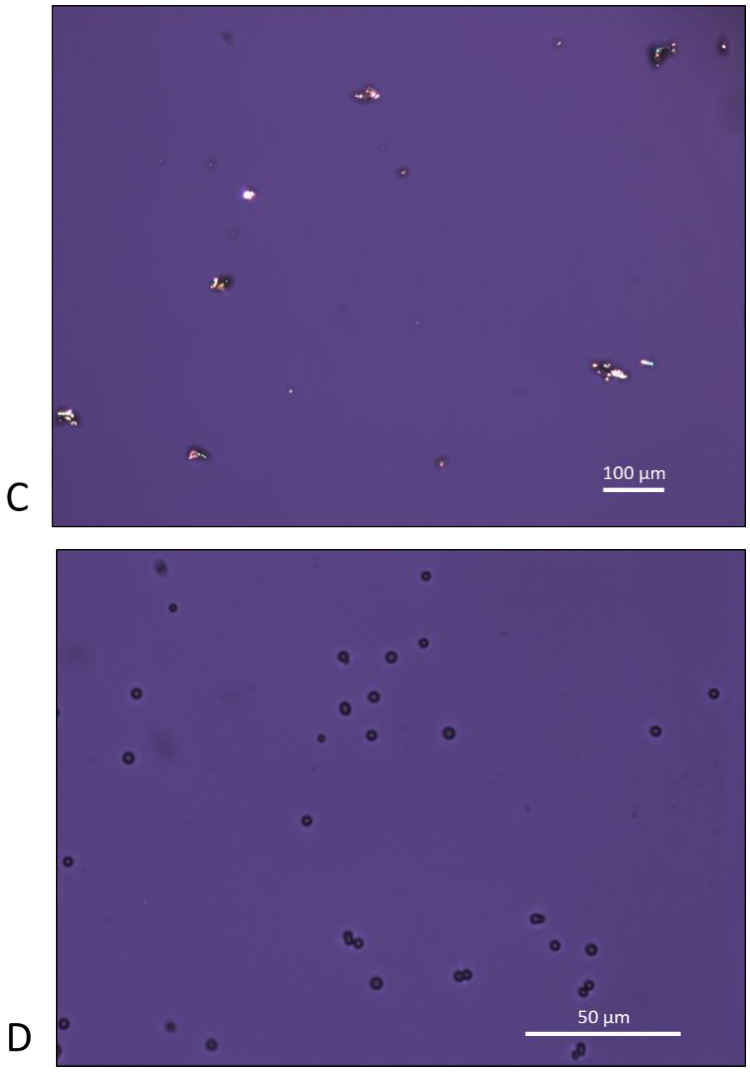

Figure 12. Characterization of DZP precipitate. (**A**) Overlaid DSC curves. Crystalline DZP standard (blue) with T_m = 131.5 – 134.5 °C, H_f = 26.0 kJ/mol. Amorphous reaction precipitate (red) with T_g = 45.3 ± 0.8 °C, n = 3. (**B**) PXRD patterns. Crystalline standard shows characteristic peaks for DZP (blue). Amorphous halo of reaction precipitate (red). (**C**) Polarized light microscope image of crystalline DZP standard in buffer. Scale bar: 100 µm. (**D**) Polarized light microscope images of reaction mixture with precipitate particles. Image at t = 1 hr. Scale bar: 50 µm.

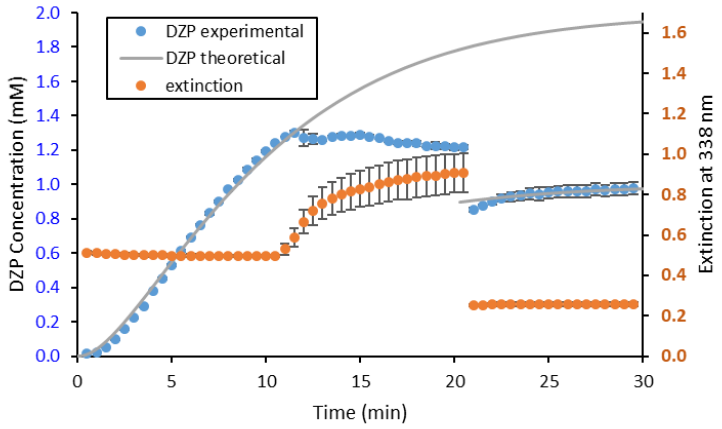

Figure 13. Dissolution of DZP precipitate. Concentration-time profiles of 2.00 mM AVF converted by 0.25 U/mL AOP in pH 7.4 PBS at 32 ºC, n = 3. Initial reaction mixture volume: 200 µL. At t = 20 min, 200 µL of buffer was added to the reaction mixture and the precipitate went back into solution. Blue points: measured $[DZP]_{aq}$. Grey line: theoretical $[DZP]_{aq}$ with and without dilution. Orange points: zero order extinction at 338 nm.

2.5 Discussion and conclusion

Using a second derivative UV spectroscopic method to monitor the conversion of AVF to DZP offers several distinct advantages over chromatographic techniques such as HPLC. Foremost, it eliminates the need to filter or centrifuge precipitated DZP in order to obtain the solution concentration. Monitoring of [AVF], [ORI], $[DZP]_{aq}$, and t_{ind} can be accomplished in real time with short time intervals between data points. The time interval is limited only by the scan rate of the instrument in the region of the analytical wavelength. Chromatographic techniques require stopping the enzymatic reaction to preserve substrate and product concentrations at a particular time point. This is commonly accomplished by adding a miscible organic solvent to denature the enzyme. However, denaturing the enzyme does not prevent ORI from progressing to DZP, resulting in measurements that

reflect the sum of $[ORI]_t$ and $[DZP]_{aq,t}$. Furthermore, adding organic solvent to denature the enzyme may also solvate precipitated DZP and lead to an erroneous measurement of the solution concentration. Nevertheless, HPLC is critical in determining the rate of conversion of AVF to ORI. Using HPLC data and enzyme parameter identifications from our previous publication in tandem with the spectroscopic determination of DZP accumulation achieved in the present work enabled us to determine the rate constant for ring closure. While Bayesian fitting of all parameters might have been a better procedure, the small improvement in fits would be unlikely to justify the added effort.

Second derivative spectra are derived from zero order spectra. Zero order spectral data can provide additional information about phase separation of solutes from supersaturated solutions. Often, a wavelength beyond the tail of the absorbance peak is chosen to determine t_{ind} for systems that form such precipitates. For example, Ext measurements at 400 nm have been used to detect precipitation upon dilution of injectable DZP formulations.[59] By selecting an isosbestic point to simultaneously measure concentration and t_{ind}, we eliminate error associated with correlating t_{ind} to C_{ind} that would arise from the time lag between measurements made by scanning between the analyte peak and tail wavelengths, such as 315 nm and 400 nm, respectively, for DZP. Error compounding in the determination of $[DZP]_{aq}$ due to the combined uncertainty in $(d^2\varepsilon/d\lambda^2)_{AVF}$ and $(d^2\varepsilon/d\lambda^2)_{DZP}$ should also be considered when selecting an analytical wavelength. At 338 nm, this error compounding is mitigated since AVF contributes < 5% to the combined calibration curve sensitivity (Appendices A1, Figure A1.55).

In addition to methodology for monitoring the conversion of AVF to DZP in real-time, an accurate predictive model was needed to scale-up the reaction for formulation at therapeutically relevant concentrations. The basic reaction model described by Equations 3-5 was successfully used to model the sigmoidal behavior of concentration-time profiles at higher substrate concentrations (Figure 6A) with $k_2 = 0.470$ min^{-1} for 0.25 U/mL AOP in PBS pH 7.4 at 32 ºC. However, directly scaling V_{max} to model different AOP concentrations resulted in substantial deviations from experimental data with slower than predicted rates of DZP production observed at higher [AOP]. Increasing [AOP] leads to an accumulation of ORI; thus, it was thought that perhaps ORI was inhibiting the AOP enzyme. Incorporating traditional enzyme inhibition models for cases where ORI, DZP, or Lys was the inhibiting species did not result in better agreement between the model and the data set. The lack of inhibition from DZP or Lys was also confirmed experimentally (Appendices A1, Figure A1.60). Instead, the AOP preparation itself was found to slow the reaction.

Commercially available AOP is a protein mixture that has endoprotease, exopeptidase, and amylase activity from at least 8 different enzymes.[60] In addition to proteins, the stock solution of AOP from the manufacturer contains 42.8% w/w water, 30% w/w sucrose, 10% w/w potassium chloride, and 0.20% w/w potassium sorbate.[61] Benzophenones and benzodiazepines tend to bind non-specifically to proteins, with the fraction unbound in plasma (f_u) estimated to be 0.21 for AVF and 0.19 for ORI based on a quantitative structure–activity relationship calculation[62,63] and $f_u = 0.01 – 0.04$ for DZP reported in the literature.[64] It was thought that intermittent binding of AVF and ORI to

proteins in the AOP preparation was responsible for the attenuation of the reaction rate observed when [AOP] was increased. Binding of AVF reduces the free concentration of AVF available to the enzyme, and binding of ORI inhibits the formation of DZP by restricting the degrees of freedom necessary for the molecule to cyclize. However, equilibrium dialysis of 130 μM DZP with 4 U/mL AOP did not result in a reduction of free DZP, suggesting that the concentration of proteins in AOP was too low for non-specific binding interactions to be significant. The expressions in Equations 6 and 7 remain empirical corrections to the model since the binding of ORI to AOP could not be verified experimentally and it is unknown which component of AOP could be causing this effect.

Although it is unlikely that a nonhuman enzyme preparation, such as AOP, would be chosen as the biocatalyst in a pharmaceutical product, the counterproductive rate of DZP production observed with high concentrations of AOP (Figure 9C) exemplifies the need for careful characterization of these prodrug/enzyme systems. When the enzymatic conversion of AVF is fast, the rate of ORI cyclization becomes reaction rate limiting. Adding excessive amounts of enzyme beyond the amount needed to achieve an optimal DZP absorption rate may also increase the possibility of an allergic reaction or other adverse effects from the enzyme.

One of the more interesting aspects of the AVF/AOP system is that $[DZP]_{aq}$ was sustained at the upper limit of the metastable zone even in the presence of precipitate and after the DZP production had ceased. A solute's amorphous solubility has been proposed to correspond to the maximum achievable free solute concentration.[65-67] Based on our observations, the amorphous solubility does indeed correspond to the upper limit of the

metastable zone. Polarized light microscopy, DSC, and PXRD analysis indicated that the DZP precipitate was amorphous. This means that the absorption rate enhancement afforded by supersaturated formulations is limited by the amorphous solubility. The amorphous solubility of DZP, hence $[DZP]_{aq,lim}$, was found to be 1.22 ± 0.03 mM (S = 9.38) at 32 °C.

This concentration limit was unaffected by pH in the range 6.0 – 7.4, but the rate of DZP production decreased with decreasing pH. The rate of DZP production also decreased with temperature. These behaviors were consistent with the pH- and temperature-dependent aminopeptidase activity of AOP reported in the literature;[60] however, the intramolecular cyclization of ORI is expected to be pH- and temperature-dependent as well. While k_2 would increase with increasing temperature according to the Arrhenius reaction rate equation, the reaction temperature for the drug product is essentially fixed at the average temperature of the nasal cavity (32 °C). On the other hand, pH can be controlled. The basic amine group of ORI, with a predicted pK_a of 7.7,[68] must be neutral to react with the ketone (Figure 3). At pH 6.0 only 1.7% would exist as the free base compared to 30% at pH 7.4, so $t_{1/2}$ of ORI is expected to be shorter at higher pH.

The ionization state of ORI would may also affect its membrane permeability. While AVF and Lys would have negligible absorption across nasal epithelium due to their hydrophilicity, ORI is somewhat hydrophobic and may undergo passive transcellular diffusion (pH 7.4 cLogD = -1.71 for AVF, -4.98 for Lys, 1.69 for ORI, and 3.08 for DZP).[68] Membrane permeability to ORI is expected to contribute to the delivery of DZP into systemic circulation, so controlling the concentration of ORI may be important. As an

intermediate, ORI reaches peak concentrations at early time points. In our experiments the highest [ORI] reached was 1.8 mM with no detectable precipitation in the vicinity of that time point. Thus, adjusting the formulation parameters to produce higher [ORI] may be desirable from a drug delivery perspective. Although the toxicological profile of ORI is unknown, the overall *in vivo* exposure would be low because the lifetime of ORI is short. Investigations to characterize the biopharmaceutical significance of ORI are ongoing in our lab.

At the outset of these studies, our goal was to understand how formulation parameters such as pH, buffering agent, temperature, and enzyme concentration affected the maximum level of DZP supersaturation that could be obtained and the time course of precipitation. We intended to use this information to balance the DZP production rate with the rate of DZP diffusion across cell membranes to afford rapid absorption while avoiding precipitation. However, we found that the amorphous precipitate, lacking long-range crystalline order and the accompanying crystal lattice energy barrier to dissolution, readily underwent dissolution (Figure 13). Therefore, precisely controlling the prodrug conversion rate to avoid precipitation of DZP is moot. The non-crystalline precipitate acts as a source for DZP and serves a useful function in the formulation by maintaining maximum supersaturation during the absorption process. It may also contribute directly to permeation across the membrane. In general, a high and consistent supersaturation was obtained at each experimental condition, demonstrating that the co-administration of AVF with a converting enzyme is a robust strategy to generate predictable levels of supersaturated DZP.

We conclude by reiterating that AOP, while inexpensive and therefore useful in conducting the studies reported in this contribution, is unsuitable for human use due to its fungal origin. Furthermore, as purchased, it is a mixture of several enzymes. We do not know how each fraction contributes to the conversion of AVF to ORI, and ultimately DZP. Recently we discovered that a human enzyme, *aminopeptidase B* (APB) is also active against AVF. A purified stock has been produced and characterized. A report of *in vivo* DZP pharmacokinetic studies in rats receiving intranasal AVF/APB solutions is in preparation.

Chapter 3: Intranasal co-administration of a diazepam prodrug with a converting enzyme results in rapid absorption of diazepam in rats

The contents of this chapter were published in:

Rautiola D, Maglalang PD, Cheryala N, Nelson KM, Georg GI, Fine JM, Svitak AL, Faltesek KA, Hanson LR, Mishra U, Coles LD, Cloyd JC, Siegel RA. Intranasal co-administration of a diazepam prodrug with a converting enzyme results in rapid absorption of diazepam in rats. *Journal of Pharmacology and Experimental Therapeutics*. **2019** Sept; 370:796-805

3.1 Summary

Intranasal administration is an attractive route for systemic delivery of small, lipophilic drugs because they are rapidly absorbed through the nasal mucosa into systemic circulation. However, the low solubility of lipophilic drugs often precludes aqueous nasal spray formulations. A unique approach to circumvent solubility issues involves co-administration of a hydrophilic prodrug with an exogenous converting enzyme. This strategy not only addresses poor solubility, but also leads to an increase in the chemical activity gradient driving drug absorption. Herein, we report plasma and brain concentrations in rats following co-administration of a hydrophilic diazepam prodrug, avizafone, with the converting enzyme *human aminopeptidase B*. Single doses of avizafone equivalent to diazepam at 0.500, 1.00, and 1.50 mg/kg were administered intranasally, resulting in 77.8 ± 6.0, 112 ± 10, and 114 ± 7 % bioavailability; maximum plasma concentrations 71.5 ± 9.3, 388 ± 31, and 355 ± 187 ng/mL; and times to peak plasma concentration 5, 8, and 5 min for each dose level respectively. Both diazepam and a transient intermediate were absorbed. Enzyme kinetics incorporated into a physiologically based pharmacokinetic model enabled estimation of the first order absorption rate constants: 0.0689 ± 0.0080 min^{-1} for diazepam and 0.122 ± 0.022 min^{-1} for the intermediate. Our results demonstrate that diazepam, which is practically insoluble, can be delivered intranasally with rapid and complete absorption by co-administering avizafone with aminopeptidase B. Furthermore, even faster rates of absorption might be attained simply by increasing the enzyme concentration, potentially supplanting intravenous diazepam or lorazepam or intramuscular midazolam in the treatment of seizure emergencies.

3.2 Introduction

Status epilepticus and acute repetitive seizures are serious medical emergencies that can cause lasting neurological damage and other life-threatening complications. Prolonged seizure activity associated with these conditions may lead to hypoxia, metabolic acidosis, hyperthermia, aspiration, pulmonary edema, brain injury, and an increase in the likelihood of experiencing additional seizures in the future.[69] The risk of injury, medical complications, or death can be mitigated by prompt medical treatment.[2,7] Benzodiazepines are the drugs of choice for treating seizure emergencies. Intravenous (IV) diazepam (DZP), IV lorazepam, or intramuscular midazolam (MDZ) are the preferred first-line rescue therapies.[10] However, drug delivery by injection can be problematic, especially when administered by non-medical personnel. Injection is difficult to carry out on obese or emaciated individuals, in the presence of multiple layers of clothing, or in public places. Furthermore, treatment of seizure emergencies can be significantly delayed if the patient must wait for medical personnel or transportation to the emergency room. Therefore, there is a need for outpatient treatments that can be administered immediately at the onset of a seizure by non-medical personnel.

Currently, the only outpatient treatment of a seizure emergencies approved by the United States Food and Drug Administration (FDA) is rectally administered DZP (Diastat®). Patients often object to this route of administration despite its effectiveness.[70] Off-label alternatives to rectal diazepam including intranasal (IN) and buccal MDZ using, respectively, injectable and oral solution formulations.[71] Other routes to deliver

benzodiazepines for the treatment of seizure emergencies currently under development include buccal DZP films[72] and IN sprays for DZP or MDZ.[37,73]

Intranasal DZP is an attractive treatment option because administration is easily performed by non-medical personnel, and it has an extended duration of action with low risk of adverse events.[71] However, the poor aqueous solubility of benzodiazepines presents a challenge in formulating them as nasal sprays because they require co-solvents or other additives to improve solubility.[29] These solubilizing excipients can be highly irritating to nasal mucosa. Transient epistaxis, nasal discomfort, nasal congestion, and rhinitis have been reported as side effects with some of these formulations, including those with DZP.[30,31,37] Further, the time to reach the maximum plasma concentration (t_{max}) for IN DZP formulations utilizing solubilizing excipients is relatively slow, ranging from 0.75-1.5 hrs.[12,37,74]

One strategy to overcome these challenges is to formulate a nasal DZP spray in an aqueous vehicle employing a water-soluble lysine prodrug of DZP, avizafone (AVF). While prodrug formulations typically rely on endogenous enzymes for *in vivo* biotransformation to the active drug,[41] unpublished results from a pilot canine study performed by our group suggested that exogenous enzyme would need to be included in the formulation to achieve the desired prodrug conversion rate and bioavailability. A series of *in vitro* experiments combining water soluble benzodiazepine prodrugs with the fungal converting enzyme *Aspergillus oryzae* protease (AOP) demonstrated that the formulations were capable of producing supersaturated solutions of the active drug, leading to an enhanced permeation rate of drug across cultured cell monolayers.[28,42,43,49] Further *in vitro*

studies characterized the conversion kinetics of AVF to DZP,[75] which first involves enzymatically catalyzed release of the lysine and formation of an open ring intermediate (ORI), followed by spontaneous closure of ORI to form DZP (Figure 14). These studies also showed that supersaturated DZP undergoes liquid/liquid phase separation at a critical degree of supersaturation, and resists crystallization over periods of days.

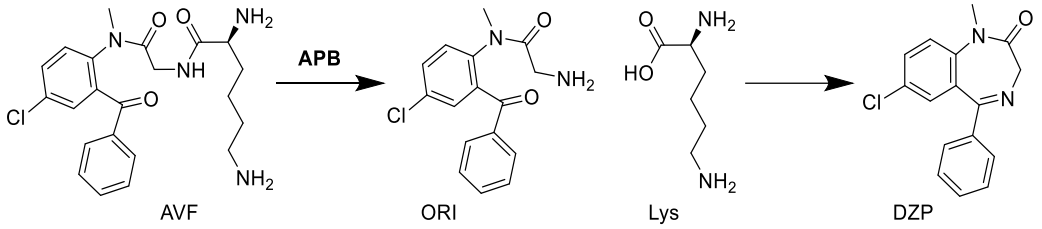

Figure 14. Prodrug/enzyme reaction scheme. Formation of DZP by enzymatic hydrolysis of AVF with APB progresses through an intermediate, ORI.

Based on these *in vitro* results, we hypothesized that intranasal administration of prodrug/enzyme formulations should result in rapid and complete *in vivo* absorption of DZP, with rapid distribution into the brain. In the present study, we tested this hypothesis in a rat model, in which we replaced AOP with a human enzyme, aminopeptidase B (APB), and compared the plasma and brain pharmacokinetics of IN AVF/APB with IN AVF and IV DZP. In addition to standard noncompartmental pharmacokinetic analyses, we augmented an established physiologically based pharmacokinetic (PKPB) model to incorporate mechanistic components, including enzyme reaction kinetics, absorption of both ORI and DZP across the nasal mucosa, supersaturation of DZP, and liquid-liquid phase separation of DZP. Finally, we carried out preliminary histological studies to determine whether acute damage would result from the AVF/APB formulations.

3.4 Materials and methods

3.4.1 Experimental design

The primary aim of this study was to determine whether IN administration of an AVF/APB combination to rats would result in rapid absorption of DZP without damaging the nasal mucosa. In brief, single doses of admixed solutions of AVF and APB equivalent to DZP at either 1.50 mg/kg, 1.00 mg/kg, or 0.500 mg/kg were deposited in the nasal cavities of rats. Plasma samples and brains were collected at time points ranging from 2 to 90 min. DZP concentrations measured in these tissues were compared against concentrations measured in samples collected from rats that were administered a 1.00 mg/kg dose of DZP intravenously (IV). Nasal tissue samples collected from rats sacrificed at the 90 min time point were examined for lesions. Details about the dosing and sample collection schedule are given in the sections that follow and summarized in the Appendices A2, Table A2.5.

3.4.2 Animals

All animal experiments were approved by the Institutional Animal Care and Use Committees of the University of Minnesota (protocol 1508-32889A, principal investigator: J.C. Cloyd) and HealthPartners (protocol 14-073, principal investigator: L.R. Hanson). The experiments were conducted at the HealthPartners Animal Care Facility and in accordance with the Guide for the Care and Use of Laboratory Animals (U.S. National Institutes of Health). Sixty-six male Sprague Dawley rats 8-9 weeks old (0.271 ± 0.023 kg) from Envigo RMS, Inc. (Indianapolis, IN) were used for this study. Rats were housed

under controlled environmental conditions with a standard 12 hr light/dark cycle and free access to food and water.

3.4.3 Formulation components

S-avizafone dihydrochloride (AVF•2HCl) was synthesized with > 99% purity, 99% ee from 5-chloro-2-methylaminobenzophenone according to the procedure described previously.[42] Recombinant human aminopeptidase B enzyme (APB) was produced by inserting the RNPEP DNA sequence encoding for APB and a His tag into a pQE-30 Xa vector, transforming JM109 *E. coli* with the resultant plasmid, inducing APB expression with IPTG, and purifying the expressed APB by affinity capture chromatography.[76,77] Purity of APB was >80% by gel electrophoresis. Phosphate buffered saline (PBS) IN delivery vehicle was prepared at pH 7.4 and concentration 20 mM using sodium phosphate dibasic and sodium phosphate monobasic purchased from Fisher Scientific, Inc. (Hampton, NH: cat# BP332 and BP329), made isotonic with sodium chloride purchased from EMD Millipore (Burlington, MA: cat# 567440), and sterile filtered during formulation. For the IV control arm of the study, a commercial formulation of injectable diazepam USP (5 mg/mL DZP, 40% propylene glycol, 10% alcohol, 5% benzoate-benzoic acid, and 1.5% benzyl alcohol) was purchased from Hospira, Inc. (Rocky Mount, NC: NDC 0409-3213-12, lot 58-257-EV).

3.4.4 Enzyme kinetics

The Michaelis constant (K_M) and maximum reaction velocity (V_{max}) for the hydrolysis of AVF by APB in pH 7.4 PBS at 32 °C were determined by fitting the

Michaelis-Menten equation to the initial rates of substrate consumption for a series of AVF concentrations. Reactions with 62.5 – 4000 µM AVF and 15 µg/mL (0.203 µM) APB were carried out in an Eppendorf Thermomixer 5436 at 500 rpm. After 1 min, APB was denatured by addition of methanol. Cyclization of ORI to DZP was allowed to progress to completion before measuring UV spectra of the quenched reaction mixtures in a Cary 100 Bio UV/Vis spectrophotometer (Agilent Technologies, Inc., Santa Clara, CA). The second derivative of the spectrum at 338 nm was used to quantify DZP, and this quantity was taken to be the molar equivalent to the amount of AVF consumed. A curve was fit to the AVF consumption versus initial AVF concentration with K_M and V_{max} as fitting parameters using the nlinfit function in MATLAB® version R2017b by The MathWorks, Inc. (Natick, MA).

3.4.5 Dosing

For IN dosing, rats were anesthetized, placed in the supine position, and cannulated. Rats designated for nasal tissue histology were not cannulated. Solutions of AVF and APB prepared in PBS were admixed to the appropriate concentration for each animal immediately prior to administration. See Table 1 for dose levels. After mixing, the formulation was quickly instilled into the nasal cavity using an Eppendorf pipettor with a gel loading pipette tip inserted to a depth of 14 mm past the nares. A total volume of 30 µL was delivered, 15 µL into the right nostril followed by 15 µL into the left nostril within 0.5 min. There were four IN dose groups: AVF/APB at low, medium, and high doses, and an AVF-only group at the medium dose. These doses were chosen because DZP near 1 mg/kg is commonly used in rat studies and results in plasma concentrations in rats that are clinically relevant.

Table 1. IN doses.

Dose level	Equivalent DZP (mg/kg)	AVF·2HCl (mg/kg)	APB (µg/kg)
high	1.50	2.66	91.4
med	1.00	1.77	60.7
low	0.500	0.885	30.4

For IV dosing, a commercial formulation of DZP was injected directly into the femoral vein. A small incision was made in the skin along the mid line of the left hind leg of anesthetized rats that were already cannulated in the right femoral vein. The incision was enlarged by blunt dissection to expose the left femoral vein. A 30-gauge needle was inserted into the vein to deliver a bolus dose of 1 mg/kg (medium dose level, ~54 µL) of DZP using a 100 µL syringe. Upon withdrawal of the needle, moderate pressure was applied to the site of injection with a cotton swab for 5-10 seconds to facilitate coagulation and seal the puncture.

3.4.6 Sample collection

Prior to cannulation for serial blood draws, rats were anesthetized with a 1.0 mL/kg subcutaneous ketamine cocktail containing 43 mg/mL ketamine HCl, 8.6 mg/mL xylazine HCl, and 1.4 mg/mL acepromazine. Anesthesia was maintained throughout surgery, dosing, and sample collection by administering subcutaneous boosters of 50 mg/kg ketamine alternating with boosters of ketamine cocktail. Blood was drawn from the right femoral vein through an PU 3Fr 25cm catheter (Instech Laboratories Inc., Plymouth

Meeting, PA: cat# C30PU-RFV1308). Leapfrog sampling was performed, with one cohort of 3 rats sampled at 2, 10, 20, 30, and 60 min and another cohort of 3 rats sampled at 5, 15, 45, 75 and 90 min for each dosing group. Each blood draw was 500 µL, with a 500 µL saline replacement volume pushed following every other draw. Whole blood was centrifuged at 2000 g for 3 min in BD Microtainer™ Tubes (Becton Dickinson Co., Franklin Lakes, NJ: cat# 365974) containing EDTA to obtain plasma. Additional cohorts of 3 rats each were designated for destructive sampling to obtain 2, 5, 8, and 10 min brain samples for the medium dose IV DZP and medium dose IN AVF/APB groups. At the final time points, blood samples were collected by cardiac puncture. The rats were then euthanized by transcardial perfusion with 120 mL saline. Brains, including the olfactory bulbs, were removed by gross dissection and hemisected sagittally. Brain and plasma samples were snap-frozen in liquid nitrogen and stored at -80 °C until analysis.

3.4.7 LC-MS/MS method

DZP and AVF were extracted from plasma and brain samples and quantified by LC-MS/MS. For extraction, brain tissue was first combined with two volumes (w/v) of lysis buffer and homogenized. The lysis buffer was composed of 25% methanol in PBS. An internal standard, tolbutamide, was spiked into 50 µL aliquots of plasma and 200 µL aliquots of brain lysates. The aliquots were then extracted with 2.5 mL ethyl acetate. The supernatant was removed by centrifugation at 2500 rpm for 10 min and evaporated to dryness under nitrogen at 37 °C. The dried extract was resuspended in 150 µL of mobile phase for LC–MS/MS analysis.

A Dionex™ UltiMate™ 3000 LC and TSQ Quantum™ Access MAX triple quadrupole mass spectrometer (MS/MS) with electrospray ionization (ESI) manufactured by Thermo Fisher Scientific, Inc. (Waltham, MA) was used for the analysis. Analyte separation was performed at a flow rate of 0.2 mL/min through a Zorbax Eclipse XDB C18 (3.0 x 150 mm x 3.5µm) column (Agilent Technologies, Inc., Santa Clara, CA: cat# 963954-302) with a step gradient mobile phase. Retention times for AVF, DZP, and internal standard were 3.4, 9.3, and 7.6 min, respectively. The mobile phase consisted of acetonitrile (solvent A) and 0.1% acetic acid in water (solvent B). The composition of the mobile phase was held for 2 min at 5:95 A/B, increased to 60:40 A/B for 8 min, and finally decreased to 5:95 A/B for 3 min to condition the column before the next injection. The mass spectrometer was operated in multiple reaction monitoring (MRM) mode with a capillary voltage of 3200 V and capillary temperature of 2500 °C. Precursor and product ions for the analytes were detected in positive ion mode with m/z 431 $[MH]^+ \rightarrow$ 246 for AVF and 286 $[MH]^+ \rightarrow$ 193 for DZP; the internal standard was detected in negative mode with m/z 269 $[M-H]^- \rightarrow$ 170. The concentration ranges for DZP were 25.0–1600 ng/mL in plasma and 6.25–400 ng/mL in brain lysate.

3.4.8 Nasal tissue histology

A separate cohort of rats was utilized to assess potential trauma to the nasal mucosa from the prodrug/enzyme formulation. This cohort did not receive catheters and no blood or brain samples were collected, but the animals did receive anesthesia and were dosed intranasally in the same manner as the others. Three rats at each dose level (vehicle-only, low, medium, and high, n = 12) were euthanized 90 min post-dose by perfusion with 120

mL saline followed by 120 mL of 10% neutral buffered formalin (NBF). The heads were removed, fixed in 10% NBF, and submitted to Colorado Histo-Prep (Fort Collins, CO) for histopathological evaluation by a board-certified veterinary pathologist. The samples were decalcified, trimmed, processed, embedded, and sectioned. Five sections of the nasal turbinates from each of the rats were stained with hematoxylin and eosine for microscopic imaging. Slides of the sections were read without knowledge of the dose group. The observed tissue changes were categorized using standardized toxicological pathology criteria.[78,79]

3.4.9 Noncompartmental analysis

Naïve pooled noncompartmental analysis (NCA) of plasma and brain concentration-time profiles was performed using WinNonlin® software version 8.0.0.3176 by Certara USA, Inc. (Princeton, NJ). Maximum concentration (C_{max}) and the t_{max} were determined from the average concentrations at nominal time points. The apparent terminal rate constant (λ_z) was estimated by regression of the log-linear portion of the concentration-time profiles. The apparent terminal half-life ($t_{1/2,z}$) was calculated as $\ln(2)/\lambda_z$. Concentrations measured from animals subjected to destructive and repeated sampling were pooled. Data was treated as sparse and the linear trapezoidal method was used for calculating the area under the curve (AUC) from the time of dosing to 90 min. Intranasal bioavailability (F) was calculated by

$$F = \frac{AUC_{IN,plasma}/Dose_{IN}}{AUC_{IV,plasma}/Dose_{IV}} \times 100 \quad (1)$$

Drug targeting efficiency (DTE) was used to assess direct nose-to-brain transport via the olfactory or trigeminal pathways.[80] DTE represents the time average partition ratio

between brain and plasma for IN administration versus IV administration. Data from the medium dose level from time of dosing to 90 min was used to calculate DTE from the following equation

$$\mathrm{DTE} = \frac{(\mathrm{AUC}_{\mathrm{brain}}/\mathrm{AUC}_{\mathrm{blood}})_{\mathrm{IN}}}{(\mathrm{AUC}_{\mathrm{brain}}/\mathrm{AUC}_{\mathrm{blood}})_{\mathrm{IV}}} \times 100 \quad (2)$$

3.4.10 PBPK model

A physiologically based pharmacokinetic (PBPK) model was used for further analysis. The model's structure and parameters for DZP disposition in rats were originally reported by Igari et al.[81] Variants of the model have been utilized by other researchers, such as Gueorguieva et al.[82] and Thompson et al.,[83] to explore aspects of predicting DZP concentration in tissues. We have appended the model with a nasal compartment for IN delivery of AVF and APB as illustrated in Figure 15.

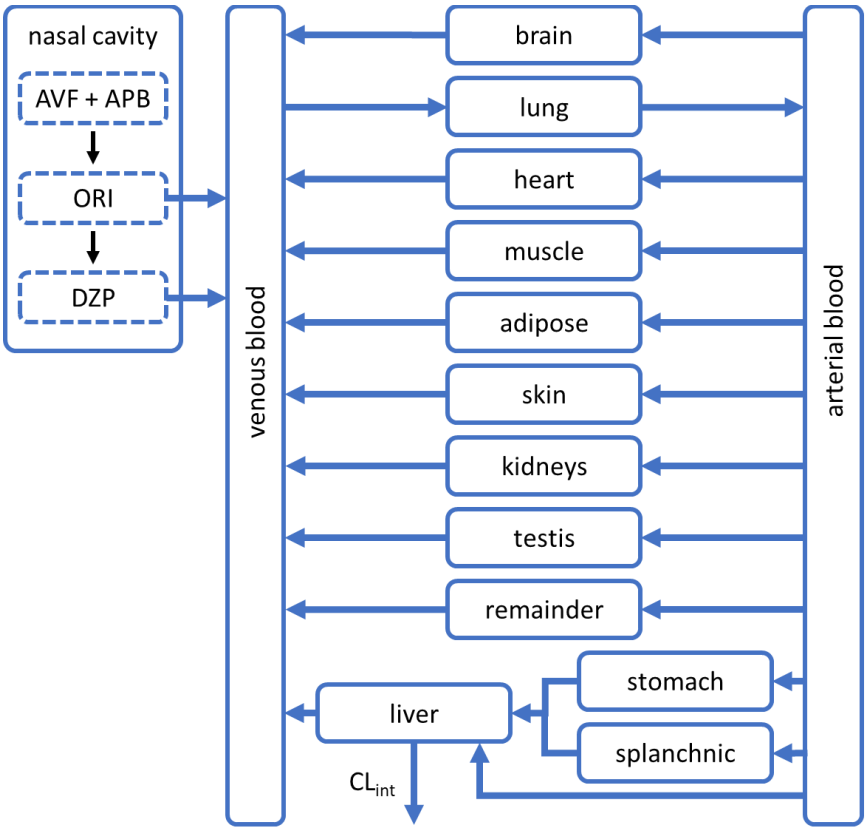

Figure 15. PBPK model schematic. An established PBPK model for DZP disposition in rats was modified to include a nasal cavity compartment. ORI and DZP absorb from the nasal cavity into circulation after IN administration of AVF and APB.

The conversion rate for AVF to DZP in the nasal cavity is governed by enzyme kinetics and the rate of ORI cyclization. To characterize the enzyme reaction, K_M and V_{max} were measured *in vitro* in the formulation vehicle (pH 7.4 PBS) at 32 °C. This temperature is approximately the average temperature of rodent nasal passages.[84] The catalytic rate constant (k_{cat}) for enzymatic hydrolysis was then calculated from V_{max}, i.e. $k_{cat} = V_{max}/C_{nasal,APB}$ where $C_{nasal,APB}$ is the concentration of enzyme in the nasal cavity. Thus, the rate of AVF hydrolysis *in vivo* can be predicted by

$$\frac{dC_{nasal,AVF}}{dt} = -\frac{k_{cat}C_{nasal,APB}C_{nasal,AVF}}{K_M + C_{nasal,AVF}} \quad (3)$$

where $C_{nasal,AVF}$ is the concentration of AVF in the nasal cavity. ORI, the immediate product of AVF hydrolysis, can accumulate in the nasal cavity and has physicochemical properties such that this species has the potential to passively diffuse across nasal epithelium. Transport of ORI was modeled as unidirectional due to the relatively small volume of the nasal cavity. The volume of the nasal cavity (V_{nasal}) was assumed to be the volume of the deposited formulation, 30 µL. Thus, the rate of change in the concentration of ORI ($C_{nasal,ORI}$) in the nasal cavity can be expressed as

$$\frac{dC_{nasal,ORI}}{dt} = \frac{k_{cat} C_{nasal,APB} C_{nasal,AVF}}{K_M + C_{nasal,AVF}} - \left(k_2 + k_{a,ORI}\right) C_{nasal,ORI} \quad (4)$$

where k_2 is the first order intramolecular cyclization rate constant of ORI and $k_{a,ORI}$ is the nasal absorption rate constant of ORI. Similarly, DZP has an associated absorption rate constant ($k_{a,DZP}$). However, DZP generated in excess of $C_{DZP,lim}$ forms an amorphous phase separate from the solution phase. Assuming drug transport only occurs from the solution phase, the rate of change in the concentration of DZP ($C_{nasal,DZP}$) in the nasal cavity can be expressed as

$$\frac{dC_{nasal,DZP}}{dt} = k_2 C_{nasal,ORI} - k_{a,DZP} C_{nasal,DZP,sol} \quad (5)$$

where $C_{nasal,DZP,sol}$ is the concentration of DZP in the solution phase and $C_{nasal,DZP,sol} \leq C_{DZP,lim}$.

This PBPK model assumes perfusion rate-limited distribution and tissue compartment concentrations that are in instantaneous equilibrium with venous blood flows.

A general expression for the rate of change in concentration of DZP in non-eliminating organ or tissue compartments can be written as

$$\frac{dC_{tissue}}{dt} = \frac{Q_{tissue}}{V_{tissue}}\left[C_{artery} - \frac{C_{tissue}}{K_{P,tissue}}\right] \quad (6)$$

where C_{tissue} is the concentration in the specified tissue, V_{tissue} is the volume of that tissue, Q_{tissue} is the blood flow rate, C_{artery} is the concentration in the arterial blood, and $K_{P,tissue}$ is the partition coefficient.

DZP is extensively metabolized in the liver and minimally excreted unchanged, so elimination was assumed to be solely by hepatic metabolism. The hepatic extraction ratio for DZP in rats is approximately unity, even for doses as high as 4 mg/kg.[85] Therefore, the concentration of DZP in the liver was assumed to stay well below K_M for metabolism by liver enzymes. An expression for the rate of change in the concentration of DZP in the liver can be written as

$$\frac{dC_{liver}}{dt} = \frac{1}{V_{liver}}\left[\frac{Q_{stomach}C_{stomach}}{K_{P,\,stomach}} + \frac{Q_{splanchnic}C_{splanchnic}}{K_{P,\,splanchnic}} + Q_{liver}C_{artery} - \frac{CL_{int}C_{liver}(f_u/R)}{K_{P,liver}R} - \frac{(Q_{stomach} + Q_{splanchnic} + Q_{liver})C_{liver}}{K_{P,\,liver}}\right] \quad (7)$$

where CL_{int} is intrinsic clearance, f_u is the fraction unbound in plasma, and R is the blood to plasma ratio. In rats, the blood to plasma DZP concentration ratio has been reported to be R = 1.037 ± 0.007 with the fraction unbound in plasma f_u = 0.14 ± 0.003.[81,86]

Expressions for the rate of change in the concentration of DZP in the venous and arterial blood compartments are

$$\frac{dC_{vein}}{dt} = \frac{1}{V_{vein}}\left[\sum_{i}\frac{Q_i C_i}{K_{P,i}} + V_{nasal}\left(k_{a,ORI}C_{nasal,ORI} + k_{a,DZP}C_{nasal,DZP,sol}\right) - Q_{lungs}C_{vein}\right] \quad (8)$$

$$\frac{dC_{artery}}{dt} = \frac{1}{V_{artery}}\left[\frac{Q_{lungs}C_{lungs}}{K_{P,lungs}} - \sum_{j} Q_j\, C_{artery}\right] \quad (9)$$

where i represents each tissue compartment that has an outflow to the venous pool and j represents each tissue compartment that has an inflow from the arterial pool. At pH 7.4, the half-life for cyclization of ORI is 1.47 min,[75] so we assume most of the conversion to DZP occurs in the nasal cavity. Absorbed ORI would continue to transform into DZP in the mucosa and in the blood.[87] Therefore, systemic exposure to ORI was limited, and any ORI that did reach the circulation was regarded as DZP for the purposes of pharmacokinetic analysis.

The PBPK model, represented by Equations 3-9, was constructed in MATLAB®. Values for the parameters of interest (CL_{int}, $k_{a,ORI}$, $k_{a,DZP}$, and $C_{DZP,lim}$) were determined by fitting numerically solved solutions of the differential equations to experimental data using the ode45 function in conjunction with the lsqcurvefit function. Experimental data was input as averages of the DZP concentrations measured at the nominal time points, with data from animals subjected to destructive and repeated sampling pooled. Fitting was performed in two stages. First, CL_{int} was determined by fitting the model to DZP concentrations measured in plasma from rats administered IV DZP. Tissue compartment volumes, blood flow rates, and partition coefficients were fixed at the values reported by Gueorgieva et al.[82] and Thompson et al.[83] These constants are listed in Appendices A2, Table A2.6. Then, CL_{int} was fixed and *in vivo* values for $k_{a,ORI}$, $k_{a,DZP}$, and $C_{DZP,lim}$ were

determined by fitting the model to a matrix of DZP concentrations measured in plasma from rats administered IN AVF/APB at the low, medium, and high dose levels.

3.4.11 Statistical methods

Naïve pooled noncompartmental analysis was performed using sparse sampling computations.[88] Concentrations of DZP measured below the limit of quantification were retained in the data set.[89] Squared correlation coefficients adjusted (R^2_{adj}) for the number of points used in the estimation of λ_z were >0.7 for all treatment groups. For AUC, standard error (SE) of the mean estimate was calculated using WinNonlin®, which employs equations described by Nedelman and Jia[90] and unbiased sample covariance estimation described by Holder.[91] The SEs associated with F estimates were calculated by propagating the SEs from the AUCs. Similarly, the SEs of DTEs were calculated by propagating the SEs from the AUCs. Descriptive statistics for the variability in t_{max} are not reported because leapfrog serial and destructive sampling data were pooled. The standard deviation (SD) of measured concentrations at t_{max} was used to describe the dispersion of C_{max}. SEs reported for determined PBPK parameter estimates were obtained from MATLAB® by back-calulating from 95% confidence intervals computed using the nlparci function with the Jacobian from the lsqcurvefit function. Root mean square error (RMSE) for the model fits were calculated from the average concentrations at the nominal time points.

3.5 Results

3.5.1 Noncompartmental analysis

As shown in Figure 16, DZP generated from IN administration of the AVF/APB formulation appeared rapidly in plasma. Plasma and brain tissue samples were also analyzed for AVF, but concentrations were below the limit of quantification. The short half-life of ORI did not allow for its quantification. The average plasma concentration of DZP at the first measured time point, 2 min, was greater for IN AVF/APB than for IV DZP at an equivalent dose due to rapid distribution following IV dosing (Figure 16A). Plasma concentrations from IN administration continued to rise, reaching C_{max} = 388 ± 31 ng/mL at t_{max} = 8 min for the medium dose level. Similar t_{max} values were observed at each dose level, but C_{max} was not proportional to the dose. In fact, C_{max} for the high dose was not statistically different from that of the medium dose (Figure 16B). When AVF was administered without APB, there was a prominent decrease in the rate of DZP absorption. As shown in Table 2, C_{max} was nearly fourfold lower without co-administered enzyme.

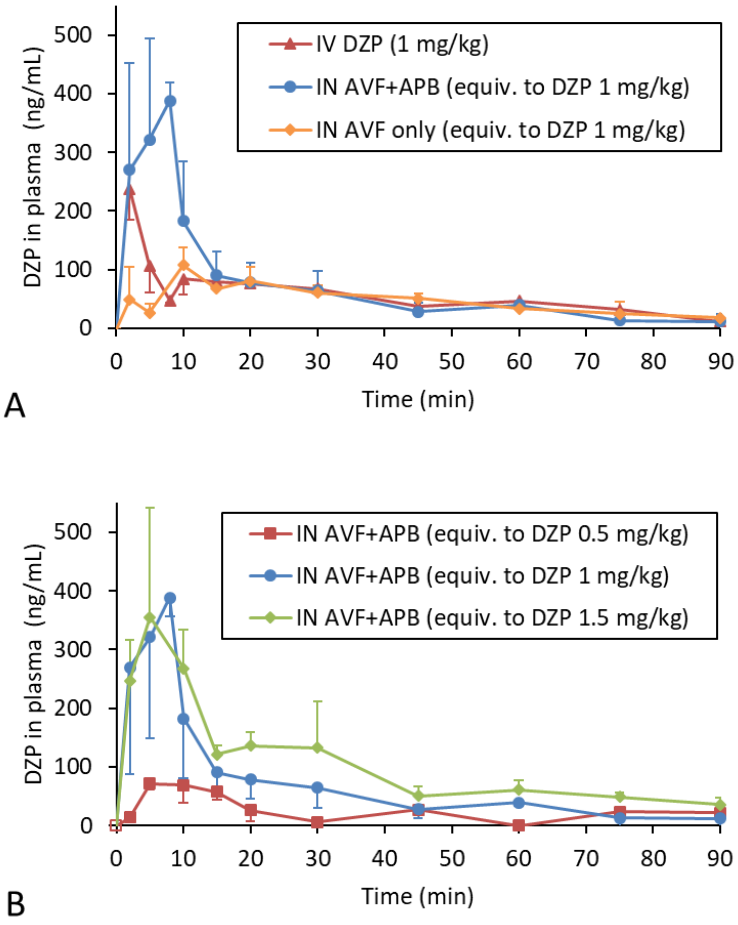

Figure 16. DZP concentration-time profiles measured in plasma. Error bars are SD. For IV DZP and IN AVF/APB at the medium dose level (equivalent to DZP at 1.00 mg/kg), n = 6 at 2, 5, and 10 min time points; n = 3 for all other data points. (**A**) IN-administered AVF/APB compared with IV-administered DZP indicated high bioavalability of the IN formulation, F = 112 ± 10 % (±SE). The IN-administered AVF/APB formulation has a pharmacokinetic advantage with regards to C_{max} and $AUC_{0\text{-}15min}$ when compared to the AVF-only control. (**B**) Saturation of the absorption process resulted in nearly identical initial rates of absorption for IN-administered AVF/APB at the medium and high dose levels.

There was complete absorption of DZP from IN AVF/APB at the medium and high dose levels, as was evident by bioavailabilities of 112 ± 10 and 114 ± 7 % respectively. The AVF-only control group and low dose APB/AVF group had nearly identical bioavailability (F = 77.8%) based on exposure from 0 to 90 min. However, there was a notable difference between these groups at early time points (Figure 16B). Dose normalized $AUC_{0\text{-}15min}$ was twice as large for the AVF/APB low dose group compared to the AVF-only control (Table 2). $AUC_{0\text{-}15min}$ for the IN AVF/APB medium and high dose groups were similar, suggesting saturation of the DZP absorption rate.

Table 2. Noncompartmental analysis of plasma DZP concentrations.

Formulation	**DZP**	**AVF**	**AVF/APB**	**AVF/APB**	**AVF/APB**
Route	IV	IN	IN	IN	IN
Equiv. DZP dose (mg/kg) [dose level]	1.00 [medium]	1.00 [medium]	0.500 [low]	1.00 [medium]	1.50 [high]
T_{max} (min)	0 [a]	10	5	8	5
C_{max} ± SD (ng/mL)	441 [a]	108 ± 30	71.5 ± 9.3	388 ± 31	355 ± 187
$t_{1/2,z}$ (min)	32.9	33.4	136 [b]	26.7	37.8
$AUC_{0\text{-}15min}$ (min.ng/mL)	1910 ± 70	837 ± 28	793 ± 54	3250 ± 190	3850 ± 270
$AUC_{0\text{-}90min}$ ± SE (min.ng/mL)	5430 ± 190	4230 ± 120	2110 ± 150	6080 ± 510	9280 ± 470
F % ± SE	n/a	77.8 ± 3.5	77.8 ± 6.0	112 ± 10	114 ± 7

[a] C_{max} reported for IV DZP is the concentration extrapolated to t = 0 min (i.e. the initial concentration C_0) as calculated by WinNonlin® NCA analysis. [b] Overestimation of $t_{1/2,z}$

due to inherent variability of data below limit of quantification in terminal phase of low dose group.

NCA results for DZP measured in brain tissue are listed in Table 3. For the IN AVF/APB medium dose group, t_{max} was reached at 8 min in both plasma and brain tissue. However, the concentration of DZP measured in plasma at the first time point ($C_{plasma,DZP}$ = 270 ± 181 ng/mL ±SD at t = 2 min) was already greater than the therapeutic concentration that is expected to lead to seizure threshold elevation in rats, $C_{plasma,DZP} \geq 70$ ng/mL.[92] Brain concentrations were not measured at time points between 10 and 60 min, but comparable concentrations were observed at 8 and 10 min (415 ± 32 and 404 ± 35 ng/g respectively), suggesting the true maxima were in this region. Brain C_{max} for IV DZP was recorded at the first time point, 2 min. Rapid transport from blood into brain tissue is normal for small, lipophilic drugs. DTE, a metric commonly used to assess nose-to-brain transport, was less than unity, negating significant transport of DZP through direct nose-to-brain pathways.

Table 3. Noncompartmental analysis of brain DZP concentrations.

Formulation	Equiv. DZP dose (mg/kg)	t_{max} (min)	C_{max} ± SD (ng/mL)	$AUC_{0\text{-}90min}$ ± SE (min.ng/mL)	DTE % ± SE
IV DZP	1.00	2	938 ± 142	18600 ± 200	n/a
IN AVF/APB	1.00	8	415 ± 33	15400 ± 500	74.0 ± 7.3

3.5.2 PBPK model

Concentration-time profiles were well described by a PBPK model with the rate of drug input controlled by enzyme kinetics. At 32 °C in pH 7.4 PBS, the Michaelis-Menten enzyme kinetic parameters for APB measured *in vitro* were K_M = 370 ± 63 µM and k_{cat} = 1250 ± 60 min^{-1} ±SE (see Appendices A2, Figure A2.67). The rate constant, k_2 ±SD, for cyclization of ORI, previously measured *in vitro* under the same conditions [75], was assumed to remain constant at 0.470 ± 0.012 min^{-1} *in vivo*. As listed in Table 1, the APB concentrations were scaled with the AVF concentration so that hydrolysis of AVF would be complete at t ≈ 4 min, regardless of the dose level. This also means that the predicted mole fraction of the total dose that had been converted to DZP was the same for each dose level at a given time point. For example, approximately 75% of the dose was expected to be converted to DZP at t = 5 min regardless of the dose level.

Fitting the PBPK model to DZP concentrations measured in plasma samples from the IV DZP group resulted in CL_{int} = 15.4 L/min, which was expected since DZP is well known to have a hepatic extraction ratio of approximately one in rats[93] and confirms the assumption that DZP clearance from the liver was flow-limited in this PBPK model. Subsequent fitting of the model to DZP concentrations measured in plasma samples from the IN APB/AVF groups allowed estimation of the parameters governing *in vivo* absorption from the nasal cavity: $k_{a,ORI}$ = 0.122 ± 0.022 min^{-1}, $k_{a,DZP}$ = 0.0689 ± 0.0080 min^{-1}, and $C_{DZP,lim}$ = 20.8 ± 3.1 mM (±SE). Conversion of AVF to DZP was faster than the combined absorption of ORI and DZP, leading to an accumulation of DZP in the nasal cavity. Since the aqueous equilibrium solubility of DZP is only 130 µM, concentrations entered the

supersaturated region. The apparent concentration at which supersaturated DZP began to phase separate from solution in the nasal cavity, $C_{DZP,lim}$, was a useful parameter to model the nonlinear absorption kinetics observed at early time points. However, the value of $C_{DZP,lim}$ should be interpreted within the context of the assumptions that V_{nasal} was equal to the dose volume and only DZP in the solution phase could be absorbed.

Well-stirred PBPK models predict high initial plasma concentrations with IV administration because the initial volume of distribution is assumed to be the volume of the venous blood compartment. This is illustrated in Figure 17A where the predicted plasma concentration for the IV DZP group decreases dramatically from the time of dosing as it distributes out of the venous compartment to reach the first measured plasma concentration at t = 2 min. The high concentrations of DZP measured in the brain at the first time point were predicted more accurately with this PBPK distribution behavior compared to a modeling approach which relied on a standard two-compartment model function to drive brain concentrations. In general, concentrations of DZP in the brain were predicted reasonably well by the PBPK model. For the IN AVF/APB medium dose group, brain concentrations lagged behind plasma concentrations during the first few min. This observation provided additional evidence that transport of DZP through direct nose-to-brain pathways was not significant.

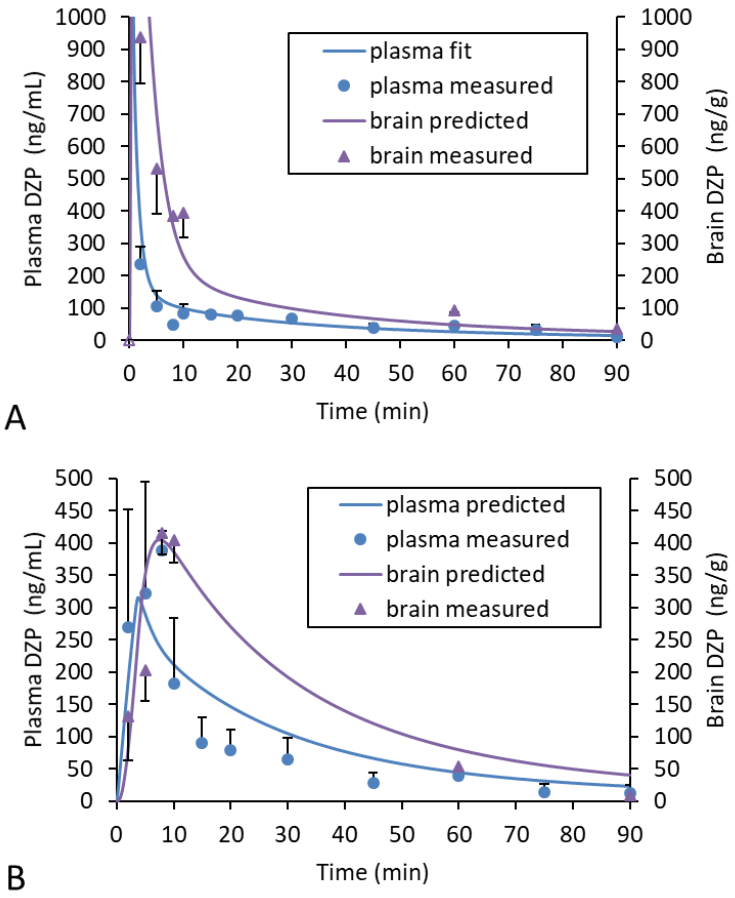

Figure 17. DZP concentration-time profiles in plasma and brain tissue. Experimental data (points) and model predictions (lines) at the medium dose level (equivalent to DZP at 1.00 mg/kg). For plasma concentrations, n = 6 at 2, 5, and 10 min time points; n = 3 at all other time points for plasma and brain. Error bars are SD. (**A**) IV-administered DZP. RMSE of the predicted curve was 44 ng/mL for plasma and 246 ng/g for bain. The open purple triangle at the origin is a marker to highlight the steep initial increase in brain DZP concentration; it is not a measured data point. (**B**) IN-administered AVF/APB. Predicted curve RMSE = 66 ng/mL for plasma and 67 ng/g for bain.

Although there was significant variablity in the data, similar average plasma concentrations were observed for the medium and high IN AVF/APB dose groups at early time points (Figure 18A). This indicated the absorption process was saturable. The

nonlinearity was likely caused by phase separation of DZP from solution when $C_{DZP,lim}$ was reached in the nasal cavity, a phenomenon that has been observed *in vitro*.[75] Phase separation attenuated DZP absorption and produced a shoulder at t = 10 min in the predicted concentration-time profile for the high dose group (Figure 18A, green curve). The peak preceding the shoulder comes from the absorption of ORI, which contributes to the concentration of DZP observed in plasma. In the first few min after administration, the amount of DZP produced by the reaction is relatively low compared to ORI. Predictions for the relative amount of each reaction species in the nasal cavity are shown in Figure 18B. Decomposition of the plasma concentration-time profile for the medium IN AVF/APB dose group, shown in Figure 18C, illustrates how absorption of ORI contributes to the rate at which DZP enters the circulation.

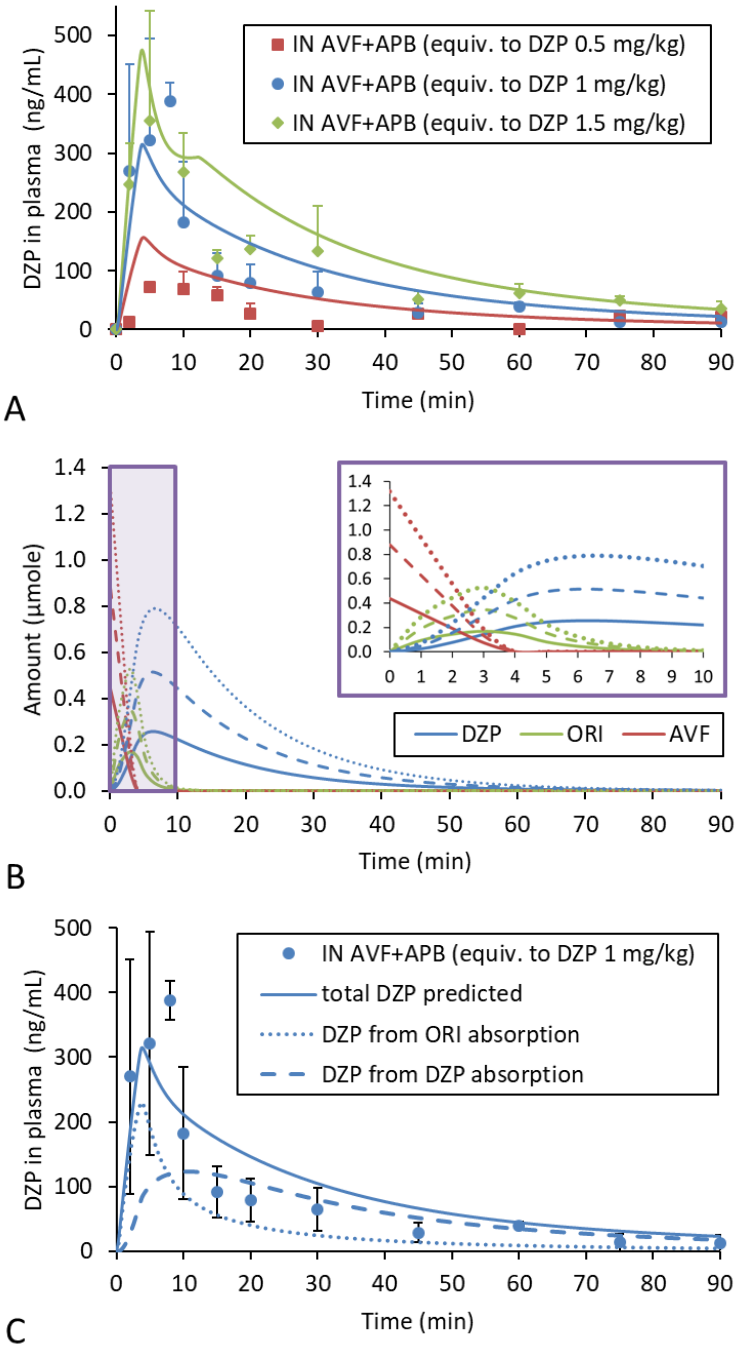

Figure 18. DZP concentration-time profiles in plasma from IN administration of AVF/APB at each dose level. Experimental data (points) and model predictions (lines). For medium dose level (equivalent to DZP at 1.00 mg/kg), n = 6 at 2, 5, and 10 min time points; n = 3 for all other data points. Error bars are SD. (**A**) Saturation of absorption rate observed with the high dose. Predicted curve RMSE = 43 ng/mL for low dose, 66 ng/mL

for medium dose, and 61 ng/mL for the high dose. (**B**) Predicted amounts of each reaction species in the nasal cavity. Solid lines represent the low dose, dashed lines medium dose, and dotted lines high dose level for a 0.250 kg rat. Inset shows expanded view of the first 10 min. (**C**) Absorption of ORI contributes to the rate of DZP delivery into the systemic circulation.

3.5.3 Nasal tissue histology

No inflammatory response was observed in the nasal tissue samples. Lesions (changes) found in the samples were few, with severities graded as either minimal or mild. These were located in the anterior portion of the nasal cavity and were consistent with mechanical trauma from insertion of the pipette tip used for dosing. There were some small, focal areas of missing epithelium on the wall of the nasal septum and/or nasoturbinate, and occasionally the maxilloturbinate. Cellular debris, consisting of small clusters of sloughed epithelial cells and cellular fragments, were found on the wall of the nasal septum or the nasoturbinate and anterior meatus. Other than two instances of minimal focal hemorrhage, the blank vehicle control group was unremarkable. There were no lesions observed in the ethmroid turbinates, olfactory nerves, and olfactory bulbs. The low, medium, and high dose groups (IN AVF/APB equivalent to 0.500, 1.00, and 1.50 mg/kg DZP respectively) did not display a dose response with regard to location, frequency, or severity of the lesions. Some examples of the tissue sections are shown in Figure 19. A detailed enumeration of the locations and severity of the observations can be found in Appendices A2, Table A2.8.

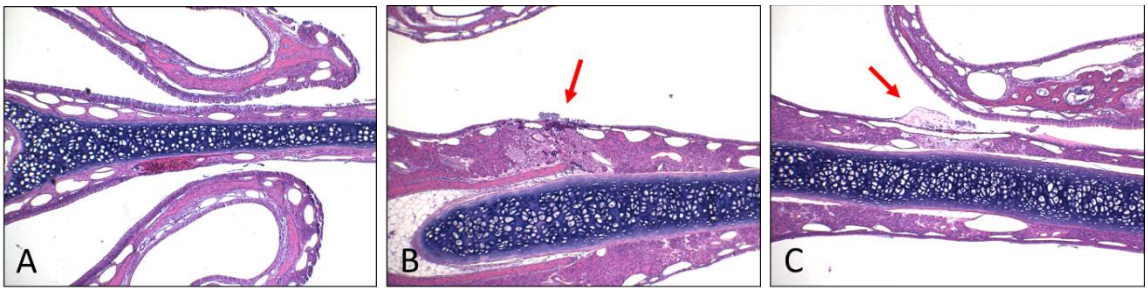

Figure 19. Representative examples of nasal tissue section images. Minor mechanical trauma from insertion of the dosing pipette tip was observed in some animals. There were no lesions attributed to the drug formulation. (**A**) Normal tissue. (**B**) Hemorrhage. (**C**) Necrosis.

3.6 Discussion and conclusion

Intranasal co-administration of AVF and APB resulted in rapid absorption of DZP with excellent bioavailability, thus demonstrating that a prodrug/enzyme combination in an aqueous vehicle efficiently delivers a hydrophobic drug. PBPK analysis indicated that both DZP and transient ORI were readily absorbed through the nasal mucosa into the systemic circulation. There was no evidence of transport through direct nose-to-brain pathways. Histological analysis of the nasal tissues post-dose did not reveal significant differences between the vehicle-only control group and treatment groups, suggesting that the formulation was well tolerated.

Although aminopeptidases capable of hydrolyzing Lys from AVF to produce DZP exist in the nasal mucosa and blood of both rats and humans,[94-96] exogenous APB is necessary to ensure complete and rapid conversion of AVF. In Figure 16B, the appearance of DZP in plasma at early time points for the IN AVF-only control group suggests that some AVF conversion occurred in the nasal cavity by endogenous enzymes. However, the

therapeutic concentration of DZP that is expected to lead to seizure threshold elevation in rats ($C_{plasma,DZP} \geq 70$ ng/mL)[92] was not reached until t = 10 min and was not sustained thereafter. AVF also converts to DZP when absorbed into the circulation. Upshall et al.[87] found the half-life for conversion of AVF in blood was 0.49 ± 0.06, 3.17 ± 0.09, and 3.85 ± 0.26 min for guinea pig, rhesus monkey, and human, respectively (blood and plasma were not significantly different). However, substantial transport of AVF across nasal epithelium is unlikely since it does not readily partition into membranes. Using wild type Madin-Darby canine kidney epithelial cell (MDCKII-wt) monolayers as an *in vitro* model for nasal epithelium to estimate apparent permeability coefficients (P_{app}), we observed negligible permeation of AVF ($P_{app} = 1.0\text{-}1.5\times10^{-6}$ cm/s) compared to DZP ($P_{app} = 2.2\times10^{-5}$ cm/s).[28]

IN-administered drugs tend to exhibit variable absorption rates and bioavailabilities when mucociliary clearance to the digestive tract competes with absorption though the nasal mucosa. The high bioavailability calculated for the medium and high IN AVF/APB dose groups suggests that those doses were fully converted and absorbed through the nasal mucosa of the rats (Table 2). The lower bioavailability observed for the low dose IN AVF/APB and AVF-only groups may have been due to a portion of the dose being cleared from the nasal cavity before complete conversion could occur. The first order rate constant for mucociliary clearance is roughly 0.035 min^{-1} in healthy adult humans[97] and 0.14 min^{-1} in Sprague-Dawley rats.[98] However, the rate of clearance depends on many factors including dose volume, viscosity, pH, tonicity, component concentrations, and

pharmacodynamic effects on the cilia. A separate study to assess the effects of dose level on the beat frequency of cilia may be warranted to reconcile the discrepant bioavailabilities.

From the plasma DZP concentration-time profiles measured at each dose level (Figure 18A), absorption during the first 15 min displayed nonlinear pharmacokinetics while concentrations at later time points were approximately dose proportional. This behavior was not entirely unexpected since it was known that phase separation of DZP would occur if the accumulation of DZP in the nasal cavity exceeded $C_{DZP,lim}$. However, it was surprising that the *in vivo* estimate of $C_{DZP,lim}$ (20.8 ± 3.1 mM ±SE), determined by fitting the PBPK model, was nearly 17 times greater than $C_{DZP,lim}$ measured *in vitro* (1.22 ± 0.03 mM ±SD).[75] The *in vivo* estimation is conspicuously high because V_{nasal} was assumed to be equivalent to the dosed formulation volume. However, the total volume would increase when the deposited dose mixes with nasal mucus.

Absorption of DZP directly from phase separated DZP could also cause overestimation of $C_{DZP,lim}$. Transcytosis of the precipitated DZP colloidal particles presents one possible mechanism of transport across the nasal epithelium. Brooking et al.[99] reported size dependent transcytosis of latex nanoparticles through the nasal mucosa and into the blood of rats. Another potential mechanism invokes an increase in driving force for absorption arising from higher local concentrations of DZP in the diffuse layer of particles that are proximal to cell membranes. Both mechanisms require that DZP precipitate particles be close to cell membranes. Confounding of DZP absorption from solution with absorption from the precipitated phase is exacerbated by the small volume-to-surface area

ratio that results when the formulation spreads across the surface of the mucosa, minimizing the distance particles need to travel to reach the cell membranes.

The hydrophobic reaction intermediate, ORI, can accumulate in the nasal cavity as well, so there is potential for phase separation of this species. Since we did not observe precipitate formation at time points where there was expected to be high concentrations of ORI during our *in vitro* experiments,[75] phase separation of ORI was not considered in this PBPK model. However, it was necessary to incorporate absorption of ORI into the model to account for the rapid appearance of DZP in plasma and the shape of the concentration-time profiles. Satisfying Lipinski's rule of five, with cLogD = 1.69 at pH 7.4,[68] ORI can partition into membranes and permeate epithelium. P_{app} for ORI across MDCKII-wt monolayers was predicted to be 1.77×10^{-5} cm/s using structure activity relationship calculations.[100,101] Since ORI quickly transforms into DZP, absorption of ORI fortuitously contributes to the rate at which DZP appears in plasma. This contribution is illustrated by the dotted curve in Figure 18C, but the area under the ORI curve is not representative of exposure. Exposure to ORI was miniscule due to its short half-life.

Exposure to the other reaction species, AVF and APB, was similarly short and most likely only topical. Based on enzyme kinetic calculations, AVF was completely hydrolyzed in the nasal cavity in less than 4 min and increasing the amount of APB could easily speed up its consumption. The residence time of APB in the nasal cavity is controlled by mucociliary clearance and possibly by proteases in the mucus. Once APB or its degradation products reach the digestive tract, they would be digested like any other protein. Histological analysis of the posterior, absorptive nasal tissue sections suggested

that the formulation was innocuous. However, the histological findings are incomplete. Collection of tissue samples 90 min post-dose does not provide sufficient time to develop an inflammatory response. Future *in vivo* studies will incorporate later time points to more fully assess acute nasal toxicology.

Approximately 50% of the nasal surface in a rat is olfactory epithelium.[102] Although dosing did not specifically target the olfactory epithelium, rats were in the supine position during treatment. Presumably the formulation spread across the olfactory epithelium, providing ample opportunity for direct nose-to-brain transport via the olfactory bulb. However, there was no evidence that direct nose-to-brain transport was an important pathway for delivery of DZP to the brain, in agreement with the findings of Kaur and Kim.[103] DTE was only 74% (Table 3) and DZP concentrations in plasma preceded brain concentrations (Figure 17B), indicating absorption into the blood and subsequent advection to the brain was faster than diffusive transport along olfactory or trigeminal nerves.

In conclusion, the pharmacokinetic results presented here demonstrate that IN co-administration of AVF with APB is a viable method to rapidly deliver DZP into the systemic circulation and, subsequently, the brain. Since the highly concentrated formulation does not contain organic solvents, it is expected to be better tolerated and absorb faster than IN formulations of DZP that utilize solubilizing excipients. Administered as a noninvasive nasal spray, IN AVF/APB could be used to quickly terminate seizure emergencies in humans, resulting in reduced emergency department visits and an improved quality of life for patients who experience seizure emergencies. Further progress necessitates development of a device which can store the prodrug and

enzyme separately, and then combine them as into sprayed solution at the time of administration.

Chapter 4: Substrate stabilizes human aminopeptidase B during lyophilization

4.1 Summary

Human aminopeptidase B (APB) is a hydrolytic zinc metalloenzyme currently being investigated as a biocatalyst for intranasal delivery of prodrug/enzyme combinations. APB is known to be unstable in solution, with significant degradation over the course of 24 hr at room temperature. Therefore, enzyme stability is a major concern to ensure a viable drug product. Lyophilization is one technique commonly used to increase the activation energy for denaturization of proteins and confer an extended shelf-life. However, the lyophilization process itself can cause conformational changes and aggregation, leading to inactivation of the enzyme. In this study, we demonstrate the use of the substrate avizafone (AVF), a prodrug for diazepam, as a stabilizer to minimize inactivation of APB during lyophilization. Permutations of APB samples combined with AVF, trehalose, and/or mannitol were snap frozen and lyophilized at 0.016 mbar and 24 °C for 18 hr. The lyophilizates were then reconstituted in pH 7.4 PBS at 32 °C to measure the activity of APB. Of the permutations, an APB+AVF+trehalose combination resulted in minimum degradation with 71% retention of activity. This was followed by APB+AVF and APB+trehalose with 60% and 56% retention of activity respectively. In comparison, APB+mannitol and APB alone retained only 16% and 6.4% activity. Lyophilizates of the APB+AVF+trehalose formulation were subjected to a 6-month accelerated stability study, at the end of which negligible reduction in activity was observed. These results suggest co-lyophilization of an enzyme with its substrate can impart stability on par with the commonly used lyoprotectant, trehalose, but the combination of substrate and trehalose provides a greater stabilizing effect than either additive alone.

4.2 Introduction

Stabilization of enzymes by lyophilization is a common process that is used ubiquitously across many industries, from textiles to food processing.[104] Enzymes tend to lose activity during the lyophilization process and many can become completely inactivated. To prevent inactivation, cryo- and lyo-protecting excipients are added to the enzyme formulation before lyophilization. A variety of excipients can be used for this purpose, but the quantity and combination required for adequate stabilization can differ for a given enzyme and lyophilization cycle. Some common additives are trehalose (Tre), polyvinylpyrrolidone, and serum albumin. These excipients are not substrates, so they do not naturally dock into the active sites of enzymes. They are added in high concentrations relative to the concentration of the enzyme in order to limit molecular mobility, thereby minimizing perturbations in the protein structure that can lead to denaturation during the freezing and drying steps.[105] Conscientious selection and reduction of excipient is especially important in pharmaceutical preparations where the physicochemical properties (e.g. viscosity, rate of dissolution, volume) and biocompatibility (e.g. tonicity, pH, toxicity, immunogenicity) of the formulation are critical.[106,107]

Herein, we report the use of an enzyme's substrate as a stabilizer for lyophilization. We hypothesized that substrate occupation of the active site (i.e. substrate binding pocket) during lyophilization would prevent collapse of the active site in a similar fashion as traditional excipients. Furthermore, substrates offer the potential to preserve enzymatic activity at lower concentrations than other excipients because they have high binding affinity and are structurally complimentary to the arrangement of amino acid residues in the

active site. Our experiments suggest that substrate alone can be as effective at stabilizing enzymes as non-substrate excipients. A cooperative effect was also observed in which the inclusion of both substrate and the common stabilizing excipient, Tre, resulted in greater enzyme stability than the use of either additive by itself.

This work was born out of a desire to stabilize human aminopeptidase B (APB) in a pharmaceutical preparation. We have been developing pharmaceutical formulations that allow intranasal delivery of poorly soluble drugs via co-administration of a soluble prodrug with an exogenous converting enzyme.[42,108] One such formulation contains the diazepam prodrug avizafone (AVF) and APB. When combined and sprayed into the nasal cavity, hydrolysis of AVF by APB produces an open ring intermediate (ORI) species that spontaneously cyclizes to form supersaturated, rapidly permeating diazepam (DZP) (Figure 3). This drug delivery strategy requires AVF and APB to be in an inactivated state during storage. Segregating the two reactive components in a nasal spray device as two separate solutions was not feasible because APB is unstable in solution and AVF is marginally stable in solution. Storing AVF and APB as solids and reconstituting them at the time of administration seemed to be the most expedient way to achieve an acceptable shelf-life. It was thought that co-lyophilizing AVF and APB would improve the overall stability of the formulation, reduce the need for high concentrations of stabilizing excipients, and result in a homogeneous mixture that produces DZP upon reconstitution in a nasal spray.

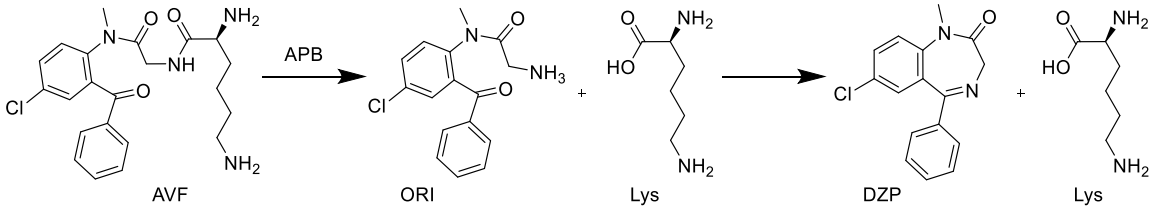

Figure 20. Reaction scheme for the hydrolysis of AVF by APB. Transformation of AVF to DZP progresses through an open ring intermediate, ORI.

The process of combining AVF and APB in a pre-lyophilization solution relies on reduced enzymatic activity of APB at low temperatures. When solutions of the two components were cooled in an ice bath, they could be mixed without generating DZP. The mixtures were then cooled further to freeze for lyophilization. After drying under vacuum, the resulting lyophilizates contained both AVF and APB in a stable, unreactive solid state. Reconstitution of the lyophilizates at room temperature activated the reactive system, producing DZP and allowing quantification of active APB. This process and the concept of using substrates as stabilizers for lyophilizing enzymes may be applicable to a variety of substrate/enzyme pairs.

4.3 Methods

4.3.1 Materials

S-avizafone dihydrochloride (AVF) was synthesized with > 99% purity, 99% ee from 5-chloro-2-methylaminobenzophenone according to the procedure described previously.[42] Recombinant human aminopeptidase B enzyme (APB), expressed and isolated with > 80% purity from JM109 *E. coli* cells, was produced by the procedure described previously.[108] Aspergillus oryzae protease, S-Lys-*para*-nitroanilide dihydrobromide (L*p*NA), and *para*-nitroaniline (*p*NA) were purchased from Sigma-

Aldrich, Inc. (St. Louis, MO: cat# P6110, L7002, and 31569). D-trehalose (Tre) as a dihydrate and D-mannitol (Man) were purchased from MP Biomedicals, LLC (Solon, OH: cat# 103097 and 102248). Tris(hydroxymethyl)aminomethane (Tris) and pH 7.4 phosphate buffered saline (PBS) were purchased from Fisher Scientific (Hampton, NH: cat# BP152 and 10010-023). The mass of the anhydrous form of Tre was reported for the sample concentrations.

4.3.2 Lyophilization procedure

Aqueous stock solutions of APB, AVF, Tre, Man, pH 7.4 Tris, and pure water were cooled in an ice bath to ~ 0 °C. Aliquots of the stock solutions were pipetted into cold 2 mL glass vials in the appropriate ratios to give the indicated component concentrations and an equal final volume for each sample. For samples that contained AVF, the AVF solution was added last. These cold pre-lyophilization solutions were mixed briefly with a pipette before placing the vials in liquid nitrogen for 5 min to snap freeze the contents. The vials were then removed from the liquid nitrogen, transferred to a lyophilization flask, and dried at room temperature under 0.016 mbar vacuum for 18 hrs using a Labconco, Inc. (Kansas City, MO) FreeZone 6 manifold freeze dryer. The vials containing the lyophilizates were capped and stored in desiccators until analysis. Storage was at room temperature unless otherwise stated.

4.3.3 Measurement of active enzyme

The amount of active enzyme remaining after sample processing, lyophilization, and storage was determined using spectroscopic techniques. Absorbance (Abs)

measurements to track the hydrolysis of substrates were made using an Agilent Technologies, Inc. (Santa Clara, CA) Cary 100 Bio UV/Vis double beam spectrophotometer equipped with a temperature controller. Unless stated otherwise, the temperature controller was set to 32 °C, which is the average temperature of the human nasal cavity.[54] Samples were analyzed in a quartz ultra-microcuvette with 1 cm pathlength (ℓ) and 50 µL minimum fill volume. Solutions of APB, Tre, Tris, and Man at the concentrations used in this study were transparent at the wavelengths used for spectroscopic quantification of the substrate and product concentrations.

To measure specific enzyme activity, lyophilizates were reconstituted with 1.00 mM L*p*NA in PBS that had been warmed to 32 °C. The resulting solutions were immediately transferred to a cuvette already positioned in the temperature-controlled block of the spectrophotometer. The change in Abs due to hydrolysis of L*p*NA was monitored at 405 nm. Readings were taken every 100 ms. The slope of the absorbance change (dAbs/dt) during the first 0.25 min was used to calculate the reaction rate (d[*p*NA]/dt) by

$$\frac{\mathrm{d}[p\mathrm{NA}]}{\mathrm{dt}} = \left(\frac{\ell^{-1}}{\varepsilon_{p\mathrm{NA}} - \varepsilon_{\mathrm{L}p\mathrm{NA}}}\right)\frac{\mathrm{dAbs}}{\mathrm{dt}} \qquad (1)$$

where ε denotes molar absorptivity. In pH 7.4 PBS at 32 °C, $\varepsilon_{p\mathrm{NA}}$ = 9860 $\mathrm{M^{-1}cm^{-1}}$ and $\varepsilon_{\mathrm{L}p\mathrm{NA}}$ = 55.9 $\mathrm{M^{-1}cm^{-1}}$ at 405 nm. (Refer to Appendices Table A3.9 for the temperature dependence of ε.) Specific enzyme activity was calculated by (d[*p*NA]/dt)/[APB].

The chromogenic substrate, L*p*NA, could not be used to measure the amount of active APB in samples that contained the prodrug substrate, AVF. To measure active APB

in these samples, the lyophilizates were reconstituted with 100 µL of either PBS or 1.00 mM AVF in PBS that had been warmed to 32 °C, and the resulting solutions were immediately transferred to a cuvette embedded in the spectrophotometer as described above. The change in Abs due to conversion of AVF to DZP was monitored for 20 min at 315 nm. Readings were taken every 0.25 min. The concentration of DZP at time t was calculated by

$$[\mathrm{DZP}]_t = \frac{\mathrm{Abs}_t - \mathrm{Abs}_0}{(\varepsilon_{\mathrm{DZP}} - \varepsilon_{\mathrm{AVF}})\ell} \tag{2}$$

where Abs_0 is the initial absorbance of the sample and Abs_t is the absorbance measured at time t. In pH 7.4 PBS at 32 °C, $\varepsilon_{\mathrm{DZP}}$ = 2040 $\mathrm{M^{-1}cm^{-1}}$ and $\varepsilon_{\mathrm{AVF}}$ = 753 $\mathrm{M^{-1}cm^{-1}}$ at 315 nm. The temperature dependence of $\varepsilon_{\mathrm{DZP}}$ and $\varepsilon_{\mathrm{AVF}}$, and the validity of neglecting $\varepsilon_{\mathrm{ORI}}$ in the calculation of DZP concentrations from absorbance measurements, have been discussed previously.[75] After obtaining DZP concentration-time profiles, the following set of coupled differential equations was fit to the data with [APB] as the lone fitting parameter:

$$\frac{\mathrm{d[AVF]}}{\mathrm{dt}} = -\frac{k_{\mathrm{cat}}[\mathrm{APB}][\mathrm{AVF}]}{K_M + [\mathrm{AVF}]} \tag{3}$$

$$\frac{\mathrm{d[ORI]}}{\mathrm{dt}} = \frac{k_{\mathrm{cat}}[\mathrm{APB}][\mathrm{AVF}]}{K_M + [\mathrm{AVF}]} - k_2[\mathrm{ORI}] \tag{4}$$

$$\frac{\mathrm{d[DZP]}}{\mathrm{dt}} = k_2[\mathrm{ORI}] \tag{5}$$

Fitting was performed using the ode45 function in conjunction with the lsqcurvefit function in MATLAB® version R2017b by The MathWorks, Inc. (Natick, MA). The catalytic rate

constant (k_{cat}), Michaelis constant (K_M), and cyclization rate constant (k_2) for conversion of AVF to DZP by APB in pH 7.4 PBS at 32 °C were reported previously: K_M = 370 μM, k_{cat} = 1250 min^{-1}, k_2 = 0.470 min^{-1}.[108]

4.3.4 Accelerated stability studies

Accelerated stability studies were performed at three storage temperatures for solid state APB and solution state AVF. Each study was 6 months long with measurements of active analyte remaining in the samples taken every 30 days. For AVF, the natural log of the ratios of AVF concentration remaining at time t to the initial concentration were plotted as a function of time. Linear regression was performed, and the degradation rate constant (k_{deg}) at each temperature was determined from the slopes according to the integrated first order rate equation:

$$\ln\left(\frac{[\mathrm{AVF}]_t}{[\mathrm{AVF}]_0}\right) = -k_{deg}t \qquad (6)$$

4.4 Results

The enzymatic activity of APB was temperature dependent. For hydrolysis of L*p*NA, the maximum enzyme activity was observed at 25 °C (Figure 21A, blue circles). At 1 °C, the rate of hydrolysis was more than 34 times slower. Solutions of L*p*NA and APB could be held at 1 °C for several minutes without causing substantial product formation as demonstrated by a lack of increase in Abs from 0-2.5 min in Figure 21B. When temperature was increased to 32 °C at the 2.5 min time point, enzyme activity recovered, and Abs measurements began to increase due to production of *p*NA. A similar

rate of Abs increase was observed for a control reaction initiated at 32 °C (Figure 21B, red line) compared to the reaction that had been initiated at 1 °C and subsequently brought to 32 °C, indicating that stalling the reaction at low temperatures did not cause loss of enzyme activity. The reaction could be successfully stalled at low temperatures for longer periods, but the maximum duration a reaction could be stalled without adverse effect was not determined.

Similarly, the rate of DZP production increased with increasing temperature, with the highest rate observed at the highest temperature condition tested, 40 °C (Figure 21A, red diamonds). However, the trend was not strictly due to temperature effects on the rate of enzymatic hydrolysis. Conversion of AVF to DZP is a two-step reaction (Figure 3). The rate of the second step, cyclization of to form the diazepine, is known to increase with increasing temperature.[48,109] No DZP production was observed over the course of 20 min at 1 °C. In order to determine if the low temperature had stalled the enzymatic hydrolysis reaction step or the ring closing reaction step, the enzymatic reaction was quenched by denaturing APB with the addition of 2x volume of methanol after being held at 1 ^{o}C for 20 min. Subsequently raising and holding the temperature at 32 ^{o}C did not result in the formation of DZP in the quenched solution. This observation suggested that ORI had not accumulated, and the enzymatic reaction was indeed stalled at 1 ^{o}C.

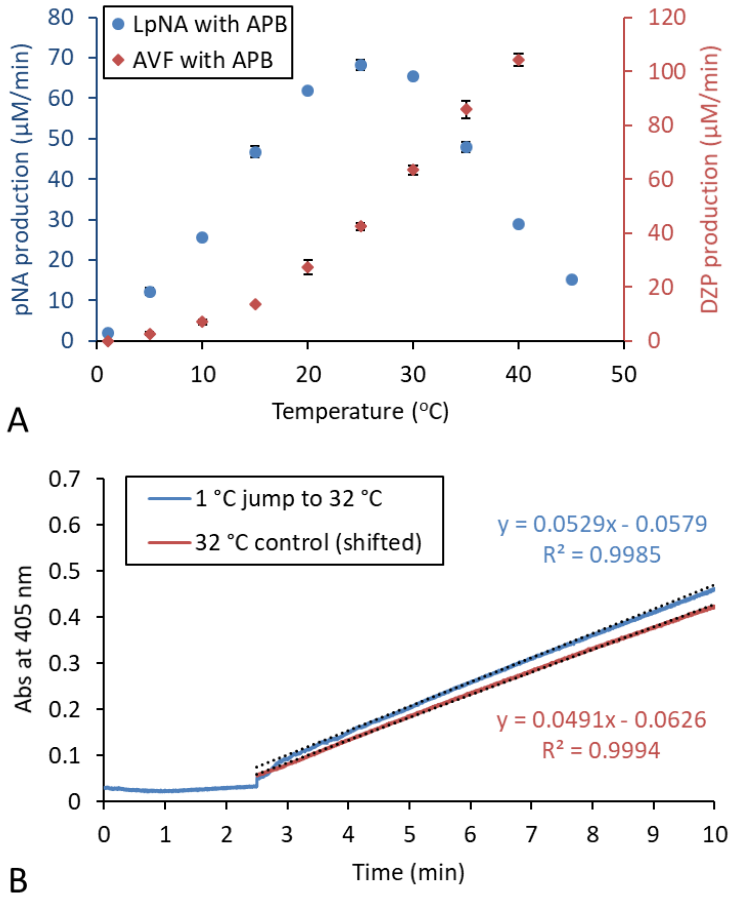

Figure 21. Temperature dependence of APB enzyme activity. (**A**) Slow rate of product formation at 1 °C allowed APB and AVF to be combined in the pre-lyophilization solution without substantial changes in the species concentrations. Reaction conditions: 1.00 mM L*p*NA or 2.00 mM AVF with 5.0 µg/mL APB in pH 7.4 PBS, n = 3, ±SD. The rate of DZP production was determined by regression of the linear portion of measured concentration-time profiles. (**B**) 1.00 mM L*p*NA with 0.50 µg/mL APB in pH 7.4 PBS did produce the chromophore product *p*NA when held for 2.5 min at 1 °C. The enzymatic activity of APB fully recovered when the temperature was brought to 32 °C. n = 1.

APB was not stable when stored in solution. Aliquots from solutions of APB stored at 4 °C in PBS were taken at specified time points and combined with a solution of L*p*NA in PBS to measure the change in enzyme activity over the course of a day (Figure 22A).

Production of *p*NA in the analytical samples, containing 1.00 mM L*p*NA and 12 µg/mL APB, was measured at 32 °C. A comparison of the average enzyme activity at each time point by one-way ANOVA indicated that statistically significant degradation had occurred, $F(3,8) = 35.2$, $p < 0.0001$. A Tukey HSD post hoc test revealed that the average enzyme activity ±SD was significantly lower at the 4 hr time point (8.9 ± 0.3 U/mg, $p = 0.0396$) and 16 hr time point (7.7 ± 0.2 U/mg, $p < 0.0001$) compared to the 1 hr time point (9.5 ± 0.1 U/mg). There was no statistically significant difference between the 1 hr and 2 hr time points, $p = 0.174$.

A large initial drop in enzyme activity was observed when APB solutions were lyophilized (Figure 22B). The loss in activity was most dramatic when no excipient was added (i.e. stock solutions of APB diluted to pre-lyophilization sample concentrations with just water), with only 6.4% recovery of active enzyme after lyophilization. Adding Tre to the formulation stabilized APB during the lyophilization process. The extent of stabilization was dependent on the Tre concentration, with concentrations 12.5 mg/mL or greater providing ~57% recovery of active APB. Co-lyophilizing APB with L*p*NA, also had a stabilizing effect. There were no statistically significant differences between the average enzyme activity for APB lyophilized in the presence of 1.00 mM L*p*NA, 12.5 mg/mL Tre, or 25.0 mg/mL Tre as determined by one-way ANOVA, $F(2,6) = 0.853$, $p = 0.472$.

The pre-lyophilization controls, shown as blue bars in Figure 22B, demonstrate that enzyme activity was unaffected by the presence of Tre or Man. Although the addition of the bulking agent, Man, produced elegant cakes, it did not markedly stabilize APB during

the lyophilization process. The cakes produced by samples with APB and 12.5 and 25.0 mg/mL Tre were uniform, but samples with 6.25 or 3.13 mg/mL Tre were non-uniform and wispy. Similarly, the low mass contained in lyophilizates produced from samples of APB lyophilized in the presence of L*p*NA resulted in diminutive, non-uniform, wispy cakes. The lyophilized samples that contained only APB did not contain enough mass to produce visible cakes. However, changes in cake appearance do not necessarily impact product quality.[110]

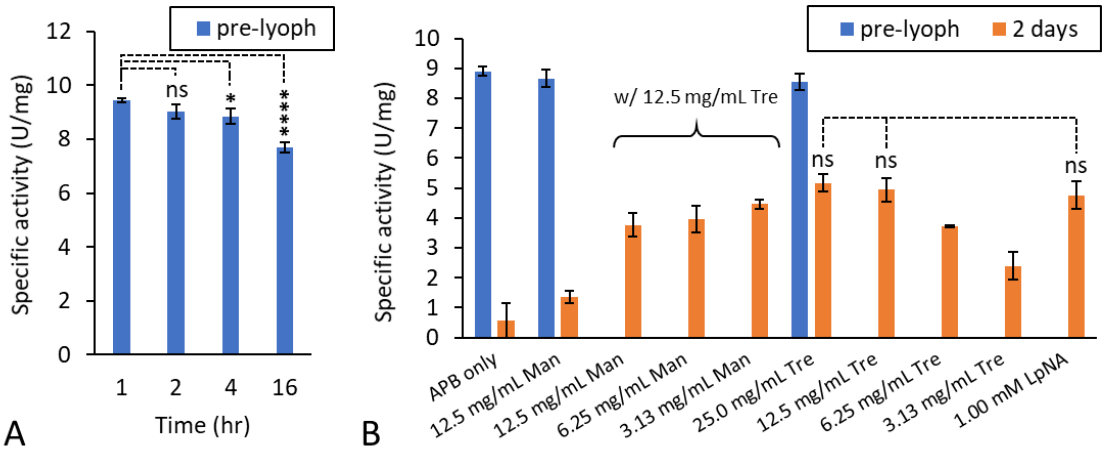

Figure 22. Pilot stability studies for APB. The chromogenic substrate, L*p*NA, was used to measure enzyme activity for preliminary formulation studies. Reactions performed in pH 7.4 PBS at 32 °C, n = 3, ±SD. (**A**) Solution state stability of 50 µg/mL APB stored in pH 7.4 PBS at 4 °C. Statistically significant degradation was observed over the course of a day. (**B**) Stability of APB upon lyophilization. Lyophilizates made from solutions containing 15 µg/mL APB with mannitol (Man) and/or trehalose (Tre) were stored for 2 days at room temperature before analysis. Reconstitution of APB only lyophilizates with 1.00 mM L*p*NA in PBS showed nearly complete loss of enzyme activity, while those containing 12.5 mg/mL or greater Tre provided optimum stabilization of APB. Lyophilizing APB in the presence of 1.00 mM L*p*NA substrate resulted in equivalent stabilization compared to the high concentration Tre formulations.

Inclusion of the prodrug substrate, AVF, in the lyophilizate formulation had a stabilizing effect against degradation of APB during the lyophilization process (Figure 23A). A two-way ANOVA conducted to examine the effect of formulation composition and time on active APB concentration in the lyophilizates indicated there were significant differences between the formulation groups [$F(2,18) = 90.6$, $p < 0.0001$], significant differences over time [$F(2,18) = 21.5$, $p < 0.0001$], and a significant interaction effect [$F(4,18) = 3.59$, $p = 0.0255$]. Tukey HSD post hoc analysis comparing the formulation groups revealed that the AVF+APB+Tre formulation provided statistically significant better stabilization than the AVF+APB ($p < 0.0001$) or APB+Tre ($p < 0.0001$) formulations, but no significant difference between the AVF+APB and APB+Tre formulation groups ($p = 0.928$). Therefore, the combination of AVF and Tre had a greater stabilizing effect against degradation during the lyophilization process than either additive alone.

As was observed with APB only lyophilizates, the low concentration of the AVF+APB lyophilizates did not allow visible cakes to form. Instead, the collapsed material appeared as residue adhering to the surface of the vial. There was a gradual loss in enzyme activity observed over the course of 6 months with the AVF+APB formulation, as can be seen in Figure 23A. Tukey HSD analysis comparing the average active APB concentration in the AVF+APB lyophilizates stored for 2 days with concentrations measured after storage for 90 and 180 days confirmed that there was significant degradation of APB over time ($p < 0.0001$ for both comparisons). When Tre was included

in the formulation, uniform cakes were formed and the loss of enzyme activity over the course of 6 months was not statistically significant. For the AVF+APB+Tre formulation on day 2 compared to day 90 and 180, p = 0.502 and 0.356, respectively. For the APB+Tre formulation on day 2 compared to day 90 and 180, p = 0.523 and 0.120, respectively.

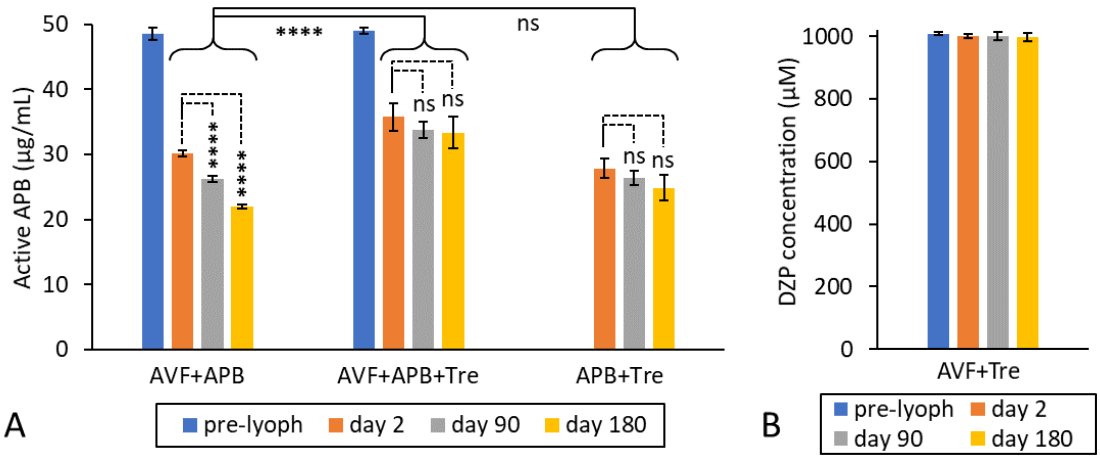

Figure 23. Room temperature stability studies. Error bars are SD with n = 3. (**A**) Optimum stability was achieved by co-lyophilization of APB with AVF and Tre. Concentrations of active APB in the lyophilizates were measured in pH 7.4 PBS at 32 °C after storage for the specified time at 24 °C. Pre-lyophilization solutions contained AVF = 1.00 mM, APB = 50 µg/mL, and/or Tre = 12.5 mg/mL. (**B**) Controls of 1.00 mM AVF lyophilized with 12.5 mg/mL Tre and subsequently reconstituted with 50 µg/mL APB in pH 7.4 PBS at 32 °C produced an equimolar concentration of DZP, indicating AVF was stable in the lyophilizate.

The concentration of active APB was also measured in a series of lyophilizate formulation controls in order to rule out potential mechanisms of degradation or stabilization. Lyophilizate controls containing AVF and Tre, but no APB, indicated that AVF was stable during the lyophilization process and upon subsequent storage as a solid

at room temperature (Figure 23B). The addition of pH 7.4 Tris buffer to the pre-lyophilization solutions did not result in greater enzyme stability (Appendices, Figure A3.73). Likewise, formulations containing pH 5.5 PBS or phosphate buffer without salt did not result in greater enzyme stability.

The lyophilizate formulation showing the greatest stability at room temperature, that which contained AVF+APB+Tre, was subjected to an accelerated stability study (Figure 24A). The production of DZP upon reconstitution of the lyophilizates was measured, and curve fitting the coupled differential equations (Equations 3-5) to the resulting concentration-time profiles allowed the concentration of active APB to be determined. A two-way ANOVA conducted to examine the effect of temperature and time on active APB concentration in the lyophilizates indicated that there were no significant differences over time [$F(6,42) = 1.93$, $p = 0.0977$] and that the interaction of the factors was not significant [$F(12,42) = 0.243$, $p = 0.994$]. However, there were significant differences observed between the temperature groups [$F(2,42) = 6.28$, $p = 0.00412$]. Tukey HSD post hoc analysis indicated storage at 4 ^{o}C was not statistically different than storage at 24 ^{o}C ($p = 0.840$), while statistically significant lower active APB concentrations were observed upon storage at 40 ^{o}C compared to 4 ^{o}C ($p = 0.00533$) and 24 ^{o}C ($p = 0.0234$). The results suggest APB was highly stable in the AVF+APB+Tre lyophilizates even though there was an initial loss of active enzyme from the lyophilization procedure.

The solution state stability of the prodrug, AVF, was also investigated (Figure 24B). The initial AVF concentration and subsequent concentrations remaining in samples prepared for the stability study were determined by measuring the total DZP produced after

hydrolysis with 2.0 U/mL of *Aspergillus oryzae* protease. (APB was not used here as it was unnecessary and more expensive.) The degradation of AVF was found to follow first order kinetics with degradation rate constants, k_{deg} ±SE = 0.31 ± 0.03, 0.44 ± 0.04, and 2.9 ± 0.1 yr^{-1} for 4, 24, and 60 °C, respectively.

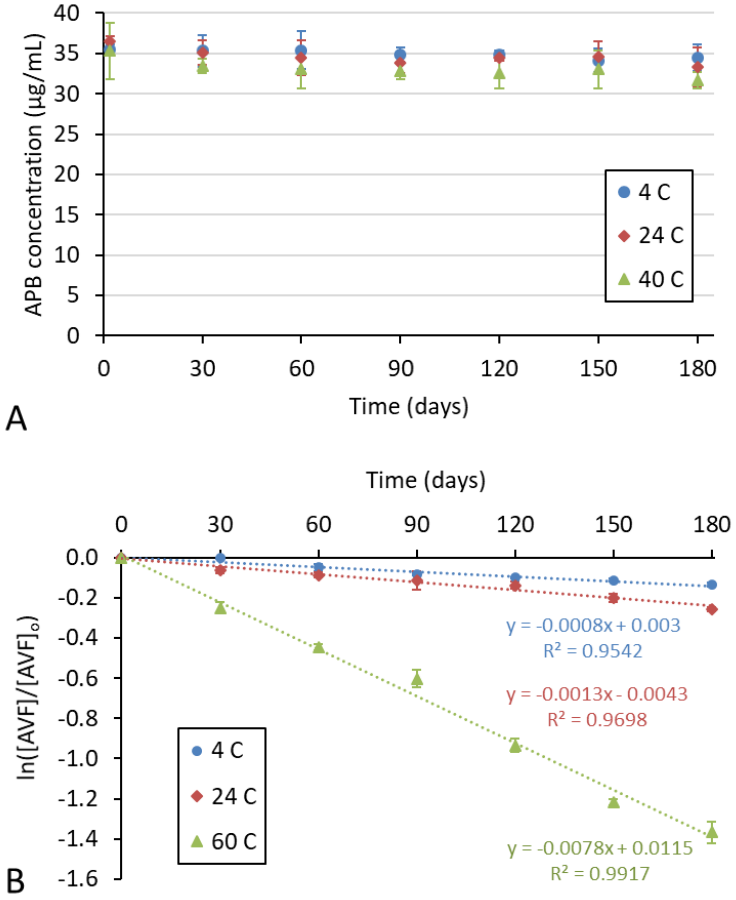

Figure 24. Accelerated stability studies. Error bars are ±SD. (**A**) Solid state stability of 50 µg/mL APB co-lyophilized with 1.00 mM AVF and 12.5 mg/mL Tre. (**B**) Solution state stability of 2.00 mM AVF in pH 7.4 PBS.

4.5 Discussion

Aminopeptidase B (BRENDA:EC3.4.11.6) has been isolated from animals, plants, bacteria, and fungi.[111] It is an endopeptidase with catalytic activity confined to the cleavage

of basic amino acids from the N-terminus of certain oligopeptides or synthetic substrates by hydrolysis of the peptide bond. There are conflicting reports in the literature regarding the stability of this enzyme that seem to depend on the source species and expression system, but the consensus is that purified enzyme preparations tend to be unstable.[112,113] We found that recombinant human aminopeptidase B, referred to here as APB, was stable enough in PBS to work with at room temperature for several hours, but there was a noticeable decrease in enzyme activity by the end of the day. Figure 22A demonstrates the solution state instability of APB. The enzyme did not tolerate freeze/thaw cycles well either. Considerable reduction in enzyme activity was observed after thawing from overnight storage at -20 °C. It may be that the difference in enzyme activity between the pre-lyophilization solutions and day 2 lyophilizates shown in Figure 23A was due to insufficient cryoprotection.

AVF is a Lys-Gly dipeptide derivative of a 2-methylamino-5-chlorobenzophenone and substrate for APB (Figure 3). There are conflicting reports in the literature regarding the stability of AVF. Clair *et al*. measured the solution state stability of a combination drug product over a 6 month period at pH 4 and temperatures as high as 40 °C and found only 5% degradation of AVF.[114] Breton *et al*. performed 24 hr photolytic, oxidative, hydrolytic, and thermal stress testing of solid and solution state AVF.[115] The latter authors concluded that AVF in solution was susceptible to photolytic and thermal degradation but was stable in the solid state. Both stability studies utilized chromatographic techniques that would not be able to distinguish between the S and R isomers of AVF. Therefore, degradation by enantiomerization to the inactive isomer would not be detected.[42] In the present study,

active AVF was measured by product formation from enzymatic hydrolysis. Using this technique, we found that AVF was stable in the solid state (Figure 23B) but predicted only 42% active AVF would remain after room temperature storage in solution at pH 7.4 for 2 yr based on k_{deg} at 24 °C determined from the data represented by red diamonds in Figure 24B.

Since the intention was to use both APB and AVF in a nasal spray formulation, we began investigating ways to prepare them as a mixture of stable, unreactive solids that could be rapidly reconstituted and subsequently atomized for deposition in the nasal cavity. Co-lyophilizing the components into a single lyophilizate offered several advantages in this regard: homogeneous mixtures of the components could be made in the pre-lyophilization solutions, the increased surface area due to cake formation would facilitate rapid dissolution, and the solid state of the lyophilizates would extend the shelf-life of the drug product.[116] The AVF+APB+Tre formulation provided the most stabilization, with 71% recovery of active APB immediately after lyophilization and minimal degradation thereafter (Figure 23A). In comparison, APB+Tre provided 56% and AVF+APB provided 60% recovery of active APB immediately after lyophilization. Interestingly, lyophilization of APB in the presence of a chromogenic substrate, L*p*NA, also conferred stabilization on par with Tre (Figure 22B). The relatively high initial recovery observed with just substrate and enzyme was an impressive result, even though the amount of active APB in the AVF+APB lyophilizate steadily decreased over time (Figure 23A). Presumably enough molecular mobility remained in the samples to slowly turnover the docked substrate that

was supporting the active site structure, thus leading to eventual degradation. Further studies are needed to investigate this behavior.

The effect of varying substrate concentration on the stabilization of APB during the lyophilization process was not examined here, but the exceptionally low concentration of substrate used for the experiment (1.00 mM, i.e. 0.504 mg/mL of AVF or 0.428 mg/L of L*p*NA) demonstrates the remarkable potential to stabilize enzymes with the addition of far less material than is normally required with the use of traditional cryoprotectant or lyoprotectant excipients. For example, the molar concentration of APB in the samples shown in Figure 23A was 0.68 µM based on the molecular mass of APB (74 kDa), giving a mole ratio of 1,500 AVF:APB. In comparison, the molar concentration of Tre was 36.5 mM, giving a mole ratio of 54,000 Tre:APB. The prevailing theories used to explain the stabilization of proteins by sugars such as Tre involve maintenance of the native protein structure through vitrification and water replacement.[117] The sugars are thought to act as scaffolding, preventing molecular mobility that can lead to unfolding and chemical degradation. Smaller, flexible oligosaccharides that can more easily occupy the cavities within a protein structure have been shown to be more effective stabilizers than rigid, polymeric sugars.[118] In this view, a large number of excipient molecules would be needed to provide structural support to the entire protein. Thus, the high mole ratio of Tre to APB needed for stabilization seems reasonable.

Preservation of the peripheral protein structure is not as critical to the retention of enzyme activity as preserving the structure of the active site.[119,120] Docking of a substrate in the active site of APB provides a well-tailored support scaffold, preventing misalignment

of the binding/catalytic residues and collapse of the active site pocket as water molecules are removed during the drying step. This mechanism for the stabilization of APB does not rely on protection of the entire protein, which explains why stabilization was observed with a much lower concentration of substrate compared to Tre. In the solution state, the degree of enzyme stabilization has been shown to depend on substrate structure. Better substrates (those with lower K_M values) were better stabilizers.[121] The trend is likely to extend to improved stabilization during lyophilization.

Reports of the inclusion of an enzyme substrate as a stabilizer for lyophilization are scant, presumably because substrate turnover complicates the process and would need to be controlled to produce consistent lyophilizates. However, the technique we describe for limiting substrate turnover by combining the formulation components at low temperature can be generalized to a wide variety of enzymes.[122] For example, Dai and Klibanov described snap freezing substrate/enzyme pairs during the lyophilization process to improve enzyme activity upon reconstitution of the lyophilizates in organic solvents.[123] They tested four different oxidases with several substrates and observed complete elimination of lyophilization-induced activity loss in some cases. There are some reports of using enzyme inhibitors for stabilization of lyophilizates, but inhibitors have the potential to imprint an altered conformation for the active site thereby changing the selectivity and specificity of the enzyme.[124]

We conclude by recognizing that this study, while demonstrating the effect of substrate on the stability of an enzyme during lyophilization, was limited in scope to APB. The primary goal of these experiments was to assess the feasibility of co-lyophilizing the

AVF/APB pair to stabilize the pharmaceutical formulation for further translational development and guide design requirements for a specialized nasal spray device. Additional experiments for scale-up to therapeutically relevant concentrations, optimization of the lyophilization process parameters, full characterization of the lyophilizates, and performance testing in the delivery device are ongoing.

Chapter 5: Reactive formulations for intranasal delivery of midazolam

5.1 Summary

Systemic delivery of many lipophilic drugs can be achieved quickly and conveniently by intranasal administration. However, the low aqueous solubility of these drugs can make it difficult to formulate a therapeutic dose in the small volume required for nasal sprays. One formulation strategy to circumvent solubility issues relies on *in situ* production of drug from co-administration of soluble reactants. Herein, we describe how a prodrug/enzyme reaction or an acid/base reaction could be used to formulate the lipophilic drug, midazolam, in an aqueous solution for intranasal delivery. In both formulation approaches, the reactions progress through an intermediate open ring form of midazolam. The half-life of the open ring form was measured at 32 °C by UV spectroscopy and found to be pH dependent, with a local minimum of 3.45 ± 0.27 min at pH 5.0 and local maximum of 17.2 ± 1.7 min at pH 6.5. *In vitro* drug transport studies were performed at pH 5.5, 6.5, and 7.4 using MDCKII-wt cell monolayers as a model for nasal epithelium. Apparent permeability coefficients respective to each pH condition were found to be 33 ± 20, 40 ± 14, and 145 ± 64 nm/s for the open ring form. Permeability of midazolam was also pH dependent and over twofold greater than that of the open ring form. Generation of midazolam in these low volume reactive formulations led to metastable supersaturated solutions and an upper limit to the supersaturation was observed. The upper limit of supersaturation for unionized midazolam was determined to be 1.15 mM. Above this limit, amorphous midazolam phase separated from solution. The prodrug/enzyme reaction was less flexible in regard to setting the formulation pH for optimum enzyme activity and drug absorption, whereas the final pH of the acid/base formulation can be adjusted by choosing the appropriate base concentration. Absorption of midazolam generated from these

reactive formulations would be controlled by the upper limit of supersaturation and cyclization rate of the open ring form.

5.2 Introduction

Midazolam (MDZ) is a short-acting central nervous system depressant with hypnotic, sedative, anxiolytic, amnesic, muscle relaxant, and anticonvulsant properties. It is the most common sedative administered prior to anesthesia in the United States, and it is a drug of choice for first-line rescue therapy in the treatment of seizure emergencies, such as status epilepticus.[10,125] Considered safe and effective for addressing a variety of public health needs globally, MDZ has been deemed an essential medication by the World Health Organization.[126] The dosage forms currently available on the market are oral tablets, oral syrups, oromucosal solutions (only available in Europe), and solutions for intravenous or intramuscular injection.[127,128] Several intranasal (IN) formulations have been investigated[35,129-134] or are under development,[135] but a dosage form specifically designed for IN delivery has not yet become commercially available.

IN delivery of MDZ is attractive because it offers many important advantages over other routes of administration, especially in emergency situations.[14] A therapeutic plasma concentration can be attained quickly due to the large absorptive surface area, high vascularization, and thin epithelium of the nasal mucosa. Orally administered MDZ reaches a peak plasma concentration in approximately 1 hr and has low bioavailability (~30%) due to extensive gastrointestinal and hepatic first-pass metabolism.[136,137] In comparison, peak plasma concentrations have been reported in the 10-20 min range with bioavailabilities ranging from 50-90% for IN formulations.[29,34,133] Furthermore, IN administration is convenient and noninvasive. Operation of nasal spray devices does not require special skills and is generally intuitive. There is no need to remove articles of

clothing or puncture the skin, posing a lower risk of injury to the patient compared to parenteral routes of administration.

For three decades, caregivers have been administering commercially available injectable MDZ formulations 'off-label' through the IN route by using a needleless syringe or attaching a nasal mucosal atomization device (MAD) to a syringe and spraying the solution into the nose of the patient.[138-140] An IN dose of 0.2 mg/kg (max 10 mg) is often used for treating status epilepticus and 0.4-0.5 mg/kg (max 10 mg) for sedation in pediatric patients.[10,141] Although generally effective, the injectable MDZ formulations are not ideal for IN delivery. A large volume of the injectable formulation (2 mL split between each nostril) is required to administer a 10 mg dose. The volume of liquid that can be deposited in the human nasal cavity without causing significant loss of drug by drainage from the nostril or into the nasopharynx is less than 200 µL,[22,24] and low bioavailability due to runoff is a well-known issue with IN administration of injectable MDZ formulations.[129,142] Therefore, a highly concentrated MDZ nasal spray is needed to reliably deliver the intended dose.

Although MDZ has been touted as the first water-soluble benzodiazepine, its solubility is pH dependent.[143] The lipophilic, neutral microspecies predominates at pH 7.4 and has a thermodynamic aqueous solubility of only 0.018 ± 0.001 mg/mL (55 ± 4 µM).[42] The nitrogen at position 2 of the imidazole ring has an estimated pK_a of 6.2,[68] producing a somewhat water-soluble cation when protonated. At pH < 5, protonation of the imine in the diazepine ring leads to a reversable ring-opening reaction and a highly soluble open ring species (MDZ_{open}) that is in equilibrium with the closed ring species. The oromucosal,

intravenous, and intramuscular dosage forms are formulated to a concentration of 5 mg/mL by lowering the pH to ~3 and contain up to 25% MDZ_{open}.[128,144,145] Reducing the pH further would permit higher concentrations; however, the pH of an IN formulation should be close to the physiological pH range of the nasal cavity to avoid causing discomfort, inducing secretion, hampering absorption, and damaging the mucosa.[146,147] The average anterior pH of the nasal cavity is 6.40 (range: 5.17 – 8.13) and average posterior pH is 6.27 (range: 5.20 – 8.00).[55] Temporary distress, a burning unpleasant taste, stinging, sneezing, coughing, swallowing, watery eyes, and other mild adverse events reported from IN administration of aqueous MDZ formulations have been attributed to low pH.[148-150] Concentrated formulations of MDZ have been made by utilizing organic co-solvents[130,134,151,152] to increase the thermodynamic solubility or by sequestering the drug in carriers like emulsions,[131] polymeric particles,[132] or inclusion complexes.[129] However, these additives can reduce the driving force for permeation of drug across membranes[38,39,153] and irritate sensitive nasal tissues.[34,40]

Our group has been developing a new approach to formulate drugs that have low solubility or poor stability in an aqueous vehicle. The strategy involves co-administration of a two-part, reactive system to generate drug *in situ*. In the case of small lypophilic drugs, such as MDZ, a metastable supersaturated solution of the drug can be produced at the site of administration and result in rapid absorption. We previously reported *in vitro*[28,42,43,49,75] and *in vivo*[108] experiments that demonstrated enhanced permeation of drug across cell membranes using reactive prodrug/enzyme formulations to generate supersaturated solutions of phenytoin, diazepam, or MDZ. The MDZ prodrug/enzyme formulation

consisted of MDZ_{open} derivatized at the primary amine with lysine (Lys-MDZ_{pro}) and a fungal converting enzyme, *Aspergillus oryzae* protease (AOP). Cleavage of the N-terminal lysine from Lys-MDZ_{pro} is catalyzed by AOP through enzymatic hydrolysis of the peptide bond and liberates MDZ_{open}. MDZ_{open} can then undergo spontaneous intramolecular cyclization to form MDZ. In the current report, an analogous version of the prodrug derivatized with phenylalanine (Phe-MDZ_{pro}) is introduced. Phe-MDZ_{pro} can be hydrolyzed by a human enzyme, aminopeptidase N (APN).

The MDZ_{pro}/enzyme formulations were compared to a reactive acid/base formulation approach that combines the dihydrochloride salt of MDZ_{open} (MDZ_{open}•2HCl) with an aqueous base at the time of administration to produce a supersaturated solution of MDZ with a pH and volume appropriate for IN delivery. Figure 25 illustrates the relationship between these reactive formulation approaches. Both approaches rely on water-soluble forms of MDZ_{open} that do not undergo cyclization during storage because the amine is occupied, either by a covalent bond with an amino acid or as a primary ammonium salt. We hypothesized that recovery of the free amine through deprotonation of MDZ_{open}•2HCl with a strong base would result in faster reaction rates and more rapid delivery of MDZ than could be achieved by cleavage of an amino acid moiety with an enzyme. However, further investigation revealed that the ring closing step was rate limiting. Thus, rapid liberation of MDZ_{open} from the precursor species would result in accumulation of MDZ_{open} in the nasal cavity. These observations prompted a series of experiments aimed at determining the pH dependence of the first-order cyclization rate constant (k_2), supersaturation behavior of MDZ, and permeation of each reaction species

across epithelium to evaluate the viability of using an open ring precursor for rapid IN delivery of MDZ.

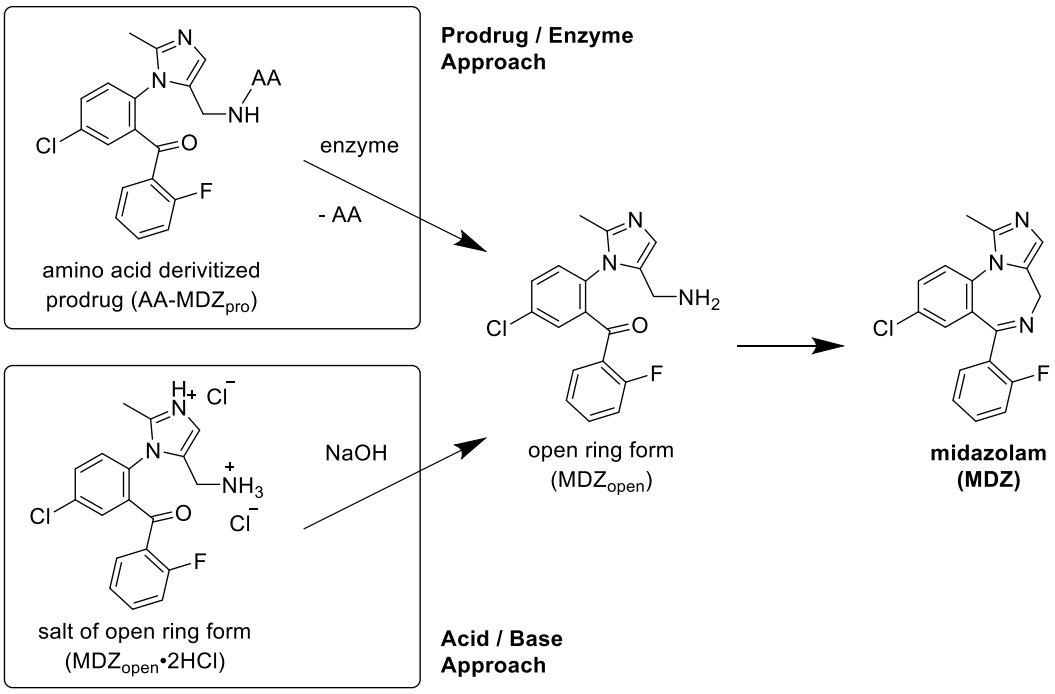

Figure 25. Reactive IN formulations produce MDZ *in situ*. Potential two-part, reactive formulations for IN delivery of MDZ include a prodrug/enzyme pair or an acid/base pair. The reactants would be stored in separate compartments of a specially designed nasal spray device. Upon actuation of the device, the reactants are rapidly mixed and atomized into a spray to be deposited as a single solution onto the surface of the nasal mucosa. Production of MDZ from the mixed formulation proceeds in the nasal cavity. AA = amino acid moiety.

5.3 Materials

5.3.1 Prodrugs

The trihydrochloride salt of the S-lysyl-midazolam prodrug (Lys-MDZ_{pro}•3HCl) was synthesized with > 99% purity and > 94% ee from MDZ by opening the diazepine ring and adding a lysine group. Similarly, the dihydrochloride salt of the S-phenylalanyl-midazolam prodrug (Phe-MDZ_{pro}•2HCl) was synthesized with > 99% purity and 98% ee by adding a phenylalanine group to the open ring form of MDZ. Details for the synthesis, purification, and characterization of Lys-MDZ_{pro} were described previously.[42]

5.3.2 Converting enzymes

Recombinant human aminopeptidase N (APN), expressed and isolated with > 95% purity from an NS0 murine cell line, was purchased from R&D Systems (Minneapolis, MN: cat# 3815-ZN, lot PQP011809A). Recombinant human aminopeptidase B enzyme (APB), expressed and isolated with >80% purity from a JM109 *E. coli* cell line, was produced in house by the procedure described previously.[76] Purity of APB was >80% by gel electrophoresis. *Aspergillus oryzae* protease (AOP) was purchased from Sigma-Aldrich, Inc. (St. Louis, MO: cat# P6110, lot SLBQ4182V).

5.3.3 Midazolam open ring salt

MDZ_{open} was isolated as a solid dihydrochloride salt (MDZ_{open}•2HCl) by opening the diazepine ring of MDZ in acidic medium using a procedure first described by Walser et al.[154] MDZ (253 mg, 777 µmol), purchased from MEDISCA Pharmaceutique Inc. (Plattsburgh, NY: NDC 38779-2519-06, lot 888378/G), was dissolved in 140 µL of 12 N

HCl. Then, 2 mL of isopropanol (IPA) was added, and the mixture was azeotropically dried by reducing the volume to approximately 0.5 mL with a rotovap. The solids were collected by filtration and purified by co-solvent recrystallization. Recrystallization was performed by dissolving the crude in a minimum volume of MeOH. IPA was added slowly until the cloud point was reached. After cooling to -20 °C, the purified material was collected by filtration, washed with cold IPA, and dried under vacuum to yield 87% (281 mg, 674 µmol) of (2-(5-(aminomethyl)-2-methyl-1H-imidazol-1-yl)-5-chlorophenyl)(2-fluorophenyl)methanone dihydrochloride as shiny, white, hygroscopic crystals. Mp: 247 °C dec. ATR-FTIR neat: imidazole 3100-2300 cm^{-1} (s, br), aromatic overtones 1956 and 1799 cm^{-1} (w), C=O 1651 cm^{-1} (s, sh). ^{1}H NMR (400 MHz, D2O) δ 7.92 (dd, 1H), 7.89 (s, 1H), 7.72-7.47 (m, 4H), 7.31 (t, 1H), 7.23 (q, 1H), 4.10 (s, 2H), 2.37 (s, 3H). See Appendices A4, Section A4.1 for ART-FTIR and ^{1}H NMR spectra.

5.4 Methods

5.4.1 Determination of ring closing reaction rate

To obtain the cyclization reaction rate dependence with respect to pH, UV absorbance (Abs) spectra were measured using an Agilent Technologies, Inc. (Santa Clara, CA) Cary 100 Bio UV/Vis double beam spectrophotometer equipped with a temperature controller. The temperature controller was set to the average temperature of the nasal cavity, 32 °C.[54] Prior to data collection, solutions of 23 mM phosphate buffered saline (PBS) or 23 mM citrate buffered saline (CBS), 8.00 mM MDZ_{open}•2HCl in water, and 1 cm pathlength (ℓ) quartz ultra-microcuvettes were warmed to 32 °C. A 25.0 µL aliquot of the MDZ_{open}•2HCl solution was mixed with 175 µL of buffer in the sample cuvette to

obtain a 1.00 mM total analyte concentration ([total]) in 20 mM of buffer. The concentration of MDZ_{open} at the start of data collection ($[MDZ_{open}]_0$) was not 1.00 mM because MDZ_{open} began to equilibrate with MDZ as soon as solid MDZ_{open}•2HCl was dissolved to make the stock solution. The reaction progress was monitored by collecting scans over time from 300-400 nm at a scan rate of 600 nm/min using the Cary WinUV version 3.10(246) Scan Application. The molar absorptivities (ε) of MDZ_{open} and MDZ at 300 nm were used to calculate concentrations of each species at time t.

$$\left[\mathrm{MDZ_{open}}\right]_t = \frac{\mathrm{Abs_t}/\ell - \varepsilon_{\mathrm{MDZ}}[\mathrm{total}]}{\varepsilon_{\mathrm{MDZ_{open}}} - \varepsilon_{\mathrm{MDZ}}} \quad (1)$$

$$[\mathrm{MDZ}]_t = [\mathrm{total}] - \left[\mathrm{MDZ_{open}}\right]_t \quad (2)$$

Linear regression of $\ln([MDZ_{open}]_t/[MDZ_{open}]_0)$ versus t, plotted from t = 0-15 min, gave the first-order ring closing rate constant (k_2) as the slope according to the integrated reaction rate law.

$$\ln\left(\frac{\left[\mathrm{MDZ_{open}}\right]_t}{\left[\mathrm{MDZ_{open}}\right]_0}\right) = -k_2 t \quad (3)$$

The half-life ($t_{1/2}$) of MDZ_{open} was calculated by $t_{1/2} = \ln(2)/k_2$.

5.4.2 Polarized light microscopy

MDZ_{open}•2HCl (100 µL, 8.00 mM) was combined with 100 µL of 16.0 mM NaOH in a small glass vial. The solution became turbid as MDZ phase separated. Aliquots of the turbid reaction mixture were removed at regular intervals to view under a Nikon, Inc.

(Tokyo, Japan) P-1 microscope equipped with a Nikon 40x/0.65 NA - WD 0.65 Pol objective, Nikon Digital Sight DS-Fi1 camera, and temperature-controlled stage. Images were captured using NIS-Elements F 3.0 software.

5.4.3 Differential scanning calorimetry (DSC)

Samples for DSC were placed in hermetically sealed aluminum Tzero pans. Measurements were performed from 40-300 ºC at a heating rate of 10 °C/min under nitrogen purge (45 mL/min) using a TA Instruments Q2000 V24.11 Build 124 DSC with a standard cell and Universal V4.5A software. Glass transition temperatures (T_g) were determined at the inflection point. Melting temperature (T_m) and cold crystallization (T_{cc}) ranges were determined by the onset and peak of the melting endotherm or crystallization exotherm. For the MDZ precipitate samples, MDZ_{open}•2HCl (14.2 mg) in 100 µL of water was combined with 100 µL of 0.681 M NaOH to form MDZ which subsequently phase separated from solution. The precipitate from the reaction was allowed to sediment before the supernatant containing soluble species was removed. The precipitate was then washed once with 50 µL of water and dried under high vacuum at room temperature for 3 hr before performing measurements. There were no special preparation steps for the MDZ standard or MDZ_{open}•2HCl sample.

5.4.4 Liquid Chromatography (HPLC)

Measurements of Phe-MDZ_{pro} and MDZ concentrations were performed using an Agilent 1260 Infinity LC system: quaternary pump G1311B, autosampler G1329B, thermostatted column compartment G1316A, diode-array detector G4212B, and Agilent OpenLAB CDS software. The isocratic mobile phase was 10 mM acetate buffer pH 5.0

and acetonitrile (60:40 v/v) with a flow rate of 0.65 mL/min through an Agilent ZORBAX Eclipse XDB-C18 column (3.0 x 150 mm, 3.5 µm particle size). Diazepam was used as the internal standard (IS). Aqueous samples were spiked with IS prepared in acetonitrile to obtain 8.00 µM (2.28 µg/mL) IS. Analytes from 25 µL injections of each sample were detected at 310 nm with retention times of 3.6, 6.3, and 8.4 min observed for Phe-MDZ_{pro}, MDZ, and IS respectively. Calibration curves were constructed in triplicate using MDZ standard solutions prepared in the mobile phase with IS. For Phe-MDZ_{pro}, LOD (3.3×SEy/slope) was 0.297 µM (0.146 µg/mL), and LOQ (10×SEy/slope) was 0.901 µM (0.443 µg/mL). For MDZ, LOD was 0.0696 µM (0.0227 µg/mL), and LOQ was 0.211 µM (0.0687 µg/mL). Representative examples of the chromatograms and calibration curves can be found in Appendices A4, Section A4.1. The peak area ratios (Phe-MDZ_{pro} or MDZ/IS) and dilution factors were used to calculate the analyte concentrations in the samples.

5.4.5 Enzyme kinetics

The Michaelis constant (K_M) and maximum reaction velocity (V_{max}) for hydrolysis of Phe-MDZ_{pro} by APN in pH 5.5 CBS at 32 °C were determined by fitting the Michaelis-Menten equation to the initial rates of product formation for a series of Phe-MDZ_{pro} concentrations. Reactions with 62.5 – 2000 µM Phe-MDZ_{pro} and 15 µg/mL APN were carried out at a volume of 50 µL in an Eppendorf Thermomixer 5436 at 500 rpm. After 1 min, the enzymatic reaction was quenched by denaturing APN with 100 µL of acetonitrile. Cyclization of the liberated MDZ_{open} to MDZ was allowed to progress to completion before measuring MDZ in the reaction mixtures by HPLC. A curve was fit to the MDZ production

versus initial Phe-MDZ_{pro} concentration with K_M and V_{max} as fitting parameters using the nlinfit function in MATLAB® version R2017b by The MathWorks, Inc. (Natick, MA).

5.4.6 Cell culture

Madin-Darby canine kidney II-wild type (MDCKII-wt) epithelial cells provided by The Netherlands Cancer Institute, Amsterdam were used as a model for nasal epithelium. Cells were cultured in DMEM media with 10% FBS and antibiotics (100 mg/ml streptomycin, 100 U/mL penicillin, and 250 ng/mL amphotericin B) in T-25 flasks at 37 °C with 5% CO_2 atmosphere. Only cells between passages 10-20 were used for experiments. Confluent cells were trypsinized and seeded at 0.5×10^5 cells/mL into cell culture plates for drug transport experiments. Media was replaced every second day until cell monolayers had formed. The media was removed, and the cells were rinsed with PBS prior to treatment with drug formulations.

5.4.7 Drug transport studies

MDCKII-wt cell monolayers were cultured on the apical insert of Transwell® 12-well tissue culture plates from Corning Inc. (Corning, NY: cat# 3460). Transepithelial electrical resistance (TEER) was monitored regularly using an EVOM Epithelial Voltohmmeter with STX2 electrode from World Precision Instruments, Inc. (Sarasota, FL). The monolayers were considered confluent and ready for experiments when the TEER measurements were no longer increasing, which took approximately 5 days. For transport experiments, the wells and confluent monolayers were first rinsed with assay buffer (specified by the apical well treatment group). Then 1.50 mL of assay buffer was added to the basal well and 0.500 mL of the drug formulation was added to the apical well. The

apical wells contained either: pH 7.4 PBS only, pH 6.5 PBS only, pH 5.5 PBS only, pH 5.5 CBS only, 500 µM MDZ_{open}•2HCl solution in each buffer, 500 µM supersaturated solution of MDZ in each buffer, 500 µM Phe-MDZ_{pro} in CBS, 200 µg/mL APN in CBS, or 500 µM Phe-MDZ_{pro} with 200 µg/mL APN in CBS. Each condition was performed in triplicate. The treated cells were placed in an incubator at 32 °C with a 150 rpm orbital shaker. At t = 5, 15, and 30 min, a 65 µL sample for analysis was removed from the basal wells. After the last sample was collected, the cells were rinsed with pH 7.4 PBS and checked for confluency by confirming that TEER had not decreased and by performing a standard Lucifer yellow dye permeability assay.[155] MDZ and Phe-MDZ_{pro} were quantified in the basal well samples by HPLC.

To infer the permeation of each reaction species across the cell monolayers, a mathematical model of drug transport was constructed using MATLAB®. A schematic of the model is shown in Figure 26, where k_1 and k_{-1} are rate constants for reversible binding of Phe-MDZ_{pro} to the active site of APB, and k_{cat} is the enzyme catalytic rate constant for conversion of Phe-MDZ_{pro} to MDZ_{open}. The relationship of these rate constants to Michaelis–Menten enzyme kinetic parameters is given by $K_M = (k_{-1}+k_{cat})/k_1$ and $V_{max} = k_{cat}[APN]$. In the prodrug/enzyme formulation pathway, endogenous enzyme activity was assumed to be small and negligible. In the acid/base formulation pathway, deprotonation of cationic MDZ_{open} to the ionization state prescribed by the buffer pH was assumed to be fast and negligible.

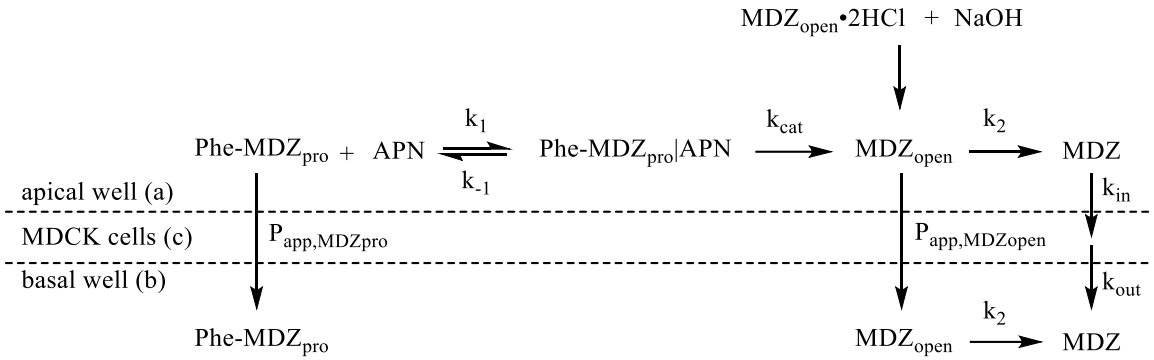

Figure 26. Schematic of transport in Transwell assay.

Values for the apparent permeability coefficient (P_{app}) of Phe-MDZ_{pro}, P_{app} of MDZ_{open}, and rate constants for transport of MDZ through the cell monolayer (k_{in} and k_{out}) were determined by fitting numerical solutions of the following differential equations to experimental data:

$$\frac{dA^a_{MDZ_{pro}}}{dt} = -\frac{k_{cat}A^a_{APN}A^a_{MDZ_{pro}}}{V^a K_M + A^a_{MDZ_{pro}}} - P_{app,MDZ_{pro}} S\left(\frac{A^a_{MDZ_{pro}}}{V^a} - \frac{A^b_{MDZ_{pro}}}{V^b}\right) \tag{4}$$

$$\frac{dA^a_{MDZ_{open}}}{dt} = \frac{k_{cat}A^a_{APN}A^a_{MDZ_{pro}}}{V^a K_M + A^a_{MDZ_{pro}}} - k_2 A^a_{MDZ_{open}} - P_{app,MDZ_{open}} S\left(\frac{A^a_{MDZ_{open}}}{V^a} - \frac{A^b_{MDZ_{open}}}{V^b}\right) \tag{5}$$

$$\frac{dA^a_{MDZ}}{dt} = k_2 A^a_{MDZ_{open}} - k_{in}A^a_{MDZ} \tag{6}$$

$$\frac{dA^c_{MDZ}}{dt} = k_{in}A^a_{MDZ} - k_{out}A^c_{MDZ} \tag{7}$$

$$\frac{dA^b_{MDZ_{pro}}}{dt} = P_{app,MDZ_{pro}} S\left(\frac{A^a_{MDZ_{pro}}}{V^a} - \frac{A^b_{MDZ_{pro}}}{V^b}\right) \tag{8}$$

$$\frac{dA^{b}_{MDZ_{open}}}{dt} = -k_2 A^{b}_{MDZ_{open}} + P_{app,MDZ_{open}} S\left(\frac{A^{a}_{MDZ_{open}}}{V^{a}} - \frac{A^{b}_{MDZ_{open}}}{V^{b}}\right) \quad (9)$$

$$\frac{dA^{b}_{MDZ}}{dt} = k_2 A^{b}_{MDZ_{open}} + k_{out} A^{c}_{MDZ} \quad (10)$$

where A is mole amount with the species denoted by subscripts and the compartment ('a' for apical well, 'b' for basal well, and 'c' for cell monolayer) denoted by superscripts, V is the volume of the compartment denoted by the superscript, and S is the surface area of the cell monolayer. Experimental data was input as averages of the concentrations measured in the basal well at each sampling time point. Model fits were obtained using the ode45 function in conjunction with the lsqcurvefit function, and standard errors (SEs) for each parameter estimate were calculated from confidence intervals given by the nlparci function in MATLAB®.

Fitting to estimate the P_{app} of MDZ_{open} was performed in two stages. First, Equations 6, 7, and 10 were used to estimate k_{in} and k_{out} by adding supersaturated MDZ (500 µM) to the apical well and fitting the model to concentrations of MDZ measured in the basal well. The supersaturated solutions of MDZ were created by admixing MDZ_{open}•2HCl with assay buffer 1.5 hr before addition to the apical well, so the concentration of MDZ_{open} was assumed to be zero. Then k_{in} and k_{out} were fixed at the determined values, and Equations 5, 6, 7, 9, and 10 were used to estimate the P_{app} of MDZ_{open} from the combined transport of MDZ_{open} and MDZ when 500 µM of MDZ_{open}•2HCl was added to the apical well. Concentrated stock solutions of MDZ_{open}•2HCl were prepared immediately before addition to assay buffer in the apical wells, so the initial concentration of MDZ was assumed to be zero. Since cyclization of

MDZ_{open} continued to completion in the samples removed from the basal wells for analysis, the concentrations of MDZ measured at each time point were considered to be equivalent to the sum of the basal MDZ_{open} and MDZ concentrations.

5.5 Results

5.5.1 Rate limitation for MDZ_{pro}/enzyme formulations

A fungal enzyme, AOP, was used to convert lysyl derivatives of the open ring forms of diazepam and MDZ in our previous work, although the catalytic efficiency (k_{cat}/K_M) for hydrolysis of the Lys-diazepam prodrug was 36 fold greater than for Lys-MDZ_{pro}.[42] Co-administering an exogenous human enzyme with an amino acid derivatized prodrug is preferable over the fungal enzyme to avoid potential immune responses.[156] A human enzyme, APB, was found to efficiently convert the Lys-diazepam prodrug (K_M = 0.370 mM and V_{max} = 0.254 mM/min with 15 µg/mL APB at 32 °C in pH 7.4 PBS, determined by HPLC).[108] However, there was essentially no conversion of Lys-MDZ_{pro} with 15 µg/mL APB under the same conditions, and incomplete conversion with 500 µg/mL APB. Therefore, a different MDZ_{pro}/enzyme combination was sought. Various peptido-2-aminobenzophenone prodrugs have been shown to convert to their respective benzodiazepine parent drugs *in vivo* by endogenous enzymes.[46,157] The rate of hydrolysis was dependent on the amino acid moiety, with Phe and Lys derivatives cleaving faster than Gly and Glu derivatives. It was thought that APN, a human endopeptidase that catalyzes cleavage of neutral amino acids, would efficiently convert a phenylalanyl version of MDZ_{pro}. Indeed, Phe-MDZ_{pro} was found to be fully converted to MDZ by APN, but

cyclization of the intermediate species MDZ_{open} was slow at pH 7.4. Figure 27 illustrates this point. The absorbance for each reaction mixture started near 2.5 and progressed to 1.3 as a molar concentration of MDZ equivalent to the initial MDZ_{pro} concentration was formed. The time course of the absorbance change was the same for the Phe-MDZ_{pro}/APN combination and the Lys-MDZ_{pro}/AOP combination regardless of enzyme concentration, suggesting that the ring closing step was rate limiting.

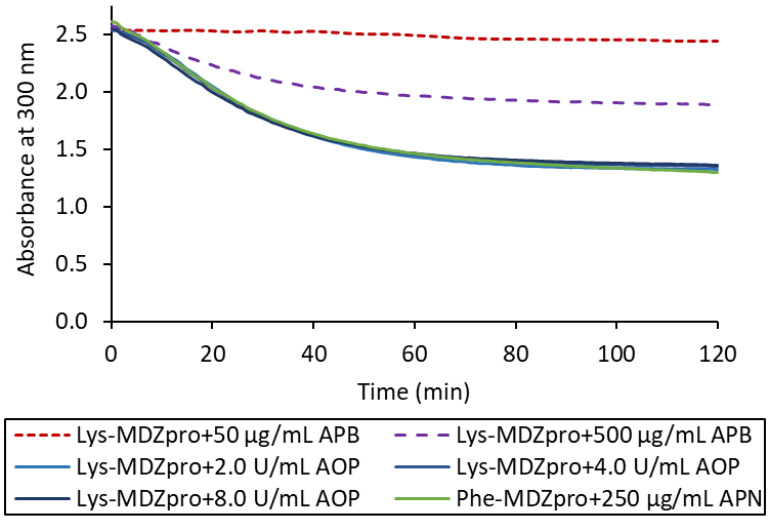

Figure 27. MDZ_{pro}/enzyme reactions tracked by UV spectroscopy. Identical time courses were observed for Lys-MDZ_{pro}/AOP and Phe-MDZ_{pro}/APN, regardless of enzyme concentration. Incomplete conversion to MDZ was observed with the Lys-MDZ_{pro}/APB combination. Reactions performed with the indicated enzyme and 1.00 mM MDZ_{pro} at 32 °C in pH 7.4 PBS, n = 1.

5.5.2 pH dependence of MDZ_{open} cyclization

A dynamic equilibrium exists between MDZ_{open} and MDZ when the pH is below 5.[158] Above pH 5, equilibrium is completely in the direction of MDZ. MDZ_{open} can be isolated as a solid in the form of a dihydrochloride salt, MDZ_{open}•2HCl, by bringing the pH

very low and removing the solvent. This salt was convenient for studying the ring closing rate as a function of pH by UV spectroscopy. Aqueous solutions of the salt are acidic with predicted pK_as of 5.7 at the imidazole nitrogen and 8.4 at the primary amine.[68] Aliquoting a stock solution of the salt into a buffer led to rapid deprotonation of the MDZ_{open} cation and an absorbance change at 300 nm corresponding to the formation of MDZ. The cyclization rate constant, k_2, was measured by tracking this absorbance change. Figure 28 shows the $t_{1/2}$ of MDZ_{open} calculated from k_2. The slowest ring closing rate occurred at pH 6.5 with $t_{1/2}$ = 17.2 ± 1.7 min, ±SD. The fastest ring closing rate occurred at pH 5.0 with $t_{1/2}$ = 3.45 ± 0.27 min.

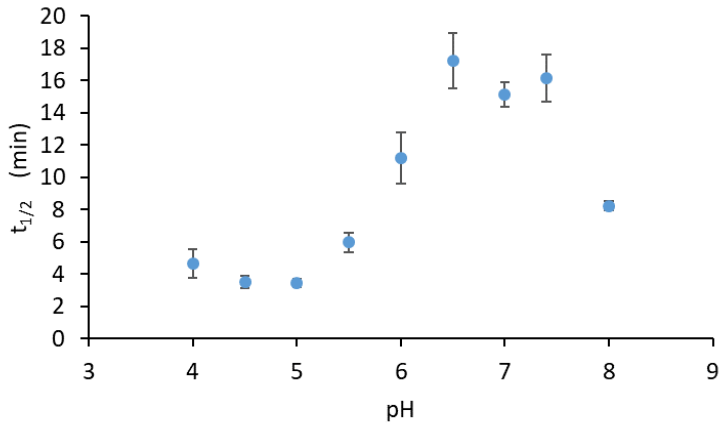

Figure 28. pH dependence of MDZ_{open} half-life. Formation of MDZ from cyclization of MDZ_{open} became slow between pH 6.5-7.4, 32 °C, n = 3, ± SD.

5.5.3 Phase separation of MDZ from supersaturated solutions

Cyclization of MDZ_{open} produced supersaturated solutions of MDZ. When the MDZ concentration was driven sufficiently high, an upper limit of supersaturation was reached, and spontaneous phase separation of amorphous MDZ occurred throughout the liquid. This process, known as 'oiling out' or liquid-liquid phase separation (LLPS),[52,53]

caused the samples to become turbid. The total extinction (absorbance + scattering) of transmitted light was monitored at a wavelength beyond the tail of analyte absorbance peaks ($\lambda = 400$ nm) to detect the onset of light scattering and LLPS. Figure 29A shows the abrupt increase in extinction that was observed when solution concentrations of MDZ generated from the cyclization of MDZ_{open} reached the upper limit of supersaturation. The reactions were performed under alkaline conditions by adding an excess of strong base to solutions of MDZopen•2HCl, so the resultant MDZ was unionized. Samples that produced a final concentration of 1.14 mM MDZ or less did not undergo LLPS. For higher concentration samples, LLPS consistently initiated when the reactions progressed to about 1.15 mM MDZ. Therefore, the upper limit of supersaturation or amorphous solubility was estimated to be 1.15 mM for the neutral MDZ microspecies.

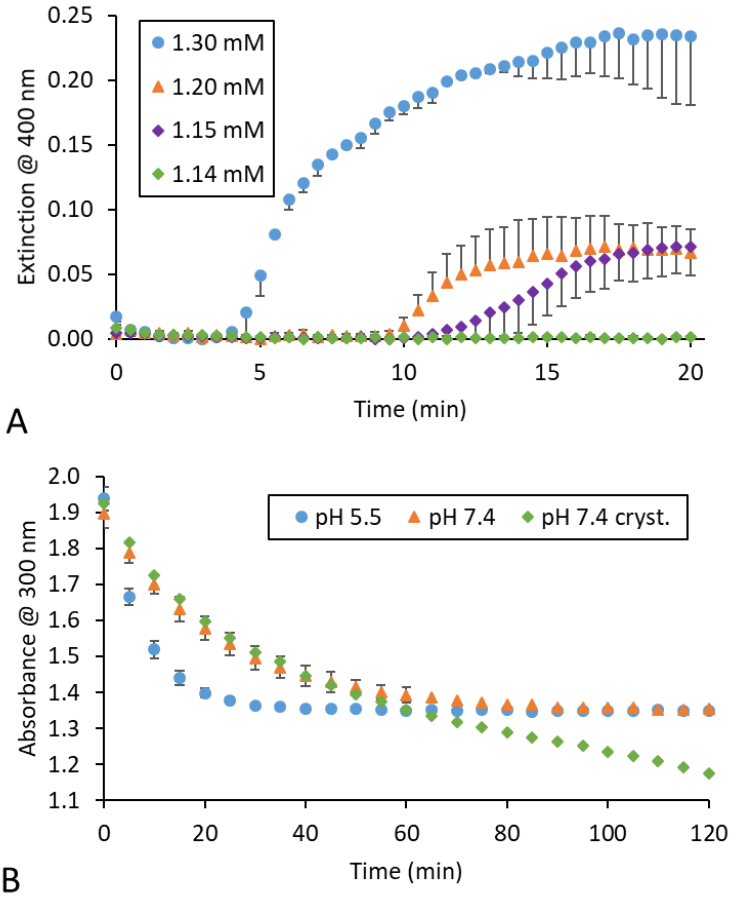

Figure 29. Precipitation of MDZ observed by UV spectroscopy. (**A**) Light scattering from precipitation of amorphous MDZ was observed when the concentration reached the upper limit of supersaturation: ~1.15 mM MDZ. Reaction conditions: 1.30, 1.20, 1.15, or 1.14 mM MDZ_{open}•$2HCl_{(aq)}$, 4.34 mM NaOH, 32 °C, n = 2 for 1.30 mM condition and n = 3 for all other conditions. (**B**) Occasional crystal nucleation and growth led to a continual drop in absorbance for some samples (green diamonds). Reaction conditions: 1.00 mM MDZ_{open}•$2HCl_{(aq)}$ in PBS, 32 °C, n = 1 for pH 7.4 sample that began to form crystals and n = 3 for all other data. Error bars are SD.

Crystallization events were also observable by UV spectroscopy. Figure 29B shows absorbance measurements for MDZ_{open} cyclization upon the addition of a MDZ_{open}•2HCl stock solution to buffer. The reactions, at a concentration of 1.00 mM,

were below the upper limit of supersaturation but above the equilibrium solubility of MDZ. When crystallization occurred, the measured absorbance of the reaction continued to decrease after the reaction was complete (Figure 29B, green diamonds). Sequestering of MDZ in the crystalline phase caused the absorbance to fall below that which was expected for the final supersaturated MDZ solution (1.00 mM), towards the absorbance of MDZ at its thermodynamic equilibrium solubility (55 μM MDZ at pH 7.4 and 32 °C with Abs ≈ 0.07 at 300 nm). Crystallization was also observed with irregularity in higher concentration samples that had already undergone LLPS.

Images of the amorphous precipitate from MDZ_{open} cyclization reactions performed above the upper limit of supersaturation for MDZ were captured by polarized microscopy. When the LLPS process initiated, an abundance of very small colloidal particles distributed homogeneously throughout the reaction mixture was observed. These particles coalesced and continued to grow, eventually forming aggregates (Figure 30A). The lack of birefringence under polarized light and the spherical shape of the MDZ precipitate particles from LLPS indicated that the precipitate was amorphous. Figure 30B demonstrates that crystals can be formed from the amorphous precipitate by introducing nucleation sites. As the crystals grew, the amorphous precipitate particles began to shrink. Samples that did not have crystal nucleation sites introduced would sometimes spontaneously form crystals early on, while others remained amorphous for more than 24 hr.

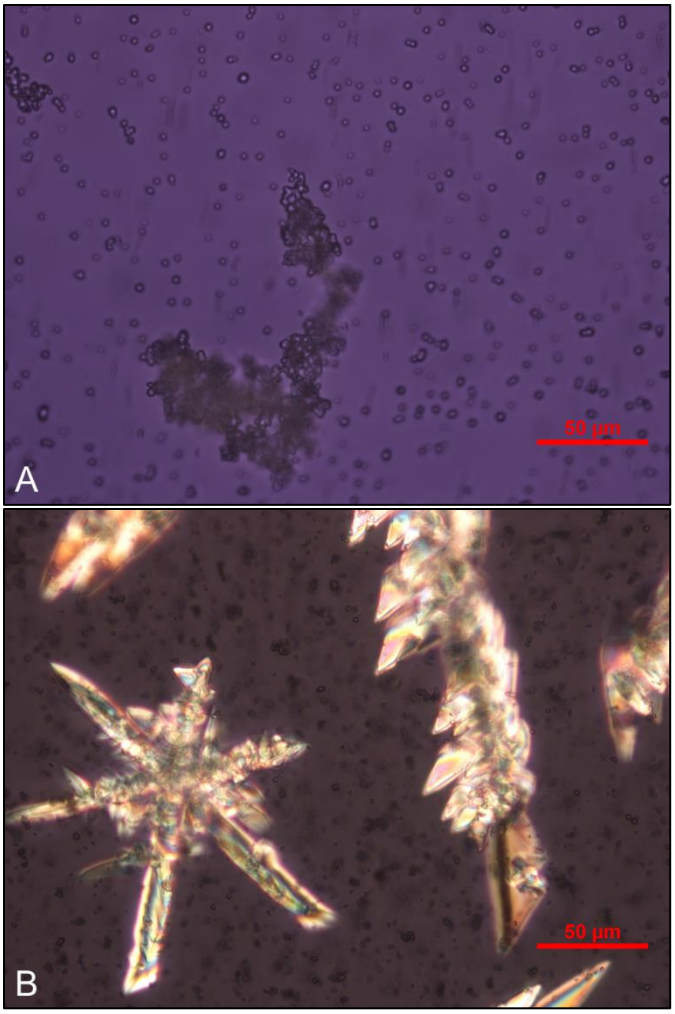

Figure 30. Polarized microscope images of MDZ precipitate. (**A**) Amorphous precipitate in the reaction mixture at t = 40 min after turbidity was observed. (**B**) Induced MDZ crystal formation.

Calorimetry performed on precipitates collected from a reaction mixture that had undergone LLPS showed a glass transition at T_g = 60.2 °C, cold crystallization exotherm at T_{cc} = 127-136 °C, and characteristic melting endotherm for MDZ at T_m = 159-163 °C (Figure 31A). The T_m of a crystalline MDZ standard (162-163 °C, Figure 31B) was similar to the T_m of the precipitate and in agreement with values that have been reported for MDZ in the literature, 158-160 °C and 161-164 °C.[56,159] There were no other features present in

the MDZ standard thermogram besides the melting endotherm. The thermogram of MDZ_{open}•2HCl did not reveal a T_g and did not have a melting endotherm corresponding to MDZ, suggesting there was no MDZ in the sample (Figure 31C). The observed melting range was broad due to fusion of a metastable modification overlapping with fusion of a stable form that had T_m = 146-147 °C.

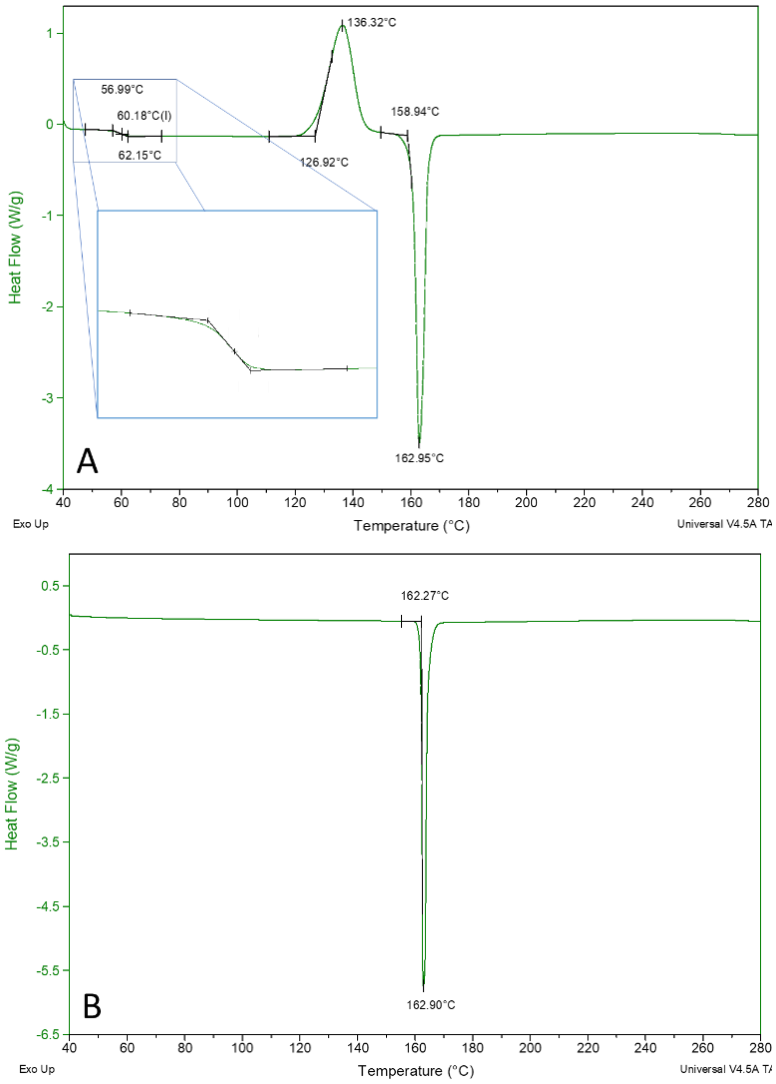

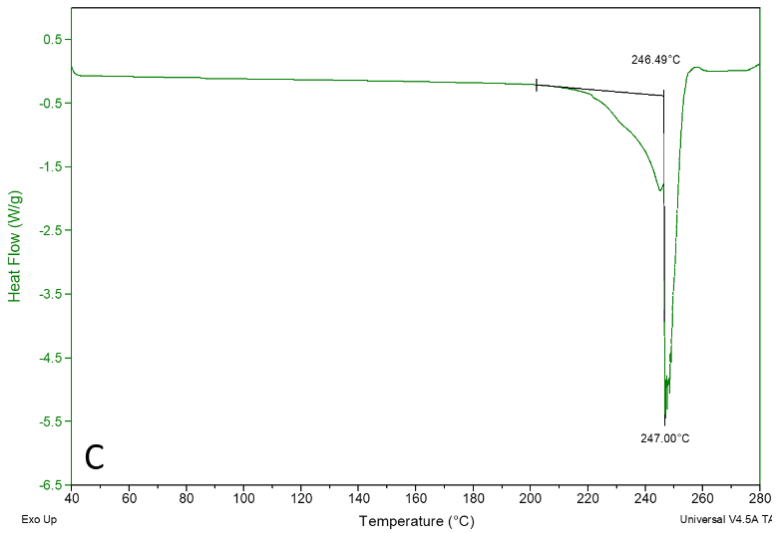

Figure 31. DSC thermograms. (**A**) MDZ precipitate from reaction of MDZ_{open}•2HCl with NaOH solution. (**B**) MDZ standard. (**C**) MDZ_{open}•2HCl.

5.5.4 Drug transport studies

To investigate the permeation of MDZ_{open} across epithelium and the ability of this species to contribute to the rate of MDZ delivery, transport studies were performed with MDCKII-wt cell monolayers using Transwell® plates. Freshly prepared, concentrated stock solutions of MDZ_{open}•2HCl were added to buffer on the apical side of the monolayers in order to expose the cells to a known initial concentration of MDZ_{open} at a specified pH. Since MDZ_{open} is a transient species, the basal well MDZ concentrations shown in Figure 32A are the result of cyclization with simultaneous transport of both species. Any MDZ_{open} present in the samples removed from the basal well for analysis would have continued to form MDZ, so only MDZ was observed by the time the samples were processed.

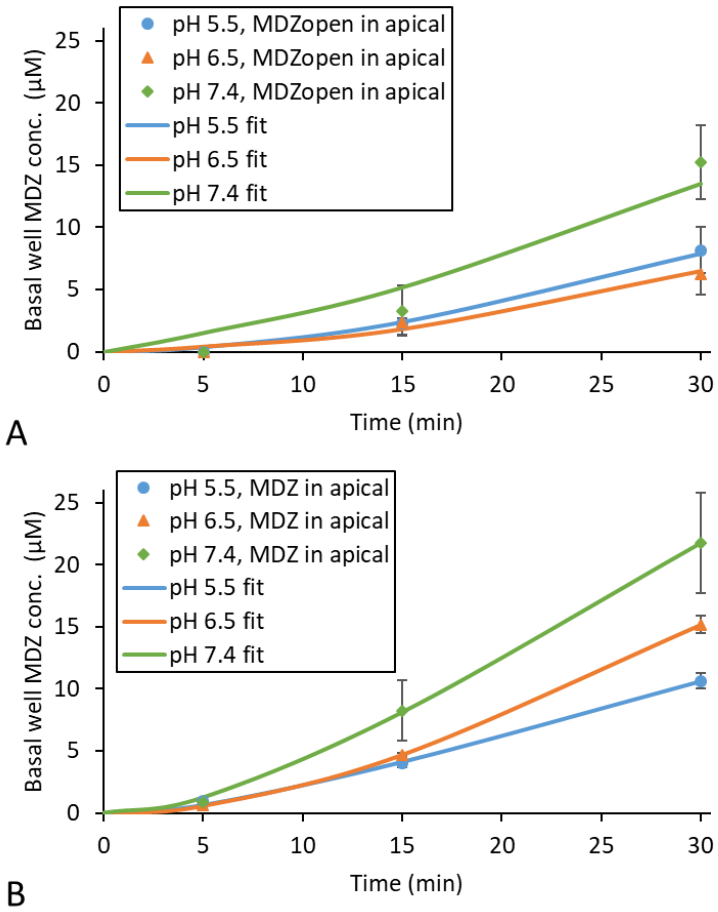

Figure 32. Transport of MDZ across MDCKII-wt cell monolayers from acid/base formulation approach. n = 3, averages ±SD. (**A**) pH dependence of MDZ_{open} transport from 500 µM MDZ_{open} in apical well. MDZ measured in the basal well represents the sum of MDZ_{open} and MDZ at each time point. Lines are model fits with k_{in}, k_{out}, and k_2 as fixed parameters and P_{app} for MDZ_{open} as a fitting parameter. (**B**) pH dependence of MDZ transport from 500 µM MDZ (supersaturated) in apical well. Lines are model fits with k_{in} and k_{out} as fitting parameters.

The permeation of MDZ at each pH was needed to deconvolute the permeation of MDZ_{open} from MDZ. Previously we had reported P_{app} = 2.65 $\times 10^{-5}$ cm/s for MDZ measured at pH 7.4 with 55 µM MDZ in the apical well.[42] However, there was a lag observed for the appearance of MDZ in the basal wells of monolayers treated with supersaturated MDZ (Figure 32B). To account for this lag, the cell monolayers were

modeled as a separate compartment where MDZ could accumulate (Figure 26). The rate constants determined for MDZ transport from the apical compartment into the monolayer compartment, k_{in}, and out of the monolayer compartment to the basal compartment, k_{out}, are listed in Table 4. (For reference, P_{app} ±SE for MDZ would have been $1.54 \pm 0.19 \times 10^{-5}$ cm/s at pH 5.5, $2.15 \pm 0.44 \times 10^{-5}$ cm/s at pH 6.5, and $3.24 \pm 0.56 \times 10^{-5}$ cm/s at pH 7.4 in this data set if the lag had been ignored.) Literature values for P_{app} of MDZ across MDCK cells at pH 7.4 are generally higher, ranging from 4.2-7.0 $\times 10^{-5}$ cm/s.[160-164] With k_{in}, k_{out}, and k_2 as fixed parameters, P_{app} of MDZ_{open} could be estimated as a fitting parameter from the data shown in Figure 32A.

Table 4. Parameters for transport of each reaction species across MDCKII-wt cell monolayers.

Species	Parameter ± SE	pH		
		5.5	**6.5**	**7.4**
Phe-MDZ_{pro}	P_{app} ($\times 10^5$ cm/s)	0.545 ± 0.056 *	ND	ND
MDZ_{open}	P_{app} ($\times 10^5$ cm/s)	0.326 ± 0.195	0.396 ± 0.135	1.45 ± 0.64
MDZ	k_{in} (min^{-1})	0.144 ± 0.080	0.0405 ± 0.0056	0.105 ± 0.036
	k_{out} (min^{-1})	0.00284 ± 0.00051	0.00783 ± 0.00079	0.00674 ± 0.00100

ND = not determined, * Phe-MDZ_{pro} transport measured in CBS, all other species measured in PBS.

Phe-MDZ_{pro} and MDZ were found in the basal wells when Phe-MDZ_{pro} without enzyme was added to the apical wells of the cell monolayers (Figure 33A). MDCK cells express small amounts of endogenous APN that is localized to the apical side of the

membrane.[165] So some hydrolysis of Phe-MDZ_{pro} likely occurred in the apical well and MDZ subsequently permeated to the basal well. When conversion of Phe-MDZ_{pro} by endogenous enzymes is ignored, the P_{app} for Phe-MDZ_{pro} at pH 5.5 was 0.545 min^{-1} (Table 4). The Michaelis–Menten parameters for enzymatic hydrolysis of Phe-MDZ_{pro} by 15 μg/mL APN in pH 5.5 CBS at 32 °C were K_M = 336 ± 39 μM and V_{max} = 16.5 ± 0.6 μM/min (±SE). APN is a 104 kDa enzyme, so this V_{max} gave k_{cat} = 114 ± 5 min^{-1}. Under the same conditions, measured k_2 was 0.126 ± 0.015 min^{-1} ±SD. When all of the model parameters (K_M, k_{cat}, k_2, P_{app} for Phe-MDZ_{pro}, P_{app} for MDZ_{open}, k_{in}, and k_{out}) were fixed, the basal well concentrations resulting from a Phe-MDZ_{pro}/APN reaction in the apical well could be predicted remarkably well by numerically solving Equations 4-10. Curves of the predictions are shown in Figure 33B.

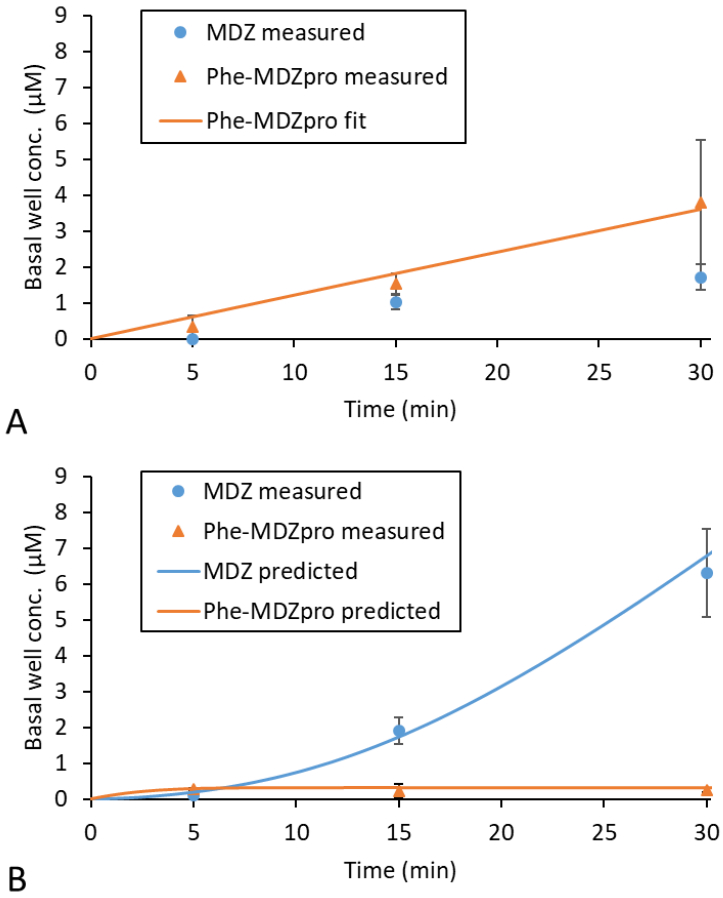

Figure 33. Transport of MDZ across MDCKII-wt cell monolayers from prodrug/enzyme formulation approach. n = 3, averages ±SD. (**A**) Transport of Phe-MDZ_{pro} and MDZ in pH 5.5 CBS from 500 µM Phe-MDZ_{pro} in apical well. Line is model fit with P_{app} of Phe-MDZ_{pro} as a fitting parameter. Some conversion to MDZ from endogenous enzymes occurred. (**B**) Transport of Phe-MDZ_{pro} and MDZ in pH 5.5 CBS from 500 µM Phe-MDZ_{pro} combined with 200 µg/mL APN in apical well. Lines are predicted concentrations with all model parameters fixed.

5.6 Discussion

The cyclization rate of MDZ_{open} is an important factor to consider when using an open ring precursor to generate MDZ in a two-part, reactive formulation for rapid IN delivery. Cyclization was slow in pH 7.4 buffer at 32 °C, with $t_{1/2}$ = 16.1 ± 1.5 min. Other

researchers have reported similar $t_{1/2}$ for the cyclization of MDZ_{open}. Walser et al. estimated the $t_{1/2}$ to be ~10 min at neutral pH, although the temperature was not specified.[154] Gerecke also estimated ~10 min in pH 7.4 buffer at 37 °C.[158] Loftsson et al. reported $t_{1/2} > 2$ min at pH 7.4 in human serum at 37 °C by HPLC.[129] Differences in temperature and analytical technique likely account for the discrepancy between these measurements. The fastest rates for cyclization of MDZ_{open} were observed near pH 5; however, transepithelial transport of both MDZ and MDZ_{open} was found to be optimal at alkaline pH. Note that slow cyclization of MDZ_{open} will delay the pharmacodynamic effect of MDZ regardless of whether the cyclization occurs in the nasal cavity or in the body.

The polynomial like profile observed for the pH dependent cyclization rate (shown in terms of $t_{1/2}$ in Figure 28) can be explained by a change in the protonation state of functional groups at different locations on the MDZ_{open} molecule, thereby changing the rate determining step for imine formation. Deprotonation of the primary ammonium cation in the basic region increases the concentration of the free amine, which is a better nucleophile to attack the carbonyl carbon of the benzophenone moiety. In the acidic region, the carbonyl can be activated by protonating the oxygen, and dehydration of the carbinolamine intermediate is facilitated by subsequent protonation of the hydroxyl (i.e. imine formation is acid catalyzed). Alprazolam, a triazolo-benzodiazepine, and oxazolam, a benzodiazepine derivative, also display polynomial like pH dependence to their cyclization rates.[109,166,167]

Cyclization of MDZ_{open} in the nasal cavity will lead to supersaturation of MDZ if production of MDZ outpaces absorption. Supersaturated solutions are metastable[50,51] and

can phase separate to form crystalline or amorphous precipitates. Crystallization is undesirable because drug trapped in the crystal lattice is of lower activity and could be transported from the nasal cavity to the digestive tract by mucociliary clearance, diminishing the bioavailability. Our *in vitro* experiments suggest crystallization of MDZ is a sporadic process at short time scales, requiring a nucleation event that only occurred in some samples. When MDZ concentrations were driven beyond the upper limit of supersaturation, LLPS was spontaneous and the dispersed phase was amorphous MDZ. The amorphous precipitate has no crystal lattice energy barrier to dissolution; therefore, it exists in quasi-equilibrium with the supersaturated solution. This allows the amorphous precipitate to act as a source for MDZ and maintains the solution concentration at the upper limit of supersaturation during the absorption process. In other words, LLPS effectively caps the driving force for absorption of MDZ from the solution phase at the upper limit of supersaturation, but MDZ in the amorphous precipitate is still bioavailable.

Supersaturated solutions of MDZ had a greater propensity to crystalize than supersaturated solutions of diazepam generated from Lys-diazepam prodrug/enzyme reactions. This difference between the two benzodiazepine drugs was also manifest in DSC analysis of the dried reaction precipitates. Diazepam reaction precipitates showed a glass transition, but no cold crystallization or melting peaks.[75] In contrast, MDZ reaction precipitates showed a glass transition, cold crystallization exotherm, and melting endotherm (Figure 31A). The presence of a cold crystallization peak suggested that MDZ readily underwent rearrangement in the amorphous regions to form a crystalline phase. Furthermore, the molar heat of solidification (ΔH_s) was often slightly lower than the molar

heat of fusion (ΔH_f). For the sample shown in Figure 31B, ΔH_s = 24.1 kJ/mol and ΔH_f was 26.5 kJ/mol, indicating the MDZ precipitate was initially only 91% amorphous.

The rate at which MDZ could be delivered systemically by IN administration of an open ring precursor would be primarily controlled by the absorption rate of MDZ, absorption rate of MDZ_{open}, and cyclization rate of MDZ_{open}, all of which are pH dependent. Both MDZ and MDZ_{open} exhibited higher permeation at higher pH. The charge of the predominate microspecies reflected the differences in permeation observed at each pH as well as differences observed between the two species. Based on a pK_a of 6.2, about 94% of MDZ is expected to exist as the neutral microspecies at pH 7.4 while 82% is monocationic at pH 5.5. With pK_as at 5.7 and 8.4, about 89% of MDZ_{open} is expected to exist as the monocation at pH 7.4 while 60% is dicationic at pH 5.5. Since MDZ was less charged than MDZ_{open} at a given pH, it was more readily transported across the membrane. Therefore, the cyclization rate in the nasal cavity is also important. This is demonstrated in Figure 32B. At pH 5.5 (blue circles), MDZ was ultimately delivered to the basal wells at a faster rate than at pH 6.5 (orange triangles) even though MDZ and MDZ_{open} had higher permeation at pH 6.5.

A formulation pH of 7.4 for delivery of MDZ is desirable because it would afford rapid absorption and is within the pH range of the nasal cavity. For MDZ_{pro}/enzyme formulations, the pH dependent solubility of MDZ_{pro} must be taken into consideration. Precipitation of Phe-MDZ_{pro} from solution was observed at pH 5.8 and concentration of 160 mM (Appendices A4, Figure A4.86). At this concentration, which is equivalent to 52 mg/mL of MDZ, a volume of 192 µL would be needed to deliver a 10 mg dose of MDZ.

Transport studies and enzyme kinetics for the Phe-MDZ_{pro}/APN formulation were performed at pH 5.5 because of this solubility limitation.

The amount of enzyme required to hydrolyze high concentrations of Phe-MDZ_{pro} within a reasonable time frame is another factor that must be considered for the MDZ_{pro}/enzyme formulation approach. To hydrolyze Phe-MDZ_{pro} equivalent to 10 mg MDZ in 10 min at pH 5.5, 2.8 mg of APN would be needed. Even then, the cyclization reaction would take additional time to complete. Slow reaction rates coupled with slow absorption could lead to low bioavailability if a significant portion of the dose is carried to the digestive tract by mucociliary clearance. The transit time for mucus in the nasal cavity has been reported to be 15-20 min at a rate of 5 mm/min.[168] Depending on the scalability of enzyme production, the amount of enzyme required for sufficiently fast hydrolysis could make the cost per dose prohibitively expensive. It should be noted that the enzymatic activity of APN was suboptimal at pH 5.5 (Appendices A4, Figure A4.84). Different MDZ_{pro}/enzyme combinations formulated at different pH may not require such large amounts of enzyme. The stability of the enzyme and level of endogenous enzymes in the nasal cavity that can convert MDZ_{pro} will also affect the amount of exogenous enzyme needed per dose.

At low pH, the open ring forms of benzodiazepines like diazepam undergo chemical degradation.[169] Open ring forms of triazolo- and imidazo-benzodiazepines such as alprazolam and MDZ do not allow for further acid hydrolysis and are chemically stable in solution.[129] Thus, the stability of MDZ_{open} at low pH presents the possibility of delivering MDZ by co-administering MDZ_{open}•2HCl with a solution of base to bring the pH within

an acceptable range for IN delivery and rapid absorption. MDZ_{open}•2HCl is highly soluble and undergoes very rapid dissolution. An amount equivalent to 10 mg of MDZ can be dissolved in as little as 50 µL of water. With this acid/base formulation approach, there is no need for amino acid derivatization and subsequent hydrolysis of the amino acid moiety to liberate MDZ_{open} as is the case with the MDZ_{pro}/enzyme formulation approach.

5.7 Conclusions

Despite a long history of off-label IN administration of MDZ injectable solutions, an approved nasal spray formulation has been elusive. This is because MDZ has low aqueous solubility. Formulations that utilize solubilizing excipients or low pH to achieve a dose volume appropriate for IN delivery tend to irritate the nasal mucosa. However, it is possible to generate aqueous MDZ in a volume and at a pH appropriate for IN delivery by mixing a precursor with a reactant immediately before administration. The metastable, supersaturated solution of MDZ that results provides an increased driving force for enhanced permeation across membranes, but there is a limit to the degree of supersaturation that can be reached without causing spontaneous phase separation of MDZ. Precipitate from MDZ generated above the supersaturation limit was found to be amorphous. MDZ in the amorphous precipitate remains available for absorption. Phase separation of MDZ into a crystalline phase was also observed, but only sporadically. It is unclear if nucleation would occur *in vivo* or if crystallization would sequester a significant amount of MDZ before the dose is absorbed. The most critical barrier to achieve rapid delivery and high bioavailability of MDZ using an open ring precursor was found to be the cyclization rate of MDZ_{open}. Cyclization was pH dependent. A formulation pH of 7.4 was found to be

optimal for permeation of MDZ and MDZ_{open} across cell membranes, but the slow cyclization rate for MDZ_{open} at this pH would control the rate at which MDZ appears in the body.

Different reactions can be used to liberate MDZ_{open} in an aqueous formulation and generate MDZ. The acid/base formulation approach is preferable to the MDZ_{pro}/enzyme formulation approach, because the latter is more difficult to optimize. Enzyme stability is often an issue, and catalytic activity can be sensitive to changes in pH or temperature. Furthermore, the prodrugs themselves may have solubility limits, as was the case with Phe-MDZ_{pro}. In contrast, an acid/base reaction is robust and straightforward. The final pH of the acid/base formulation can be selected simply by choosing the appropriate base concentration, but the acid and base components must be adequately mixed during administration to avoid heterogeneous deposition and pH spikes on the surface of the nasal mucosa. Either formulation approach requires the reactants to be kept segregated during storage. This is most conveniently accomplished with a nasal spray device specifically designed to store, mix, and atomize two-part reactive formulations. When the dose is ready to be administered, mixing of the two formulation components would be initiated and the mixture sprayed into the nasal cavity where formation of MDZ would occur. Our group is currently prototyping and testing nasal spray devices for administration of these types of formulations.

Chapter 6: Nasal spray device for administration of two-part drug formulations

6.1 Summary

Intranasal drug delivery is an attractive route to noninvasively achieve a rapid therapeutic effect, avoid first pass metabolism, and bypass the blood brain barrier. However, the types of drugs that can be administered by this route have been limited, in part, by device technology. Herein, we describe a pneumatic nasal spray device that is capable of mixing liquid and solid components of a drug formulation as part of the actuation process during dose administration. The ability to store a nasal spray drug formulation as two separate components can be leveraged to solve a variety of stability issues that would otherwise preclude intranasal administration. Examples of drugs that could be delivered intranasally by utilizing this two-part formulation strategy include biomolecules that are unstable in solution and low solubility drugs that can be rendered into metastable supersaturated solutions. A proof of concept nasal spray device prototype was constructed to demonstrate that a liquid and solid can be rapidly mixed and atomized into a spray in a single action. The primary breakup distance and angle of the spray cone were measured as a function of the propellant gas pressure, and silicone nasal cavity molds were used to assess the effect of cone angle on formulation deposition within the nasal cavity. Higher pressures produced wider cone angles, but the deposition area within the nasal cavity was found to be generally independent of cone angle. Variations of two-part drug formulations for intranasal delivery of insoluble benzodiazepines in an aqueous vehicle were tested with the prototype device. An acid/base formulation that generates midazolam demonstrated rapid dissolution of the solid component and effective mixing, while a prodrug/enzyme formulation that generates diazepam demonstrated the ability to conveniently store and administer labile biomolecules with this device.

6.2 Introduction

The intranasal route for systemic drug delivery has been gaining popularity in recent years. This is because it offers several advantages over traditional routes of administration. The highly vascularized nasal mucosa contains fenestrated capillaries and has a porous basement membrane, making the tissue an ideal site for rapid drug absorption.[20] Since the capillaries drain directly into the systemic circulation, the bioavailability of drugs that undergo first pass metabolism or gastrointestinal degradation by the oral route can be improved by delivery through the intranasal route. In addition to capillaries, the nasal mucosa has a network of lymphatic vessels that can be targeted for efficient, needle-free delivery of vaccines.[170] The intranasal route also offers the possibility of bypassing the blood brain barrier and delivering drugs directly to the brain via the olfactory or trigeminal nerve pathways.[171] From a patient perspective, convenient and essentially painless dosing makes the intranasal route preferable to other parenteral routes. Furthermore, the nasal cavity is easily accessible and operation of a nasal spray device is generally intuitive, so administration can be performed by untrained individuals even in emergency situations.[33]

Even though intranasal delivery has been shown to be practical and safe for many drugs,[33] there are challenges that have prevented formulation of certain types of drugs as nasal sprays. Most notably, the volume that can be reliably deposited in the nasal cavity is limited to 200 µL.[172] Larger volumes tend to drain out of the nostrils and/or into the nasopharynx, causing slower absorption and lower bioavailability. Organic solvents and other solubilizers have been investigated to obtain an acceptable dose volume for drugs

with low solubility, but these additives tend to cause irritation and can damage sensitive nasal tissues.[34,40] Another major challenge to formulating some drugs as nasal sprays is poor stability.[19] Biopharmaceuticals have notoriously short shelf lives when stored in solution because they are susceptible to denaturation, aggregation, and chemical degradation reactions. Degradation reactions are also accelerated for small molecule drugs stored in solution. Challenges related to low solubility or poor stability can be overcome for a variety of drugs by strategically selecting some components of the formulation to be stored separately as solids. Immediately prior to administration, the liquid and solid parts would be combined to make supersaturated or metastable solutions that can be sprayed into the nasal cavity without concern for processes that would normally render the formulation unstable over a longer timescale.

To our knowledge, there is no marketed nasal spray device that is capable of mixing liquid and solid parts of a formulation during administration of the dose. The availability of such a device would revolutionize intranasal delivery by enabling two-part formulation strategies and opening up the pharmacokinetic advantages of intranasal delivery to drugs that cannot be stored in solution. Born out of a desire to co-administer reactive prodrug/enzyme combinations for intranasal delivery of drugs with low solubility,[42,75] we have designed a pneumatically driven, dual chamber nasal spray device for rapid mixing and atomization of pre-metered doses. A description of the device mechanism, demonstration of a proof of concept prototype, results from preliminary testing of the proof of concept prototype with two-part drug formulations, and an example of a functional prototype follow.

6.3 Device mechanism

6.3.1 Dual chamber drug cartridge

The nasal spray device relies on disposable drug cartridges that contain a single, pre-metered dose. The drug cartridge, illustrated in Figure 34, has two compartments to keep the liquid and solid parts of the drug formulation separate during storage. The liquid part of the drug formulation (e.g. buffer, water, solvent, liquid drug, drug that is stable in solution, liquid excipients, excipients in solution, etc.) is contained between two pistons in the first compartment. Solids that are reactive or otherwise unstable in solution are hermetically sealed in the second compartment between Piston 2 and a check valve or breakable membrane near the atomizer tip.

During actuation of the device, a burst of propellant such as compressed air or inert gas is released into the aft end of the drug cartridge. Initially, the force of the propellant gas causes Piston 1, the liquid, and Piston 2 to move down the drug cartridge barrel with the same displacement. When Piston 2 reaches the slot near the center of the barrel it becomes stationary as the liquid moves around Piston 2, through Channel 1, and into the solids compartment. The liquid and solid parts of the formulation mix as Piston 1 continues to advance down the cartridge barrel, pushing liquid into the solids compartment. When Piston 1 reaches Piston 2, they make contact. This contact forces Piston 2 past the slot region, at which point Piston 1 becomes stationary and Piston 2 advances down the barrel under the force of the propellant gas. The movement of Piston 2 causes the mixed drug formulation to fill the atomizer tip and exit the drug cartridge as a spray. When Piston 2

reaches the atomizer tip, the propellant gas flows through Channel 2 and expels any remaining drug formulation out of the atomizer tip.

6.3.2 Propellant gas system

The drug cartridge can be integrated with a small, mechanical system to generate a single burst of propellant as illustrated in Figure 35. Actuation of the device is as simple as pressing the button. The button moves a compressed gas cartridge toward a flow regulating, hollow puncture pin. When the pin punctures the gas cartridge, the gas is released into the drug cartridge. This iteration of the propellant gas system is for one-time use, making the entire device disposable.

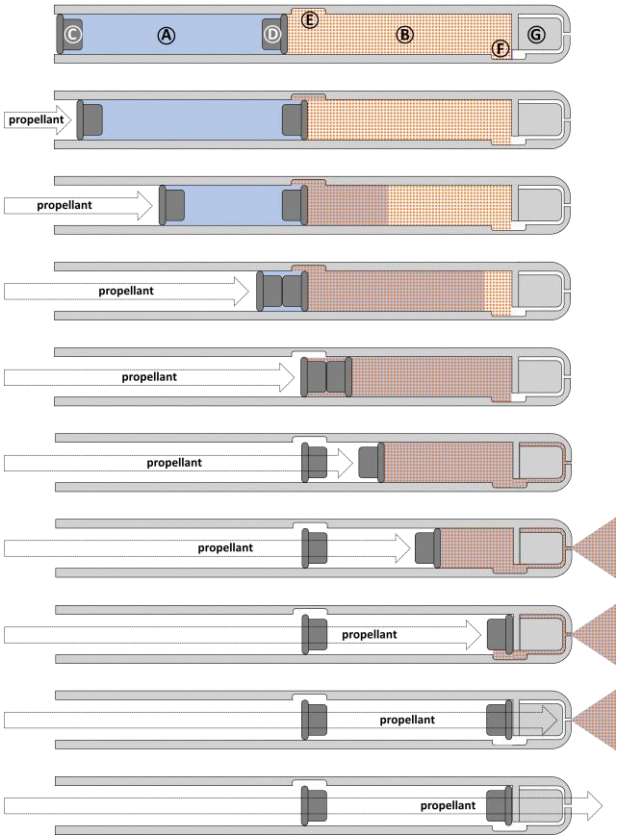

Figure 34. Sequence of drug cartridge cross sections demonstrate mechanism for mixing and spraying the drug formulation. The cartridge body is a long, thin, hollow cylinder. (**A**) Compartment for storing liquid portion of formulation. (**B**) Compartment for storing solids portion of formulation. (**C**) Piston 1. (**D**) Piston 2. (**E**) Channel 1. (**F**) Channel 2 with a membrane to seal the solids compartment during storage. (**G**) Atomizer tip.

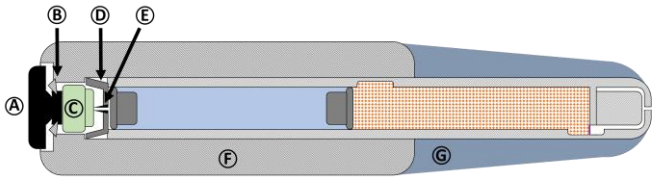

Figure 35. Cross section of disposable, single dose, dual chamber nasal spray device. (**A**) Mechanical button for actuation. (**B**) Locking mechanism to keep button depressed. (**C**) Micro sized propellant gas cartridge charged for single use. (**D**) Elastomer receiver to create seal with gas cartridge. (**E**) Hollow piercing pin to puncture gas cannister. (**F**) Plastic body. (**G**) Soft foam tip for contact with nostril.

Alternatively, the propellant gas system could be reusable as illustrated in Figure 36. In this iteration of the design the drug cartridge is still single use, removable, and disposable. The body of the device is meant to be reused. The gas cartridge is also replaceable and disposable, but it contains enough charge to be used many times before replacement. The device has an electronically controlled solenoid to release a metered burst of propellant gas into the drug cartridge when the button is pushed. A discharge counter would keep track of how many times the device was used and be reset every time

a fresh gas cartridge is installed. The status of the device (ready, full, empty, battery warning, etc.) can be indicated to the user on a display or with led lights.

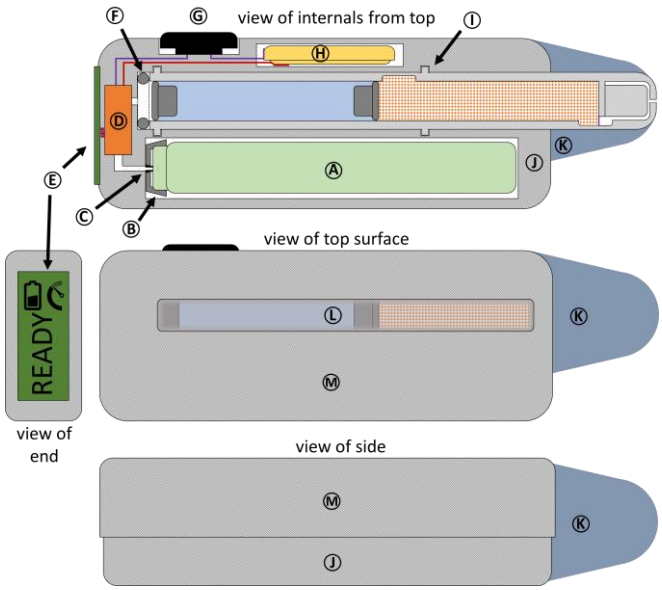

Figure 36. Reusable nasal spray device that accepts disposable, single use, dual chamber drug cartridges. (**A**) Propellant gas cartridge charged for multiple doses. (**B**) Elastomer receiver to create seal with gas cartridge. (**C**) Hollow piercing pin to puncture gas cannister. (**D**) Metered flow solenoid and counter. (**E**) Status indicator display. (**F**) O-ring. (**G**) Button for actuation. (**H**) Power cell. (**I**) Drug cartridge positioning pins. (J) Main plastic body molded to house the components. (**K**) Soft foam tip for contact with nostril. (**L**) Viewing window to determine if cartridge has been spent. (**M**) Top shell that can be removed to access and replace the internal components (drug cartridge, propellant gas cartridge, and power cell).

6.4 Materials and methods

6.4.1 Proof of concept device prototype construction

A fully functional proof of concept nasal spray device was constructed with the following basic elements: dual chamber drug cartridge, propellant gas cartridge, flow

regulator, valve, and switching mechanism. A 0.3 mL polypropylene insulin syringe (Becton Dickinson Co., Franklin Lakes, NJ: cat. #324702) having an ID of 3.2 mm and length of 50 mm was repurposed for the drug cartridge barrel. Slots, approximately 4 mm long, were cut through the wall of the barrel and covered with sections of silicone tubing to form Channels 1 and 2 as illustrated in Figure 34. Polyisoprene pistons 2.5 mm in length were fashioned from syringe plunger tips. The pistons were lightly lubricated with PFPE based DuPont Krytox GPL 100 Oil (DowDuPont Inc., Midland, MI), which is compatible with elastomeric seal materials and engineering plastics. After loading the drug cartridge with a test formulation, a pressure-swirl type atomizer tip was affixed to one end of the drug cartridge using silicone tubing as shown in Figure 37. The atomizer tip was obtained from a generic nasal spray bottle (Pirlo International Co., Zhejiang, China: cat. # 391333528). The other end of the drug cartridge was connected to a fast response (< 20 ms), normally closed solenoid valve (WIC Valve Co., San Jose, CA: cat. #2ACK-1/4). The valve was operated using a triggered relay timer that was programmable in millisecond increments with 0.1% precision (QiYuanFei Electronic Technology Ltd., Shanghai, China: cat. #JDQSX11SH). Triggering the relay caused the release of propellant gas into the drug cartridge for a specified time interval. The propellant gas was pressurized CO_2 from a standard 8 gr cartridge attached to an adjustable regulator with 0-125 psi gauge (Interstate Pneumatic Manufacturing, Vista, CA: cat. #WRCO2).

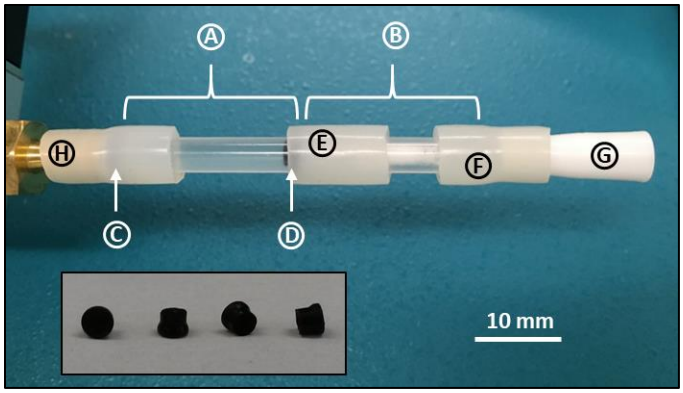

Figure 37. Prototype drug cartridge prior to actuation. Inset shows examples of the elastomer pistons, which are situated in the cartridge but obscured by opaque tubing in the main image. (**A**) Liquid compartment containing buffer. (**B**) Solids compartment containing lyophilized prodrug and enzyme. (**C**) Location of elastomer piston 1. (**D**) Location of elastomer piston 2. (**E**) Location of channel 1. (**F**) Location of channel 2. (**G**) Atomizer tip. (**H**) Barbed connector from solenoid that releases a controlled burst of propellant gas, CO_2.

6.4.2 Spray cone measurements

Drug cartridges were loaded with 150 µL water in the liquid compartment and 15 mg mannitol lyophilizate in the solids compartment to simulate a two-part drug formulation. The relay timer and regulator were set to release CO_2 into the drug cartridge at specified stagnation pressures for a duration of 100 ms. The resulting spray was filmed with a Sony Exmor RS 12 MP camera at a frame rate of 240 fps. Individual frames were examined to locate three representative images of the fully developed spray cone at each condition tested. Examples of the images are shown in Figure 38. To measure the primary breakup distance and cone angle, the features and margins of the spray were identified using the Sobel edge detector in the Fiji distribution of ImageJ software version 1.51s.[173] Primary breakup distance (d) was defined as the axial distance from the atomizer tip orifice

to the point at which the liquid sheet became unstable and began to form droplets. Cone angle (θ) was defined as the angle between two rays drawn from a vertex located at the atomizer tip orifice along the upper and lower margins of the droplet cone.

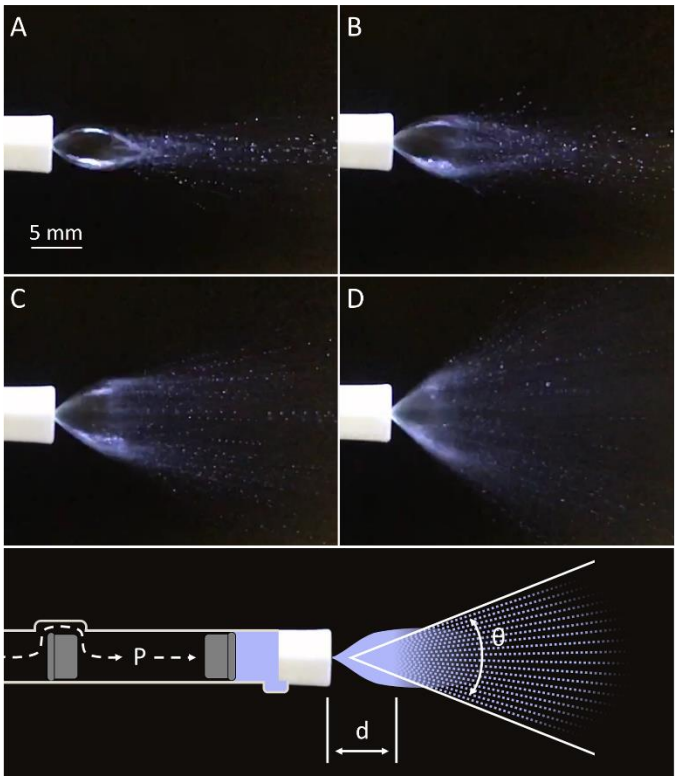

Figure 38. Images of fully developed spray cone produced by different stagnation pressures. (**A**) 30 psi. (**B**) 35 psi. (**C**) 40 psi. (**D**) 45 psi.

6.4.3 Nasal cavity deposition tests

Human and canine nasal cavity molds were made by 3D printing a cast of the interstitial space using a water-soluble polymer, molding clear silicone around the cast, and then dissolving out the cast with water. To print the casts, 3D renderings were required. For the human nasal cavity, an STL file (3DPX-002305) was downloaded from the NIH 3D Print Exchange.[174] For the canine nasal cavity, the interstitial space representing the

cavity of a 21.6 kg mixed breed canine with a mesocephalic snout was segmented from CT scan DICOM files (103 images, voxel spacing 0.449×0.449×3 mm) using ITK-SNAP version 3.6.0 developed by Yushkevich *et al*.[175] The STL files were cleaned up to remove artifacts and unnecessary sinuses in Meshmixer version 3.5 (Autodesk Inc., San Rafael, CA), sliced using Ultimaker Cura version 4.0 (Ultimaker, Geldermalsen, Netherlands) to generate the G-code, and subsequently printed on a CR-10 3D Printer (Creality3D Technology Co., Shenzhen, China) using Atlas Support water soluble polyvinyl alcohol (PVA) blend filament (Formfutura BV, Nijmegen, Netherlands: cat. # 901034).

To create the molds, two-part SYLGARD® 184 Silicone Elastomer (Dow Corning Co., Midland, MI) was mixed in a glass container and degassed under vacuum. Then the 3D printed nasal cavity casts were submerged in the silicone and the combination placed in an oven to cure at 50 °C for 8 hr. After curing, the glass was fractured for easy removal from the outer surface. The PVA casts were dissolved from the inside of the silicone molds using a combination of water bath soaking and periodic pressurized water rinses from a Water Flosser (Water Pik Inc., Fort Collins, CO). Removal of the PVA took about 3 days.

Before each spray test, the nasal cavity molds were prepared by rinsing them with an aqueous solution of 100 mg/mL surfactant (Alconox Inc., White Plains, NY: cat# MFCD00145747) and dried to leave a thin coat of surfactant on the inner surface. The surfactant mitigated the amount of beading, pooling, and dripping that occurred when dye was sprayed into the cavities. The drug cartridges used for deposition experiments contained 150 µL of aqueous erioglaucine dye (FD&C Blue #1) in the liquid compartment and 15 mg mannitol lyophilizate in the solids compartment to simulate a two-part drug

formulation. The CO_2 propellant gas system set to 30, 35, 40, and 45 psi with a gate interval of 100 ms was used to spray the dye formulation into the nasal cavity molds. The anatomical regions where dye deposited was determined by visual inspection through the sides of the clear molds, and the penetration depth was measured from the opening of the nare to the furthest boundary of bulk solution deposition (light splattering and mists were ignored).

6.4.4 Acid/base formulation testing

An acid/base drug formulation was used to assess the ability to mix reactive species using the dual chamber drug cartridges. The acid component was a solid dihydrochloride salt of an open ring form of midazolam (MDZ_{open}•2HCl), which is a water-soluble precursor to the insoluble drug midazolam (MDZ). MDZ_{open}•2HCl was synthesized from MDZ according to the procedure described in Chapter 5. To load the drug cartridge, a lyophilizate of MDZ_{open}•2HCl was formed and stored within the solids compartment. The lyophilizate was prepared by dissolving MDZ_{open}•2HCl in water at ~0 °C in an ice bath to obtain a solution concentration of 0.154 M. Then, 100 µL of the solution (equivalent to 5 mg of MDZ) was quickly transferred into a drug cartridge that had a plunger situated near Channel 1 to prevent the sample from leaking out of the other end. The cartridge containing the solution was dipped in liquid nitrogen to freeze the liquid, the plunger was removed, and the cartridge containing the frozen sample was placed in a lyophilization chamber to dry under 0.016 mbar vacuum at room temperature for 18 hr using a FreeZone 6 manifold freeze dryer (Labconco Inc., Kansas City, MO). After lyophilization, the cartridge assembly was completed by placing an atomizer tip at the end of the solids compartment,

positioning Piston 2 near Channel 1, filling the liquid compartment with 100 µL of pH 13.4 NaOH in water (0.276 M), capping the end of the liquid compartment with Piston 1, and attaching the loaded drug cartridge to the CO_2 propellant gas system set to 40 psi with a 50 ms gate interval.

To test the performance of the drug cartridges that contained this acid/base formulation, the pH profile of the spray pattern was visualized on pH indicator paper. The cartridge contents were sprayed onto a sheet of either blue litmus paper or red litmus paper from Precision Laboratories, LLC (Waukegan, IL: cat# 280-24-810 and 290-24-8X10). The distance between the atomizer tip and the litmus paper was 7 cm. Images of the spray pattern were captured ~10 s after the formulation had been sprayed.

6.4.5 Prodrug/enzyme formulation testing

A prodrug/enzyme formulation was used to assess the ability to reconstitute and atomize lyophilized fragile biomolecules using the dual chamber drug cartridges. The prodrug, avizafone (AVF), was synthesized in house according to the procedure described previously.[42] The enzyme, recombinant human aminopeptidase B enzyme (APB), was also produced in house by the procedure described previously.[108] In the drug cartridge, both AVF and APB were contained in the solids compartment as a lyophilizate. To prepare the lyophilizate, stock solutions of AVF, APB, and the lyoprotectant trehalose were mixed at ~0 °C in an ice bath to obtain a sample concentration of 1.00 mM AVF, 35 µg/mL APB, and 25 or 50 mg/mL trehalose. Then, 150 µL of the resulting solution was injected into the end of a drug cartridge that had a plunger situated near Channel 1 to prevent the sample from leaking out of the other end. The cartridge containing the solution was dipped in

liquid nitrogen to freeze the solution, the plunger was removed, and the cartridge containing the frozen sample was placed in a lyophilization chamber to dry under 0.016 mbar vacuum at room temperature for 18 hr. After lyophilization, the cartridge assembly was completed by placing an atomizer tip at the end of the solids compartment, positioning Piston 2 near Channel 1, filling the liquid compartment with 150 µL of pH 7.4 phosphate buffered saline (PBS), capping the end of the liquid compartment with Piston 1, and attaching the loaded drug cartridge to the CO_2 propellant gas system set to 45 psi with a 50 ms gate interval.

To test the performance of the drug cartridges that contained this prodrug/enzyme formulation, the concentration of active APB in the spray was calculated from the rate of drug production in the ejected solution. When AVF and APB are combined in solution at physiological temperature, they generate the drug diazepam (DZP).[108] DZP was measured by second derivative UV spectroscopy as described previously.[75] In brief, the contents of a cartridge were expelled directly into a quartz ultra-microcuvette that was pre-warmed to 32 °C in the temperature controlled block of Cary 100 Bio UV/Vis double beam spectrophotometer (Agilent Technologies Inc., Santa Clara, CA). Scans from 300-400 nm were collected every 0.25 min for 20 min. The second derivative of the extinction measured at 338 nm was used to determine the DZP concentration. Then the concentration of active APB was determined by fitting the differential equations that describe the reaction kinetics to the measured DZP concentration-time profiles (Chapter 4, Section 4.3.3).

6.5 Results and Discussion

6.5.1 Device functionality

Visual inspection of spent drug cartridges indicated that the prototype device was operating properly. The final position for Piston 1 was at Channel 1, and the final position of Piston 2 was at Channel 2. Nearly all of the formulation was cleared from the cartridge and atomizer tip. The way that the dual chamber drug cartridge functions in this nasal spray device is similar to that of prefilled dual chamber syringes.[176] Dual chamber syringes are marketed for parenteral drug delivery by injection. These syringes use a mechanical plunger, so there will always be some amount of drug left in the dead space between the plunger and end of the needle. Since volumes on the order of milliliters are common for injectable formulations, the amount trapped in the dead space of a dual chamber syringe is only a small fraction of the dose. Much smaller dose volumes (25 – 200 µL) are required for nasal spray formulations.[172] The amount of drug left in the dead space and atomizer tip would be a significant fraction of the dose if a mechanical plunger were to be used as the driving force. Unspent drug can be dangerous or abused. By using compressed air or propellent gas as the driving force for actuation, virtually all of the drug can be expelled from the drug cartridge. This means that cartridges do not have to be loaded with excess drug, and the empty cartridges can be safely disposed in household trash.

The pre-metered drug cartridges and automated action of this nasal spray device reduce the risk of improper dosing, but adequate deposition of the dose in the correct region of the nasal cavity is also important for effective intranasal delivery. Deposition is controlled by the atomizer tip insertion depth and angle, as well as spray plume

characteristics. Spray characteristics include cone angle, spray pattern, breakup distance, droplet velocity, and droplet size. As one might expect, the spray characteristics were found to be dependent on the type of atomizer tip used, composition of the formulation, propellant gas pressure, and duration of the applied pressure. When these device conditions were held constant, the cone angle and primary breakup distance for the jet were reproducible. Other spray characteristics were not measured during preliminary testing. Cone angle was approximately proportional and breakup distance was inversely proportional to pressure, for pressures between 30 and 45 psi as shown in Figure 39. Below 30 psi, erratic spray patterns were observed, and the device occasionally failed to expel the entire dose. Pressures above 45 psi produced a qualitatively finer mist but did not result in larger cone angles.

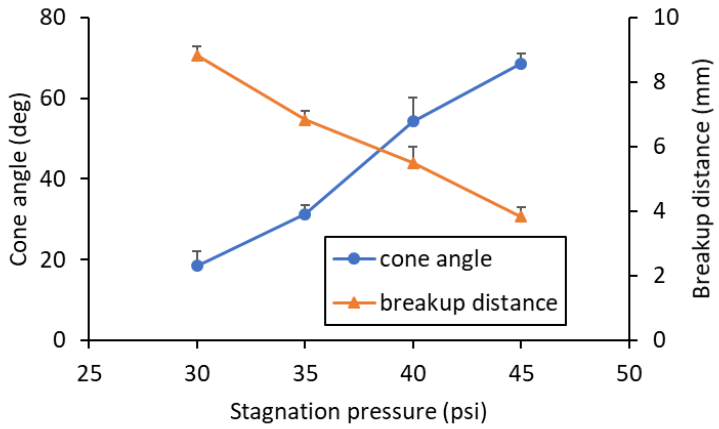

Figure 39. Fully developed spray cone geometry as a function of stagnation pressure. Averages +SD plotted, n = 3.

6.5.2 Nasal cavity deposition

Some spray parameters, such as droplet size, have a relatively minor influence on deposition efficiency and area of deposition within the nasal cavity compared to cone angle

and administration angle.[177] For small cone angles, the orientation of the device in the nostril becomes more important. A stream-like spray could impact a surface at the anterior of the nasal cavity, limiting the deposition to a smaller area in a region that is not optimal for drug absorption. Conversely, spray plumes with large cone angles may not clear the nasal valve (tapered region between the vestibule and atrium) and deposit predominantly in the vestibule rather than the nasal cavity. Ideally the spray would develop beyond the valve and deposit on the highly permeable respiratory epithelium at the anterior region of the turbinates.[32,178] The surface tension of the drug formulation and lateral movement of the mucus layer towards the nasopharynx (a process known as mucociliary clearance)[97] will cause the formulation to spread over the surface of the turbinates.[177] Deposition too deep within the nasal cavity, at the posterior of the turbinates, would limit the residence time of the drug in the nasal cavity and may lead to lower bioavailability if absorption cannot occur before mucociliary clearance carries the drug to the digestive tract.

Images of a human nasal cavity mold that was used for spray deposition testing are shown in Figure 40. The contents of drug cartridges with a solution of blue dye in the liquid compartment and a mannitol lyophilizate in the solids compartment were sprayed into the mold using the CO_2 propellant gas system set to various stagnation pressures to produce a range of spray cone angels (θ = 19, 31, 54, and 67°). The primary deposition area, regardless of spray cone angle, was in the atrium region of the nasal cavity. Spray cone angles of 67° tended to impact the nasal valve, and the buildup of solution in that area caused dripping of the formulation back out though the nare (Figure 40D1). The higher pressures used to produce wider cone angles also led to more splattering within the nasal

cavity, but the boundaries of the splattered region did not extend much further than the atrium region. This is because the meatus of the atrium and turbinates form a thin, tortuous path with no linear route for spray droplets to travel to the deeper recesses of the nasal cavity. Formulations sprayed with the smallest cone angle tested, 19°, deposited beyond the nasal valve region and were less likely to drip back out through the nare (Figure 40D2). One of the most critical factors affecting the region where dye deposited in the nasal cavity was found to be the angle of administration. Perhaps not surprisingly, greater deposition on the respiratory epithelium at the anterior of the turbinates could be achieved by angling the spray device towards the turbinates (at about a 40° angle from the plane of the nare). These observations and deposition areas are similar to the findings of other researchers.[16,17] Suman *et al*. noted that benchtop spray plume characterization measurements (droplet size, cone angle, ovality ratio, etc.) that can portray two spray devices as having different performance does not necessarily equate to differences in performance in vivo.[179]

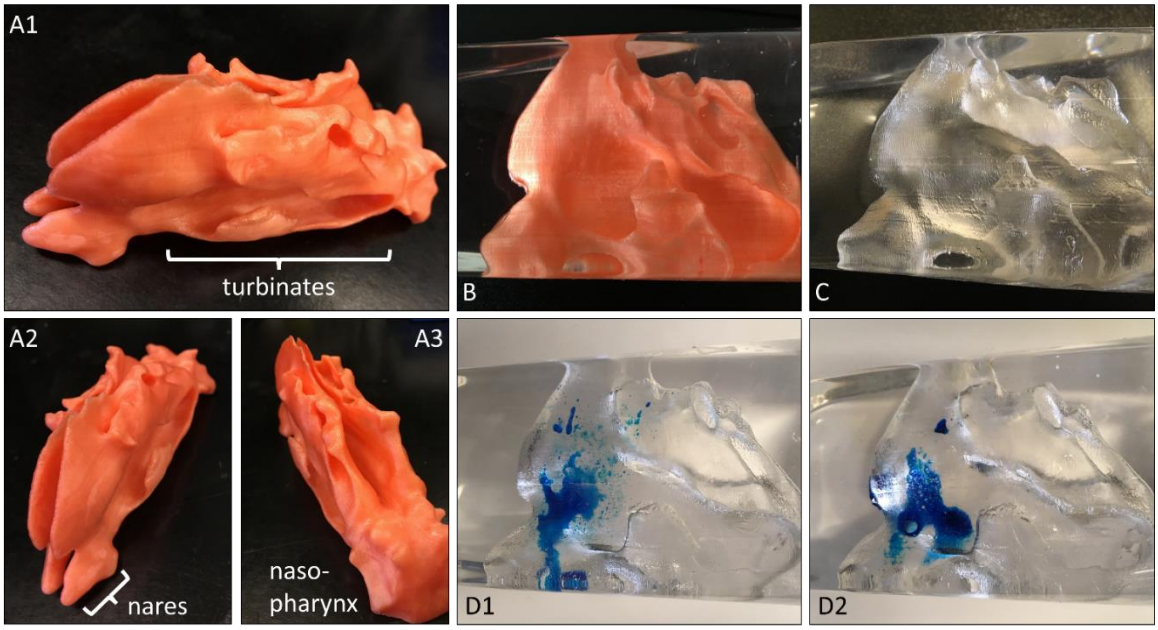

Figure 40. Human nasal cavity mold. (**A1-3**) Cast of interstitial space of human nasal cavity that was 3D printed with soluble PVA filament. (**B**) Nasal cavity cast inside of silicone mold. (**C**) PVA dissolved out of silicone to leave empty mold of nasal cavity. (**D1-2**) Blue dye from drug cartridge sprayed though left nare into nasal cavity mold deposited in the atrium region. Spray impacting the nasal valve tended to drip back out of the nare as shown in D1.

A canine nasal cavity mold was also made to test the device for preclinical trials and potential applications in veterinary medicine (Figure 41). Again, the deposition area was found to be largely independent of spray cone angle. The narrow meatus of the nasal cavity and impact of the dye formulation on the walls of the nasal cavity did not allow for fully developed spray plumes even at the smallest cone angle tested, 19°. The region of deposition was at the anterior of the nasal cavity and was well distributed between the dorsal, middle, and ventral meatus when the spray was directed toward the common meatus and aligned parallel to the rostral axis (Figure 41C). This is likely the ideal region for deposition since mucociliary clearance will carry the formulation across the respiratory

epithelium from the anterior to the posterior of the nasal cavity, allowing maximal residence time for drug absorption to occur.

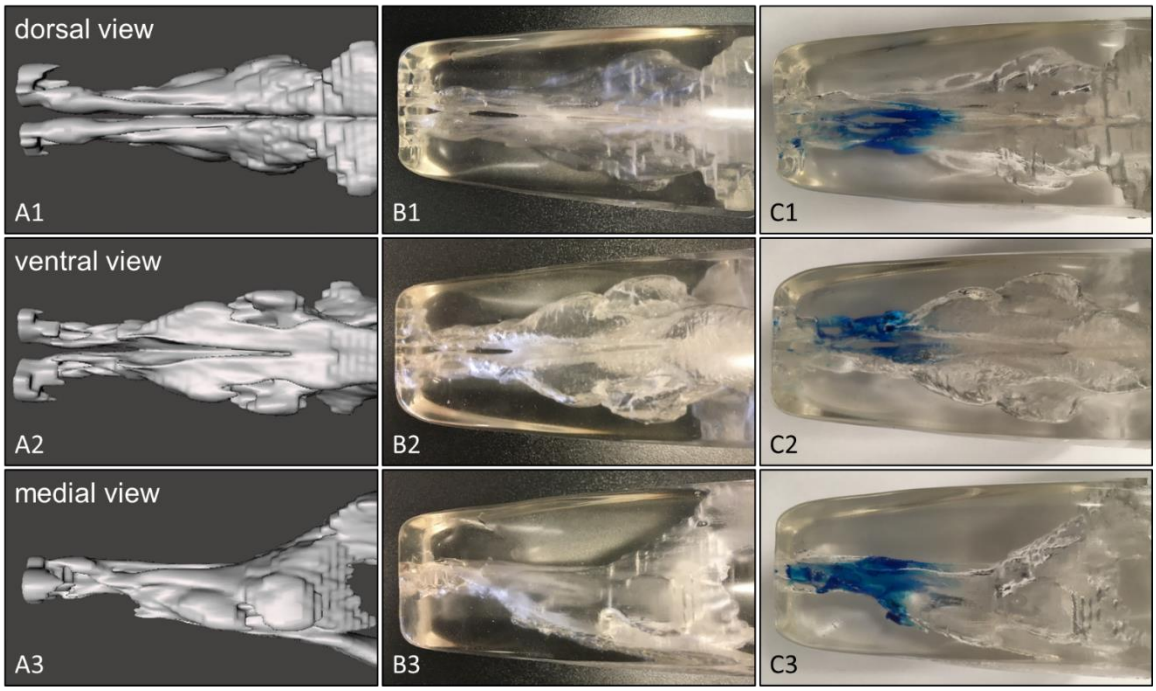

Figure 41. Canine nasal cavity mold. (**A1-3**) 3D rendering of the nasal cavity interstitial space obtained from CT scan segmentation. (**B1-3**) Empty silicone mold. (**C1-3**) Blue dye from drug cartridge sprayed though left nare into nasal cavity mold deposited past the osseous nasal aperture and spread across the anterior regions of the dorsal, middle, ventral meatus.

6.5.3 Drug formulation testing

Our group is currently investigating a two-part formulation strategy for the intranasal delivery of insoluble benzodiazepines to treat seizure emergencies. These formulations contain reactive species that must be kept separate during storage. When the reactants are combined and sprayed into the nasal cavity, a metastable supersaturated solution of the benzodiazepine is created which leads to very rapid absorption across the

nasal mucosa into the systemic circulation.[108] Two different versions of these two-part benzodiazepine formulations were tested in the drug cartridges. An acid/base formulation that generates the benzodiazepine MDZ was used to demonstrate rapid dissolution and mixing, and a prodrug/enzyme formulation that generates the benzodiazepine DZP was used to demonstrate the applicability of this strategy to the delivery of unstable molecules or molecular assemblies.

6.5.3.1 Acid/base formulation

The drug MDZ is insoluble in water at physiological pH. Formulations that are concentrated enough to deliver a therapeutic dose in a volume acceptable for intranasal delivery rely on low pH, organic co-solvents, or inclusion complexes. These formulation strategies can irritate sensitive nasal tissues and slow drug absorption. MDZ_{open}•2HCl is a soluble precursor of MDZ. When dissolved in water at high concentrations, MDZ_{open}•2HCl results in an acidic solution and exists predominately as an inactive open ring form of MDZ. Increasing the pH of the solution shifts the equilibrium toward MDZ, creating a supersaturated solution and a bioavailable amorphous phase. This slurry of supersaturated and amorphous MDZ cannot be stored for long periods of time without leading to undesirable crystallization of MDZ. Therefore, the pH shift should be performed at the time of administration. Refer to Chapter 5 for background and details about this formulation.

The dual chamber drug cartridges offer an opportunity to conveniently store MDZ_{open}•2HCl separately from a base and the ability to rapidly atomize a mixture of them for deposition in the nasal cavity at the time of administration. In the drug cartridge,

MDZ_{open}•2HCl was stored within the solids compartment as a lyophilizate. The base component, aqueous NaOH, was stored in the liquid compartment. In order to avoid a heterogenous mixture and pH spikes on the surface of the nasal mucosa, a two-part acid/base formulation would need to undergo very rapid mixing or dissolution. As a lyophilizate, dissolution of MDZ_{open}•2HCl was observed to be nearly instantaneous. The formation of low density, porous cakes during lyophilization greatly increases the surface area of the solid material and enhances dissolution.[180] Additionally, the lyophilization process can result in high energy amorphous and/or polymorphic crystalline forms of a material that are more readily solvated compared to the thermodynamically stable crystal form.[181] Samples of the MDZ_{open}•2HCl lyophilizates characterized by differential scanning calorimetry according to the procedure described in Chapter 5 indicated amorphous MDZ_{open}•2HCl was present in the lyophilizates, evident by the glass transition at 74.3 °C and crystallization exotherm at 154-163 °C (Figure 42). As the lyophilized samples were heated, several metastable modifications were observed that corresponded to high energy polymorphs. Lyophilization will likely improve the dissolution rate of many drugs or drug precursors as it does for MDZ_{open}•2HCl, but the extent of improvement will depend on the specific compound, excipients, and lyophilization cycle parameters.

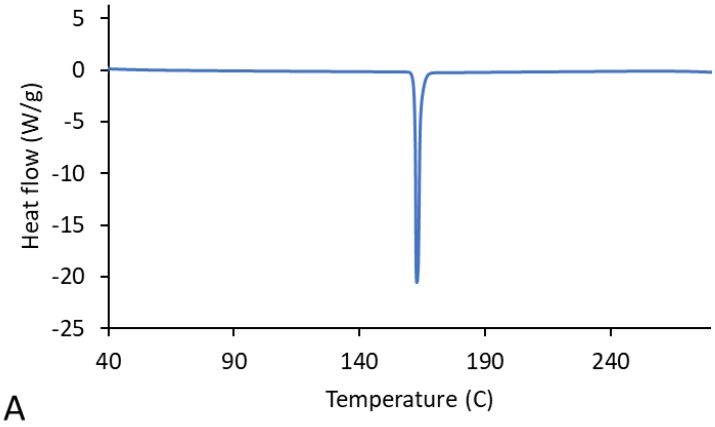
5
0
-5
-10
-15
-20
-25
Heat flow (W/g)
40
90
140
190
240
Temperature (C)

A

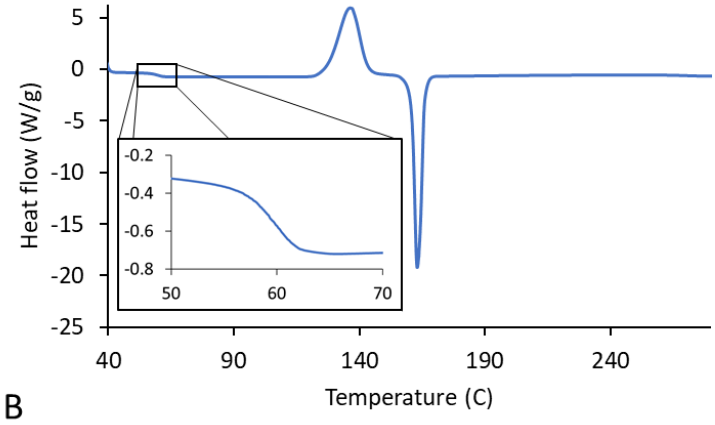
5
0
-5
-10
-15
-20
-25
Heat flow (W/g)
-0.2
-0.4
-0.6
-0.8
50
60
70
40
90
140
190
240
Temperature (C)

B

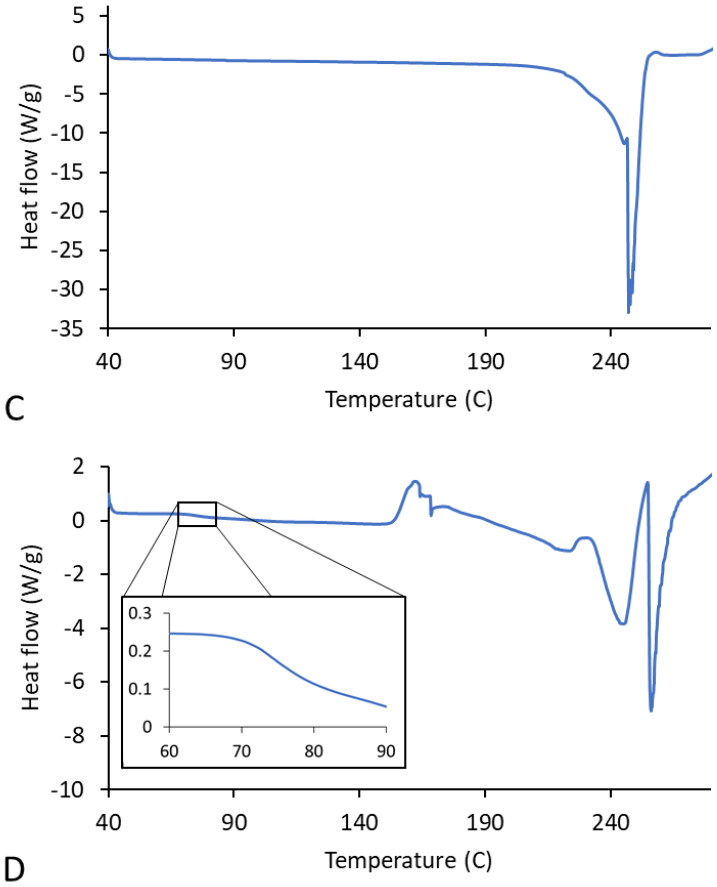

Figure 42. DSC thermograms of the MDZ acid/base formulation reactants and products. (**A**) Insoluble, crystalline MDZ standard. (**B**) Amorphous MDZ precipitate recovered from reaction of MDZ_{open}•2HCl with NaOH solution. (**C**) Crystalline MDZ_{open}•2HCl from synthesis of stock. (**D**) Rapidly dissolving amorphous material and metastable modifications present after lyophilization of MDZ_{open}•2HCl.

Homogeneous mixing of the formulation components at the site of deposition is important for two-part reactive formulations such the MDZ acid/base formulation. The reactive species should be thoroughly mixed to ensure that complete and efficient production of the active drug occurs. To test the mixing of NaOH in solution with MDZ_{open}•2HCl in the lyophilizate, permutations of the formulation were sprayed from drug

cartridges onto litmus paper using the CO_2 propellant gas system. Control drug cartridges containing water and MDZ_{open}•2HCl lyophilizate sprayed onto blue litmus paper created a circular orange spray pattern (Figure 43A). Blue litmus becomes orange when exposed to acidic solutions. This control demonstrated that rapid dissolution of the MDZ_{open}•2HCl lyophilizates resulted in an acidic spray plume. The pH of the expelled solution was measured to be 1.3 when the spray was captured in a vial and subsequently measured with a low volume pH meter. Figure 43B shows the converse control with only NaOH solution in the liquid compartment of the drug cartridge and nothing in the solids compartment sprayed onto red litmus paper. (Red litmus becomes blue when exposed to basic solutions.) Figure 43C and Figure 43D show the spray patterns from drug cartridges containing both NaOH solution and MDZ_{open}•2HCl lyophilizate. On blue litmus, a light orange hue (corresponding to pH ~7.4) was observed in a circular pattern with a smaller radius than the radius of the full spray plume, suggesting a higher concentration of MDZ_{open}•2HCl at the center of the plume. However, a faint blue hue (corresponding to pH ~8) was observed in the same area from the same formulation sprayed on red litmus. Multiple replicates yielded the same conflicting results. It seems likely that the entire plume had a pH 7.4-8.0, but a color change was only detectable at the center of the blue litmus because that is where a larger volume of formulation deposited. The pH profile of the spray pattern from this acid/base formulation demonstrates that large pH shifts can be performed with this device, opening up the possibility to administer soluble salts of poorly soluble drugs at a pH appropriate for intranasal delivery.

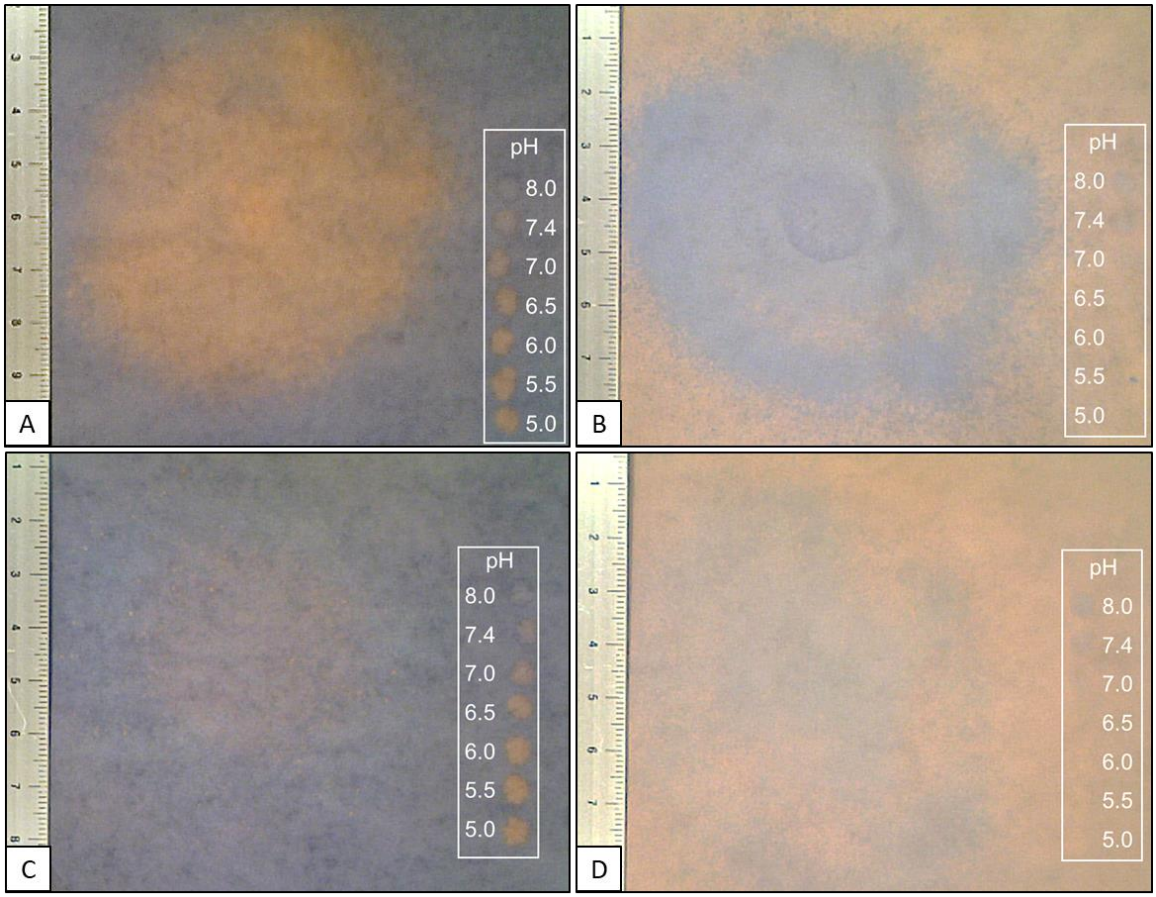

Figure 43. Images of acid/base formulations sprayed onto litmus paper. Each image shows the pH profile of the spray pattern that resulted from spraying drug cartridges containing a two-part formulation with 100 µL liquid and 6.4 mg solid of the stated components onto pH indicator paper. Scale bar on left is in units of cm. Buffer solutions spotted on right to show color scale for pH. Each condition was tested in triplicate. (**A**) Water and solid MDZ_{open}•2HCl sprayed onto blue litmus paper. (**B**) pH 13.4 NaOH solution and no solid sprayed onto red litmus paper. (**C**) pH 13.4 NaOH solution and solid MDZ_{open}•2HCl sprayed onto blue litmus paper. (**D**) pH 13.4 NaOH solution and solid MDZ_{open}•2HCl sprayed onto red litmus paper.

Instantaneous dissolution and content uniformity between individual spray droplets may not be as critical as homogeneous mixing on the surface of the nasal mucosa. As can be seen in Figure 43C and D, orange speckles were observed throughout the spray pattern,

indicating punctate acidity. The formulation in those experiments was expelled from the drug cartridges with a 50 ms burst of CO_2 propellant. Given this short time frame, it is reasonable to assume that some of the lyophilized material exits the atomizer as a slurry. For an acid/base formulation, these scattered droplets of low acidity would quickly dilute in the nasal mucus and probably do not contain enough acidic material to overcome the natural buffering capacity of the mucus. Furthermore, mixing of the acid and base components does not necessarily have to occur in the cartridge. Figure 44 demonstrates mixing on a deposition surface rather than inside the drug cartridge. The drug cartridge containing a liquid/liquid formulation with an aqueous solution of tartrazine dye (FD&C Yellow #5) in one compartment and an aqueous solution of erioglaucine dye (FD&C Blue #1) in the other compartment was sprayed onto a paper towel. The blue dye exited the atomizer first, followed by the yellow dye. The resultant spray pattern was a green color because the deposition area for the blue dye was the same as the deposition area of the yellow dye. As long as the components of a two-part reactive formulation are deposited on the same area of the nasal mucosa, homogeneous mixing within the drug is not imperative.

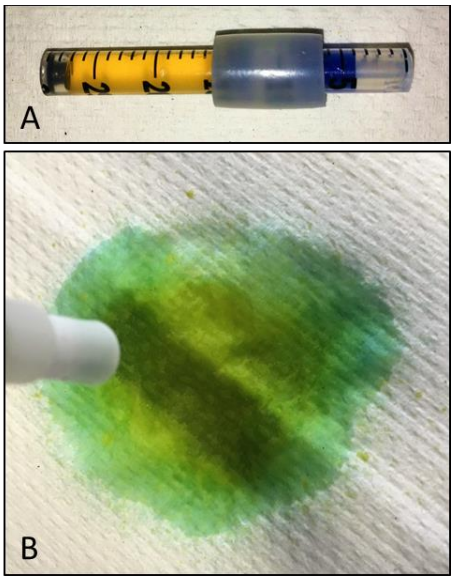

Figure 44. Mixing of a sprayed liquid/liquid dye formulation. (**A**) Drug cartridge contained 125 µL yellow dye in one compartment and 50 µL blue dye in the other. The liquids were separated by an elastomer piston that was obscured from view under the silicone tubing. (**B**) Cartridge pictured in A sprayed onto a paperer towel produced a green spray pattern from the mixing of the yellow and blue dyes. Image captured immediately after spraying.

6.5.3.2 Prodrug/enzyme formulation

Intranasal delivery is an attractive alternative for drugs that would otherwise need to be administered intravenously. In the case of biologics and molecular assemblies, the intranasal route also offers the potential to bypass the blood brain barrier through direct nose-to-brain pathways.[182] However, the solution state physicochemical instability of many of these therapeutics does not provide adequate shelf life to formulate them as nasal sprays.[15] Solid state stability is typically much better, thus lyophilization has been used as a means to extend the shelf life of unstable pharmacuticals.[183] For example, liposomal formulations tend to be unstable in solution and lyophilization is often unavoidable.[184]

Enzymes also tend to be unstable when stored in solution. We have been investigating the feasibility of co-administrating a soluble prodrug with a converting enzyme in an aqueous vehicle for rapid intranasal delivery of insoluble drugs.[42] One such formulation employs the labile enzyme, APB. APB can be stabilized for long-term storage by lyophilizing it in the presence of its prodrug substrate, AVF, and a common lyoprotectant, trehalose (Chapter 4). In fact, the impetus for designing a dual chamber nasal spray device was the desire to quickly reconstitute these APB lyophilizates and subsequently atomize the solution for convenient intranasal administration of the prodrug/enzyme formulation.

There are several mechanisms by which APB can degrade during the processes of filling the drug cartridges and actuating the device to atomize formulation. Lyophilizing material in long, slim containers can be problematic because the geometry is prone to uneven heat and mass transfer.[185] Differences in APB lyophilizate cake morphology were observed at the closed end of a drug cartridge compared to the open end when frozen solutions of the APB and trehalose were lyophilized with Piston 2 in place. While changes in cake appearance do not necessarily equate to changes in product performance, if the morphology difference was due to partial melt-back there could be excess moisture trapped in that region that would affect stability and the reduction in surface area could cause slower dissolution.[110] Leaving both ends of the drug cartridge open during lyophilization produced uniform cakes; however, the freezing and drying steps caused ~30% loss in APB activity regardless of the container material or geometry that was used to prepare the lyophilizate. The degradation associated with the lyophilization process is evident when

comparing the active APB concentration in pre-lyophilization solutions shown in Figure 45A to the active concentration after lyophilization shown by the blue bars in Figure 45B.

During actuation, shear stress from forcing the formulation out of the drug cartridge and through the atomizer orifice can damage fragile molecules, especially biomolecules like APB.[186] The amount of shear stress introduced, hence the extent of degradation, is correlated to the shear rate. Figure 45A shows that the concentration of active APB, measured by turnover of the prodrug substrate AVF, was unchanged when the solutions were sprayed manually using a syringe attached to an atomizer tip. Depressing the syringe plunger by hand generated relatively low shear rates. Much higher shear rates can be obtained using the CO_2 propellant gas system to discharge drug formulations from the drug cartridges. The orange bars in Figure 45B show a reduction in APB activity when the prodrug/enzyme formulation was sprayed at high pressure (P = 45 psi) compared to simply reconstituting the formulation without pressure or spraying (blue bars). Samples containing different concentrations of the lyoprotectant excipient, trehalose, were tested (25 and 50 mg/mL in the pre-lyophilization solution). Two-tailed, unpaired t-test analysis indicated that there was no statistical difference in enzyme activity with these concentrations of trehalose: $t(4) = 0.80$ with $p = 0.47$ for the controls and $t(4) = 1.1$ with $p = 0.35$ for the sprayed samples. Testing of prodrug/enzyme formulations for tolerance to shear stress using the dual chamber nasal spray device prototype is ongoing.

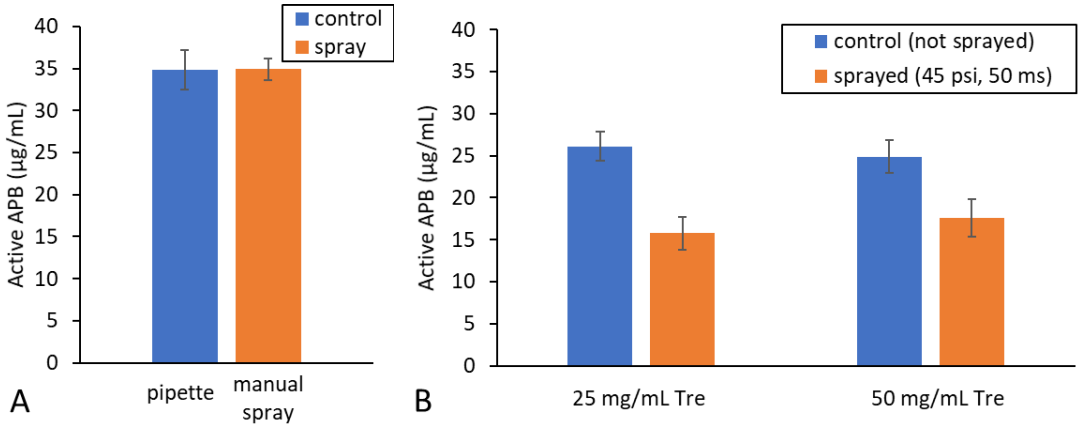

Figure 45. Stability of enzyme upon spraying prodrug/enzyme formulations. (**A**) No difference in active enzyme concentration was observed between prodrug and enzyme admixed from stock solutions without spraying (blue bar) versus mixtures that were drawn into a syringe and sprayed though an atomizer by thumb pressure on the syringe plunger (orange bar). The components were not lyophilized. Reactions were performed in PBS, n = 3, ±SD. (**B**) Reduction in active enzyme was observed between prodrug/enzyme lyophilizates reconstituted with PBS and rinsed out (blue bars) versus those that were sprayed out of the drug cartridge using the CO_2 propellant gas system (orange bars), n = 3, ±SD.

6.5.4 Example of a functional prototype

The laboratory CO_2 propellant gas system used for benchtop testing of the proof of concept prototype was too bulky to incorporate in a handheld device, so a functional prototype was constructed that forces air through the drug cartridge using a compressed spring air pump. Since air is a compressible gas, the pump needs to push a volume of air larger than the volume of the drug cartridge in order to generate enough pressure to expel the formulation from the cartridge. Additionally, there is an inverse relationship between the pressure that can be generated from the spring force and the area of the piston within the pump. In the prototype pictured in Figure 46, the air pump was fashioned from a 1 mL

syringe that had an inner cross-sectional area 2.3 times larger than the inner cross-sectional area of the drug cartridge. With a compression spring rate of 1.05 lbs/in, this prototype was able to produce fully developed spray cone angles of ~ 40° when the drug cartridge was loaded with 150 µL water in the liquid compartment and 15 mg mannitol lyophilizate in the solids compartment. Frictional forces, formulation properties, and atomizer tip geometry had a significant impact on the performance of the device. The air pump and drug cartridge pistons required a thin coat of lubrication to reduce friction and operate consistently. Some test formulations with high viscosity or slowly dissolving lyophilizates caused too much back pressure to be effectively atomized with this prototype. Each nasal spray drug formulation will have different fluid properties such as viscosity, density, thixotropic behavior, elasticity, and surface tension. These properties influence spray characteristics and ultimately nasal cavity deposition,[45] so the device parameters (spring force, atomizer orifice, etc.) would need to be optimized to suit the properties of specific formulations. If the device is to be reusable, then a mechanism to retract the spring when a new drug cartridge is inserted would also need to be incorporated into the design.

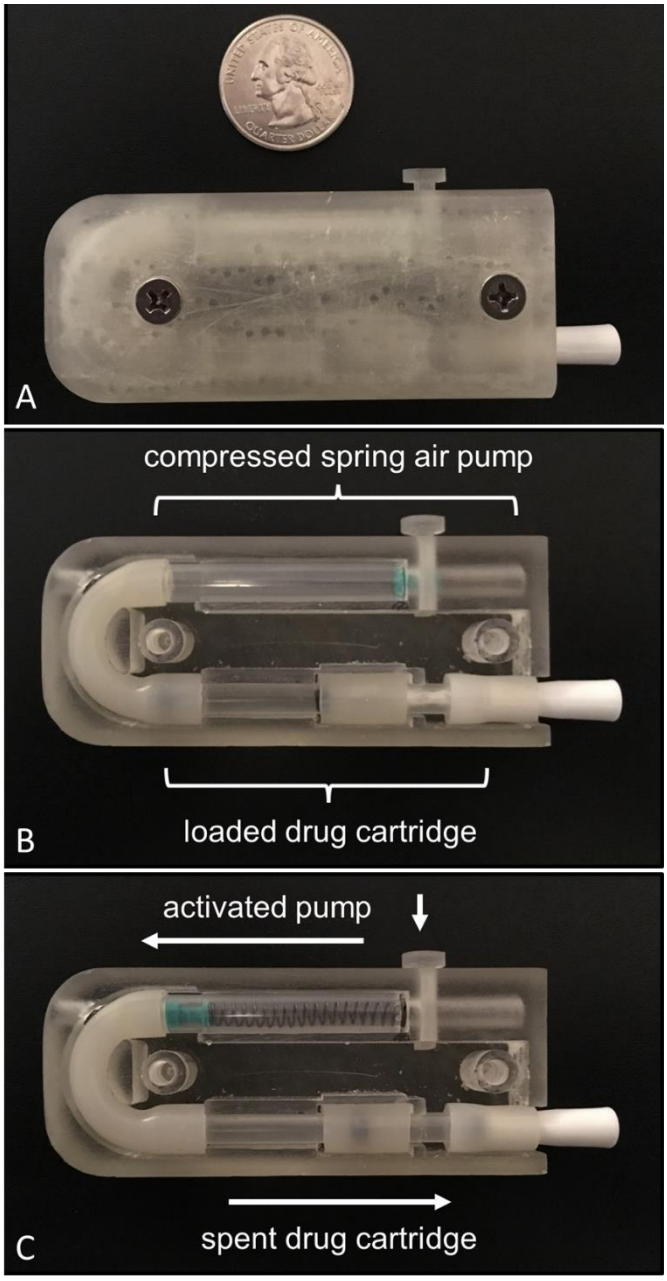

Figure 46. Functional prototype. (**A**) External surface. (**B**) Internal components showing liquid compartment of drug cartridge containing water, solid compartment containing mannitol, and retracted spring of air pump held in place by a trigger mechanism. (**C**) Internal components after actuation of device by pressing the trigger button. Extension of the spring forced air though the drug cartridge, causing the pistons to advance forward and expel the formulation.

6.6 Conclusions

Many drugs cannot be formulated as nasal sprays for use in standard nasal spray devices because they are either too unstable or poorly soluble to be stored in solution. The dual chamber nasal spray device we have described enables shelf-stable formulations of these types of drugs by segregating the reactive or otherwise unstable components of the formulation into separate compartments during storage. Actuation of the device at the time of administration combines the components to create a metastable mixture that is sprayed into the nasal cavity.

We began this report by describing the device mechanism, which is a pneumatically driven adaptation of dual chamber syringe technology. A proof of concept prototype was constructed and tested with a placebo formulation, demonstrating that the spray plume geometry could be controlled by adjusting the propellant pressure. However, using the device to spray dyed placebo formulations into silicone nasal cavity molds and observing the extent of deposition in the target region revealed that optimizing the spray cone angle is less important than controlling the angle of administration. Then, the device was tested using two-part reactive formulations that generate supersaturated solutions of benzodiazepines. An acid/base formulation that generates supersaturated midazolam demonstrated rapid mixing solid and liquid components could be achieved during actuation of the device. A prodrug/enzyme formulation that generates supersaturated diazepam demonstrated the feasibility of using this device to stabilize and deliver labile proteins. In general, examples of drugs that could be used in this device include biomolecules, water/air/heat sensitive compounds, combinations that produce metastable states such as

supersaturation, lyophilized molecular assemblies such as liposomes and emulsions, reactive species, or any other incompatible formulation components that need to be separated during storage but combined during administration.

Chapter 7: Future directions

The series of experiments described thus far provides a basic framework for investigating potential two-part reactive formulations for intranasal delivery of poorly soluble drugs and demonstrates a viable path from benchtop to pharmaceutical product. However, there is much that remains to be discovered by expanding the experiments to support generalization of this formulation strategy to other drugs and to delve deeper into the minutiae of the phenomena that have been observed. The following subsections provide examples of avenues that are ripe for exploration.

7.1 Phase separation processes

The prodrug/enzyme and acid/base reactions could be used as tools to further study amorphous solubility. Even though the thermodynamic equilibrium solubilities of DZP and MDZ are different, they were observed to have essentially the same intrinsic amorphous solubility, as determined by the upper limit for their superstation concentrations at a pH in which the reaction products are neutral. Theoretical calculations of 'amorphous solubility advantage' rely on accurate measurement of the equilibrium solubility of a stable crystalline form and Gibbs free energy difference between the amorphous and crystalline forms.[187] Perhaps correlations between the upper limits of supersaturation measured from for a curated series of compounds and the theoretical calculations of their corresponding free energies of mixing can be found which will shed light on the molecular properties that dictate solubility limits in non-ideal solutions. This may lead to an empirical or theoretical model for accurate prediction of amorphous solubility without the need to perform a priori measurements.

The reactions could also be used to investigate precipitation behavior when the upper limit of supersaturation is reached. A metastable zone (i.e. supersaturated concentration range) exists between the binodal and spinodal curves of a phase diagram.[188] The binodal curve is defined as the mole fraction of a mixture where the chemical potential of the all the components are equal. The binodal curve corresponds to the boundary between conditions where a solution is thermodynamically favored versus conditions where phase separation is thermodynamically favored. The spinodal curve is defined as the mole fraction of a mixture where the second derivative of the free energy of mixing with respect to mole fraction is zero.[189] The spinodal is the boundary beyond which the solution is unstable and there is essentially no barrier to phase separation. Spinodal decomposition (i.e. rapid growth and coalescence of phase separated solute clusters) occurs spontaneously throughout the solution when solute is generated in excess of the spinodal.[190] These initial solute clusters and their aggregation behavior may explain some of the aberrant light scattering observed that was not inversely proportional to wavelength under certain reaction conditions (Figure 47). Furthermore, DZP and MDZ precipitates displayed different aggregation behaviors (Figure 48). Experiments such as measuring the changes in the particle count and size distributions by dynamic light scatting as a function of time for different rates of solute production, measurements of zeta potential to characterize the tendency for the clusters of different drugs to coalesce or flocculate during spinodal decomposition, and cryogenic transmission electron microscopy of the initial stages of spinodal decomposition could be useful to characterize this process and identify the physiochemical properties that control it.

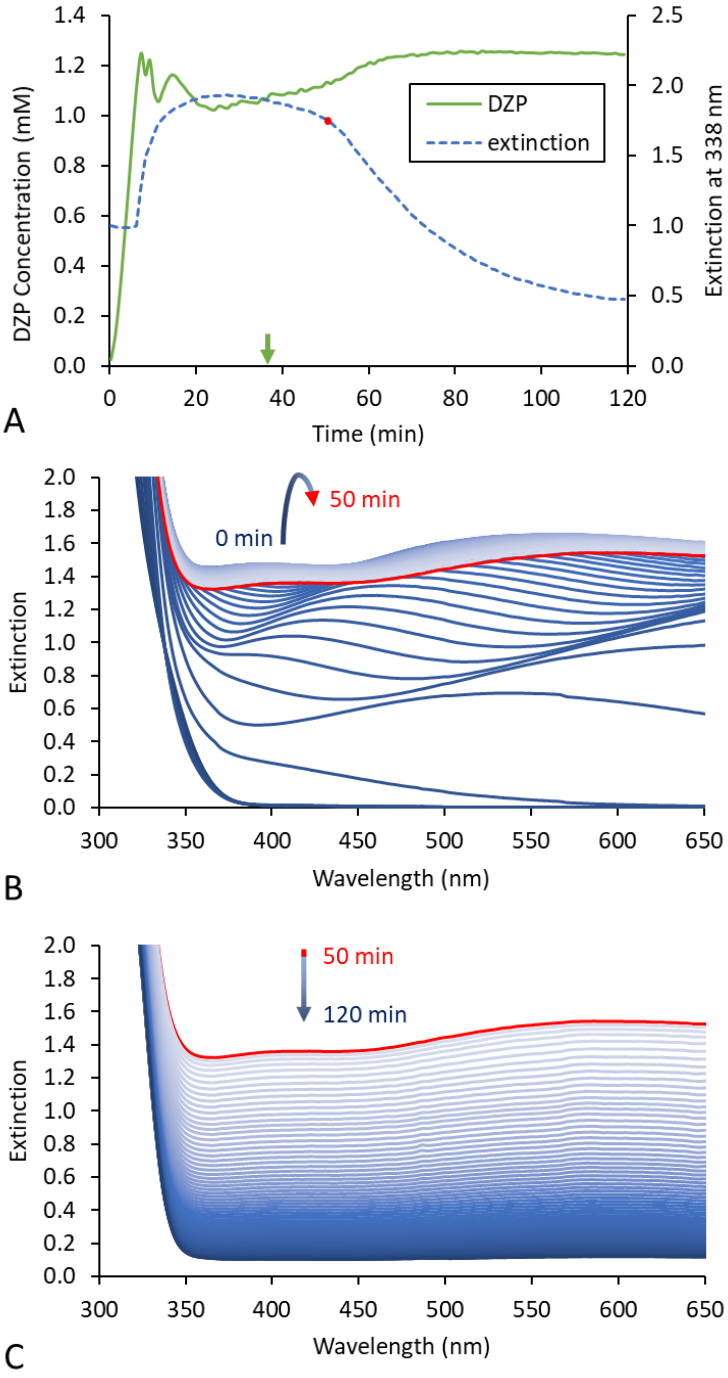

Figure 47. Evolution of light scatting from a high concentration reaction. Reaction conditions: 3.90 mM AVF, 0.25 U/mL AOP, pH 7.4 PBS, 32 ºC. (**A**) DZP solution state concentration-time profile (green line) as determined by second derivative spectroscopy overlaid with corresponding extinction-time profile (blue dashes). Green arrow marks approximate time of reaction completion (98% conversion of $[AVF]_0$ to DZP at t = 35.3

min). Red point marks t = 50 min, corresponding to the time point of the red colored spectrum shown in B and C. (**B**) Spectra of reaction measured from t = 0 to 50 min, 1 scan/min. Precipitate particle formation, growth, and aggregation. (**C**) Spectra of reaction measured from t = 50 to 120 min, 1 scan/min. Precipitate settling.

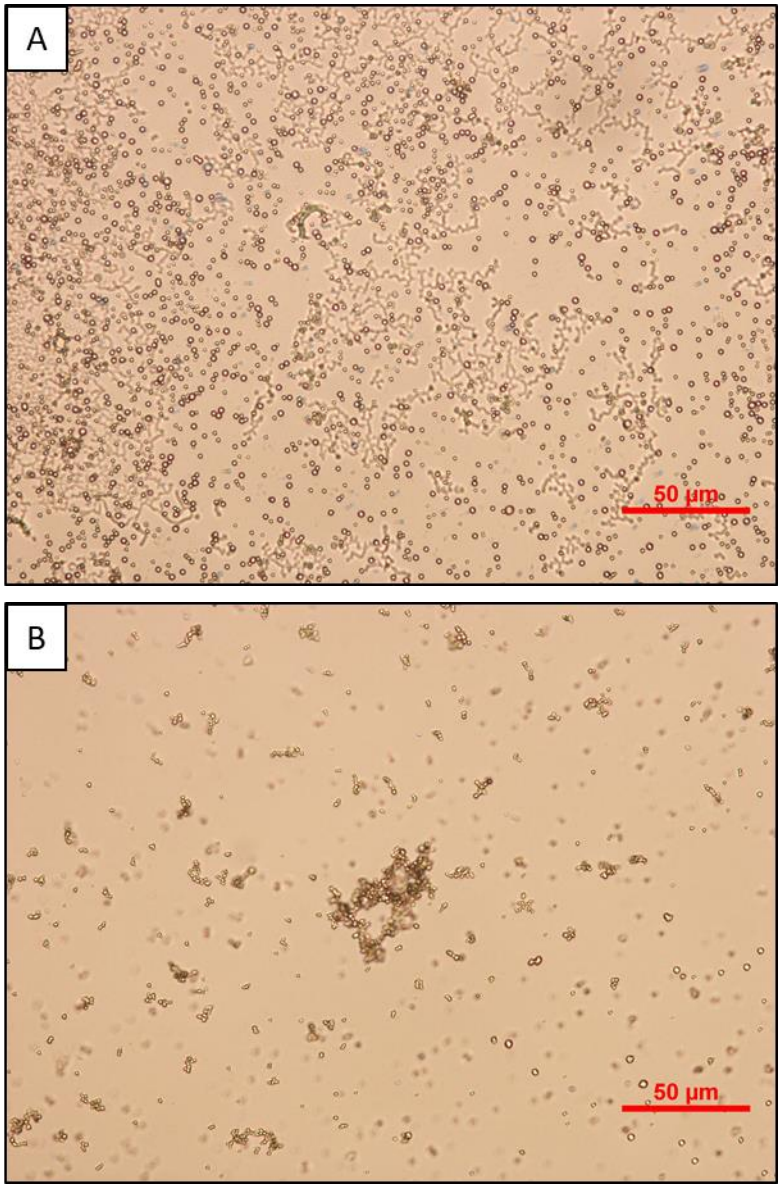

Figure 48. Microscope images of precipitate. (**A**) Ramified aggregation of DZP precipitate particles. Behavior is typically associated with a fast or diffusion limited aggregation regime.[191] Image captured 60 min after combining AVF and AOP in pH 7.4

PBS. (**B**) Compact clustering of MDZ precipitate particles. Behavior is typically associated with a slow or reaction limited aggregation regime.[191] Image captured 20 min after combining solutions of MDZ_{open}•2HCl and NaOH.

7.2 *In vivo* versus *in vitro* supersaturation limits

A much higher limit of DZP supersaturation was inferred from fitting the PBPK model to plasma concentration-time in the *in vivo* rat study ($C_{DZP,lim}$ = 20.8 ± 3.1 mM ±SE, Chapter 3) compared to *in vitro* measurements ($C_{DZP,lim}$ = 1.22 ± 0.03 mM ±SD in PBS, Chapter 2). Some data has been collected suggesting that higher limits of supersaturation can be obtained in different media, such as the in the presence of albumin (Appendices A1, Figure A1.61). In addition to lipids, nasal mucus contains proteins such as mucin, albumin, immunoglobulins, lysozyme, and lactoferrin. Thus, protein binding may play a role in the higher limit that was observed *in vivo*. Testing the two-part reactive drug formulations in simulated nasal mucus would help gauge the influence of the matrix on the upper limit of supersaturation. Recipes for simulated nasal mucus can be found in references [192] and [193]. If the upper limit of supersaturation cannot be increased in simulated mucus as dramatically as the *in vivo* data suggests, then another possibility for the apparently high *in vivo* value for the upper limit of supersaturation could be overestimation due to transport of DZP across the nasal mucosa directly from the phase separated DZP. The PBPK model in Chapter 3 assumes that only DZP in the solution phase is absorbed. Reconciling the discrepancy between the *in vivo* and *in vitro* determinations of $C_{DZP,lim}$ would help make predictive PK models more accurate for DZP as well as other supersaturating drug delivery systems.

7.3 Propensity to crystalize

In vitro, MDZ was observed to have a greater tendency to crystallize compared to DZP. A series of physiochemical characterization experiments to measure differences in mobility and lattice stacking interactions between these molecules would likely explain why MDZ crystalizes more readily, but the more interesting question would be whether or not MDZ crystallization would be slowed or even non-existent when supersaturated solutions are created in a biological system. A difference in the propensity of MDZ to crystalize in buffer versus a biological medium would be relativity easy to test using the simulated nasal mucus recipes mentioned in Section 7.2.

When attempting to measure crystal nucleation frequency and growth rates, the method used to generate the supersaturated state may be important. We have observed a greater tendency for crystallization from supersaturated solutions created by a solvent shift method compared to a prodrug/enzyme reaction method. It may be that the protein in the prodrug/enzyme reaction has some crystallization inhibiting effect, or it could be that creating supersaturation by a solvent shift offers more opportunity for crystal nucleation from very high concentration spikes during the mixing process. If crystallization proceeds in nasal mucus, then the crystallization observed with the MDZ formulations (albeit slow and sporadic) may not be negligible. The fraction of the dose sequestered in the crystalline phase within the timeframe of mucociliary should be quantified to assess the potential impact on the bioavailability of MDZ delivered intranasally via a two-part reactive formulation.

7.4 Absorption of ORI

All of the prodrugs and precursors used in our studies were derived from open diazepine ring structures of the parent benzodiazepines. There are reasons why creating an intermediate species in the pathway from precursor to active drug may be desirable, and there are reasons why avoiding the creation of an intermediate may be desirable. The ORI species of DZP and MDZ are able to permeate membranes (the ORI of MDZ to a lesser extent than the ORI of DZP), and they are more soluble than the closed ring DZP and MDZ drugs. Therefore, higher concentrations of the ORI can be created in the two-part reactive formulations compared to the insoluble parent drugs that quickly reach an upper limit of supersaturation and subsequently phase separate. The high concentration of accumulated ORI, hence high driving force for absorption across membranes, may lead to faster delivery of drug into the body than could be achieved if the active drug was the only permeating species. The absorption rate advantage of these two-part formulations can be evaluated though modeling since estimates of the ORI permeability coefficients can be obtained from Transwell drug transport studies: MDZ_{open} $P_{app} = 1.45 \pm 0.64 \times 10^5$ cm/s (Table 4) and ORI of DZP $P_{app} = 5.54 \pm 2.07 \times 10^5$ cm/s (unpublished data) across MDCKII-wt cell monolayers at pH 7.4 and 32 ^{o}C. External and internal exposure to ORI also depends on the ring closing rates in the respective biological media, i.e. cyclization rates should be characterized in nasal mucus mixed with the drug formulation as well as in blood to more accurately predict the time course of ORI and active drug in the body. Although the exposure to ORI is expected to be short, it would be prudent to assess its toxicity.

7.5 Cytotoxicity

The high concentrations of ORI that can accumulate in the nasal cavity and potential for ORI to enter the body beg the question of whether or not the ORI species are toxic. There are a variety of software tools commercially available for the prediction of Absorption, Distribution, Metabolism, Excretion, and Toxicity (ADMET) properties. These tools offer a starting point to help identify potential mechanisms of toxicity, thereby aiding in the design of *in vitro* experiments to quantify toxic effects or selection of tissues/biomarkers to examine for signs of toxicity in *in vivo* studies.

In Transwell drug transport studies, we observed a reduction in the confluency MDCKII-wt cell monolayers exposed to the DZP and MDZ two-part formulations for long periods of time (~2 hr). Confluency was assessed by comparing transepithelial electrical resistance (TEER) measurements before and after treatment, and by measuring dye permeability at the conclusion of the experiments. It should be noted that a 2 hr timeframe is not physiologically relevant considering the rate of mucociliary clearance and continual reduction in direct exposure to the nasal epithelium from dilution, conversion, and transport *in vivo*. However, cell monolayer toxicity data does provide some indication of the limits of exposure that can lead to compromised membranes.

Figure 49 shows representative images of live/dead staining of epithelial cell monolayers grown in tissue culture plates after exposure to permutations of the MDZ two-part reactive formulation. The cells were then exposed to 200 µL of each treatment. The treatment groups for experiments performed at pH 7.4 were: PBS only, 1.00 mM MDZ_{open}•2HCl solution that was admixed in PBS immediately before exposure, and 1.00 mM supersaturated solution of MDZ that was created by admixing MDZ_{open}•2HCl with

PBS 1 hr before exposure. The treatment groups for experiments performed at pH 5.5 were: CBS only, 1.00 mM MDZ_{open}•2HCl solution that was admixed in CBS at immediately before exposure, 1.00 mM Phe-MDZ_{pro} in CBS, 1.00 mM Phe-MDZ_{pro} with 200 ug/mL APN in CBS admixed immediately before exposure, and 1.00 mM supersaturated solution of MDZ that was created by admixing MDZ_{open}•2HCl and CBS 1 hr before exposure. After exposing the cells for 30 min at 32 °C on a 150 rpm orbital shaker, the treatment solutions were removed, and cell survival was assessed by live/dead staining using acetoxymethyl calcein (Calcein AM) live cell stain and ethidium homodimer-1 (EthD-1) dead cell stain. The results indicated that the cells remained viable after 30 min exposure in all treatment groups. The monolayers did become damaged with exposures longer than 1 hr. However, the residence time for the drug formulation in the nasal cavity is expected to be less than 30 min due to MDZ permeation through nasal epithelium and mucociliary clearance of any remaining formulation components. The formulation is likely to be well tolerated, though more extensive histology and toxicity studies should be performed.

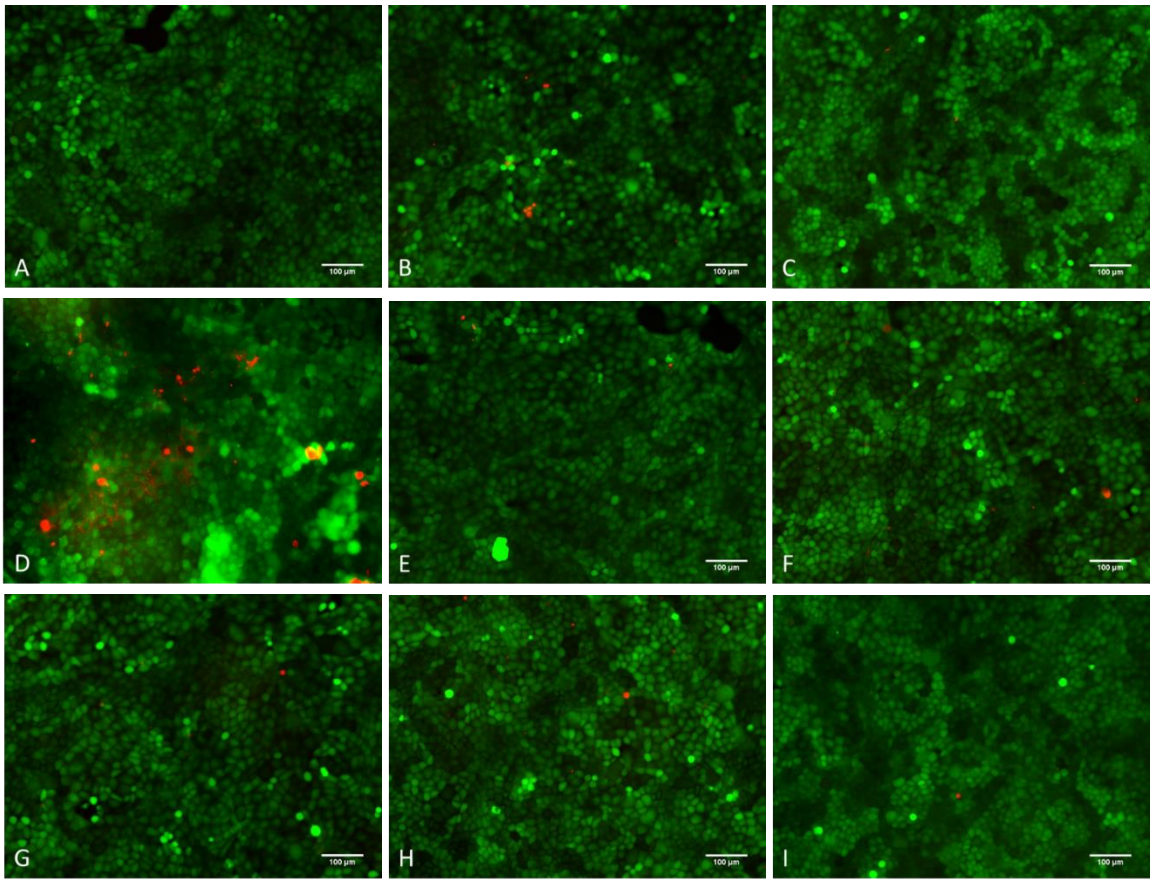

Figure 49. Fluorescence images of MDCKII-wt cells exposed to MDZ formulations. Green color indicates live cells; red color indicates dead cells. Exposure duration was 30 min, except where indicated. Experiments at pH 7.4 were performed in PBS and pH 5.5 in CBS. Scale bar = 100 µm. (**A**) pH 7.4 PBS buffer only. (**B**) 1.00 mM MDZ_{open}•2HCl, pH 7.4. (**C**) 1.00 mM MDZ, pH 7.4, t = 30 min. (**D**) 1.00 mM MDZ, pH 7.4, t = 60 min. (**E**) ph 5.5 CBS only. (**F**) 1.00 mM MDZ_{open}•2HCl, pH 5.5. (**G**) 1.00 mM Phe-MDZ_{pro}, pH 5.5. (**H**) 1.00 mM Phe-MDZ_{pro} with 200 ug/mL APN, pH 5.5. (**I**) 1.00 mM MDZ, pH 5.5.

Flow cytometry could be used for more detailed quantification of live, dead, and injured cells. For example, red-flourescent C12-resorufin could be used to mark metabolically active (live) cells and green-flourescent SYTOX could be used to mark the nucleic acids released from late apoptotic and necrotic cells. Injured cells then would have

combined red and green fluorescence.[194] Or, the amount of lactate dehydrogenase released into the medium by the cells with damaged membranes can be used as a metric for cell injury. Lactate dehydrogenase is normally quantified using commercially available kits and a plate reader. The morphology and function of the cells after exposure could also be examined. Light microscopy can be used to determine if the cells maintain their shape or show abnormalities like crenation. Finally, any cytotoxicity observed may be temporary. Some of these techniques can also be used to determine if and when the cells recover after exposure.

7.6 Acid/base formulations

The acid/base formulation for MDZ that was described in Chapter 5 eliminates the need for an enzyme in the formulation. Enzymes require additional characterization, can be more challenging to stabilize, increase the cost of the drug product, may cause an immune response, and have potential for off target action. It is possible to make a DZP acid/base formulation, but creation of the DZP open ring salt is more challenging due to hydrolysis of the open ring structure at the low pH required to open the diazepine ring. However, the side products could be removed by purification of the salt or the salt could be obtained under milder conditions by convergent synthesis. A DZP acid/base formulation may be a better choice for a commercial product than a DZP prodrug enzyme formulation.

Acid/base reactions are exothermic. Some amount of heat evolution may be desirable. The ring closing rate of MDZ has been observed to be temperature dependent and follows standard Arrhenius reaction rate kinetics. Therefore, allowing temperature of

the formulation to quickly rise from room temperature to physiological temperature, or even a couple of degrees above physiological temperature, may result in more rapid delivery of MDZ. Too much heat generation would be undesirable, since it also has the potential to damage tissues and cause pain. The enthalpy change for the MDZ_{open}•2HCl + NaOH reaction could be quantified using calorimetry. Results from calorimetry experiments would help determine if the heat generated by this reaction is of any concern and allow for a more accurate prediction of the ring closing rate of MDZ_{open} in solutions that are concentrated to deliver a full dose intranasally.

7.7 Enzyme engineering

APB was found to be more effective at hydrolyzing Lys from AVF than from Lys-MDZ_{pro} (Figure 27). This difference in APB activity presents an opportunity to study substrate binding mechanisms in the active site of APB. By identifying the substrate-enzyme interactions responsible for binding and correctly positioning the substrate in the active site, it may be possible to modify the primary structure of APB so that it more readily accepts MDZ_{pro} as a substrate. Strategic amino acid substitutions in the active site could be guided by simulations of substrate docking into the 3D structure of APB. Currently, there is no experimentally determined 3D structure of APB available in the protein databanks because APB is difficult to crystalize.[195] Finding the right conditions (pH, temperature, cosolvents or other additives) can be accomplished with automated instrumentation that enables identification of the optimum crystallization conditions for biomolecules by high throughput, low volume, sample processing.

In lieu of a crystal structure, molecular modeling approaches can be used. APB has 37.2 % sequence identity with human leukotriene A4 hydrolase (LTA4H).[196] Both APB and LTA4H are members of the M1 peptidase family that encompasses zinc metalloenzymes with aminopeptidase activity. LTA4H has been crystalized, so its secondary and tertiary structure can be used as a template to model the 3D structure of APB. This approach has been used by researchers at the University of Paris to model rat APB (rAPB).[195] The catalytic domains of rAPB and LTA4H are similar with a Zn^{2+} catalytic site between two lobes, one α-helical and the other mixed α/β-helical. Binding of the substrate in the active site of rAPB positions the peptide bond of the substrate in proximity to the zinc cofactor (Figure 50). The carbonyl is polarized upon coordination to zinc, catalyzing cleavage of the peptide bond by nucleophilic substitution with water present in the active site.

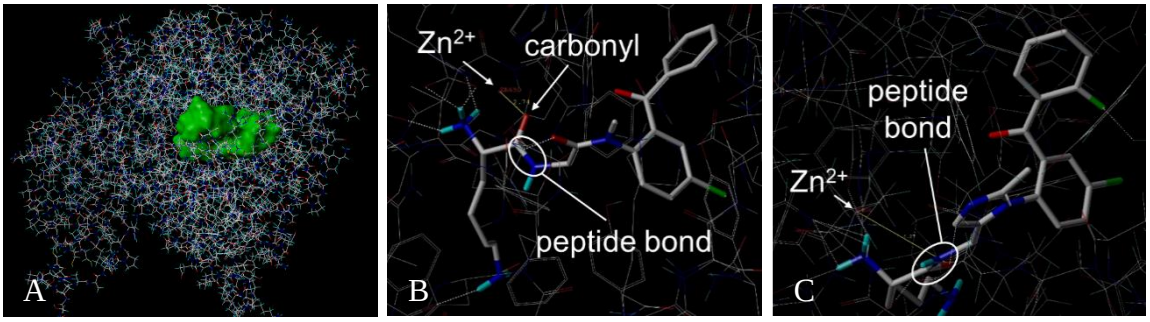

Figure 50. Docking of AVF and MDZ_{pro} into active site of rAPB. (**A**) Expanded view of rAPB stick model with active sight highlighted in green. (**B**) Close-up of AVF docked in the active site of rAPB. Surflex docking score: 12.6, distance between Zn^{2+} and carbonyl: 2.74 Å. (**C**) Close-up of Lys-MDZ_{pro} docked in the active site of rAPB. Surflex docking score: 12.7, distance between Zn^{2+} and carbonyl: 4.27 Å.

Preliminary docking studies were performed using Tripos SYBYL Surflex-Dock v. 2.1 software and the inferred rAPB enzyme structure from reference.[195] AVF and Lys-MDZ_{pro} had similar docking scores. The docking score is related to binding affinity where higher scores indicate stronger affinity. These scores indicated that both prodrugs have good affinity for the active site. However, the carbonyl at the reactive site of Lys-MDZ_{pro} was further away from the zinc atom, suggesting the positioning of Lys-MDZ_{pro} in the active site was preventing coordination to zinc. Residues Gln-169, Phe-297, Asp-406 of human APB have been shown to be involved in substrate recognition.[76,77] Docked Lys-MDZ_{pro} could be checked for favorable interactions with these residues. Unlike AVF, Lys-MDZ_{pro} has an additional basic moiety (the imidazole ring). Interactions of residues in the active site with imidazole is the most likely cause of poor substrate positioning and inactivity. One or two strategic amino acid substitutions to reposition the imidazole may lead to APB activity towards Lys-MDZ_{pro}.

7.8 Scale-up for prodrug/enzyme formulations

Experiments with the prodrug/enzyme formulations aimed at determining the Michaelis-Menten enzyme kinetics parameters, measuring *in vitro* drug transport across cell monolayers, and characterizing the precipitation behavior of drug from supersaturated solutions were performed at low concentrations relative to the concentrations that would be used to deliver a full dose to humans. The behavior of the system can change when the concentrations are scaled-up to human doses.

For example, high concentration solutions of AVF•2HCl (on the order of decimolar) are very acidic. Using a separate buffering agent to control the pH is unreasonable for the formulation since the amount of the buffering agent required would be excessive. Fortunately, AVF has a pK_a that enables the Lys moiety of the prodrug to be utilized as the buffering agent (Appendices A3, Figure A3.74). High concentration solutions of AVF titrated to pH 7.4 have been observed to drift to a more acidic pH upon storage. In turn, the pH drift was observed to affect the conversion rates to DZP when APB was added to these AVF solutions. It is important to allow adequate time for solutions of AVF to reach pH equilibrium during the titration unit operation of manufacturing. Additionally, it is important to ensure that enzyme co-factors such a Zn and Cl ions are sufficiently abundant in the formulation to maintain optimum enzyme activity.

Chapter 4 discusses a formulation stagey that entails combining AVF and APB into a single lyophilizate to stabilize APB, stabilize AVF, and ensure a homogeneous ratio of AVF:APB upon reconstitution and deposition in the nasal cavity. In order to achieve rapid dissolution of AVF and avoid clogging in the spray device atomizer orifice, the lyophilizate must have very high surface area. Sample C in Figure 51 shows a collapsed cake that was produced from lyophilizing an aqueous solution of AVF•2HCl with no other additives. Dissolution of this sample was slow due to the low surface area of the material. Adding a bulking agent and/or optimizing the lyo-cycle to produce more elegant cakes can vastly improve the rate of dissolution. Incidentally, AVF titrated to pH 7.4 produces more elegant cakes than un-titrated solutions of AVF•2HCl.

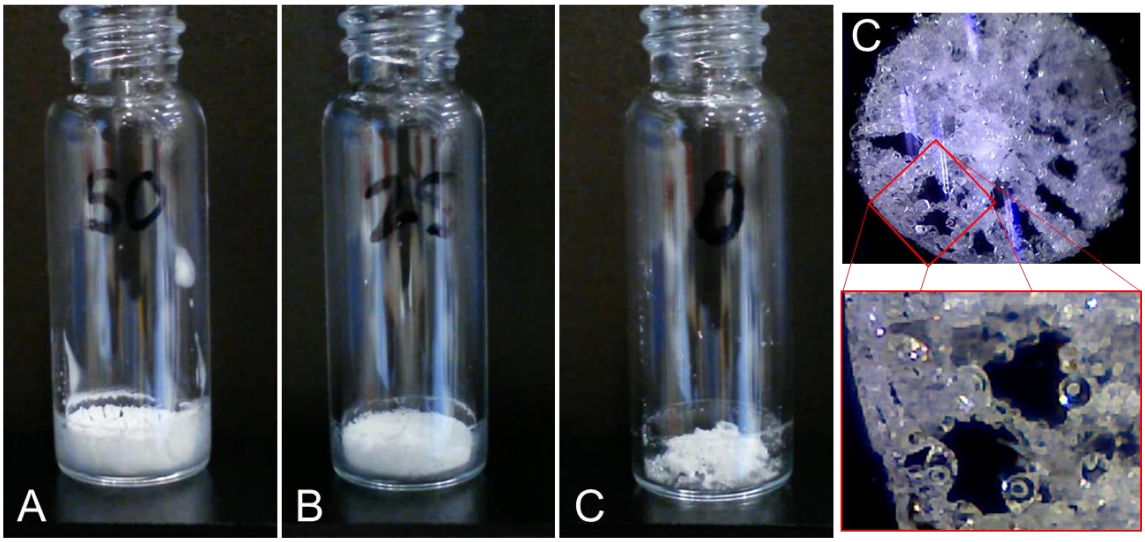

Sample	Man (mg/mL)	AVF (mM)	Volume (mL)	AVF (mg)	Man (mg)	Man sol. (% w/w)
A	50	176	0.200	17.7	10.0	50
B	25	176	0.200	17.7	5.00	33
C	0	176	0.200	17.7	0	0

Figure 51. Mannitol prevents AVF lyophilizate cake collapse. Adding the bulking agent, mannitol (man), to pre-lyophilization solutions helps to prevent the collapse of AVF cakes and improves the rate of dissolution.

7.9 Delivery device optimization

Nasal sprays have been shown to provide a more uniform distribution of drug on the nasal epithelium and lead to a slower, more consistent rate of mucociliary clearance compared to nose drops.[197,198] Preliminary testing of the dual chamber nasal spray device described in Chapter 6 has demonstrated that rapid mixing and atomization for intranasal co-administration of two-part reactive formulations is feasible. There are many other conceivable ways to automate low volume mixing and atomization in a nasal spray device. An example of an alternative design that incorporates check valves to separate solid and

liquid components prior to actuation is shown in Figure 52. Ultimately, it will be necessary to settle on a design that performs well and is user friendly.

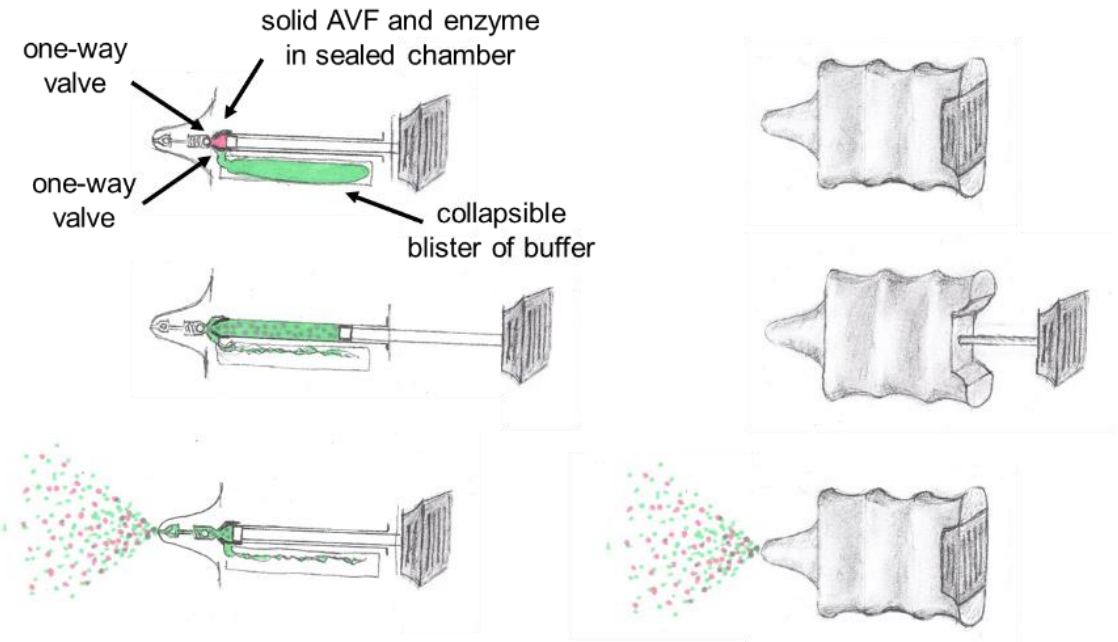

Figure 52. Alternative nasal spray device design. In this design, there is a one-way check valve between the chambers containing the components of the two-part reactive formulation. Pulling the plunger draws solution into the main barrel of the device and allows the components of the formulation to mix. Pushing the plunger back into the body of the device forces the mixed formulation through the atomizer tip to produce a spray. Note that the action of this device could be wholly or partially automated with a spring and trigger mechanism.

The total area of formulation deposition in the nasal cavity and distribution of the formulation over over ciliated versus non-ciliated nasal mucosa cells can influence the drug absorption rate and rate. Designing a device that deposits the formulation in an area of the nasal cavity conducive to optimum absorption depends, in part, on controlling the spray plume characteristics such as droplet size, diameter of the cone at a break-up length, and

cone angle.[178] The device design and physicochemical properties of the formulation, such as viscosity, dictate these characteristics.[45] The effect of device design and formulation parameters on spray characteristics could be investigated using standard imaging techniques such as particle/droplet image analysis (PDIA) and particle image velocimetry (PIV).

The homogeneity of the sprayed mixtures will also need to be well characterized to ensure full and rapid conversion to the active drug in the nasal cavity. A crude method for assessing the homogeneity of sprayed acid/base formulations was demonstrated in Figure 43. That method is qualitative, relying on changes in pH to visualize mixing of the formulation components. Testing prodrug/enzyme formulations would require a different technique. A quantitative way to assess the homogeneity of prodrug/enzyme formulations could involve spraying the formulation on a microtiter plate and monitoring wavelengths corresponding to product formation. The matrix arrangement of microtiter plates allows for spatial mapping of the deposition profile and identification of areas that have variable benzodiazepine concentration and/or result in precipitation of the benzodiazepine. An alternative to the microtiter plate method for analyzing mixing and deposition involves the use of dyes. Lys-*para*-nitroaniline (Lys-*p*NA) is a chromogenic substrate for both AOP and APB. Enzymatic hydrolysis of Lys-*p*NA releases the fluorescent chromophore para-nitroaniline (*p*NA) with a visible absorbance and emission peaks. The deposition profile for the enzyme can be visualized by spraying an enzyme-only formulation onto the surface of a native agarose or polyacrylamide gel that is impregnated with Lys-*p*NA.[60] Regions of high concentrations of active enzyme will fluoresce from the pNA reaction product. A

second chromophore or fluorophore could be included in the liquid phase of the formulation. This would allow spatial visualization (on a gel) or spatial quantification (with a microtiter plate reader) of the distribution of the liquid phase overlaid with the distribution of active enzyme.

Chapter 8: Conclusion

Systemic drug delivery by intranasal administration has been gaining popularity in recent years because the route offers a host of advantages that cannot be achieved by other routes. Dense capillary beds and thin epithelium in the nasal cavity allow drugs to quickly enter the blood stream, leading to a rapid onset of therapeutic effect. There is even potential for drugs targeting the central nervous system to bypass the blood brain barrier through direct nose-to-brain pathways. The intranasal route can be leveraged to avoid first-pass metabolism or degradation of drugs in the gut. Furthermore, operation of a nasal spray device is generally intuitive. Nasal sprays are non-invasive, convenient, and discrete, making the intranasal route of drug administration preferable to many patients.

However, not all drugs are amenable to formulation as a rapid acting nasal spray. Drugs with poor aqueous solubility or poor solution stability are often not even considered for formulation as a nasal spray. This may soon change with the introduction of reactive nasal spray formulations. Here we have demonstrated that highly effective metastable formulations can be created at the time of administration using a two-part formulation strategy. For these formulations, the reactive components are stored in separate compartments within a specially engineered nasal spray device. The components are metered, mixed, and atomized during actuation of the device.

One of the primary examples of this two-part reactive nasal spray formulation strategy we presented utilizes a highly soluble prodrug of an insoluble active drug and an exogenous enzyme to efficiently convert the prodrug into the active drug. The prodrug and labile enzyme can be stabilized for storage in the device as a homogeneously mixed solid lyophilizate. When a patient or caregiver actuates the device, the solid lyophilizate is

automatically reconstituted with buffer and simultaneously atomized into a spray. In the nasal cavity, the deposited droplets containing prodrug and enzyme react to produce a metastable supersaturated solution of the active drug. The active drug is then rapidly absorbed into the body. Other reactive nasal spray formulations utilize acid/base chemistry, click chemistry, and even simple non-reactive physical phase changes. This two-part formulation strategy to create metastable solutions of drug at the time of administration will enable many life-saving therapies that might not otherwise be possible.

Bibliography

1. Fisher RS, Acevedo C, Arzimanoglou A, Bogacz A, Cross JH, Elger CE, Engel Jr J, Forsgren L, French JA, Glynn M 2014. ILAE official report: a practical clinical definition of epilepsy. Epilepsia 55(4):475-482.

2. Pellock JM 2007. Overview: definitions and classifications of seizure emergencies. Journal of Child Neurology 22(5 suppl):9S-13S.

3. Trinka E, Cock H, Hesdorffer D, Rossetti AO, Scheffer IE, Shinnar S, Shorvon S, Lowenstein DH 2015. A definition and classification of status epilepticus–Report of the ILAE Task Force on Classification of Status Epilepticus. Epilepsia 56(10):1515-1523.

4. Dham BS, Hunter K, Rincon F 2014. The epidemiology of status epilepticus in the United States. Neurocrit Care 20:476-483.

5. Komaragiri A, Detyniecki K, Hirsch L 2015. Seizure clusters: A Common, understudied and undertreated phenomenon in refractory epilepsy. Epilepsy Behav 59:83-86.

6. DeLorenzo R, Hauser W, Towne A, Boggs J, Pellock J, Penberthy L, Garnett L, Fortner C, Ko D 1996. A prospective, population-based epidemiologic study of status epilepticus in Richmond, Virginia. Neurology 46(4):1029-1035.

7. Sutter R, Kaplan PW, Rüegg S 2013. Outcome predictors for status epilepticus—what really counts. Nature Reviews Neurology 9(9):525-534.

8. Jordan K 1994. Status epilepticus. A perspective from the neuroscience intensive care unit. Neurosurgery Clinics of North America 5(4):671-686.

9. Freestone DR, Karoly PJ, Cook MJ 2017. A forward-looking review of seizure prediction. Current Opinion in Neurology 30(2):167-173.

10. Glauser T, Shinnar S, Gloss D, Alldredge B, Arya R, Bainbridge J, Bare M, Bleck T, Dodson WE, Garrity L 2016. Evidence-based guideline: treatment of convulsive status epilepticus in children and adults: report of the guideline committee of the American Epilepsy Society. Epilepsy Currents 16(1):48-61.

11. Dreifuss FE, Rosman NP, Cloyd JC, Pellock JM, Kuzniecky RI, Lo WD, Matsuo F, Sharp GB, Conry JA, Bergen DC 1998. A comparison of rectal diazepam gel and placebo for acute repetitive seizures. New England Journal of Medicine 338(26):1869-1875.

12. Ivaturi V, Kriel R, Brundage R, Loewen G, Mansbach H, Cloyd J 2013. Bioavailability of intranasal vs. rectal diazepam. Epilepsy Research 103(2):254-261.

13. Spencer D 2014. Hope for new treatments for acute repetitive seizures. Epilepsy Currents 14(3):147-149.

14. Costantino HR, Illum L, Brandt G, Johnson PH, Quay SC 2007. Intranasal delivery: physicochemical and therapeutic aspects. International Journal of Pharmaceutics 337(1):1-24.

15. Fortuna A, Alves G, Serralheiro A, Sousa J, Falcão A 2014. Intranasal delivery of systemic-acting drugs: small-molecules and biomacromolecules. European Journal of Pharmaceutics and Biopharmaceutics 88(1):8-27.

16. Tong X, Dong J, Shang Y, Inthavong K, Tu J 2016. Effects of nasal drug delivery device and its orientation on sprayed particle deposition in a realistic human nasal cavity. Computers in Biology and Medicine 77:40-48.

17. Kundoor V, Dalby RN 2010. Assessment of nasal spray deposition pattern in a silicone human nose model using a color-based method. Pharmaceutical Research 27(1):30.

18. Rygg A, Hindle M, Longest PW 2016. Linking Suspension Nasal Spray Drug Deposition Patterns to Pharmacokinetic Profiles: A Proof-of-Concept Study Using

Computational Fluid Dynamics. Journal of Pharmaceutical Sciences 105(6):1995-2004.

19. Illum L 2003. Nasal drug delivery—possibilities, problems and solutions. Journal of Controlled Release 87(1):187-198.

20. Gizurarson S 2012. Anatomical and histological factors affecting intranasal drug and vaccine delivery. Current Drug Delivery 9(6):566-582.

21. Guilmette R, Cheng Y, Griffith W 1997. Characterising the variability in adult human nasal airway dimensions. The Annals of Occupational Hygiene 41:491-496.

22. Kublik H, Vidgren M 1998. Nasal delivery systems and their effect on deposition and absorption. Advanced Drug Delivery Reviews 29(1):157-177.

23. Liu Y, Johnson MR, Matida EA, Kherani S, Marsan J 2009. Creation of a standardized geometry of the human nasal cavity. Journal of Applied Physiology 106(3):784-795.

24. Arora P, Sharma S, Garg S 2002. Permeability issues in nasal drug delivery. Drug Discovery Today 7(18):967-975.

25. Beule AG 2010. Physiology and pathophysiology of respiratory mucosa of the nose and the paranasal sinuses. Laryngorhinootologie 89(Suppl 1):S15-S34.

26. Grassin-Delyle S, Buenestado A, Naline E, Faisy C, Blouquit-Laye S, Couderc L-J, Le Guen M, Fischler M, Devillier P 2012. Intranasal drug delivery: an efficient and non-invasive route for systemic administration: focus on opioids. Pharmacology & Therapeutics 134(3):366-379.

27. Inokuchi R, Ohashi-Fukuda N, Nakamura K, Wada T, Gunshin M, Kitsuta Y, Nakajima S, Yahagi N 2015. Comparison of intranasal and intravenous diazepam on status epilepticus in stroke patients: a retrospective cohort study. Medicine 94(7).

28. Kapoor M, Winter T, Lis L, Georg GI, Siegel RA 2014. Rapid delivery of diazepam from supersaturated solutions prepared using prodrug/enzyme mixtures: toward intranasal treatment of seizure emergencies. The AAPS Journal 16(3):577-585.

29. Kälviäinen R 2015. Intranasal therapies for acute seizures. Epilepsy & Behavior 49:303-306.

30. Sperling MR, Haas KF, Krauss G, Seif Eddeine H, Henney HR, Rabinowicz AL, Bream G, Squillacote D, Carrazana EJ 2014. Dosing feasibility and tolerability of intranasal diazepam in adults with epilepsy. Epilepsia 55(10):1544-1550.

31. Buck ML 2013. Intranasal Administration of Benzodiazepines for the Treatment of Acute Repetitive Seizures in Children. Pediatr Pharm 19(10).

32. Marx D, Williams G, Birkhoff M. 2015. Intranasal drug administration—An attractive delivery route for some drugs. Drug Discovery and Development-From Molecules to Medicine, ed.: IntechOpen.

33. Bitter C, Suter-Zimmermann K, Surber C. 2011. Nasal drug delivery in humans. Topical Applications and the Mucosa, ed.: Karger Publishers. p 20-35.

34. Kapoor M, Cloyd JC, Siegel RA 2016. A review of intranasal formulations for the treatment of seizure emergencies. Journal of Controlled Release 237:147-159.

35. De Haan GJ, Van Der Geest P, Doelman G, Bertram E, Edelbroek P 2010. A comparison of midazolam nasal spray and diazepam rectal solution for the residential treatment of seizure exacerbations. Epilepsia 51(3):478-482.

36. Buck ML 2013. Intranasal administration of benzodiazepines for the treatment of acute repetitive seizures in children. Pediatric Pharmacotherapy 19(10).

37. Agarwal SK, Kriel RL, Brundage RC, Ivaturi VD, Cloyd JC 2013. A pilot study assessing the bioavailability and pharmacokinetics of diazepam after intranasal and

intravenous administration in healthy volunteers. Epilepsy Research 105(3):362-367.

38. Theeuwes F, Gale RM, Baker RW 1976. Transference: a comprehensive parameter governing permeation of solutes through membranes. Journal of Membrane Science 1:3-16.

39. Hou H, Siegel RA 2006. Enhanced permeation of diazepam through artificial membranes from supersaturated solutions. Journal of Pharmaceutical Sciences 95(4):896-905.

40. Schrier L, Zuiker R, Merkus FW, Klaassen ES, Guan Z, Tuk B, Gerven J, Geest R, Groeneveld GJ 2017. Pharmacokinetics and pharmacodynamics of a new highly concentrated intranasal midazolam formulation for conscious sedation. British Journal of Clinical Pharmacology 83(4):721-731.

41. Jornada DH, dos Santos Fernandes GF, Chiba DE, de Melo TRF, dos Santos JL, Chung MC 2015. The prodrug approach: a successful tool for improving drug solubility. Molecules 21(1):42.

42. Kapoor M, Cheryala N, Rautiola D, Georg GI, Cloyd JC, Siegel RA 2016. Chirally pure prodrugs and their converting enzymes lead to high supersaturation and rapid transcellular permeation of benzodiazepines. Journal of Pharmaceutical Sciences 105(8):2365-2371.

43. Kapoor M, Siegel RA 2013. Prodrug/enzyme based acceleration of absorption of hydrophobic drugs: an in vitro study. Molecular Pharmaceutics 10(9):3519-3524.

44. Benfield J, Musto A 2018. Intranasal therapy to stop status epilepticus in prehospital settings. Drug R D 18:7-17.

45. Dayal P, Shaik MS, Singh M 2004. Evaluation of different parameters that affect droplet-size distribution from nasal sprays using the Malvern Spraytec®. Journal of Pharmaceutical Sciences 93(7):1725-1742.

46. Hassall C, Holmes S, Johnson W, Kröhn A, Smithen C, Thomas W 1977. Peptido-aminobenzophenones-novel latentiated benzo-1, 4-diazepines. Experientia 33(11):1492-1493.

47. Wermuth CG. 2008. Preparation of water-soluble compounds by covalent attachment of solubilizing moieties. The Practice of Medicinal Chemistry (Third Edition), ed.: Elsevier. p 767-785.

48. Masahiro N, Nobuo I, Naonori K, Takaichi A 1979. Reversible ring-opening reaction of diazepam in acid media around body temperature. International Journal of Pharmaceutics 3(4-5):195-204.

49. Siegel RA, Kapoor M, Cheryala N, Georg GI, Cloyd JC 2015. Water-soluble benzodiazepine prodrug/enzyme combinations for intranasal rescue therapies. Epilepsy & Behavior 49:347-350.

50. Sun DD, Lee PI 2015. Haste makes waste: the interplay between dissolution and precipitation of supersaturating formulations. The AAPS Journal 17(6):1317-1326.

51. Ozaki S, Minamisono T, Yamashita T, Kato T, Kushida I 2012. Supersaturation–nucleation behavior of poorly soluble drugs and its impact on the oral absorption of drugs in thermodynamically high-energy forms. Journal of Pharmaceutical Sciences 101(1):214-222.

52. Mosquera-Giraldo LI, Taylor LS 2015. Glass–liquid phase separation in highly supersaturated aqueous solutions of telaprevir. Molecular Pharmaceutics 12(2):496-503.

53. Deneau E, Steele G 2005. An in-line study of oiling out and crystallization. Organic Process Research & Development 9(6):943-950.

54. Lindemann J, Leiacker R, Rettinger G, Keck T 2002. Nasal mucosal temperature during respiration. Clinical Otolaryngology & Allied Sciences 27(3):135-139.

55. Washington N, Steele R, Jackson S, Bush D, Mason J, Gill D, Pitt K, Rawlins D 2000. Determination of baseline human nasal pH and the effect of intranasally administered buffers. International Journal of Pharmaceutics 198(2):139-146.

56. O'Neil MJ. 2013. The Merck index: an encyclopedia of chemicals, drugs, and biologicals. ed.: RSC Publishing.

57. Srinarong P, Hämäläinen S, Visser MR, Hinrichs WL, Ketolainen J, Frijlink HW 2011. Surface-active derivative of inulin (Inutec® SP1) is a superior carrier for solid dispersions with a high drug load. Journal of Pharmaceutical Sciences 100(6):2333-2342.

58. Van den Mooter G, Van den Brande J, Augustijns P, Kinget R 1999. Glass forming properties of benzodiazepines and co-evaporate systems with poly (hydroxyethyl methacrylate). Journal of Thermal Analysis and Calorimetry 57(2):493-507.

59. Yalkowsky SH, Valvani SC, Johnson BW 1983. In vitro method for detecting precipitation of parenteral formulations after injection. Journal of Pharmaceutical Sciences 72(9):1014-1017.

60. Merz M, Eisele T, Berends P, Appel D, Rabe S, Blank I, Stressler T, Fischer L 2015. Flavourzyme, an enzyme preparation with industrial relevance: automated nine-step purification and partial characterization of eight enzymes. Journal of Agricultural and Food Chemistry 63(23):5682-5693.

61. Sigma Aldrich Corporation. 2013. Composition of enzyme solution, Product P6110, Protease from Aspergillus oryzae., ed.

62. Pires DE, Blundell TL, Ascher DB 2015. pkCSM: predicting small-molecule pharmacokinetic and toxicity properties using graph-based signatures. Journal of Medicinal Chemistry 58(9):4066.

63. Pires D. 2017. pk Computer Simulated Method (pkCSM). http:// biosig.unimelb.edu.au/pkcsm/. ed.: University of Cambridge.

64. Riss J, Cloyd J, Gates J, Collins S 2008. Benzodiazepines in epilepsy: pharmacology and pharmacokinetics. Acta Neurologica Scandinavica 118(2):69-86.

65. Ilevbare GA, Taylor LS 2013. Liquid–liquid phase separation in highly supersaturated aqueous solutions of poorly water-soluble drugs: implications for solubility enhancing formulations. Crystal Growth & Design 13(4):1497-1509.

66. Murdande SB, Pikal MJ, Shanker RM, Bogner RH 2010. Solubility advantage of amorphous pharmaceuticals: I. A thermodynamic analysis. Journal of Pharmaceutical Sciences 99(3):1254-1264.

67. Almeida e Sousa L, Reutzel-Edens SM, Stephenson GA, Taylor LS 2014. Assessment of the amorphous "solubility" of a group of diverse drugs using new experimental and theoretical approaches. Molecular Pharmaceutics 12(2):484-495.

68. ChemAxon Ltd. 2016. JChem Suite: Structure-based predictions for molecules. https:// chemicalizecom/.

69. Mirski MA, Varelas PN 2008. Seizures and status epilepticus in the critically ill. Critical Care Clinics 24(1):115-147.

70. Haut SR, Seinfeld S, Pellock J 2016. Benzodiazepine use in seizure emergencies: a systematic review. Epilepsy & Behavior 63:109-117.

71. Maglalang PD, Rautiola D, Siegel RA, Fine JM, Hanson LR, Coles LD, Cloyd JC 2018. Rescue therapies for seizure emergencies: New modes of administration. Epilepsia 59:207-215.

72. Heller AH, Wargacki S, Jung C, Wyatt DJ, Bonnefois G, Tremblay P-O, Schobel AM 2018. Population Pharmacokinetic Modeling of Diazepam Buccal Soluble Film. Neurotherapeutics 15(3):819–835.

73. Bancke L, Dworak H, Halvorsen M 2013. pharmacokinetics, Pharmacodynamics, And Safety Of Three Doses Of Usl261, A Midazolam Formulation Optimized For Intranasal Administration: p178. Epilepsia 54:62.

74. Maggio ET, Pillion DJ 2013. High efficiency intranasal drug delivery using Intravail® alkylsaccharide absorption enhancers. Drug Delivery and Translational Research 3(1):16-25.

75. Rautiola D, Cloyd JC, Siegel RA 2018. Conversion of a soluble diazepam prodrug to supersaturated diazepam for rapid intranasal delivery: kinetics and stability. Journal of Controlled Release 289:1-9.

76. Ogawa Y, Ohnishi A, Goto Y, Sakuma Y, Watanabe J, Hattori A, Tsujimoto M 2014. Role of glutamine-169 in the substrate recognition of human aminopeptidase B. Biochimica et Biophysica Acta (BBA)-General Subjects 1840(6):1872-1881.

77. Ohnishi A, Watanabe J, Ogawa Y, Goto Y, Hattori A, Tsujimoto M 2015. Involvement of Phenylalanine 297 in the Construction of the Substrate Pocket of Human Aminopeptidase B. Biochemistry 54(39):6062-6070.

78. Banks WJ. 1993. Applied veterinary histology. ed.: Mosby-Year Book, Inc.

79. Boorman GE, SL; Elwell, MR; Montgomery, CA; MacKenzie, WF. 1990. Pathology of the Fischer rat: reference and atlas. ed., San Diego, CA: Acad. Press.

80. Mittal D, Ali A, Md S, Baboota S, Sahni JK, Ali J 2014. Insights into direct nose to brain delivery: current status and future perspective. Drug Delivery 21(2):75-86.

81. Igari Y, Sugiyama Y, Sawada Y, Iga T, Hanano M 1983. Prediction of diazepam disposition in the rat and man by a physiologically based pharmacokinetic model. Journal of Pharmacokinetics and Biopharmaceutics 11(6):577-593.

82. Gueorguieva II, Nestorov IA, Rowland M 2004. Fuzzy simulation of pharmacokinetic models: case study of whole body physiologically based model of diazepam. Journal of Pharmacokinetics and Pharmacodynamics 31(3):185-213.

83. Thompson MD, Beard DA, Wu F 2012. Use of partition coefficients in flow-limited physiologically-based pharmacokinetic modeling. Journal of Pharmacokinetics and Pharmacodynamics 39(4):313-327.

84. Jackson DC, Schmidt-Nielsen K 1964. Countercurrent heat exchange in the respiratory passages. Proceedings of the National Academy of Sciences 51(6):1192-1197.

85. Diaz-Garcia J, Oliver-Botana J, Fos DG 1991. Pharmacokinetics of diazepam in the rat: influence of an experimentally induced hepatic injury. European Journal of Drug Metabolism and Pharmacokinetics:94-101.

86. Igari Y, Sugiyama Y, Sawada Y, Iga T, Hanano M 1984. In vitro and in vivo assessment of hepatic and extrahepatic metabolism of diazepam in the rat. Journal of Pharmaceutical Sciences 73(6):826-828.

87. Upshall D, Gouldstone S, Macey N, Maidment M, Wast S, Yeadon M 1990. Conversion of a peptidoaminobenzophenone prodrug to diazepam in vitro. Enzyme isolation and characterisation. J Biopharm Sci 1:111-126.

88. Carter AA, Rosenbaum SE, Dudley MN 1995. Review of methods in population pharmacokinetics. Clinical Research and Regulatory Affairs 12(1):1-21.

89. Jusko WJ 2012. Use of pharmacokinetic data below lower limit of quantitation values. Pharmaceutical research 29(9):2628-2631.

90. Nedelman JR, Jia X 1998. An extension of satterth waite's approximation applied to pharmacokinetics. Journal of Biopharmaceutical Statistics 8(2):317-328.

91. Holder DJ 2001. Comments on Nedelman and Jia's extension of Satterthwaite's approximation applied to pharmacokinetics. Journal of Biopharmaceutical Statistics 11(1-2):75-79.

92. Dhir A, Rogawski MA 2018. Determination of minimal steady-state plasma level of diazepam causing seizure threshold elevation in rats. Epilepsia 59(5):935-944.

93. Rowland M, Leitch D, Fleming G, Smith B 1984. Protein binding and hepatic clearance: discrimination between models of hepatic clearance with diazepam, a drug of high intrinsic clearance, in the isolated perfused rat liver preparation. Journal of Pharmacokinetics and Biopharmaceutics 12(2):129-147.

94. Hussain MA, Seetharam R, Wilk RR, Aungst BJ, Kettner CA 1995. Nasal mucosal metabolism and absorption of pentapeptide enkephalin analogs having varying N-terminal amino acidss. Journal of Pharmaceutical Sciences 84(1):62-64.

95. Agu RU, Obimah DU, Lyzenga WJ, Jorissen M, Massoud E, Verbeke N 2009. Specific aminopeptidases of excised human nasal epithelium and primary culture: a comparison of functional characteristics and gene transcripts expression. Journal of Pharmacy and Pharmacology 61(5):599-606.

96. Sarkar MA 1992. Drug metabolism in the nasal mucosa. Pharmaceutical Research 9(1):1-9.

97. Gizurarson S 2015. The effect of cilia and the mucociliary clearance on successful drug delivery. Biological and Pharmaceutical Bulletin 38(4):497-506.

98. Donovan MD, Zhou M 1995. Drug effects on in vivo nasal clearance in rats. International Journal of Pharmaceutics 116(1):77-86.

99. Brooking J, Davis S, Illum L 2001. Transport of nanoparticles across the rat nasal mucosa. Journal of Drug Targeting 9(4):267-279.

100. Yao J, Yang J 2005. Predicting MDCK cell permeation coefficients of organic molecules using membrane-interaction QSAR analysis. Acta Pharmacologica Sinica 26(11):1322-1333.

101. Kang Y-M 2017. PreADMET. Yonsei Univversity Seoul, Republic of Korea https: //preadmetbmdrckr/.

102. Dhuria SV, Hanson LR, Frey WH 2010. Intranasal delivery to the central nervous system: mechanisms and experimental considerations. Journal of Pharmaceutical Sciences 99(4):1654-1673.

103. Kaur P, Kim K 2008. Pharmacokinetics and brain uptake of diazepam after intravenous and intranasal administration in rats and rabbits. International Journal of Pharmaceutics 364(1):27-35.

104. Singh R, Kumar M, Mittal A, Mehta PK 2016. Microbial enzymes: industrial progress in 21st century. 3 Biotech 6(2):174.

105. Carpenter JF, Izutsu K-i, Randolph TW. 2004. Freezing-and drying-induced perturbations of protein structure and mechanisms of protein protection by stabilizing additives. Freeze Drying/Lyophilization of Pharmaceutical and Biological Products, ed.: Marcel Dekker, Inc., New York. p 147-186.

106. Wang W 2000. Lyophilization and development of solid protein pharmaceuticals. International Journal of Pharmaceutics 203(1-2):1-60.

107. Pramanick S, Singodia D, Chandel V 2013. Excipient selection in parenteral formulation development. Pharma Times 45(3):65-77.

108. Rautiola D, Maglalang PD, Cheryala N, Nelson KM, Georg GI, Fine JM, Svitak AL, Faltesek KA, Hanson LR, Mishra U, Coles LD, Cloyd JC, Siegel RA 2019. Intranasal co-administration of a diazepam prodrug with a converting enzyme results in rapid absorption of diazepam in rats. Journal of Pharmacology and Experimental Therapeutics 370:796-805.

109. Kuwayama T, Kurono Y, Muramatsu T, Yashiro T, Ikeda K 1986. The Behavior of 1, 4-Benzodiazepine Drugs in Acidic Media. V.: Kinetics of Hydrolysis of Flutazolam and Haloxazolam in Aqueous Solution. Chemical and Pharmaceutical Bulletin 34(1):320-326.

110. Patel SM, Nail SL, Pikal MJ, Geidobler R, Winter G, Hawe A, Davagnino J, Gupta SR 2017. Lyophilized drug product cake appearance: what is acceptable? Journal of Pharmaceutical Sciences 106(7):1706-1721.

111. Scheer M, Grote A, Chang A, Schomburg I, Munaretto C, Rother M, Söhngen C, Stelzer M, Thiele J, Schomburg D 2010. BRENDA, the enzyme information system in 2011. Nucleic Acids Research 39(suppl_1):D670-D676.

112. Sanderink G-J, Artur Y, Siest G 1988. Human aminopeptidases: a review of the literature. Clinical Chemistry and Laboratory Medicine 26(12):795-808.

113. Thierry F, Sandrine C, Christophe P. 2004. Aminopeptidase B. Handbook of Proteolytic Enzymes, ed.: Elsevier. p 328-332.

114. Clair P, Wiberg K, Granelli I, Bratt IC, Blanchet G 2000. Stability study of a new antidote drug combination (Atropine–HI-6–Prodiazepam) for treatment of organophosphate poisoning. European Journal of Pharmaceutical Sciences 9(3):259-263.

115. Breton D, Buret D, Mendes-Oustric A, Chaimbault P, Lafosse M, Clair P 2006. LC–UV and LC–MS evaluation of stress degradation behaviour of avizafone. Journal of Pharmaceutical and Biomedical Analysis 41(4):1274-1279.

116. Nireesha G, Divya L, Sowmya C, Venkateshan N, Babu MN, Lavakumar V 2013. Lyophilization/freeze drying-an review. International Journal of Novel Trends in Pharmaceutical Sciences 3(4):87-98.

117. Mensink MA, Frijlink HW, van der Voort Maarschalk K, Hinrichs WL 2017. How sugars protect proteins in the solid state and during drying (review): mechanisms of

stabilization in relation to stress conditions. European Journal of Pharmaceutics and Biopharmaceutics 114:288-295.

118. Tonnis W, Mensink M, De Jager A, Van Der Voort Maarschalk K, Frijlink H, Hinrichs W 2015. Size and molecular flexibility of sugars determine the storage stability of freeze-dried proteins. Molecular Pharmaceutics 12(3):684-694.

119. Guo Q, He Y, Lu HP 2015. Interrogating the activities of conformational deformed enzyme by single-molecule fluorescence-magnetic tweezers microscopy. Proceedings of the National Academy of Sciences 112(45):13904-13909.

120. Siddiqui KS, Feller G, D'Amico S, Gerday C, Giaquinto L, Cavicchioli R 2005. The active site is the least stable structure in the unfolding pathway of a multidomain cold-adapted α-amylase. Journal of Bacteriology 187(17):6197-6205.

121. Lejeune A, Vanhove M, Lamotte-Brasseur J, Pain RH, Frère J-M, Matagne A 2001. Quantitative analysis of the stabilization by substrate of Staphylococcus aureus PC1 β-lactamase. Chemistry & Biology 8(8):831-842.

122. Daniel RM, Danson MJ 2010. A new understanding of how temperature affects the catalytic activity of enzymes. Trends in Biochemical Sciences 35(10):584-591.

123. Dai L, Klibanov AM 1999. Striking activation of oxidative enzymes suspended in nonaqueous media. Proceedings of the National Academy of Sciences 96(17):9475-9478.

124. Stewart NA, Taralp A, Kaplan H 1997. Imprinting of Lyophilized α-Chymotrypsin Affects the Reactivity of the Active-Site Imidazole. Biochemical and Biophysical Research Communications 240(1):27-31.

125. Kain ZN, Mayes LC, Bell C, Weisman S, Hofstadter MB, Rimar S 1997. Premedication in the United States: a status report. Anesthesia & Analgesia 84(2):427-432.

126. World Health Organization 2017. WHO model list of essential medicines, 20th list (March 2017, amended August 2017).

127. U.S. Food and Drug Administration. 2019. Orange Book: Approved Drug Products with Therapeutic Equivalence Evaluations. ed., Silver Spring, MD.

128. Strickley RG 2018. Pediatric Oral Formulations: An Updated Review of Commercially Available Pediatric Oral Formulations Since 2007. Journal of Pharmaceutical Sciences.

129. Loftsson T, Guðmundsdóttir H, Sigurjonsdottir J, Sigurðsson H, Sigfússon SD, Masson M, Stefansson E 2001. Cyclodextrin solubilization of benzodiazepines: formulation of midazolam nasal spray. International Journal of Pharmaceutics 212(1):29-40.

130. Wermeling DP, Record KA, Kelly TH, Archer SM, Clinch T, Rudy AC 2006. Pharmacokinetics and pharmacodynamics of a new intranasal midazolam formulation in healthy volunteers. Anesthesia & Analgesia 103(2):344-349.

131. Botner S, Sintov AC 2011. Intranasal delivery of two benzodiazepines, midazolam and diazepam, by a microemulsion system. Pharmacology & Pharmacy 2(03):180.

132. Desai S, Vidyasagar G, Bhandhari A 2012. Evaluation of brain-targeting for the nasal delivery of midazolam. Int J Pharm Sci Rev Res 12:109-113.

133. Haschke M, Suter K, Hofmann S, Witschi R, Fröhlich J, Imanidis G, Drewe J, Briellmann TA, Dussy FE, Krähenbühl S 2010. Pharmacokinetics and pharmacodynamics of nasally delivered midazolam. British Journal of Clinical Pharmacology 69(6):607-616.

134. Knoester P, Jonker D, Van der Hoeven R, Vermeij T, Edelbroek P, Brekelmans G, De Haan G 2002. Pharmacokinetics and pharmacodynamics of midazolam administered as a concentrated intranasal spray. A study in healthy volunteers. British Journal of Clinical Pharmacology 53(5):501-507.

135. Union Chimique Belge (UBC) 2018. FDA Accepts New Drug Application (NDA) to review Midazolam Nasal Spray, an investigational product for the acute treatment of seizure clusters. Press Release:HQ/0818/OTH/00090.

136. Payne K, Mattheyse F, Liebenberg D, Dawes T 1989. The pharmacokinetics of midazolam in paediatric patients. European Journal of Clinical Pharmacology 37(3):267-272.

137. Thummel KE, O'shea D, Paine MF, Shen DD, Kunze KL, Perkins JD, Wilkinson GR 1996. Oral first-pass elimination of midazolam involves both gastrointestinal and hepatic CYP3A-mediated metabolism. Clinical Pharmacology & Therapeutics 59(5):491-502.

138. Holsti M, Dudley N, Schunk J, Adelgais K, Greenberg R, Olsen C, Healy A, Firth S, Filloux F 2010. Intranasal midazolam vs rectal diazepam for the home treatment of acute seizures in pediatric patients with epilepsy. Archives of Pediatrics & Adolescent Medicine 164(8):747-753.

139. Holsti M, Sill BL, Firth SD, Filloux FM, Joyce SM, Furnival RA 2007. Prehospital intranasal midazolam for the treatment of pediatric seizures. Pediatric Emergency Care 22(3):148-153.

140. Wilton NC, Leigh J, Rosen DR, Pandit UA 1988. Preanesthetic sedation of preschool children using intranasal midazolam. Anesthesiology: The Journal of the American Society of Anesthesiologists 69(6):972-974.

141. University of Minnesota Masonic Children's Hospital 2007. Emergency Department Guideline: Intranasal (IN) Midazolam. Division of Pediatric Emergency Medicine.

142. Björkman S, Rigemar G, Idvall J 1997. Pharmacokinetics of midazolam given as an intranasal spray to adult surgical patients. British Journal of Anaesthesia 79(5):575-580.

143. Kanto JH 1985. Midazolam: The First Water-soluble Benzodiazepine; Pharmacology, Pharmacokinetics and Efficacy in Insomnia and Anesthesia. Pharmacotherapy: The Journal of Human Pharmacology and Drug Therapy 5(3):138-155.

144. Hospira Inc. 2018. Midazolam Injection, USP Package Insert. NDC 0409-2307-60. Distributed by Hospira, Inc., Lake Forest, IL 60045 USA. (Version 17):LAB-0847-0845.0840.

145. Hospira Inc. 2018. Seizalam (TM) - Midazolam for Intramuscular Injection, USP Package Insert, NDC 11704-650-01. Distributed by Hospira, Inc., Lake Forest, IL 60045 USA.Application number: 209566Orig209561s209000. LAB-201070-209560.209564.

146. Kulkarni V, Shaw C 2012. Formulation and characterization of nasal sprays. An examination of nasal spray formulation parameters and excipients and their influence on key in vitro tests. Inhalation:10-15.

147. Pujara CP, Shao Z, Duncan MR, Mitra AK 1995. Effects of formulation variables on nasal epithelial cell integrity: biochemical evaluations. International Journal of Pharmaceutics 114(2):197-203.

148. Verma RK, Paswan A, De A, Gupta S 2012. Premedication with midazolam nasal spray: an alternative to oral midazolam in children. Anesthesiology and Pain Medicine 1(4):248.

149. Kay L, Reif PS, Belke M, Bauer S, Fründ D, Knake S, Rosenow F, Strzelczyk A 2015. Intranasal midazolam during presurgical epilepsy monitoring is well tolerated, delays seizure recurrence, and protects from generalized tonic–clonic seizures. Epilepsia 56(9):1408-1414.

150. Humphries LK, Eiland LS 2013. Treatment of acute seizures: is intranasal midazolam a viable option? The Journal of Pediatric Pharmacology and Therapeutics 18(2):79-87.

151. Braun T, Meng T, Sequeira D, Van Ess P, Pullman W. Abstract American Epilepsy Society Annual Meeting, 2017.

152. Parhizkar E, Emadi L, Alipour S 2017. Midazolam solubility enhancement pre-formulation techniques at nasal physiological pH. International Journal of Pharmaceutical Sciences and Research 8(5):2315-2322.

153. Raina SA, Zhang GG, Alonzo DE, Wu J, Zhu D, Catron ND, Gao Y, Taylor LS 2015. Impact of solubilizing additives on supersaturation and membrane transport of drugs. Pharmaceutical Research 32(10):3350-3364.

154. Walser A, Benjamin LE, Flynn T, Mason C, Schwartz R, Fryer RI 1978. Quinazolines and 1, 4-benzodiazepines. 84. Synthesis and reactions of imidazo [1, 5-a][1, 4] benzodiazepines. The Journal of Organic Chemistry 43(5):936-944.

155. Sigma Aldrich Corporation 2013. CompoZr ADME/Tox Cell Lines, C2BBe1 BCRP Knockout and Wild Type Cell Lines, 24 Well Assay Ready Plates. Sigma Aldrich Technical Bulletin:Cat # MTOX1002PC1024.

156. Kessler M, Goldsmith D, Schellekens H 2006. Immunogenicity of biopharmaceuticals. Nephrology Dialysis Transplantation 21(suppl 5):v9-v12.

157. Bundgaard H 1989. The double prodrug concept and its applications. Advanced Drug Delivery Reviews 3(1):39-65.

158. Gerecke M 1983. Chemical structure and properties of midazolam compared with other benzodiazepines. British Journal of Clinical Pharmacology 16(S1):11S-16S.

159. Bradley J, Williams A, Lang A 2014. Jean-Claude Bradley Open Melting Point Dataset. Figshare Dataset.

160. Tolle-Sander S, Rautio J, Wring S, Polli JW, Polli JE 2003. Midazolam exhibits characteristics of a highly permeable P-glycoprotein substrate. Pharmaceutical Research 20(5):757-764.

161. Doan KMM, Humphreys JE, Webster LO, Wring SA, Shampine LJ, Serabjit-Singh CJ, Adkison KK, Polli JW 2002. Passive permeability and P-glycoprotein-mediated efflux differentiate central nervous system (CNS) and non-CNS marketed drugs. Journal of Pharmacology and Experimental Therapeutics 303(3):1029-1037.

162. Li J, Wu J, Bao X, Honea N, Xie Y, Kim S, Sparreboom A, Sanai N 2017. Quantitative and mechanistic understanding of AZD1775 penetration across human blood–brain barrier in glioblastoma patients using an IVIVE–PBPK modeling approach. Clinical Cancer Research.

163. Polli JW, Wring SA, Humphreys JE, Huang L, Morgan JB, Webster LO, Serabjit-Singh CS 2001. Rational use of in vitro P-glycoprotein assays in drug discovery. Journal of Pharmacology and Experimental Therapeutics 299(2):620-628.

164. Hakkarainen JJ. 2013. In vitro cell models in predicting blood-brain barrier permeability of drugs. ed.: University of Eastern Finland.

165. Wessels HP, Hansen GH, Fuhrer C, Look AT, Sjöström H, Norén O, Spiess M 1990. Aminopeptidase N is directly sorted to the apical domain in MDCK cells. The Journal of Cell Biology 111(6):2923-2930.

166. Kurono Y, Kuwayama T, Kamiya K, Yashiro T, Ikeda K 1985. The behavior of 1, 4-benzodiazepine drugs in acidic media. II. Kinetics and mechanism of the acid-base equilibrium reaction of oxazolam. Chemical and Pharmaceutical Bulletin 33(4):1633-1640.

167. Cho M, Scahill T, Hester Jr J 1983. Kinetics and equilibrium of the reversible alprazolam ring-opening reaction. Journal of Pharmaceutical Sciences 72(4):356-362.

168. Pires A, Fortuna A, Alves G, Falcão A 2009. Intranasal drug delivery: how, why and what for? Journal of Pharmacy & Pharmaceutical Sciences 12(3):288-311.

169. Nudelman NS, De Waisbaum R 1995. Acid hydrolysis of diazepam. Kinetic study of the reactions of 2-(N-methylamino)-5-chlorobenzophenone, with HCl in MeOH H2O. Journal of Pharmaceutical Sciences 84(8):998-1004.

170. Pal I, Ramsey JD 2011. The role of the lymphatic system in vaccine trafficking and immune response. Advanced Drug Delivery Reviews 63(10-11):909-922.

171. Pardeshi CV, Belgamwar VS 2013. Direct nose to brain drug delivery via integrated nerve pathways bypassing the blood–brain barrier: an excellent platform for brain targeting. Expert Opinion on Drug Delivery 10(7):957-972.

172. Thorat S 2016. Formulation and product development of nasal spray: an overview. Sch J Appl Med Sci 4.

173. Schindelin J, Arganda-Carreras I, Frise E, Kaynig V, Longair M, Pietzsch T, Preibisch S, Rueden C, Saalfeld S, Schmid B 2012. Fiji: an open-source platform for biological-image analysis. Nature Methods 9(7):676.

174. NIH 3D Print Excahnge 2015. Upper respiratory airways cast. File 3DPX-002305 uploaded by user Nevitdilmen.:<https ://3dprint.nih.gov/discover/3dpx-002305>

175. Yushkevich PA, Piven J, Hazlett HC, Smith RG, Ho S, Gee JC, Gerig G 2006. User-guided 3D active contour segmentation of anatomical structures: significantly improved efficiency and reliability. Neuroimage 31(3):1116-1128.

176. Michaels TM 1988. Dual chamber prefill syringes. PDA Journal of Pharmaceutical Science and Technology 42(6):199-202.

177. Foo MY, Cheng Y-S, Su W-C, Donovan MD 2007. The influence of spray properties on intranasal deposition. Journal of Aerosol Medicine 20(4):495-508.

178. Inthavong K, Tian Z, Tu J, Yang W, Xue C 2008. Optimising nasal spray parameters for efficient drug delivery using computational fluid dynamics. Computers in Biology and Medicine 38(6):713-726.

179. Suman JD, Laube BL, Lin T-c, Brouet G, Dalby R 2002. Validity of in vitro tests on aqueous spray pumps as surrogates for nasal deposition. Pharmaceutical Research 19(1):1-6.

180. Teagarden DL, Speaker SM, Martin SW, Osterberg T 2010. 21 Practical Considerations for Freeze-Drying in Dual Chamber Package Systems. Freeze Drying/Lyophilization of Pharmaceutical and Biological Products:494.

181. Jacob S, Nair A, Patil P, Panda B 2011. Solid state crystallinity, amorphous state, and its implications in the pharmaceutical process. International Journal of Pharmaceutical Sciences and Research 2(3):472.

182. Schwarz B, Merkel OM. 2019. Nose-to-brain delivery of biologics. ed.: Future Science.

183. Rey L, May JC. 2010. Freeze-Drying/Lyophilization of Pharmaceutical and Biological Products. Third ed., New York, NY: Informa Healthcare.

184. Franzé S, Selmin F, Samaritani E, Minghetti P, Cilurzo F 2018. Lyophilization of liposomal formulations: still necessary, still challenging. Pharmaceutics 10(3):139.

185. Werk T, Ludwig IS, Luemkemann J, Mahler H-C, Huwyler J, Hafner M 2016. Technology, applications, and process challenges of dual chamber systems. Journal of Pharmaceutical Sciences 105(1):4-9.

186. Bekard IB, Asimakis P, Bertolini J, Dunstan DE 2011. The effects of shear flow on protein structure and function. Biopolymers 95(11):733-745.

187. Zhang W, Haser A, Hou HH, Nagapudi K 2018. Evaluation of Accuracy of Amorphous Solubility Advantage Calculation by Comparison with Experimental

Solubility Measurement in Buffer and Biorelevant Media. Molecular Pharmaceutics 15(4):1714-1723.

188. Hurle D. 2013. Fundamentals: Thermodynamics and Kinetics. ed.: Elsevier.

189. Favvas E, Mitropoulos AC 2008. What is spinodal decomposition. Journal of Engineering Science and Technology Review 1:25-27.

190. Gebauer D, Kellermeier M, Gale JD, Bergström L, Cölfen H 2014. Pre-nucleation clusters as solute precursors in crystallisation. Chemical Society Reviews 43(7):2348-2371.

191. Lin M, Lindsay HM, Weitz D, Ball R, Klein R, Meakin P 1989. Universality in colloid aggregation. Nature 339(6223):360.

192. Marques MR, Loebenberg R, Almukainzi M 2011. Simulated biological fluids with possible application in dissolution testing. Dissolution Technol 18(3):15-28.

193. Masiuk T, Kadakia P, Wang Z 2016. Development of a physiologically relevant dripping analytical method using simulated nasal mucus for nasal spray formulation analysis. Journal of Pharmaceutical Analysis 6(5):283-291.

194. Thermo Fisher Scientific Inc 2017. LIVE/DEAD® Cell Vitality Assay Kit, C12 Resazurin/SYTOX® Green. https: //wwwthermofishercom/order/catalog/product/ L34951 Catalog number: L34951.

195. Pham V-L, Cadel M-S, Gouzy-Darmon C, Hanquez C, Beinfeld MC, Nicolas P, Etchebest C, Foulon T 2007. Aminopeptidase B, a glucagon-processing enzyme: site directed mutagenesis of the Zn 2+-binding motif and molecular modelling. BMC Biochemistry 8(1):21.

196. Fukasawa KM, Hirose J, Hata T, Ono Y 2006. Aspartic acid 405 contributes to the substrate specificity of aminopeptidase B. Biochemistry 45(38):11425-11431.

197. Bryant M, Brown P, Gurevich N, McDougall I 1999. Comparison of the clearance of radiolabelled nose drops and nasal spray as mucosally delivered vaccine. Nuclear Medicine Communications 20(2):171-174.

198. Hardy J, Lee S, Wilson C 1985. Intranasal drug delivery by spray and drops. Journal of Pharmacy and Pharmacology 37(5):294-297.

199. ICH Harmonized Tripartite 2005. Validation of analytical procedures: text and methodology. Q2 (R1).

200. Yadav LDS. 2013. Organic spectroscopy. ed.: Springer Science & Business Media.

201. Good NE, Winget GD, Winter W, Connolly TN, Izawa S, Singh RM 1966. Hydrogen ion buffers for biological research. Biochemistry 5(2):467-477.

202. Allen Jr LV 2006. Compounding nasal preparations. Secundum Artem: Paddocklabs 7(1).

203. Tsang C, Wilkinson G 1982. Diazepam disposition in mature and aged rabbits and rats. Drug Metabolism and Disposition 10(4):413-416.

204. Igari Y, Sugiyama Y, Sawada Y, Iga T, Hanano M 1982. Tissue distribution of 14C-diazepam and its metabolites in rats. Drug Metabolism and Disposition 10(6):676-679.

205. Gueorguieva I, Aarons L, Rowland M 2006. Diazepam pharamacokinetics from preclinical to phase I using a Bayesian population physiologically based pharmacokinetic model with informative prior distributions in WinBUGS. Journal of Pharmacokinetics and Pharmacodynamics 33(5):571-594.

206. Gueorguieva I, Nestorov IA, Murby S, Gisbert S, Collins B, Dickens K, Duffy J, Hussain Z, Rowland M 2004. Development of a whole body physiologically based model to characterise the pharmacokinetics of benzodiazepines. 1: Estimation of rat

tissue-plasma partition ratios. Journal of Pharmacokinetics and Pharmacodynamics 31(4):269-298.

207. Ableitner A, Wüster M, Herz A 1985. Specific changes in local cerebral glucose utilization in the rat brain induced by acute and chronic diazepam. Brain Research 359(1-2):49-56.

208. Schwartz MA, Koechlin BA, Postma E, Palmer S, Krol G 1965. Metabolism of diazepam in rat, dog, and man. Journal of Pharmacology and Experimental Therapeutics 149(3):423-435.

209. Musteata FM, de Lannoy I, Gien B, Pawliszyn J 2008. Blood sampling without blood draws for in vivo pharmacokinetic studies in rats. Journal of Pharmaceutical and Biomedical Analysis 47(4-5):907-912.

210. Fenyk-Melody JE, Shen X, Peng Q, Pikounis W, Colwell L, Pivnichny J, Anderson LC, Tamvakopoulos CS 2004. Comparison of the effects of perfusion in determining brain penetration (brain-to-plasma ratios) of small molecules in rats. Comparative Medicine 54(4):378-381.

Appendices

A1: Supporting information for Chapter 2

A1.1 Flow chart for DZP precipitation experiments

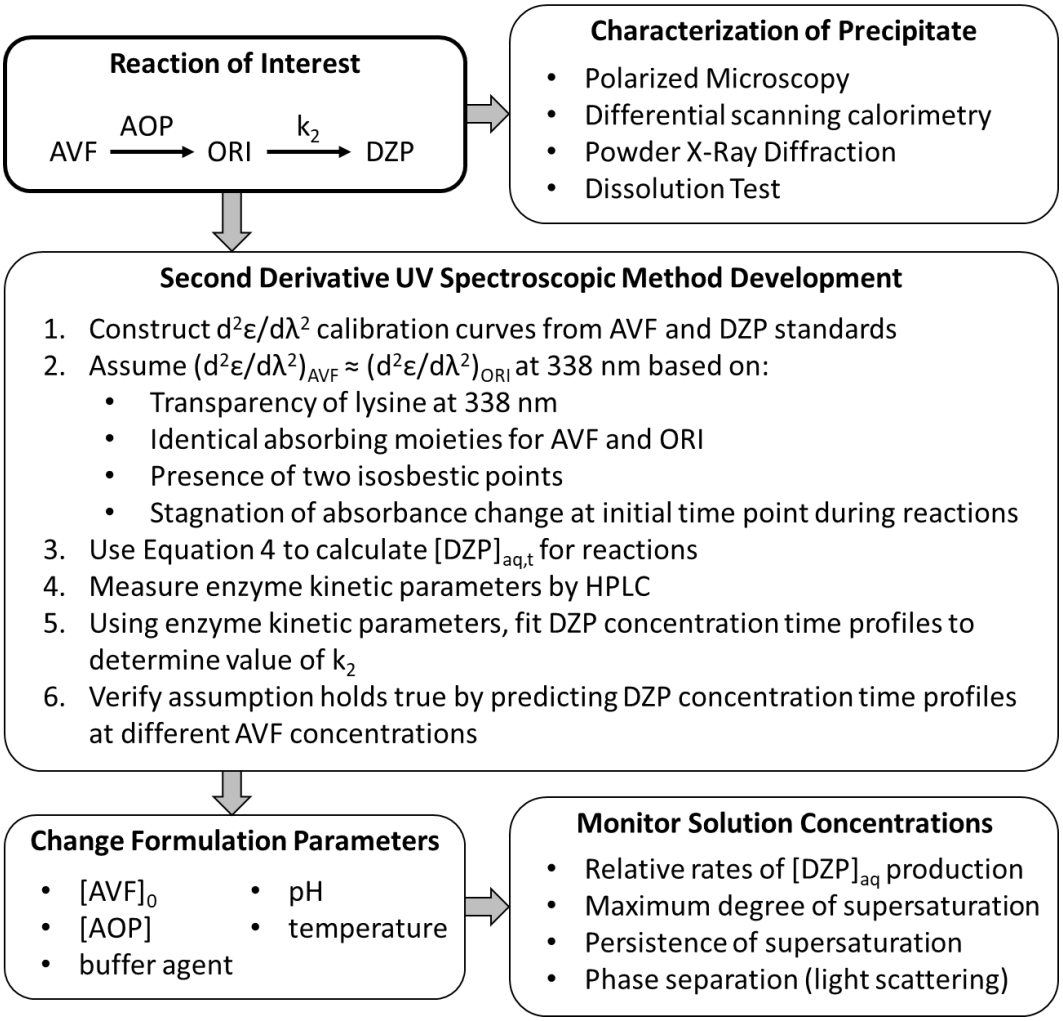

A1.2 Derivation of spectroscopic second derivative relationship (eq. 1)

Absorbances for calibration curves in Figure A1.53 A, B, C, and D were measured in pH 7.4 PBS at 32 ^{o}C. Limit of quantitation (LOQ) and limit of detection (LOD) were

calculated from the standard error in the y intercept and slope of the regression according to ICH Q2 guidelines.[199] The correlation relating supersaturated DZP concentrations to absorbance was confirmed by measuring the absorbance of AVF/enzyme reactions allowed to go to completion.

HPLC determinations of $[DZP]_{aq}$ were done on an Agilent 1260 Infinity system: quaternary pump G1311B, autosampler G1329B, thermostatted column compartment G1316A, diode-array detector G4212B, Agilent OpenLAB CDS software. The isocratic mobile phase was 50 mM phosphate buffer pH 3.0 and acetonitrile (40:60 v/v) with a flow rate of 0.4 mL/min through an Agilent ZORBAX Eclipse XDB-C18 column (3.0 x 150 mm, 3.5 µm particle size). Samples were prepared in mobile phase using 16 µM (4.33 µg/mL) tolbuatmide (Tol) as an internal standard. Analytes from 25 µL injections of each sample were detected at 220 nm with retention times of 2.75 and 3.83 min observed for Tol and DZP respectively. A DZP standard calibration curve was constructed and the peak area ratios of DZP:Tol were used to calculate DZP concentrations in the samples.

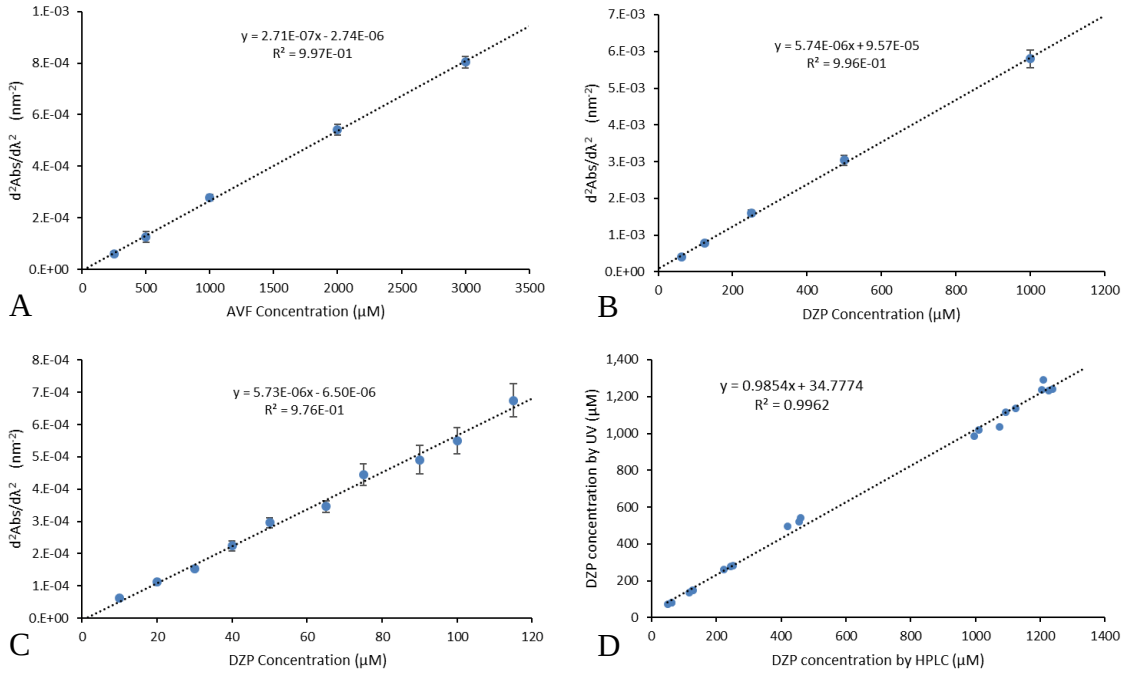

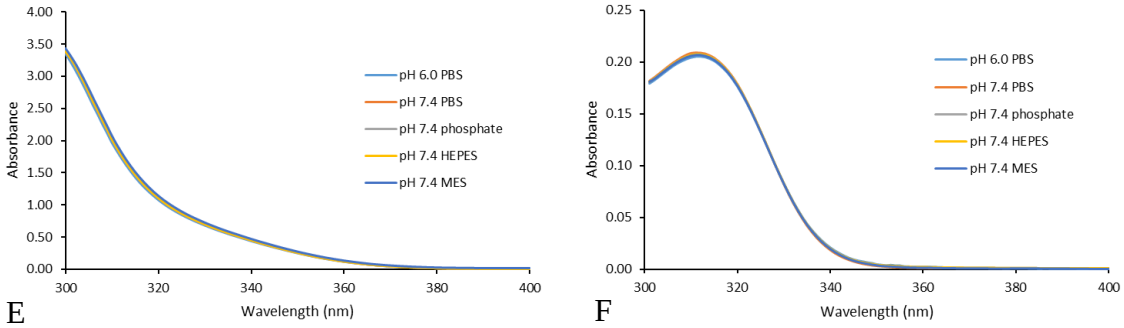

Figure A1.53. Calibration curves. (**A**) Second derivative calibration curve for AVF, LOQ = 269 µM, LOD = 88.7 µM. (**B**) Second derivative calibration curve for DZP in supersaturated region, LOQ: 83.3 µM, LOD: 27.5 µM. (**C**) Second derivative calibration curve for DZP below saturation, LOQ = 23.4 µM, LOD = 7.73 µM. (**D**) Validation of UV method by HPLC. (**E**) Zero order spectra of 2.00 mM AVF in different 20 mM buffers and at the bounds of tonicity and pH for the experimental conditions. (**F**) Zero order spectra of 0.100 mM DZP in different 20 mM buffers and at the bounds of tonicity and pH for the experimental conditions.

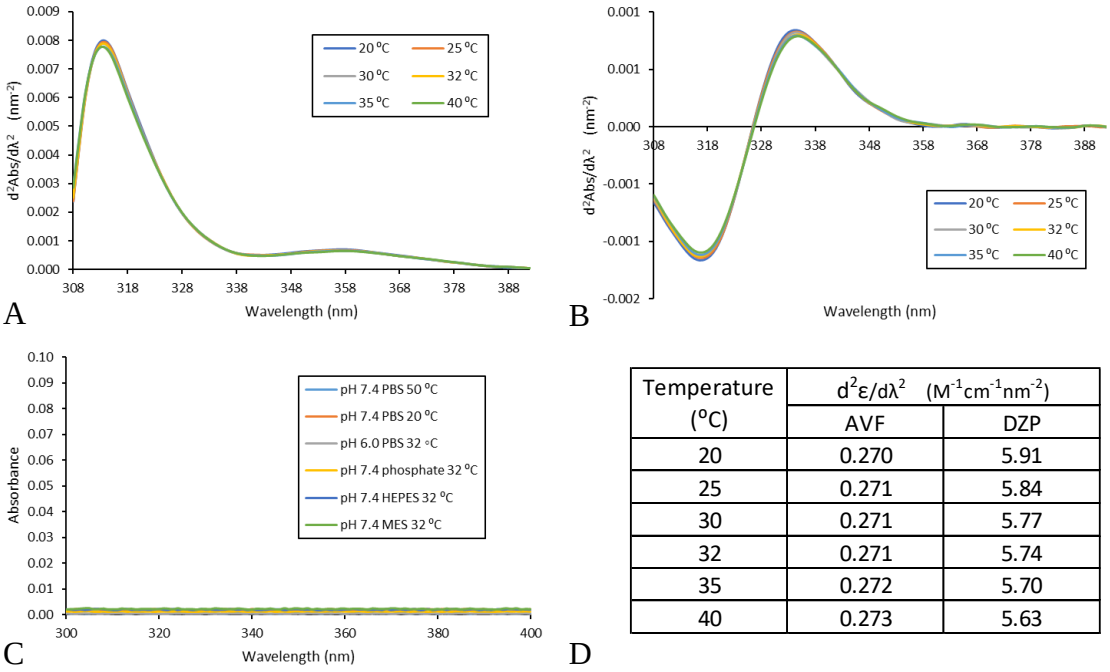

Temperature (°C)	$d^2\varepsilon/d\lambda^2$ ($M^{-1}cm^{-1}nm^{-2}$)	
	AVF	DZP
20	0.270	5.91
25	0.271	5.84
30	0.271	5.77
32	0.271	5.74
35	0.272	5.70
40	0.273	5.63

D

Figure A1.54. Effect of temperature on molar absorptivity. (A) Second derivative spectra of 2.00 mM of AVF in PBS pH 7.4 at 20 – 40 °C. (B) Second derivative spectra of 0.125 mM of DZP in PBS pH 7.4 at 20 – 40 °C. (C) Zero order spectra of 8.00 mM Lys in different 20 mM buffers and at the experimental bounds of temperature and pH. Lys was transparent in the region of interest (300 – 400 nm). (D) Calibration curve slope temperature dependence for AVF and DZP.

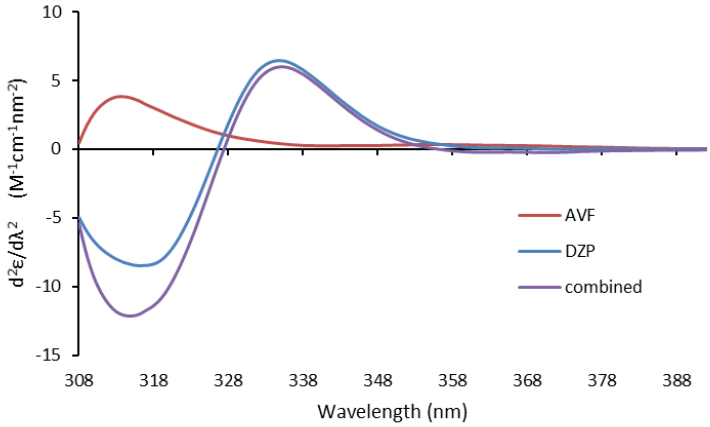

Figure A1.55. Sensitivity analysis for calibration curves at different wavelengths. At 338 nm: $d^2\varepsilon/d\lambda^2$ = 0.271 $M^{-1}cm^{-1}nm^{-2}$ for AVF, 0.275 $M^{-1}cm^{-1}nm^{-2}$ for ORI, and 5.74 $M^{-1}cm^{-1}nm^{-2}$ for DZP.

A derivation of Equation 1 for the determination of $[DZP]_{aq,t}$ is below. We start from the Beer–Lambert law for the attenuation of light, where Abs is the absorbance of light, Ext is the extinction of light, I_o is the intensity of incident light, I is the transmitted intensity, ℓ is the path length (1 cm), ε is molar absorptivity, and C is concentration with $C = [AVF] + [ORI] + [DZP]_{aq}$.

$$\text{Abs} = C \times \varepsilon \times \ell \quad \text{and} \quad \text{Ext} = \text{Abs} + \text{scattering} = \log_{10}\frac{I_o}{I}$$

In the absence of precipitate Ext = Abs. Light scatting from precipitate particles produces a very broad peak relative to sharper analyte peaks. Thus, the contribution of light scattering to the second derivative of Ext is small.

$$\frac{d}{dt}\frac{d^2\text{Ext}}{d\lambda^2} \approx \frac{d}{dt}\frac{d^2\text{Abs}}{d\lambda^2} = \frac{d}{dt}\frac{d^2}{d\lambda^2}(C \times \varepsilon \times \ell)$$

$$\frac{d}{dt}\frac{d^2\text{Ext}}{d\lambda^2} = \left(\frac{d[AVF]}{dt}\left(\frac{d^2\varepsilon}{d\lambda^2}\right)_{AVF} + \frac{d[ORI]}{dt}\left(\frac{d^2\varepsilon}{d\lambda^2}\right)_{ORI} + \frac{d[DZP]_{aq}}{dt}\left(\frac{d^2\varepsilon}{d\lambda^2}\right)_{DZP}\right)\ell$$

$$\left(\frac{d^2\varepsilon}{d\lambda^2}\right)_{AVF} \approx \left(\frac{d^2\varepsilon}{d\lambda^2}\right)_{ORI}$$

$$\frac{\mathrm{d}^2}{\mathrm{d}\lambda^2}\mathrm{dExt} = \left((\mathrm{d[AVF]} + \mathrm{d[ORI]}) \left(\frac{\mathrm{d}^2\varepsilon}{\mathrm{d}\lambda^2}\right)_{\mathrm{AVF}} + \mathrm{d[DZP]_{aq}} \left(\frac{\mathrm{d}^2\varepsilon}{\mathrm{d}\lambda^2}\right)_{\mathrm{DZP}} \right) \ell$$

$$\mathrm{d[DZP]_{aq}} = -\mathrm{d[AVF]} - \mathrm{d[ORI]}$$

$$\mathrm{d[DZP]_{aq}} = \frac{\frac{\mathrm{d}^2}{\mathrm{d}\lambda^2}\mathrm{dExt}}{\left(\left(\frac{\mathrm{d}^2\varepsilon}{\mathrm{d}\lambda^2}\right)_{\mathrm{DZP}} - \left(\frac{\mathrm{d}^2\varepsilon}{\mathrm{d}\lambda^2}\right)_{\mathrm{AVF}}\right)\ell}$$

$$\int_{[\mathrm{DZP}]_0}^{[\mathrm{DZP}]_t} \mathrm{d[DZP]_{aq}} = \int_{\mathrm{Ext}_0}^{\mathrm{Ext}_t} \frac{\frac{\mathrm{d}^2}{\mathrm{d}\lambda^2}\mathrm{dExt}}{\left(\left(\frac{\mathrm{d}^2\varepsilon}{\mathrm{d}\lambda^2}\right)_{\mathrm{DZP}} - \left(\frac{\mathrm{d}^2\varepsilon}{\mathrm{d}\lambda^2}\right)_{\mathrm{AVF}}\right)\ell}$$

$$[\mathrm{DZP}]_{\mathrm{aq,t}} - [\mathrm{DZP}]_{\mathrm{aq,0}} = \frac{\frac{\mathrm{d}^2\mathrm{Ext_t}}{\mathrm{d}\lambda^2} - \frac{\mathrm{d}^2\mathrm{Ext_0}}{\mathrm{d}\lambda^2}}{\left(\left(\frac{\mathrm{d}^2\varepsilon}{\mathrm{d}\lambda^2}\right)_{\mathrm{DZP}} - \left(\frac{\mathrm{d}^2\varepsilon}{\mathrm{d}\lambda^2}\right)_{\mathrm{AVF}}\right)\ell}$$

$$\text{where} \quad [\mathrm{DZP}]_{\mathrm{aq,0}} = 0 \quad \text{and} \quad \frac{\mathrm{d}^2\mathrm{Ext_0}}{\mathrm{d}\lambda^2} = [\mathrm{AVF}]_0 \left(\frac{\mathrm{d}^2\varepsilon}{\mathrm{d}\lambda^2}\right)_{\mathrm{AVF}} \ell$$

$$[\mathrm{DZP}]_{\mathrm{aq,t}} = \frac{\frac{\mathrm{d}^2\mathrm{Ext_t}}{\mathrm{d}\lambda^2} - [\mathrm{AVF}]_0 \left(\frac{\mathrm{d}^2\varepsilon}{\mathrm{d}\lambda^2}\right)_{\mathrm{AVF}} \ell}{\left(\left(\frac{\mathrm{d}^2\varepsilon}{\mathrm{d}\lambda^2}\right)_{\mathrm{DZP}} - \left(\frac{\mathrm{d}^2\varepsilon}{\mathrm{d}\lambda^2}\right)_{\mathrm{AVF}}\right)\ell}$$

$$[\mathrm{DZP}]_{\mathrm{aq,t}} = \frac{\frac{\mathrm{d}^2\mathrm{Ext_t}}{\mathrm{d}\lambda^2} - [\mathrm{AVF}]_{\mathrm{o}}(0.271\ \mathrm{M^{-1}cm^{-1}nm^{-2}})(1\ \mathrm{cm})}{(5.74\ \mathrm{M^{-1}cm^{-1}nm^{-2}} - 0.271\ \mathrm{M^{-1}cm^{-1}nm^{-2}})(1\ \mathrm{cm})}$$

$$[\mathrm{DZP}]_{\mathrm{aq,t}} = \frac{\frac{\mathrm{d}^2\mathrm{Ext_t}}{\mathrm{d}\lambda^2} - [\mathrm{AVF}]_{\mathrm{o}}(0.271\ \mathrm{M^{-1}nm^{-2}})}{5.47\ \mathrm{M^{-1}nm^{-2}}} \qquad q.e.d.$$

Since $(\mathrm{d}^2\varepsilon/\mathrm{d}\lambda^2)_{\mathrm{DZP}} >> (\mathrm{d}^2\varepsilon/\mathrm{d}\lambda^2)_{\mathrm{AVF}}$, error in the determination of $[\mathrm{DZP}]_{\mathrm{aq,t}}$ in the precipitation regime due to imbalance of the stoichiometric relationship between the species in solution is negligible when $[\mathrm{AVF}]_{\mathrm{o}}$ is slightly greater than $[\mathrm{DZP}]_{\mathrm{aq,lim}}$. This error

becomes more important when $[AVF]_o >> [DZP]_{aq,lim}$, and is corrected by tracking the remaining concentrations of AVF and ORI.

$$[DZP]_{aq,t} = \frac{\frac{d^2Ext_t}{d\lambda^2} - ([AVF]_t + [ORI]_t)\left(\frac{d^2\varepsilon}{d\lambda^2}\right)_{AVF}\ell}{\left(\frac{d^2\varepsilon}{d\lambda^2}\right)_{DZP}\ell}$$

$$[DZP]_{aq,t} = \frac{\frac{d^2Ext_t}{d\lambda^2} - ([AVF]_t + [ORI]_t)(0.271\ M^{-1}nm^{-2})}{5.74\ M^{-1}nm^{-2}}$$

Where $[AVF]_t$ and $[ORI]_t$ are found by solving the differential equations for the reaction:

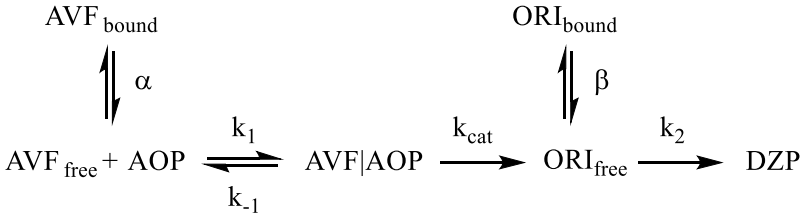

$$\frac{d[AVF]}{dt} = -\frac{V_{max}[AVF]_{free}}{K_M + [AVF]_{free}}$$

$$\frac{d[ORI]}{dt} = \frac{V_{max}[AVF]_{free}}{K_M + [AVF]_{free}} - k_2[ORI]_{free}$$

$$\text{where} \quad K_M = \frac{k_{-1} + k_{cat}}{k_1} \quad \text{and} \quad V_{max} = k_{cat}[AOP]$$

$$\text{with} \quad [AVF]_{free} = \left(\frac{[AVF]}{1 + \alpha[AOP]}\right) \quad \text{and} \quad [ORI]_{free} = \left(\frac{[ORI]}{1 + \alpha[AOP]}\right)$$

A1.3 Determination of Michaelis-Menten parameters

The enzyme kinetic parameters K_M and V_{max} for AVF substrate hydrolyzed by 0.25 U/mL AOP at pH 7.4 and 32 °C were first determined by measuring $[DZP]_{aq,5min}$ by HPLC

and fitting the integrated Michaelis-Menten equation shown below to the data using the nlinfit function in MATLAB software (The MathWorks, Inc.).

$$[\mathrm{DZP}]_{\mathrm{aq,t}} - \mathrm{K_M} \ln\left(1 - \frac{[\mathrm{DZP}]_{\mathrm{aq,t}}}{[\mathrm{AVF}]_0}\right) = \mathrm{V_{max}}\mathrm{t}$$

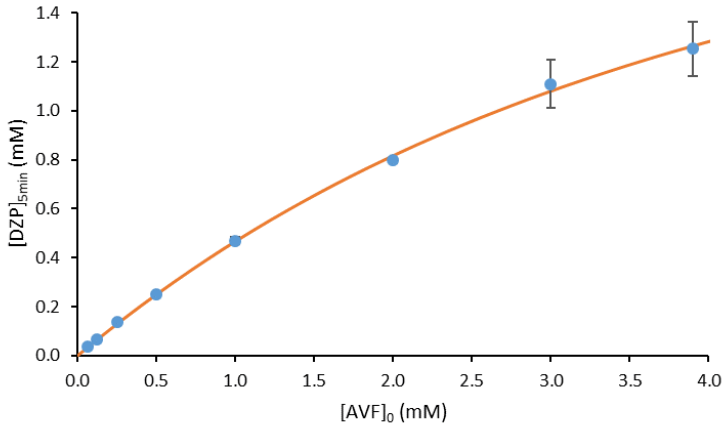

Figure A1.56. Enzyme kinetics for AVF/AOP system. Concentrations determined by HPLC (points) with least squares fit to the integrated Michaelis-Menten equation (line). K_M = 3.38 ± 0.34 mM, V_{max} = 0.518 ± 0.030 mM/min with 0.25 U/mL AOP in pH 7.4 cell assay buffer at t = 5 min.[42]

A1.4 Spectroscopic method development

In this section we demonstrate how zero order UV spectra, second derivative UV spectra, and Equations 3-5 were combined to track the conversion of AVF to DZP and formation of DZP precipitate.

Zero order spectra

UV spectroscopic determination of [AVF], [ORI], and $[\mathrm{DZP}]_{aq}$ during the course of the reaction requires knowledge of the molar absorptivity (ε) for each species in the reaction mixture. The absorbance spectra of AVF and DZP were readily obtained from standard solutions. Although Lys and AOP were also present in the reaction mixture, Lys did not have a detectable absorbance at 8.00 mM over the wavelength region of interest (300-400 nm) and AOP was included in the reference cell. The ε of ORI was more challenging to discern because this species is transient and cannot be physically isolated at

physiologically relevant pH values. However, its presence was evident from the sigmoidal shape of the absorbance-time profile. AOP hydrolysis of Lys from a chromogenic substrate, S-Lys-*para*-nitroanilide, which does not produce an intermediate species, did not display this behavior (Supporting Information, Figure A1.62 and Figure A1.63).

In the absence of precipitation ($[AVF]_0 < C_{ind}$), zero order spectra collected during enzymatic conversion of AVF to DZP exhibited isosbestic points at λ = 301 and 338 nm with $\varepsilon = 1810 \pm 60$ and 255 ± 7 $M^{-1}cm^{-1}$ ($\pm$ SD) respectively, as shown in Figure A1.57 for $[AVF]_0$ = 1.00 mM. The values of λ and ε for these isosbestic points did not deviate significantly within the range of formulation parameters tested. As the reaction progressed a characteristic absorbance peak for DZP at 315 nm developed between the isosbestic points (ε = 204 $M^{-1}cm^{-1}$ at 315 nm for DZP).

Isosbestic points typically occur when there is stochiometric conversion between two species. Therefore, the presence of two isosbestic points was a strong indication that two of the reaction species in the conversion of AVF to DZP had similar molar absorptivity throughout the 300-400 nm region. The only two reaction species that could exhibit similar spectra were AVF and ORI. AVF and ORI share the same conjugated ring structure and minimal ring strain, so the energy required to excite electrons to anti-bonding molecular orbitals is expected to be similar.[200] Furthermore, the Lys moiety of AVF was transparent in this region. The change in conjugation and ring strain from formation of the benzodiazepine moiety in DZP allows for a lower energy transition between the highest occupied and anti-boning molecular orbitals. This structural feature was responsible for the absorbance peak observed at 315 nm.

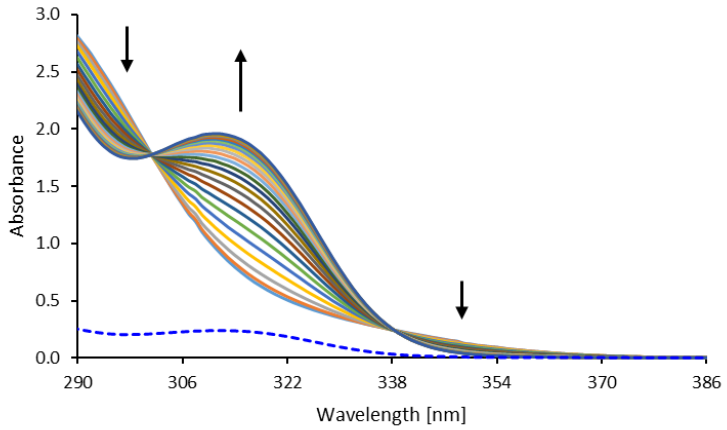

Figure A1.57. UV spectra measured during the enzymatic conversion of AVF. Sequence of spectra obtained during enzymatic conversion of 1.00 mM AVF to DZP by 0.25 U/mL AOP in pH 7.4 PBS at 32 ºC, 1 scan/min. Isosbestic points observed at 301 and 338 nm with an absorbance peak that is characteristic of DZP emerging at 315 nm.

Indeed, decomposition of the reaction mixture spectrum by subtraction of the component spectra revealed a spectrum for ORI resembling that of AVF, with ε = 753 $M^{-1}cm^{-1}$ for AVF and 707 $M^{-1}cm^{-1}$ for ORI at 315 nm. To perform the decomposition, the spectrum of a 2.00 mM reaction was captured at t = 3.75 min (Figure A1.58, purple curve). All three small molecule reaction species were expected to be present in significant quantities at this time point. The second derivative of the reaction mixture spectrum was calculated, and Equation 2 was used to determine $[DZP]_{aq,3.75min}$ from $d^2Abs/d\lambda^2$ at 338 nm, where Abs is the absorbance (note that $d^2Abs/d\lambda^2 = d^2Ext/d\lambda^2$ in this case). The use of Equation 2 is described in more detail in the following section. Then, the zero order spectrum of $[DZP]_{aq,3.75min}$ (i.e. purely $[DZP]_{aq}$ = 0.424 mM) was simulated based on ε measurements from DZP standard solutions at lower concentrations. The simulated spectrum of $[DZP]_{aq,3.75min}$, shown as a blue curve in Figure A1.58, was taken to be the absorbance contribution from DZP present in the reaction mixture. The absorbance contribution due to AVF present in the reaction mixture was obtained by using Equation 3 to predict $[AVF]_{3.75min}$, and then measuring the spectrum of an AVF standard solution prepared to the predicted concentration (i.e. purely [AVF] = 1.09 mM, Figure A1.58, red curve). Finally, the absorbance contributions form DZP and AVF were subtracted from the absorbance measured for the reaction mixture at each wavelength to obtain the spectrum of ORI shown as a green curve in Figure A1.58.

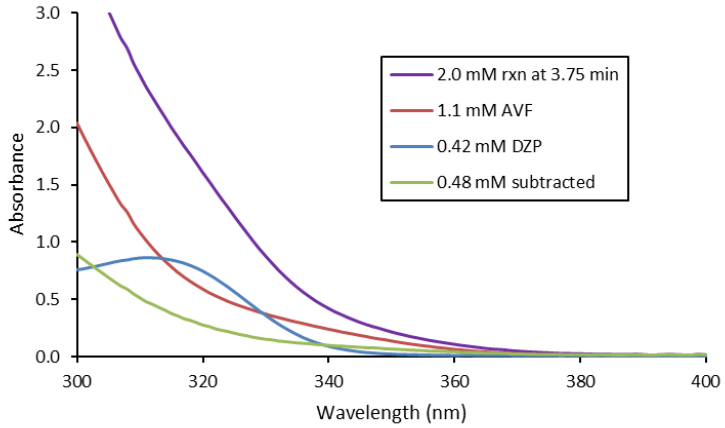

Figure A1.58. Resolving the ORI spectrum. Extraction of the zero order absorbance spectrum for ORI from the reaction mixture. Purple curve: measured absorbance spectrum captured at t = 3.75 min during the conversion of 2.00 mM AVF by 0.50 U/mL AOP in pH 7.4 PBS at 32 ºC. Red curve: measured absorbance spectrum of 1.09 mM AVF standard solution. Blue curve: simulated spectrum of 0.424 mM DZP. Green curve: spectrum of 0.485 mM ORI obtained by subtraction of AVF and DZP spectra from the spectrum of the reaction.

A1.5 Spectral subtraction for determination of ORI spectrum

To mathematically describe the decomposition the absorbance spectrum of a mixture of AVF, ORI, and DZP, we start from the Beer–Lambert law where Abs_λ is the absorbance of light at a specific wavelength (λ), ℓ is the path length (1 cm), ε_λ is molar absorptivity at λ, and C is concentration. The absorbance of any one species is given by:

$$Abs_\lambda = C \times \varepsilon_\lambda \times \ell$$

Absorbance is additive, meaning each of the species contributes to the total absorbance. Thus, the total absorbance is given by:

$$Abs_{total,\lambda} = Abs_{AVF,\lambda} + Abs_{ORI,\lambda} + Abs_{DZP,\lambda}$$

Inserting the Beer-Lambert law gives

$$Abs_{total,\lambda} = \varepsilon_{AVF,\lambda}[AVF]\ell + \varepsilon_{ORI,\lambda}[ORI]\ell + \varepsilon_{DZP,\lambda}[DZP]_{aq}\ell$$

or

$$Abs_{total,\lambda} = \varepsilon_{AVF,\lambda}[AVF]\ell + Abs_{ORI,\lambda} + \varepsilon_{DZP,\lambda}[DZP]_{aq}\ell$$

and rearranging gives

$$\mathrm{Abs}_{\mathrm{ORI},\lambda} = \mathrm{Abs}_{\mathrm{total},\lambda} - \left(\varepsilon_{\mathrm{AVF},\lambda}[\mathrm{AVF}]\ell + \varepsilon_{\mathrm{DZP},\lambda}[\mathrm{DZP}]_{\mathrm{aq}}\ell\right)$$

The variables [AVF], $[\mathrm{DZP}]_{\mathrm{aq}}$, and ℓ are constant for any given λ at a defined time. For AVF hydrolysis by AOP, the concentration of AVF at a defined time point can be predicted from Michaelis–Menten enzyme kinetics, and the concentration of DZP at that same time point can be measured using the second derivative of the spectrum produced by the mixture (Equation 2). The other variables $\varepsilon_{\mathrm{AVF},\lambda}$, $\varepsilon_{\mathrm{DZP},\lambda}$, and $\mathrm{Abs}_{\mathrm{total},\lambda}$ are dependent on λ and obtained directly from UV measurements of AVF, DZP, and the reaction mixture. With $\varepsilon_{\mathrm{AVF},\lambda}$, $\varepsilon_{\mathrm{DZP},\lambda}$, and $\mathrm{Abs}_{\mathrm{total},\lambda}$ known over the λ range of interest, the expression for $\mathrm{Abs}_{\mathrm{ORI},\lambda}$ shown above will give the spectrum of ORI.

The spectrum of ORI is not entirely useful in and of itself. The useful parameter is $\varepsilon_{\mathrm{ORI},\lambda}$. With $\mathrm{Abs}_{\mathrm{ORI},\lambda}$ calculated by the decomposition technique described above and knowledge of the stochiometric relationship between AVF, ORI, and DZP in the mixture, we can solve for $\varepsilon_{\mathrm{ORI},\lambda}$. The total concentration of the mixture is given by

$$\mathrm{C}_{\mathrm{total}} = [\mathrm{AVF}] + [\mathrm{ORI}] + [\mathrm{DZP}]_{\mathrm{aq}}$$

and rearranging gives the concentration of ORI

$$[\mathrm{ORI}] = \mathrm{C}_{\mathrm{total}} - ([\mathrm{AVF}] + [\mathrm{DZP}])$$

For AVF hydrolysis by AOP, the total concentration, $\mathrm{C}_{\mathrm{total}}$, is equal to the initial concentration of AVF, i.e. $[\mathrm{AVF}]_0$. Therefore, [ORI] can be known when [AVF] and [DZP] are known. Using the Beer-Lambert law again, $\mathrm{Abs}_{\mathrm{ORI},\lambda}$ determined from decomposition, known [ORI], and known ℓ gives the desired parameter, $\varepsilon_{\mathrm{ORI},\lambda}$

$$\varepsilon_{\mathrm{ORI},\lambda} = \frac{\mathrm{Abs}_{\mathrm{ORI},\lambda}}{[\mathrm{ORI}]\ell}$$

Second derivative spectra

At high DZP concentrations, resulting from $[\mathrm{AVF}]_0 > \mathrm{C}_{\mathrm{ind}}$, light scattering due to formation of precipitates produced a broad band signal as shown in Figure A1.59A. The increased total extinction (Ext = absorbance + scattering) exceeded the linear range of our instrument (Ext < 3.7) at 315 nm in most cases. To permit tracking of aqueous analyte concentrations in the presence of precipitates, a second derivative spectroscopic method was developed. As shown in Figure A1.59B, the broad brand effects due to scattering are essentially eliminated in the second derivative spectra. Calibration curves were

constructed based on the second derivative absorbance spectra of AVF and DZP standard solutions (Supporting Information, Figure A1.53), with $\lambda = 338$ nm chosen as the analytical wavelength. At 338 nm, $d^2\varepsilon/d\lambda^2 = 0.271 \pm 0.004$ $M^{-1}cm^{-1}nm^{-2}$ for AVF and $d^2\varepsilon/d\lambda^2 = 5.74 \pm 0.09$ $M^{-1}cm^{-1}nm^{-2}$ (± SD) for DZP in 32 ºC pH 7.4 PBS. These values were robust to changes in the buffer composition (pH, ionic strength, and buffering agent) at 32 °C; some weak temperature effects are discussed in the Supporting Information. The second derivative ORI spectrum, inferred by subtraction as for the zero order spectrum, was not significantly different than that of AVF at this isosbestic point, i.e. $(d^2\varepsilon/d\lambda^2)_{AVF} \approx (d^2\varepsilon/d\lambda^2)_{ORI}$ at 338 nm with $(d^2\varepsilon/d\lambda^2)_{ORI} = 0.275$ $M^{-1}cm^{-1}nm^{-2}$. Based on the second derivative calibration curves and the stoichiometric relationship of the absorbing species, the following equation was used to calculate $[DZP]_{aq,t}$, where Ext_t is the measured extinction of light at time t, ℓ is the path length of the sample (1 cm), and $\lambda = 380$ nm

$$[DZP]_{aq,t} = \frac{d^2Ext_t / d\lambda^2 - \ell\left(d^2\varepsilon / d\lambda^2\right)_{AVF}[AVF]_0}{\ell\left[\left(d^2\varepsilon / d\lambda^2\right)_{DZP} - \left(d^2\varepsilon / d\lambda^2\right)_{AVF}\right]} = (0.183\ M\ nm^2)\frac{d^2Ext_t}{d\lambda^2} - 0.0495[AVF]_0$$

See Figure A1.53 for a derivation of this equation and method validation by HPLC.

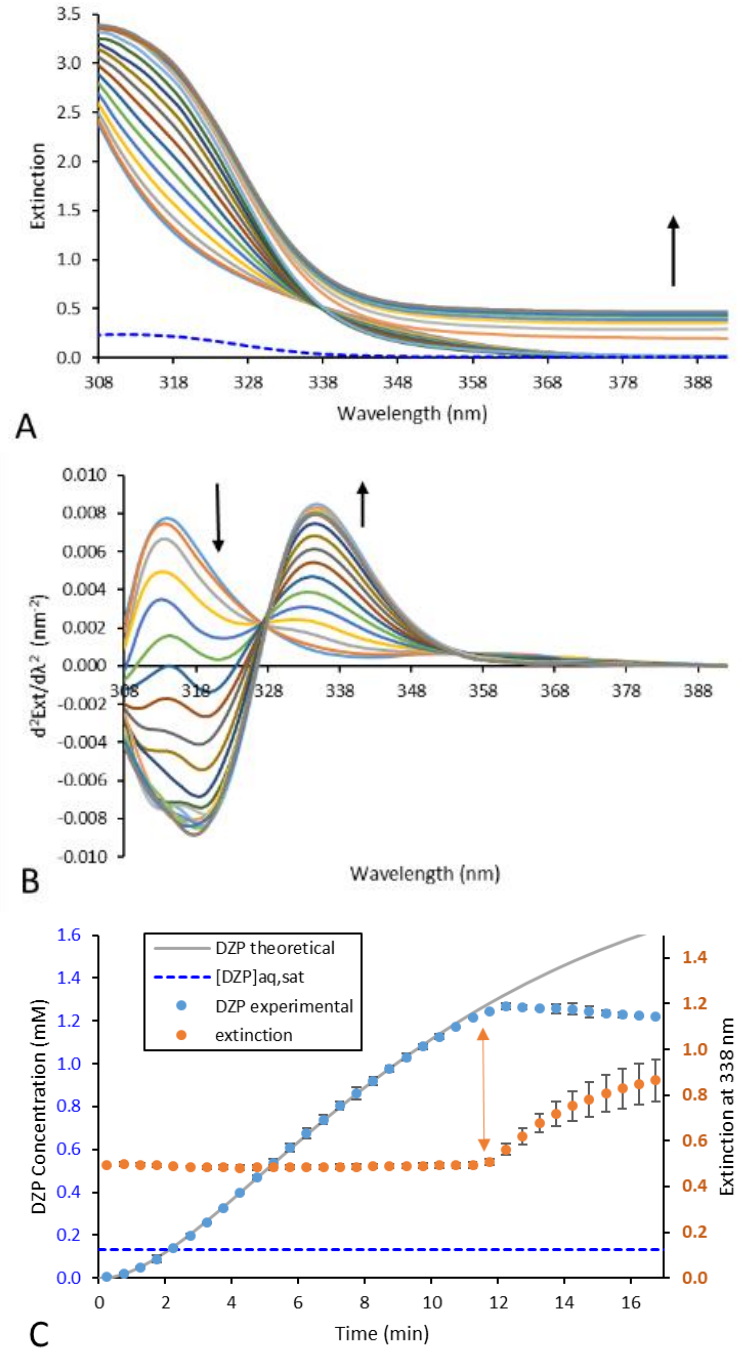

Figure A1.59. Using second derivative spectra to measure $[DZP]_{aq}$ in the presence of precipitate. Rxn: 2.00 mM AVF, 0.25 U/mL AOP, pH 7.4 PBS, 32 °C. (**A**) Sequence of UV spectra collected during conversion of AVF to DZP, 1 scan/min. Early spectra parallel those of Figure A1.57, with an isosbestic point at 338 nm. Precipitation of DZP caused turbidity and broad band interference, starting at t_{ind} = 12 min. Blue dashed line: spectrum of $[DZP]_{aq,sat}$ (0.130 mM, S = 1.00) (**B**) Second derivative spectra of data shown in A. There was a high signal to noise ratio observed at the isosbestic point, 338 nm. **(C)** DZP concentration-time profile with time course of precipitation overlaid, n = 3. Blue points:

$[DZP]_{aq}$ determined by the second derivative of Ext at 338 nm. Grey line: theoretical $[DZP]_{aq}$ in the absence of precipitation. Orange points: zero order Ext at 338 nm. Double headed arrow: onset of DZP precipitation at t_{ind} = 11.5 min, C_{ind} = 1.24 mM (S = 9.54).

The blue points in Figure A1.59C are representative of concentration-time profiles observed for the enzymatic conversion of AVF to DZP using the second derivative UV spectroscopic method with $[AVF]_0 > C_{ind}$. The concentration of DZP in solution plateaued near C_{ind} even though enzymatic hydrolysis of AVF continued to produce DZP. This plateau demarcated $[DZP]_{aq,lim}$. By neglecting the $[DZP]_{aq,lim}$ condition in Equation 5, Equations 3-5 can be used to predict the theoretical $[DZP]_{aq}$ that would result if no precipitation occurred. Departure of measured $[DZP]_{aq}$ (blue points) from theoretical $[DZP]_{aq}$ (grey curve) coincided with light scattering at t_{ind} (orange arrow). DZP produced in excess of $[DZP]_{aq,lim}$ phase separated from solution, causing light scattering from the resultant precipitate at $t > t_{ind}$ and an abrupt rise in the zero order Ext measured at the isosbestic point (orange points). Due to variations in precipitate particle positions between samples, error bars became wider once phase separation began.

A1.6 Inhibition of closing reaction by AOP

To explore potential enzyme inhibition, the following differential equations were solved numerically using MATLAB. Comparing theoretical concentration-time profiles with experimental data precluded enzyme inhibition by the small molecule reaction species.

$$\frac{d[AVF]}{dt} = -\frac{\left(\frac{1}{\alpha'}\right) V_{max}[AVF]}{\left(\frac{\alpha}{\alpha'}\right) K_M + [AVF]}$$

$$\frac{d[ORI]}{dt} = \frac{\left(\frac{1}{\alpha'}\right) V_{max}[AVF]}{\left(\frac{\alpha}{\alpha'}\right) K_M + [AVF]} + k_2[ORI]$$

$$\frac{d[DZP]_{aq}}{dt} = k_2[ORI]$$

$$\text{for } \alpha = 1 + \frac{[I]}{K_i} \text{ and } \alpha' = 1 + \frac{[I]}{K_i'}$$

$$\text{where [I] could be } [AVF]_t, [ORI]_t, [DZP]_{aq,t}, \text{ or } [Lys]_t$$

None of these enzyme inhibition models explained the observed concentrations. Instead, it was found that inhibition of the ring closing reaction was occurring with increasing [AOP]. This was thought to be due to non-specific binding of ORI to proteins in the AOP mixture. Bovine serum albumin (BSA) was added to the AVF + AOP reaction to investigate potential non-specific binding and its effect on the reaction rate. The addition of BSA did slow the reaction. However, AOP is a protease mixture with exo- and endo-peptidase activity. BSA might act as a competitive substrate thereby reducing the rate of DZP production, rending these results inconclusive.

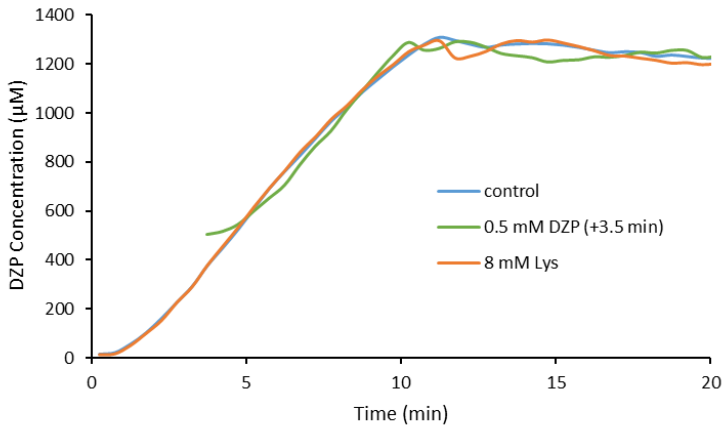

Figure A1.60. No enzyme inhibition from DZP or Lys. Experimental confirmation that neither DZP nor Lys have an inhibitory effect on the Lys endopeptidase activity of AOP. Concentration-time profiles of 2.00 mM AVF converted by 0.25 U/mL AOP in pH 7.4 PBS at 32 ^{o}C containing initial concentrations of DZP or Lys as indicated in the legend. DZP was added as a methanolic solution (10 µL) 390 µL of PBS.

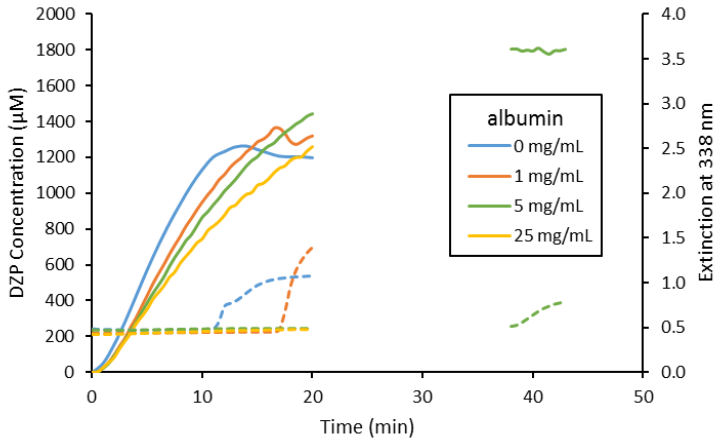

Figure A1.61. Bovine serum albumin controls to determine the effect of protein binding. Concentration-time profiles of 2.00 mM AVF converted by 0.25 U/mL AOP in pH 7.4 PBS at 32 °C containing initial concentrations of albumin (BSA) indicated in the legend. The addition of BSA reduced the rate of DZP production, increased C_{ind}, and increased $[DZP]_{aq,lim}$. C_{ind} = 1.20 mM for 0 mg/mL BSA and 1.36 mM for 1 mg/mL BSA.

A1.7 Additional figures and discussion

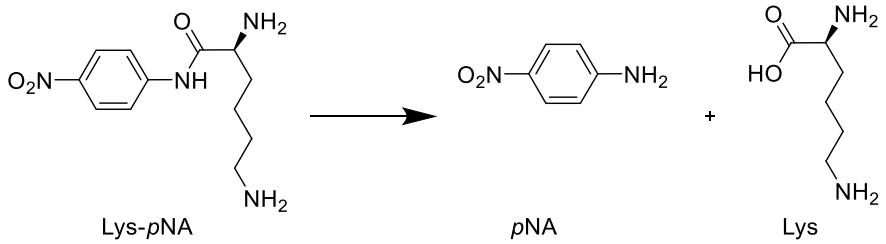

Figure A1.62. Reaction scheme for the hydrolysis of Lys-*p*NA. The chromogenic substrate, S-Lys-*para*-nitroanilide (Lys-*p*NA), can be hydrolyzed by Lys aminopeptidases to release the chromophore *para*-nitroaniline (*p*NA) that typically monitored at absorbance λ = 405 nm.

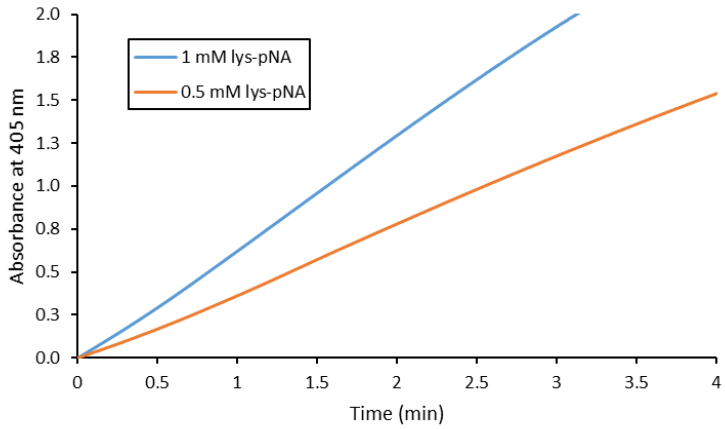

Figure A1.63. Hydrolysis of Lys-*p*NA by AOP. Concentration-time profile of S-Lys-*para*-nitroanilide (Lys-*p*NA) converted to *para*-nitroaniline (*p*NA) chromophore by 1.0 U/mL AOP in pH 7.4 PBS at 32 ºC, monitored at λ = 405 nm (ε_{405nm} = 10,600 M^{-1} cm^{-1} at pH 7.4).

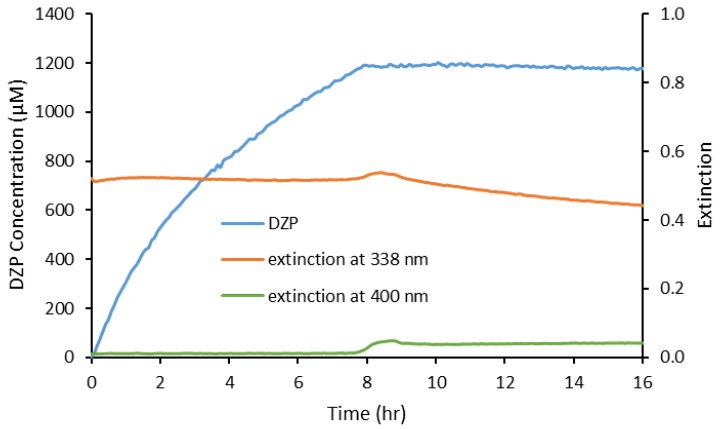

Figure A1.64. Reaction with low enzyme concentration. Concentration-time profile of 2.00 mM AVF converted by 0.005 U/mL AOP in pH 7.4 PBS at 32 ºC.

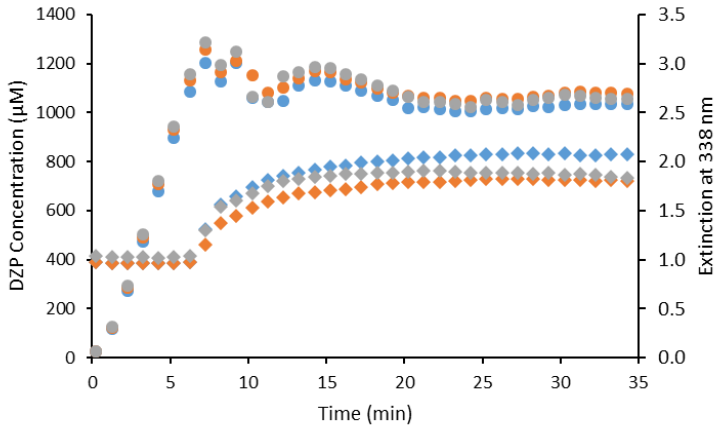

Figure A1.65. Concentration-time profile of AVF conversion with high $[AVF]_0$. Replicates of the 3.90 mM AVF reaction showed similar decreases in $[DZP]_{aq}$ after Cind was reached. Reaction conditions: 0.25 U/mL AOP in pH 7.4 PBS at 32 °C.

Other Formulation Considerations

There is considerable intersubject and intrasubject variation in nasal cavity pH. A study of 12 healthy volunteers found that the average anterior pH was 6.40 (range: 5.17 – 8.13) and average posterior pH 6.27 (range: 5.20 – 8.00)[55] In order to control the rate of enzymatic hydrolysis of AVF in the nasal cavity, an appropriate formulation buffer was needed. According to the FDA Orange Book,[127] the most common buffers used in commercial nasal spray formulations are citrate (buffering range: pH 3.0 – 6.2), phosphate (buffering range: pH 5.8 – 8.0), or a combination of citrate and phosphate (buffering range: pH 2.6 – 7.6). In addition to citrate and phosphate, HEPES (buffering range: pH 6.8 – 8.2) and MES (buffering range: pH 5.5 – 6.7) were considered as potential buffering agents. HEPES and MES are biologically compatible buffers that do not readily cross cell membranes.[201]

Nasal mucus is isotonic with 0.9% w/v NaCl. Buffers made isotonic by the addition of NaCl were used in these studies, although hypotonic solutions afforded better aminopeptidase activity with the AOP enzyme (Figure A1.66). Tonicities in the range of 0.6 – 1.8% w/v NaCl equivalency are generally acceptable for IN drug delivery applications.[202] The minimum buffer strength needed to overcome the natural buffering capacity of nasal mucus has been estimated to be 130 mM.[55] IN formulations resulting in a therapeutic dose of DZP would be in the hypertonic region when the tonicity

contributions from the buffering agent and the salt form of AVF are summed, negating the need for a tonicity adjusting agent.

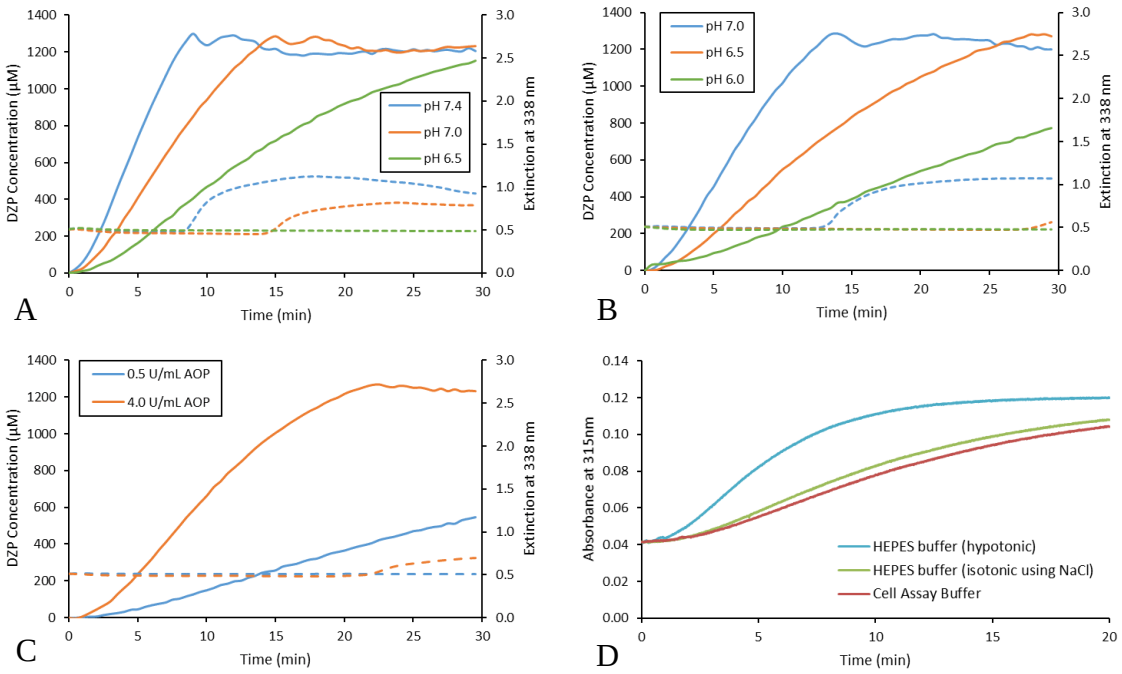

Figure A1.66. Comparison of buffers. Concentration-time profiles of 2.00 mM AVF converted by 0.50 U/mL AOP at 32 °C. (**A**) Buffered with 20 mM HEPES made isotonic with NaCl. (**B**) Buffered with 20 mM MES made isotonic with NaCl. (**C**) Buffered with 20 mM phosphate at pH 6.0 with 100 mM NaCl. (**D**) Conversion rate of AVF to DZP increased in hypotonic solution. Reaction conditions: 62.5 μM AVF, 0.25 U/mL AOP, pH 7.4, 32 °C, monitored at abs 315 nm. Cell assay buffer: 122 mM NaCl, 25 mM $NaHCO_3$, 10 mM glucose, 10 mM HEPES, 3 mM KCl, 1.2 mM $MgSO_4$, 1.4 mM $CaCl_2$, and 0.4 mM K_2HPO_4. Hypotonic: 20 mM HEPES. Isotonic: 20 mM HEPES, 145 mM NaCl.

A2: Supporting information for Chapter 3

Diazepam is commonly studied in rats at doses near 1 mg/kg.[103,203-210] To investigate dose proportionality, doses equivalent to diazepam at 0.50, 1.00, and 1.50 kg/mg were chosen. Since the prodrug has a different molar mass than the active drug, the equivalent prodrug doses were 0.885, 1.77, and 2.66 mg/kg. See Table 1S for dosing and sampling details.

Table A2.5. AVF/APB rat PK study design. Low dose level is equivalent to diazepam at 0.5 mg/kg, medium dose level is equivalent to diazepam at 1.0 mg/kg, and high dose level is equivalent to diazepam at 1.5 mg/kg. b = brain tissue, h = nasal tissues for histology.

Group	Formulation	Route	Dose level	n rats	Blood draw (min)	Tissue collection (min)
1	Vehicle	IN	n/a	3	none	90 [h]
2	AVF	IN	med	3	2, 10, 20, 30, 60	60 [b]
				3	5, 15, 45, 75, 90	90 [b]
3	AVF/APB	IN	low	3	2, 10, 20, 30, 60	60 [b]
				3	5, 15, 45, 75, 90	90 [b]
				3	none	90 [h]
4	AVF/APB	IN	med	3	2, 10, 20, 30, 60	60 [b]
				3	5, 15, 45, 75, 90	90 [b]
				3	none	90 [h]
5	AVF/APB	IN	high	3	2, 10, 20, 30, 60	60 [b]
				3	5, 15, 45, 75, 90	90 [b]
				3	none	90 [h]
6	AVF/APB	IN	med	3	2	2 [b]
				3	5	5 [b]
				3	8	8 [b]
				3	10	10 [b]
7	DZP	IV	med	3	2, 10, 20, 30, 60	60 [b]
				3	5, 15, 45, 75, 90	90 [b]
8	DZP	IV	med	3	2	2 [b]
				3	5	5 [b]
				3	8	8 [b]
				3	10	10 [b]

Table A2.6. PBPK model parameters for DZP disposition in rats. Obtained from references [82] and [83].

Tissue	Flow Q (mL/min)	Volume V (mL)	Partition coefficient K_P
Adipose	2.55	10	21.28
Brain	0.78	1.2	1.67
Heart	4.2	1	5.46
Kidney	16.61	2	5.08
Liver	3.55	11	7.62
Lung	80	1.2	4.91
Muscle	16.25	125	1.88
Skin	7.1	43.8	3.30
Splanchnic	20.25	15	3.67
Stomach	1.9	1.1	5.16
Testes	1.9	2.5	5.13
Remainder	4.91	15.8	17.44
Venous blood	80	13.6	
Arterial blood	80	6.8	

Enzyme kinetic parameters for hydrolysis of AVF by APB and the ring closing rate of ORI measured *in vitro* were used to predict the rate of DZP production *in vivo*. The Michaelis–Menten fit is shown in Figure A2.67. As illustrated in Figure A2.67B, the APB concentrations were scaled with the AVF concentration so that hydrolysis of AVF would be complete at $t \approx 4$ min, regardless of the dose level. With calculated log partition coefficients (cLogD) of -1.71 at pH 7.4 and -2.85 at pH 6.5,[68] AVF does not readily partition into membranes. However, ORI and DZP can under passive transcellular transport. Absorption of these species is illustrated in Figure A2.68.

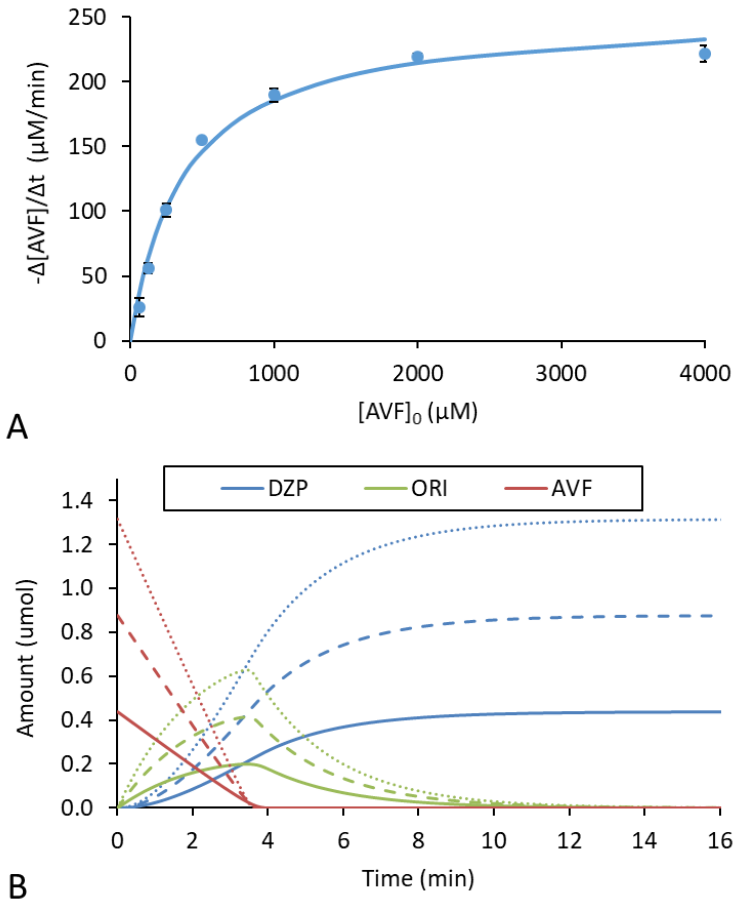

Figure A2.67. Predicted time course for the conversion of AVF to DZP by APB. (**A**) Michaelis–Menten equation fit to conversion rates measured using 15 µg/mL APB in pH 7.4 PBS at 32 °C, n = 3, R^2 = 0.988, K_M = 370±63 µM and V_{max} = 254±13 µM/min (±SE). (**B**) Time course prediction for the amounts each reaction species at each dose level based on measured Michaelis–Menten enzyme kinetic parameters, K_M and k_{cat}. Solid lines represent the low dose level (0.439 µmol AVF + 0.103 nmol APB), dashed lines medium dose level (0.878 µmol AVF + 0.205 nmol APB), and dotted lines high dose level (1.32 µmol AVF + 0.309 nmol APB) for a 0.250 kg rat. *In vitro* conditions simulated, i.e. no absorption.

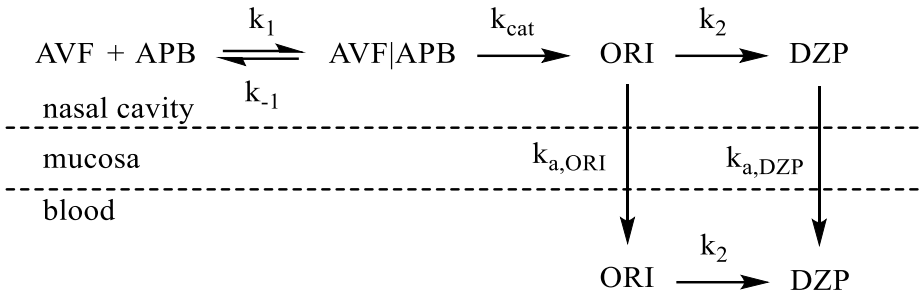

Figure A2.68. Schematic of AVF conversion to DZP. The rates constants for reversible binding of AVF to the active site of APB are k_1 and k_{-1}. The catalytic rate constant for conversion of AVF to ORI is k_{cat}. ORI spontaneously cyclizes to form DZP with cyclization rate constant, k_2. The values of these reaction rate constants were determined from *in vitro* measurements and their relationship to Michaelis–Menten enzyme kinetic parameters are shown in Equations A2.1-3.

$$K_M = \frac{k_{-1} + k_{cat}}{k_1} = 370 \pm 63\ \mu M \qquad \textbf{(A2.1)}$$

$$V_{max} = k_{cat} C_{APB} \Rightarrow k_{cat} = 1250\ \pm 60\ min^{-1} \qquad \textbf{(A2.2)}$$

$$k_2 = 0.470\ \pm 0.024\ min^{-1} \qquad \textbf{(A2.3)}$$

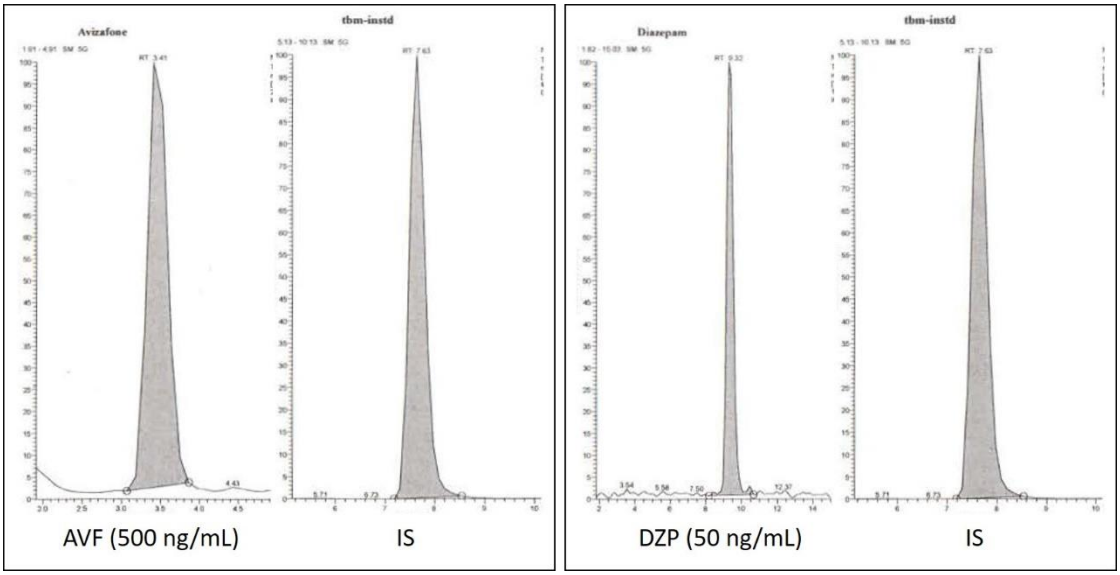

Figure A2.69. Representative LC-MS/MS chromatograms: AVF and DZP standards in plasma.

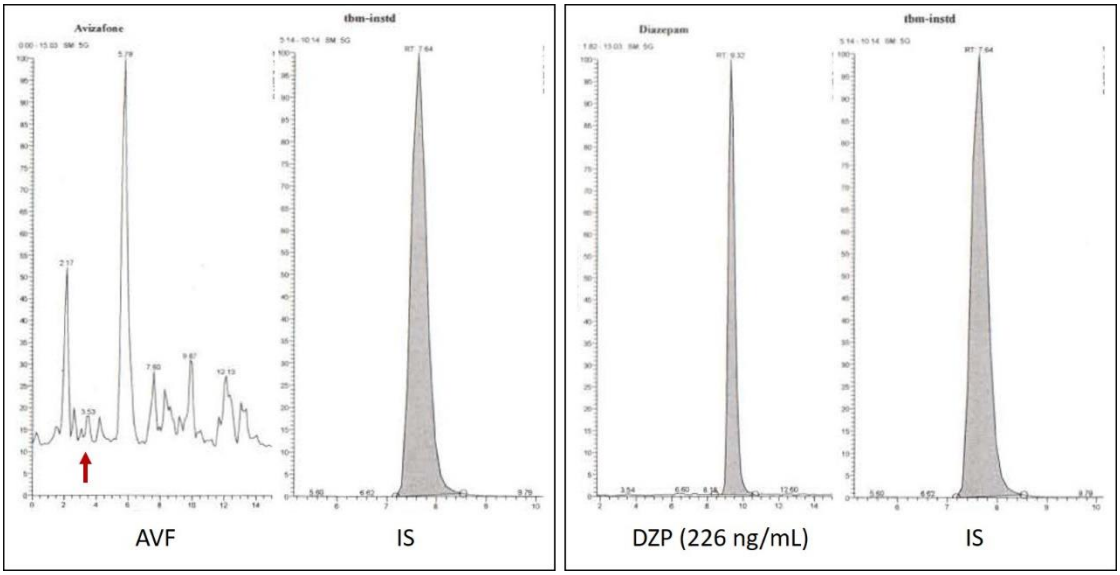

Figure A2.70. Representative LC-MS/MS chromatograms: rat #36, IN AVF+APB high dose, 10 min, plasma. In the AVF chromatogram, the red arrow indicates the location of the AVF retention time. There was no AVF detectable in this sample, only noise.

Table A2.7. Ions monitored by MS/MS.

Compound	Retention (min)	Precursor ion (m/z)	Product ion (m/z)
AVF	3.4	431 $[MH]^+$	246
DZP	9.3	286 $[MH]^+$ (Cl isotope)	193
Tolbutamide (IS)	7.6	269 $[M-H]^-$	170

Table A2.8. Nasal tissue histology incident report. NSF = nothing significant found.

		Dose Group	1	3	4	5
		Number of Animals	3	3	3	3
Tissue	**Lesion Type**	**Severity**	**Number of Incidents Observed**			
Turbinate 1	Cellular debris	Minimal		2	1	
	Cellular debris	Mild				1
	Eosinophilic fluid	Moderate			1	
	Epithelium missing	Minimal				3
	Hemorrhage	Minimal		1		
	Necrosis	Minimal		1		
	Necrosis	Mild			1	
	Ulcer	Minimal		1		
	Artifact	Minimal			1	
	NSF		3			
Turbinate 2	Cellular debris	Minimal				1
	Cellular debris	Mild				1
	Degeneration epithelium	Mild				1
	Hemorrhage	Minimal	1			
	Hemorrhage	Mild			1	
	NSF		2	3	2	1
Turbinate 3	Hemorrhage	Minimal	1			
	Hemorrhage	Mild			1	
	NSF		2	3	2	3
Turbinate 4	NSF		3	3	3	3
Turbinate 5	NSF		3	3	3	3

A3: Supporting information for Chapter 4

A4.1 Measurement of enzyme activity

An alternative non-drug chromogenic substrate, L*p*NA, was used as a surrogate for AVF in some experiments because there is no intermediate species formed upon hydrolysis. Hence, the active APB concentration (expressed as specific activity) was conveniently determined directly from the slope of linear absorbance increase at 405 nm, which is due to formation of the chromophore product, *p*NA.

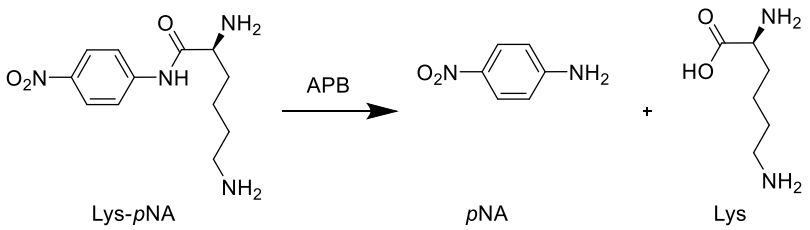

Figure A3.71. Reaction scheme for the hydrolysis of L*p*NA. The chromogenic substrate, S-Lys-*para*-nitroanilide (L*p*NA), can be hydrolyzed by Lys aminopeptidases to release the chromophore *para*-nitroaniline (*p*NA) that typically monitored at absorbance λ = 405 nm.

Table A3.9. Molar absorptivity temperature dependence.

Temp (°C)	Molar Absorptivity ($\mu M^{-1}cm^{-1}$)	
	L*p*NA	*p*NA
0	3.01E-05	0.00948
5	3.27E-05	0.00957
10	3.61E-05	0.00964
15	4.01E-05	0.00971
20	4.41E-05	0.00977
25	4.86E-05	0.00982
30	5.39E-05	0.00986
32	5.59E-05	0.00986
35	5.89E-05	0.00987
40	6.49E-05	0.00988
45	7.05E-05	0.00986

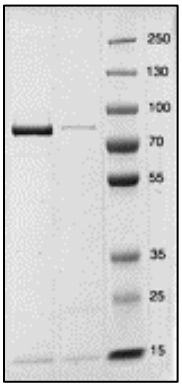

Figure A3.72. SDS-PAGE gel of APB. 4–20% gradient SDS-PAGE with purified APB in lane 1 at ~ 74 kDa and molecular-weight size marker in lane 3.

A4.2 Stability of lyophilizates at room temperature

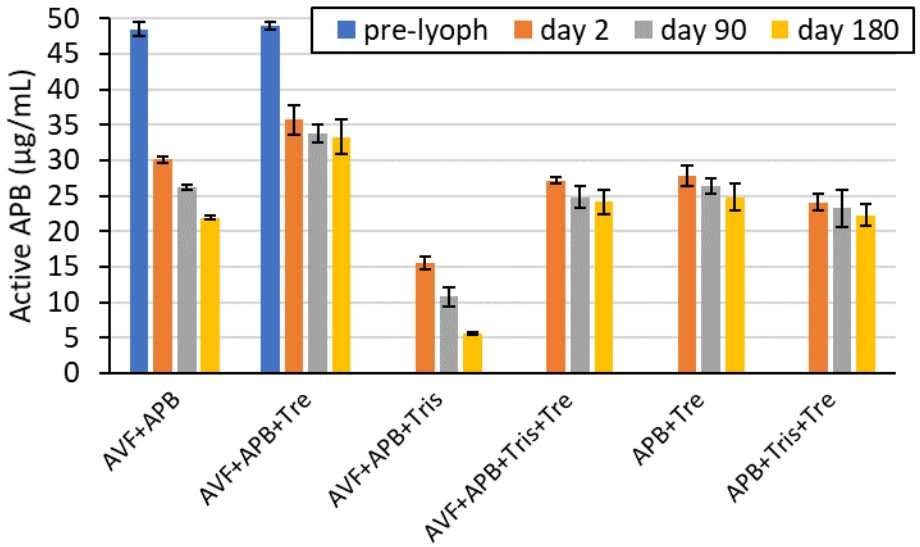

Figure A3.73. Lyophilizate formulations buffered with Tris. Optimum stability was achieved by co-lyophilization of APB+AVF+Tre without Tris buffer. Concentrations of active APB in the lyophilizates were measured in pH 7.4 PBS at 32 °C after storage for the specified time at 24 °C. Pre-lyophilization solutions contained AVF = 1.00 mM, APB = 50 µg/mL, Tre = 12.5 mg/mL, and/or pH 7.4 Tris buffer = 10 mM. Error bars are SD with n = 3.

A4.3 Base titration of AVF

The dihydrochloride salt of AVF (17.9 mg, equivalent to 10.1 mg of DZP) was dissolved in 100 µL of water and the solution was placed in the electrode well of a Horiba, Ltd. (Kyoto, Japan) LAQUAtwin pH-22 low volume pH meter. The initial concentration of AVF was 0.355 M with a measured pH of 2.72. The solution was titrated with 2.0 µL aliquots of pH 13.5 NaOH (0.316 M). The titrand solution was thoroughly mixed by stirring with the pipette tip and allowed to equilibrate to a stable pH after each addition. An inflection point indicating an apparent pK_a was observed at pH 7.54 after 56 µL of base was added.

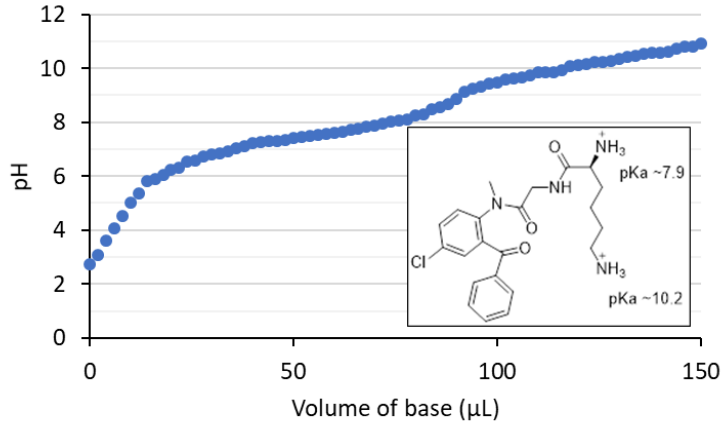

Figure A3.74. Titration curve for AVF. Titration of AVF, n = 1. Inset shows predicted pK_a values obtained from JChem by ChemAxon Ltd. https:// chemicalize.com/.

A4: Supporting information for Chapter 5

A4.1 Characterization of MDZ_{open}•2HCl

A4.1.1 Infrared spectroscopy (ATR-FTIR)

IR spectra of neat MDZ standard and MDZ_{open}•2HCl were measured at room temperature using a Bruker, Inc. (Billerica, MA) Vertex 80 spectrometer equipped with an attenuated total reflectance (ATR) accessory. The solid samples were pulverized and 64 scans from 4000-800 cm^{-1} at a resolution of 4 cm^{-1} were averaged. Samples were measured in triplicate, representative spectra a shown in Figure A4.75.

The IR spectrum of the MDZ standard was unremarkable between 1630-4000 cm^{-1} (Figure A4.75A). The fused ring structure of MDZ did not allow for the imidazole vibrational frequencies that observed with MDZ_{open}•2HCl. The unique peaks in the IR spectrum of MDZ_{open}•2HCl included a broad, jagged peak between 3100-2300 cm^{-1} that is characteristic the imidazole group; aromatic overtones at 1956 and 1799 cm^{-1}; and a carbonyl stretch from the benzophenone group at 1651 cm^{-1} (Figure A4.75B).

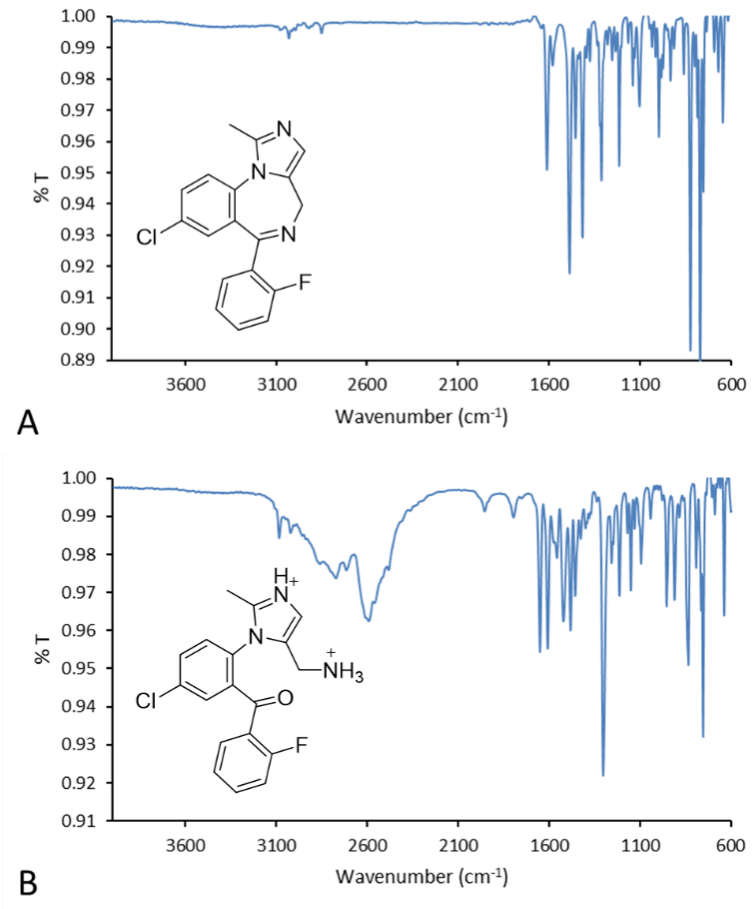

Figure A4.75. ATR-FTIR spectra. (**A**) MDZ standard. (**B**) MDZ_{open}•2HCl.

A4.1.2 Nuclear magnetic resonance (^{1}HNMR)

Solution state ^{1}HNMR spectra of MDZ standard and MDZ_{open}•2HCl were measured at room temperature using an Avance III HD spectrometer from Bruker Corporation (Billerica, MA). The spectra were processed with Mestrelab Research S.L. (Escondido, CA) MestReNova software version 12.0.4-22023. Automatic phase correction, full auto Bernstein polynomial baseline correction, and residual solvent peak suppression were performed before integrating the peaks. Samples were dissolved in D_2O, DMSO-d_6, or $CDCl_3$ had been allowed to equilibrate for more than 6 hrs. MDZ_{open}•2HCl was visibly insoluble in $CDCl_3$, even when subjected to heating and sonication.

The spectrum of MDZ_{open}•2HCl in $CDCl_3$ (Figure A4.76A) did not show analyte peaks because MDZ_{open}•2HCl was insoluble in $CDCl_3$. There were no detectable levels of

MDZ impurity as was evident by the absence of peaks from soluble analytes. Figure A4.76B shows that MDZ is readily soluble in $CDCl_3$ and produced the expected peaks. In D_2O, MDZ_{open}•2HCl converted to MDZ until equilibrium was reached (Figure A4.76C). Peak integrations in the spectrum were normalized to 8 total hydrogens in the aromatic region. There was geminal coupling of the stereotopic hydrogens on the fused diazepine ring of MDZ with a summed integration of 0.38. An integration of 1.65 was obtained for the same hydrogens that are homotopic in the open ring of MDZ_{open}, suggesting 19% of MDZ_{open} had converted to MDZ. In the same manner, 19% conversion to MDZ was calculated by comparing the 0.56 integration of the downfield shifted methyl hydrogens of MDZ to an integration of 2.44 for the same methyl hydrogens upfield in MDZ_{open}. MDZ_{open} also partially converted to MDZ in DMSO-d_6 (Figure A4.76F). Again, peak integrations in the spectrum were normalized to 8 total hydrogens in the aromatic region. One of the stereotopic hydrogens on the fused diazepine ring of MDZ was overlapping with the tail of what appeared to be a broad water peak. The hydrogen peak that was not overlapping had an integration of 0.29, indicating 29% conversion to MDZ. Two other peaks assigned to geminal coupled hydrogens in the open ring of MDZ_{open} were also obscured by the broad water peak. A 29% conversion to MDZ was confirmed by comparing the 0.87 integration of the downfield shifted methyl hydrogens of MDZ to an integration of 2.10 for the same methyl hydrogens upfield in MDZ_{open}.

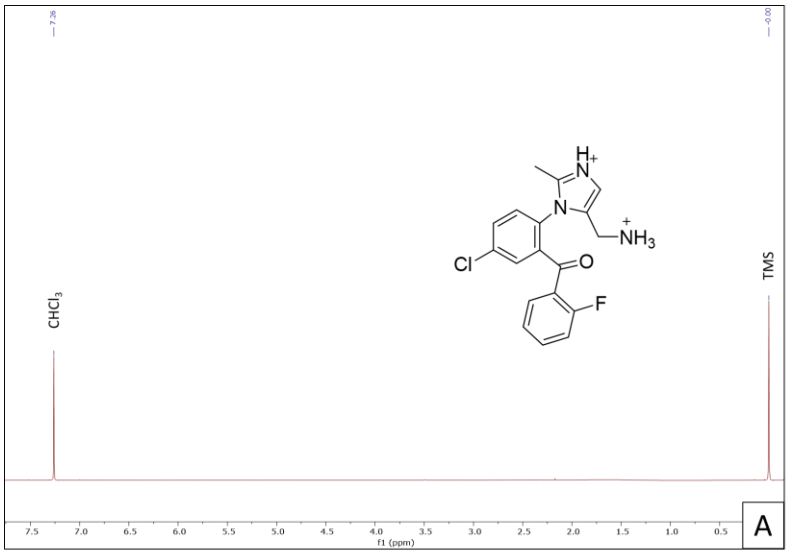
CHCl3
TMS
A

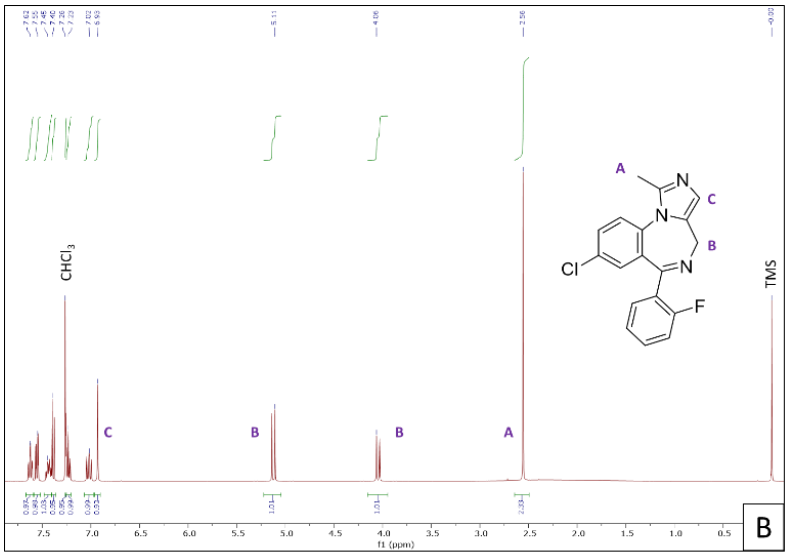
CHCl3
TMS
A
B
C
B
B
A
B

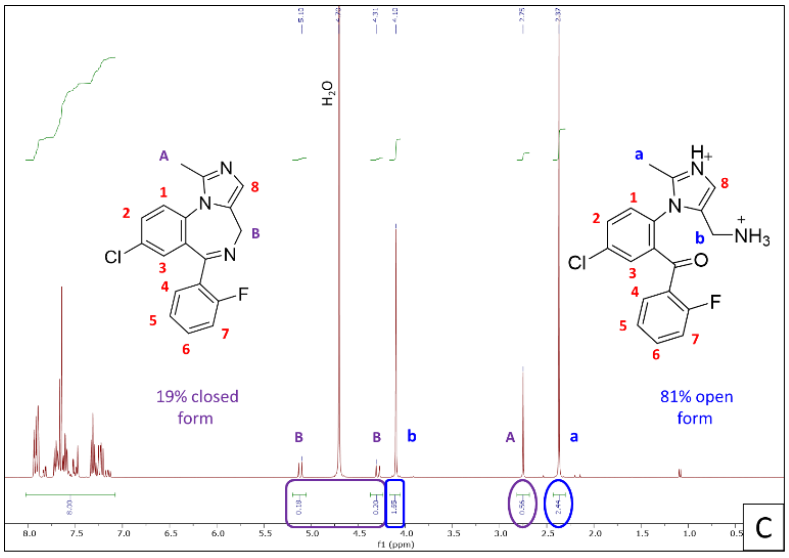
H2O
19% closed form
81% open form
B
B
b
A
a
C

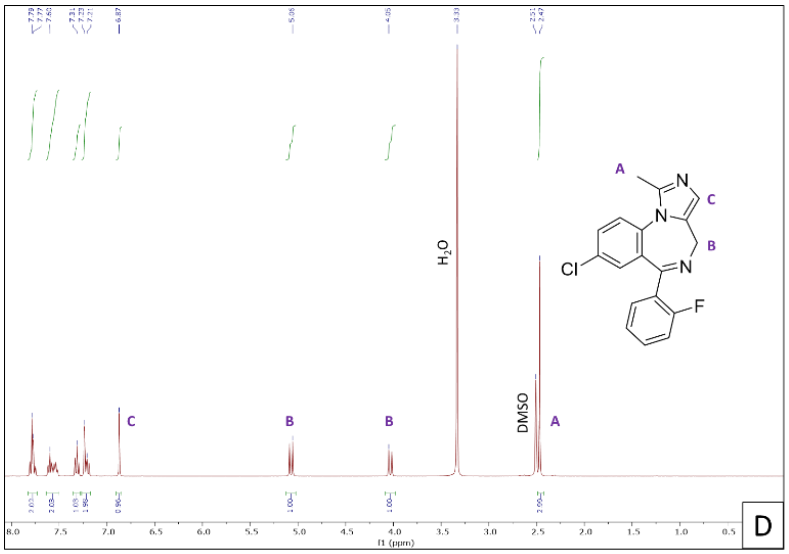
A
N
C
N
B
Cl
F
H2O
DMSO
C
B
B
A
D

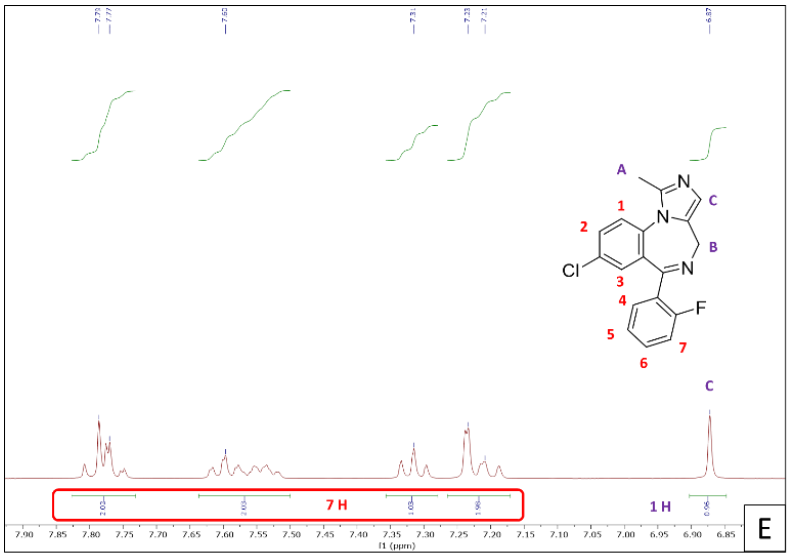
A
1
2
Cl
3
4
5
6
7
C
B
F
7 H
1 H
E

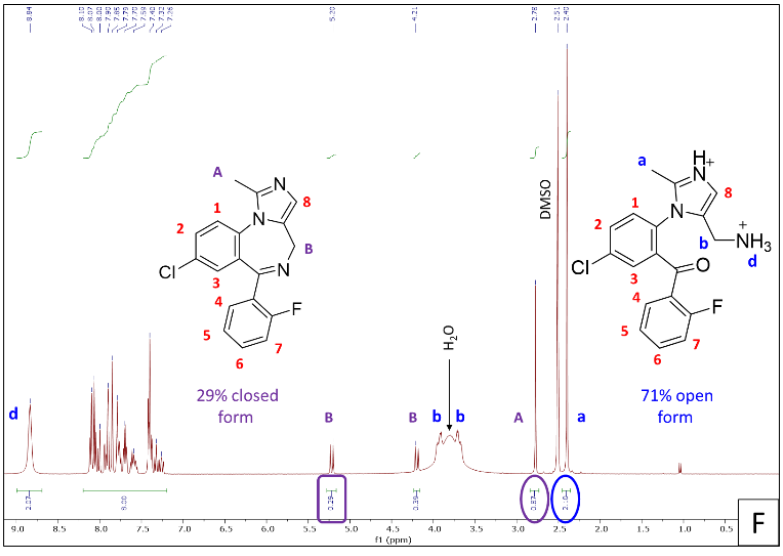
29% closed form
71% open form
DMSO
H2O
d
B
B
b
b
A
a
F

Figure A4.76. ^{1}H-NMR spectra. (**A**) MDZ_{open}•2HCl was insoluble in $CDCl_3$. (**B**) MDZ in $CDCl_3$. (**C**) MDZ_{open}•2HCl in D_2O partially converted to MDZ. (**D**) MDZ standard in DMSO-d_6. (**E**) Expanded view of the aromatic region of the spectrum shown in D. (**F**) MDZ_{open}•2HCl in DMSO-d_6. Partially converted to MDZ.

A4.1.3 Molecular dynamics simulations

Molecular dynamics simulations of the mono-cationic and di-cationic microspecies of MDZ_{open} were performed with Chem3D Ultra software version 16.0.1.4 from PerkinElmer Informatics, Inc. (Waltham, MA). A Molecular Mechanics 2 (MM2) force field was used to minimize the conformational energy at a rate of 1.000 kcal/atom/ps in 2.0 fs step intervals to a minimum RMS energy gradient of 0.010 kcal/mol/Å. Then, the intramolecular distance (d) between reactive centers (primary amine and carbonyl carbon of benzophenone) was measured in the energy minimized structures as shown in (Figure A4.77).

MM2 is a classical force field commonly used in molecular dynamics simulations to determine the 3D conformations of a broad range of small organic molecules. The calculated intramolecular distance, d, between reactive centers for cyclization of MDZ_{open} was 3.3 Å for the di-cationic microspecies and 6.1 Å for the mono-cationic microspecies (Figure A4.77). Reactive centers that are closer to each other in in the energy minimized conformation would have a higher collision frequency. Thus, the shorter distance that results from protonating the imidazole at low pH may contribute to the faster cyclization rate.

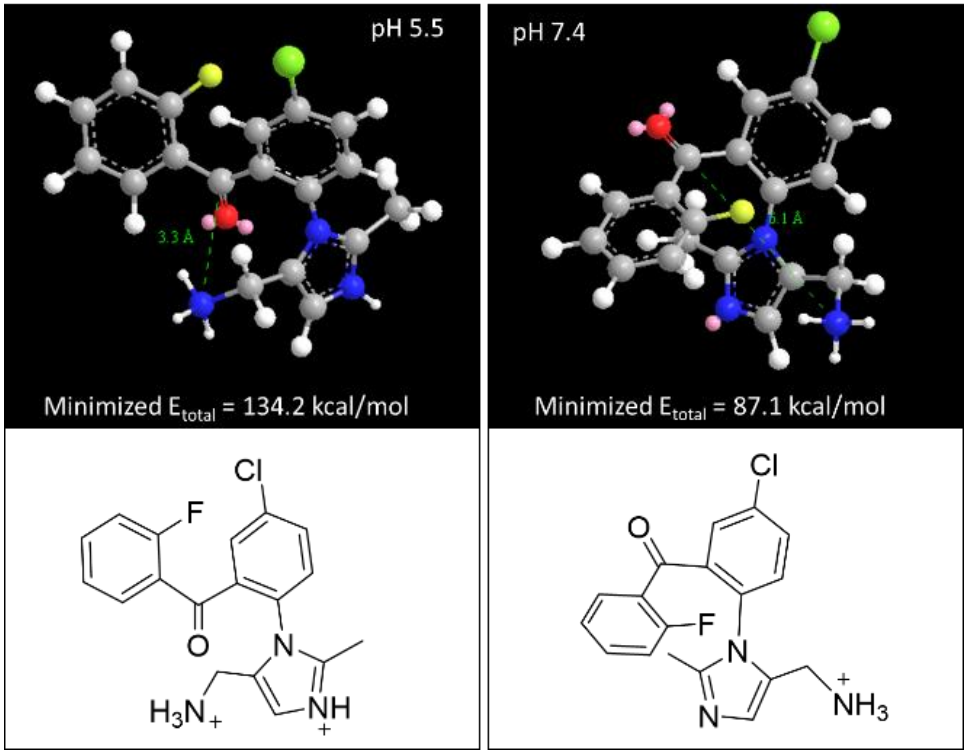

Figure A4.77. Energy minimized structures of MDZ_{open} microspecies. The proximity of reactive centers involved in the cyclization of MDZ_{open} were closer for the di-cationic microspecies (d = 3.3 Å) that predominates at pH 5.5 compared to the mono-cationic microspecies (d = 6.1 Å) that predominates at pH 7.4.

A4.2 Additional information for UV spectroscopy method

The analytical wavelength selected for UV spectroscopic monitoring of reaction progress was 300 nm, because the molar absorptivity (ε) of MDZ was not dependent on pH at this wavelength (ε = 1330 ± 50 $M^{-1}cm^{-1}$ ±SD, Figure A4.78). The absorbance spectra from 300-400 nm for Phe-MDZ_{pro}, Lys-MDZ_{pro}, and MDZ_{open} were nearly identical at a given pH owing to the relative transparency of the amino acid moiety (Figure A4.79). The ε of Lys-MDZ_{pro} and Phe-MDZ_{pro} standard solutions was 2510 ± 60 $M^{-1}cm^{-1}$ ±SD from pH 4.0-8.0 at 300 nm, with a slight increase in ε as the pH dropped below the pK_a of the imidazole (Figure A4.80). MDZ_{open} also had a similar spectrum as MDZ_{pro}. The ε of MDZ_{open} at 300 nm was assumed to have the same pH dependence as the prodrugs based on their structural similarity. Formation of the diazepine ring in MDZ caused a change in

ε at 300 nm, thus UV spectroscopy was useful for distinguishing MDZ_{open} from MDZ but not from MDZ_{pro}.

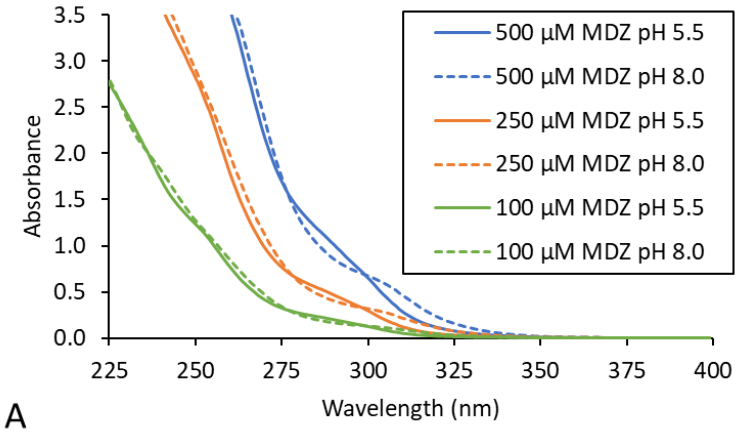

A

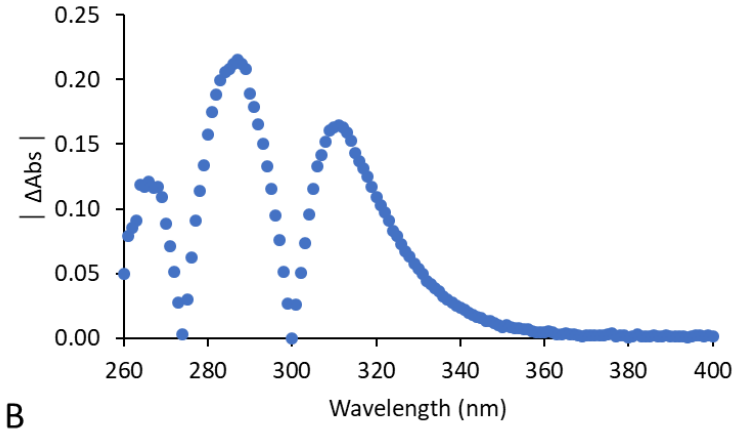

B

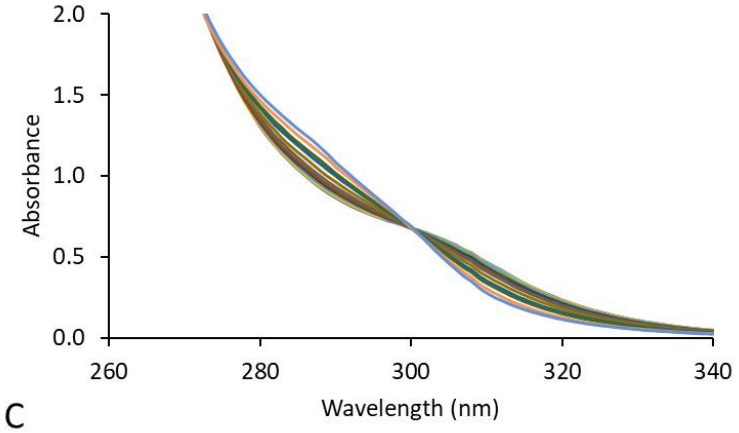

C

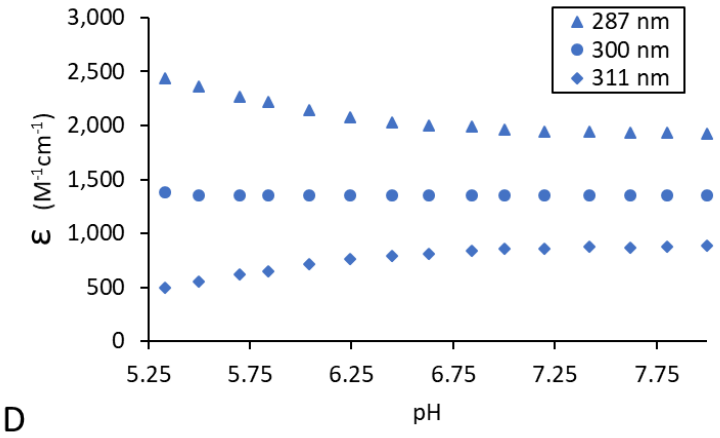

Figure A4.78. Effect of pH on the UV spectrum of MDZ. Measured in 20 mM PBS at 32 °C. (**A**) Isosbestic point at 300 nm was independent of MDZ concentration. (**B**) Absolute difference in absorbance of 500 µM MDZ at pH 5.5 and pH 8.0 shows equivalent molar absorptivities at 274 and 300 nm. (**C**) Evolution of the spectrum of 500 µM MDZ from pH 5.5 to pH 8.0 in ~0.2 pH unit increments. (**D**) Molar absorptivity pH dependence near the isosbestic point.

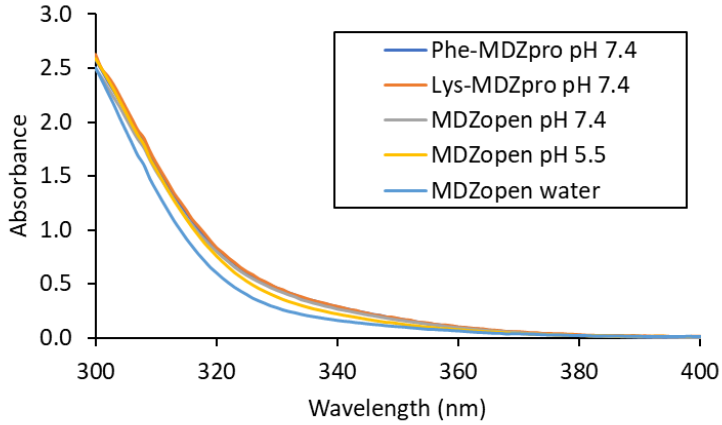

Figure A4.79. UV absorbance spectra of MDZ precursors. All samples were at 32 °C. pH was controlled at 7.4 and 5.5 with 20 PBS where indicated. MDZ_{open} samples were prepared by dissolving solid MDZopen•2HCl in pre-warmed buffer or water immediately before measurement to mitigate spontaneous conversion to MDZ.

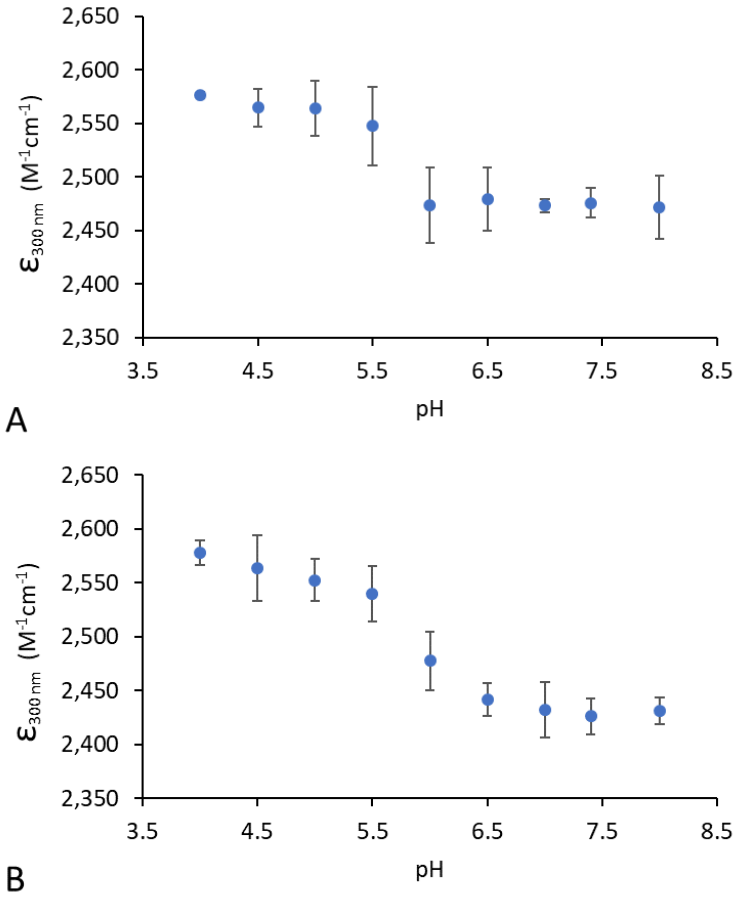

Figure A4.80. Molar absorptivity of MDZ prodrugs. Molar absorptivity (ε) measured at 300 nm and 32 °C with 1.00 mM of each prodrug in 40 mM PBS prepared at the indicated pH, n = 3. Slight change in ε observed near the pK_a of the imidazole. (A) Phe-MDZ_{pro}. (B) Lys-MDZ_{pro}.

A4.3 Additional information for HPLC method

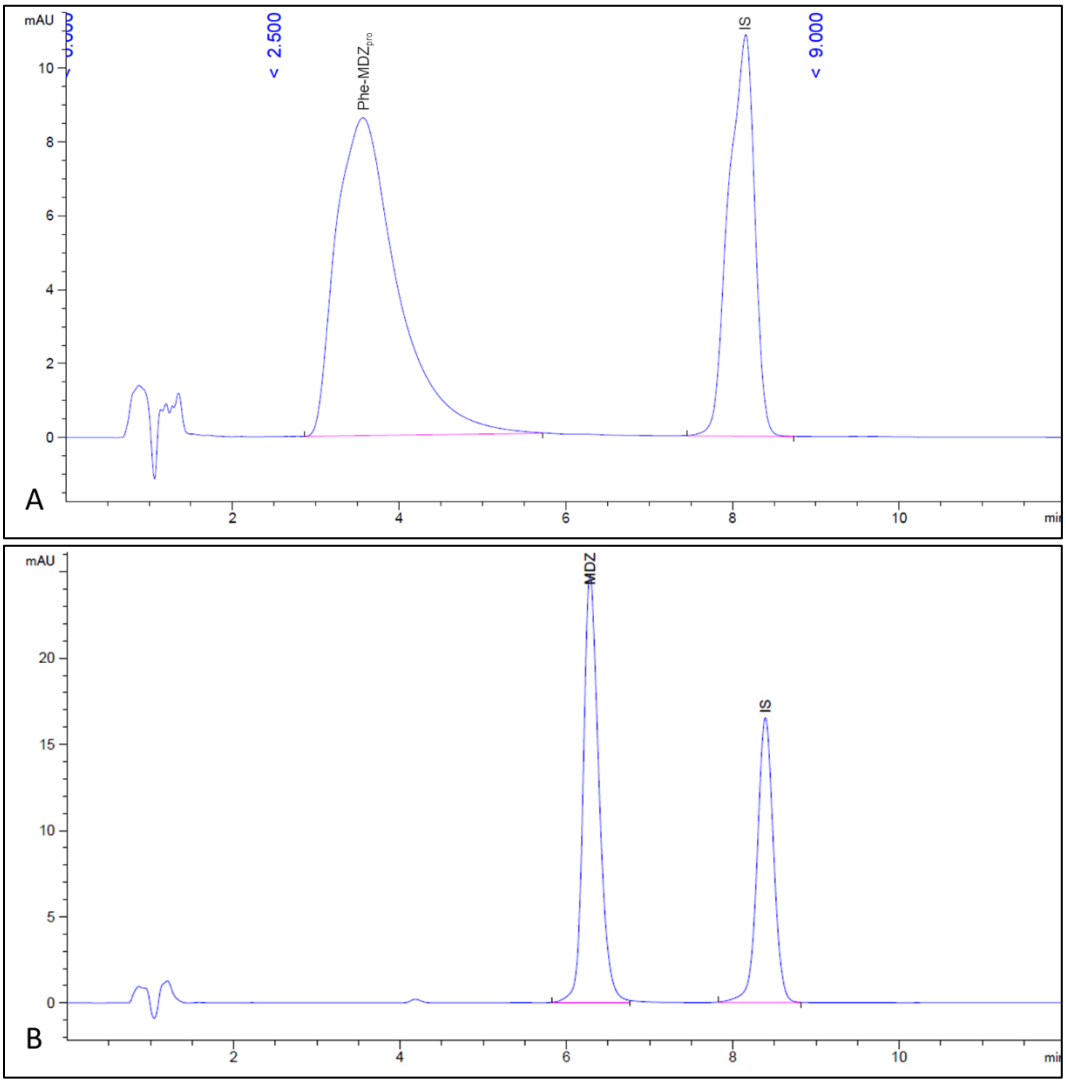

Figure A4.81. HPLC chromatograms. (**A**) 32.0 µM Phe-MDZ$_{pro}$ standard. (**B**) 32.0 µM MDZ standard.

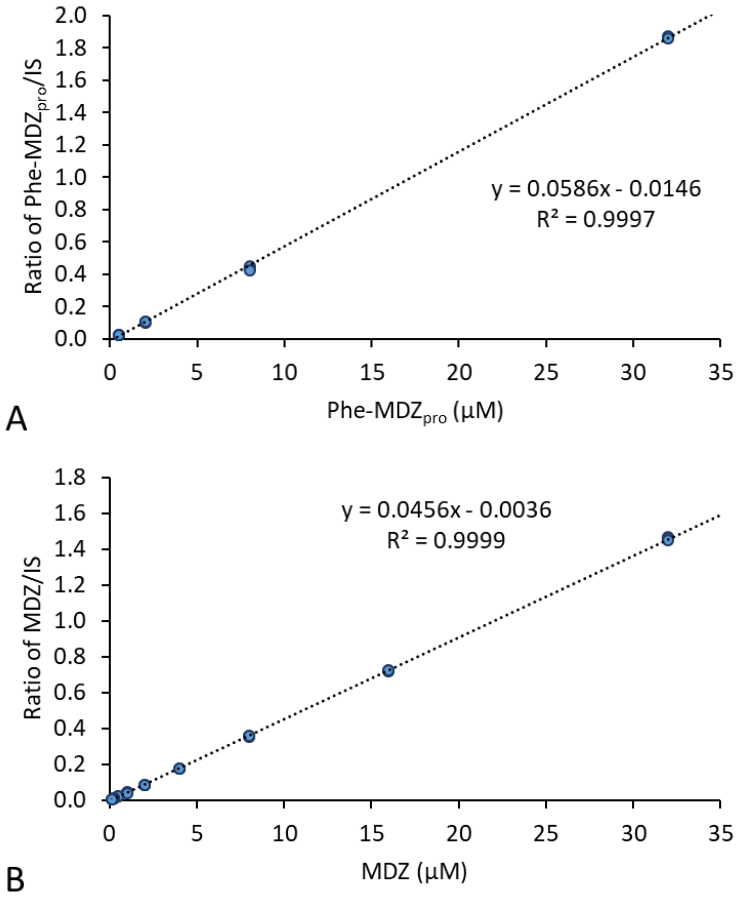

Figure A4.82. HPLC calibration curves. n = 3 (**A**) Phe-MDZ$_{pro}$: LOD = 0.297 µM (0.146 µg/mL), LOQ = 0.901 µM (0.443 µg/mL). (**B**) MDZ: LOD = 0.0696 µM (0.0227 µg/mL), LOQ = 0.211 µM (0.0687 µg/mL).

A4.4 APN enzyme kinetics

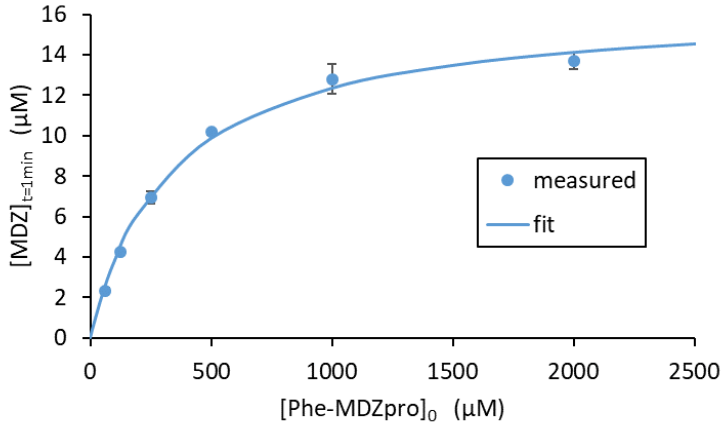

Figure A4.83. Enzyme kinetics for hydrolysis of Phe-MDZ$_{pro}$ by APN. The Michaelis–Menten equation was fit to the average MDZ concentrations measured by HPLC after

stopping the reactions with two volumes of acetonitrile. Phe-MDZ_{pro} with 15 µg/mL APN in pH 5.5 CBS at 32 °C, n = 3, R^2 = 0.996, K_M = 336 ± 39 µM and V_{max} = 16.5 ± 0.6 µM/min (± SE). The molecular weight of APN was 104 kDa, so k_{cat} = 114 ± 5 min^{-1}.

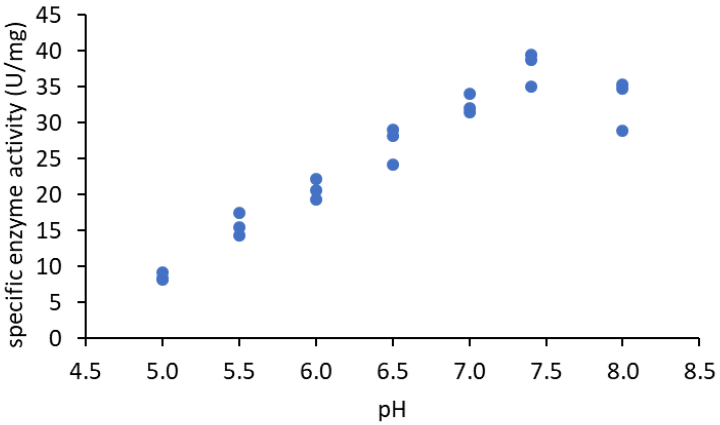

Figure A4.84. pH dependence of APN enzyme activity. The activity of 20 µg/mL APN was measured at 32 °C in 40 mM PBS using 1.00 mM of the chromogenic substrate S-phenylalanyl-*para*-nitroanilide (from a stock solution of the HCl salt in water) by the slope of the change in UV absorbance at 405 nm during the first 15 s of the reaction.

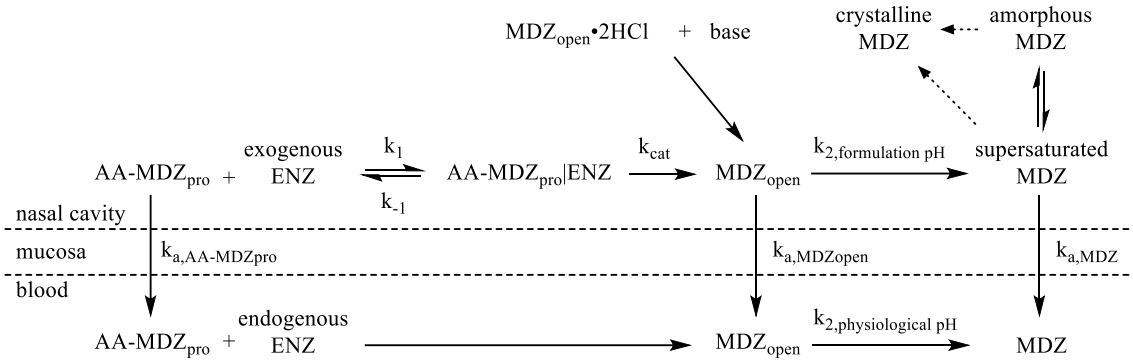

Figure A4.85. Schematic of MDZ absorption from MDZ precursor reactions. Both, prodrug/enzyme formulation and acid/base formulation, pathways proceed though the MDZ_{open} intermediate species to produce supersaturated MDZ in the nasal cavity. When the concentration of MDZ reaches the upper limit of supersaturation, MDZ will phase separate as an amorphous precipitate. The amorphous precipitate acts as a source of MDZ, so it remains available for absorption. Crystallization of MDZ (dotted arrows) could occur, but the process requires a nucleation event and lattice growth that is comparatively slower than absorption and mucociliary clearance.

A4.5 Titration of AA-MDZ_{pro}

Phe-MDZ_{pro}•2HCl (17.3 mg, equivalent to 10.0 mg of MDZ) was dissolved in 100 µL of water and the solution was placed in the electrode well of a Horiba, Ltd. (Kyoto, Japan) LAQUAtwin pH-22 low volume pH meter. The initial concentration of Phe-MDZ_{pro} was 0.307 M with a measured pH of 2.40. The solution was titrated with 2.0 µL aliquots of pH 13.5 NaOH (0.316 M). The titrand solution was thoroughly mixed by stirring with the pipette tip and allowed to equilibrate to a stable pH after each addition. The titration was stopped when persistent turbidity was observed. The titration curve is shown in Figure A3.74A.

Lys-MDZ_{pro}•3HCl (17.9 mg, equivalent to 10.0 mg of MDZ) was dissolved in 100 µL of water and the solution was placed in the electrode well of the low volume pH meter. The initial concentration of Lys-MDZ_{pro} was 0.308 M with a measured pH of 2.14. The solution was titrated with 2.0 µL aliquots of pH 13.5 NaOH (0.316 M). The titrand solution was thoroughly mixed by stirring with the pipette tip and allowed to equilibrate to a stable pH after each addition. The titration was stopped when persistent turbidity was observed. The titration curve is shown in Figure A3.74B.

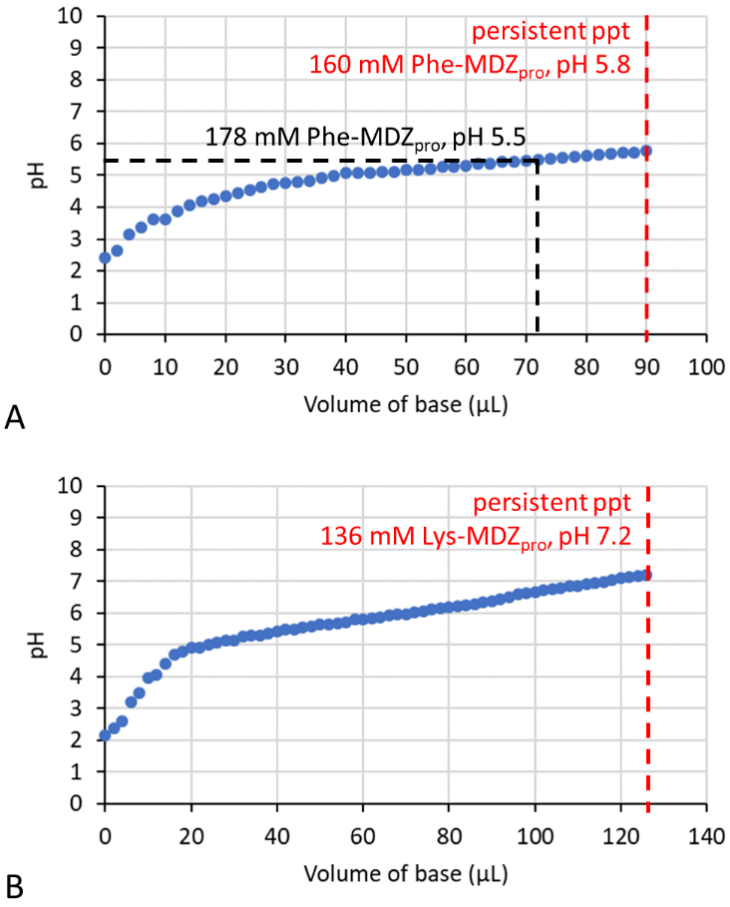

Figure A4.86. Titration curves for AA-MDZ$_{pro}$. (**A**) Titration of Phe-MDZ$_{pro}$•2HCl$_{(aq)}$, n = 1. The start of the buffering region was approximately pH 5.0. At 160 mM and pH 5.8, persistent turbidity was overserved in the titrand solution. An IN formulation utilizing Phe-MDZ$_{pro}$ would be adjusted to pH 5.5. (**B**) Titration of Lys-MDZ$_{pro}$•3HCl$_{(aq)}$, n = 1. The start of the buffering region was approximately pH 5.0. At 136 mM and pH 7.2, persistent turbidity was overserved in the titrand solution.